UNIVERSITÀ DEGLI STUDI DI MILANO

Scuola di Dottorato in Scienze e Tecnologie Chimiche

Corso di Dottorato in Scienze Chimiche – XXVIII ciclo

Magnetic Oxides Nanoparticles with Anisotropic Shape or Heterogeneous Structure

Tesi di Dottorato di:

Elena Capetti

Matr. n. R10161

Tutor: Prof. Rocco Martinazzo

Co-tutor: Dott. Alessandro Ponti

Coordinatore: Prof.ssa Emanuela Licandro

Anno Accademico 2014-2015

Table of Contents

1. Aim of the work

In order to develop successful applications in the field of nanotechnology, one of the most important challenge is to synthesize nanoparticles and nanostructures with precisely controlled size, shape, and composition in an economically and ecologically sustainable way. To achieve interesting results, it is necessary to combine an educated trial-and-error synthetic approach with very careful characterization in order to rationalize the synthetic methodology and find the relationships between size, shape, structure, and composition of the nanomaterials and their physical and chemical properties.

Nanoparticles of transition metal oxides aroused enormous interest because they are chemically stable while retaining the appearance of size-tunable properties at the nanoscale. These nanomaterials are strategic due to the wide range of fields they can be applied in. Indeed, metal oxide nanostructures are employed as:

- materials for energy, environment and sensors (catalysis and photocatalysis, fuel cells, and sensors)
- materials for electronics and hybrid photonic (light emitting transistors, transparent conductive oxides)
- material for drug development and platforms for diagnostics (drug delivery, drug development, diagnostics).
- materials for magnetic devices and spintronics (recording media, magnetic nanostructures, tunnel barriers)

In my research I focussed on the latter point, that is, the development of magnetic oxide nanoparticles with improved magnetic stability, in particular nanoparticles made of magnetic oxides (and sulfides) of the late metals of the first transition (Mn, Fe, Co, Ni). The above described research approach is particularly important for nanoparticles having magnetic properties that can be driven and tuned by controlling their composition, size and shape. It is well known that under a critical size, which typically is of the order of tens of nanometer, magnetic nanoparticles cannot be used as an information storage medium because their magnetization, which encodes information in its direction (up or down), changes direction very fast because of thermal agitation. To achieve magnetic stability, one has to improve the nanoparticle magnetic anisotropy and, *e. g.*, one can resort to shape anisotropy or to the unidirectional anisotropy caused by exchange coupling at the interface between ferromagnet and antiferromagnet (exchange bias). To introduce such anisotropies, one has to synthesize

anisotropic or heterostructured (core-shell) nanoparticles, which are very promising systems but, unfortunately, far from easy to synthesize.

The novelty of this PhD research work is that I intended to synthesize nanoparticle-based structures that exploit both approach to magnetic stabilization, that is, synthesize anisotropic core-shell nanoparticles comprising an antiferromagnetic core and a ferrimagnetic shell.

In particular, I aimed at developing synthetic methodologies (i) to prepare in a controlled way anisotropic MnO nanoparticles which could be used as anisotropic antiferromagnetic core and (ii) to coat such anisotropic antiferromagnetic cores with a ferrimagnetic iron oxide (Fe_3O_4 / γ-Fe_2O_3) shell in order to achieve an enhanced magnetic stability from the synergic effect between shape anisotropy and exchange bias. The final goal is to optimize the synthetic conditions by correlating the choice of synthetic conditions, the morphological-structural-compositional data and the resulting magnetic properties. Finally, one can note that iron and manganese are rather benign metals which do not significantly burden the environment regarding both their availability and disposal.

2. Brief summary

To briefly summarize the work reported in this PhD thesis, we can say that the study of the solvothermal synthesis of MnO NPs led to procedures to obtain anisotropic MnO NPs starting from manganese(II) oleate and stearate. A detailed investigation on the influence of the reaction conditions on the size, shape, crystal structure and magnetic properties of the obtained nanoparticles was carried out, including a detailed comparison between the two precursors (manganese oleate and manganese stearate) and surfactants (oleic acid and stearic acid) and a thorough investigation of the influence of the precursor : surfactant molar ratio.

Having used MnO as antiferromagnetic material for the core-shell structure, we were prompted to further consider the use of MnS, an antiferromagnetic sulfide with the Néel temperature ≅ 160 K (higher than the MnO T_N = 116 K). The higher Néel temperature makes MnS a good candidate for the building of an exchange-bias coupling. MnS, unlike MnO, presents three different polymorphs: cubic α-MnS (rock-salt), cubic β-MnS (zinc-blende), and hexagonal γ-MnS (wurtzite). Thus, synthetic investigation about MnS NPs was mainly focused on the control of the nanoparticle crystal phase that, in our case, could be achieve through the use of different surfactants. Polymorphism control is a crucial point because different polymorphs exhibit different physical properties, among which, the magnetic behavior.

Next, we focused on the synthetic strategy to coat anisotropic MnO NPs with a FeOx coating (FeOx stands for $Fe_{3-x}O_{4-x}$, $0 \leq x \leq 1$). We conceived to approach this problem by a two step strategy. First, we set out to develop a procedure to grow a FeOx shell (several nanometers thick) onto large (20-30 nm) isotropic MnO cores; once obtained such procedure, we will optimize it to uniformly coat anisotropic NPs. Using isotropic MnO NPs as cores, many synthetic strategies were devised and assessed with respect to the achievement of growing a significantly thick and uniform iron oxide shell simultaneously preventing the formation of undesired homogeneous iron oxide nanoparticles. We finally developed a procedure able to grow a FeOx shell of up to 6 nm on the MnO core. We are at present working on the development of a multi-step procedure to achieve a thicker and more compact FeOx shell. The synthesis of core-shell MnO@FeOx NPs and their characterization by electron microscopy (C-TEM, electron diffraction, HRTEM, Analytical TEM) are described in detail in the Thesis, while the magnetic characterization are in progress in these days.

Besides the main aim of my Thesis research, we decided to explore the feasibility to use MnO nanoparticles having different crystallographic faces as a catalysts in the water splitting reaction. We just started a collaboration with Dott. A. Minguzzi, O. Lugaresi and A. Visibile at the University of Milan to carry out an electrochemical study to investigate whether nanoparticle with different shape, the surface of which are different crystal faces, have unequal catalytic activity in the water splitting reaction. Since the work is at an early stage, here we reported only samples treatment and characterization before the electrochemical tests that are currently in progress.

Finally, a complete magnetic characterization of thin-film assemblies of Ni@NiO core-shell nanoparticles, was performed and here reported thanks to a research project carried out in collaboration with the group of Professor S. D'Addato, Dr. P. Luches, and Prof. S. Valeri at CNR NANO S3 and University of Modena and Reggio Emilia. Nanoparticles were synthesized by metal vapor deposition in Modena and their magnetic behavior was investigated in our laboratory by SQUID magnetometry. The Ni@NiO core-shell assemblies prepared by a three-layer procedure (NiO layer – Ni NPs – NiO layer) turned out to display a large exchange bias that could be accurately tuned by varying the thickness of the top NiO layer.

In order to provide a reference framework for my research work, the Introduction to this Thesis contains a brief description of the state of art regarding:

a) the solvothermal synthetic methods for MnO, MnS and MnO/FeOx nanoparticles:

b) the applications of MnO, MnS and MnO/ FeOx nanoparticles where their magnetic properties are exploited;

c) a brief description of the classes of magnetic materials and their properties.

3. Introduction

3.1. Types of synthesis

Here, we report some examples of published synthetic methods for MnO, MnS and MnO/FeOx NPs in order to clarify the motivations which prompted us to focus our attention to the solvothermal method and outline the present state of art, also to better understand the novelties emerged in our work.

3.1.1. MnO - types of synthesis

In the field of MnO nanoparticle synthesis, in the literature can be found a wide range of methods such as vapor decomposition, electro-deposition, sol–gel process, co-precipitation and hydro- or solvothermal decomposition. Among these methods, particular attention was focused on co-precipitation, hydrothermal and solvothermal decomposition, which are easy and cheap techniques (not requiring highly specific instrumentation) and are amenable to the use of not toxic and environmental friendly reagents. In these procedures the MnO nanoparticles are synthesized in a solvent, (respectively an aqueous solvent for co-precipitation or hydrothermal and an high-boiling organic solvent for solvothermal) in presence of a metal precursor of different nature. The co-precipitation method is easy and quickly but the uniformity in size and shape is not accurately controlled. Conversely, the solvothermal method is very effective to control the nanoparticle morphology. It is possible to obtain spherical NPs with a very low size dispersion and to finely control the formation of different shapes such as rod, dumbbell, octahedral, hexapod, or flower.[1]

However, optimizing the reaction conditions in a solvothermal synthesis is not easy nor quick. By now, in literature can be found many different synthetic procedures which could lead to the desired nanoparticle size, shape and crystal structures.

3.1.1.1. Co-precipitation and hydrothermal methods

A huge number of co-precipitation synthesis have been reported in the last decade. We limit ourselves to cite a few significant examples. In 2010 Ju Baek et al. synthesized water-soluble nearly spherical monodisperse MnO nanoparticles starting from $MnCl_2.4\ H_2O$ and triethylene glycol in water with the addition of NaOH for oxide NP formation and precipitation.[2] In 2011, another paper reported the comparison between water and ethanol as solvent using the same synthesis procedure. Starting from $MnCl_2$ as precursor, a 1 M solution was added to both solvents and a salt precipitation was clearly visible at pH = 10. In this type of reaction, the pH value could be increased by adding a precipitating agent such as NaOH or ammonia also because the Mn ion in aqueous solution is acidic. Hydroxyl anions react with manganese ions to form a solid precipitate via either olation or oxilation. The dissociation of NaOH occurs differently in ethanol than in water. Despite the different dissolution mechanisms, both solvents lead to the formation of amorphous MnO nanoparticles.[3]

In the same years, Thota and co-workers described an hydrothermal procedure to synthesize manganese oxides nanoparticles (which exhibit interesting magnetic properties). In this case, the authors were able to control the crystal composition (MnO, Mn_2O_3 or Mn_3O_4) and the resulting shape (sphere, rods, clusters, wires, platelets, ellipsoids, cubes, rhombohedra). The synthesis is based on the use of Mn-acetate and oxalic acid in ethanol at low temperature. This reaction gives a white gel that is decomposed at high temperature (500-800°C) under different gas (*i. e.* oxygen, nitrogen, argon) to form different MnO/Mn_2O_3 beads or clusters. Reaction conditions was tuned in order to obtain the desired shape and crystal structure.[4] An uncommon procedure was reported in 2012 by Bastami et al. who obtained MnO octahedral nanoparticles from Mn-acetate in milliQ water. The solution was circulated in the presence of EMF and then by circulating pump. The precursor solution was put in an erlenemayer flask as sonochemical vessel and then sonicated in a bath. This method is an excellent method to synthesize naked nanoparticles without the need of an organic surfactant in the reaction mixture. Nanoparticles are regular rock-salt crystals and only long reaction times give nanoparticles with some impurity of MnO_2 or Mn_3O_4.[5]

3.1.1.2. Solvothermal methods

In the last decade, solvothermal reactions were deeply investigated in order to achieve a fine control of the nanoparticles characteristics. The solvothermal reaction set up presents a number of parameters which could be changed and differently combined and it is very hard to forecast the outcome. Thus, this methodology is still largely studied and reported in a vast number of paper. Here we mention some examples, distinguishing between papers where spherical nanoparticles are synthesized and papers where MnO nanoparticles with anisotropic shapes are obtained. In particular we focus our attention on this last type of NPs.

One of the first solvothermal synthesis of MnO nanoparticles were published by Hyeon and co-workers in 2004 which synthesized regular and size uniform MnO nanospheres and nanorods reacting $Mn_2(CO)_{10}$ and oleylamine in trioctylphosphine at high temperature for 1 hour.[6] This reaction was the first of long series of very similar synthetic procedures published in the following years. An inorganic or organometallic manganese precursor such as $Mn_2(CO)_{10}$, [Mn(acac)$_2$], $MnCl_2$, Mn carboxylates (including formates, acetates, and long-chain carboxylates), and $Mn(NO_3)_2$[1] are dissolved in an very solvent (*i. e.* 1-octadecene, 1-hexadecene, dibenzyl ether, diphenyl ether, trioctylphosphine, trioctylphosphine oxide) and one or more long-chain aliphatic surfactants are added to tune the NP size, shape and crystal structure and to stabilize the final nanoparticle dispersion in a non-polar solvent such as hexane or toluene. The most popular surfactans are: a) carboxylic acids such as oleic acid (or stearic, myristic, decanoic and dodecanoic acid);[7] b) amines such as oleylamine (or octadecyl, hexadecyl and dodecyl amine) and c) thiols, such as 1,2-hexadecathiol, whose role in the reaction it is not yet completely clear, but it seems that 1,2-hexadecathiol is able to improve the NP monodispersion and the shell uniformity in the case of core-shell NPs.[8]

3.1.1.3. Examples of solvothermal synthesis of spherical NPs

In 2010, Schladt et al., by decomposition of manganese(II) oleate in 1-octadecene at very high temperature, synthesized monodisperse MnO spherical nanoparticles.[9] In the same year, Lopez-Ortega et al. obtained MnO monodisperse nanospheres with controlled dimensions. They were able to tune the desired size by changing the surfactant: Mn molar ratio from 1 to 40. They used manganese acetyl-acetonate as metal precursor, oleylamine as surfactant and dibenzyl ether as solvent in presence of a fixed amount of 1,2-hexadecanediol.[10] Some years

later, another group reported the possibility to tune the size of monodisperse spherical NPs between 6 and 32 nm by changing the reagents' amount or the reaction time. In this case, the authors started from a suspension of MnO bulk powder and oleic acid in 1-octadecene.[1] A peculiarity was reported by Chen et al. in 2011 who synthesized MnO nanoparticles by a classical route but observed that oxidizing the oleic acid by potassium permanganate it was possible to change the manganese oxide crystal phase from MnO to MnO_2.[11]

3.1.1.4. Examples of solvothermal synthesis of NPs with anisotropic shape

The first paper on MnO nanoparticles with anisotropic shape was published in 2004 by Park et al. that described the synthetic procedure to obtain size uniform MnO rods starting from a mixture of dimanganese decacarbonyl, oleylamine and trioctylphosphine. Changing the type of phosphine it is possible to tune the nanoparticle shape from sphere to rod.[6]

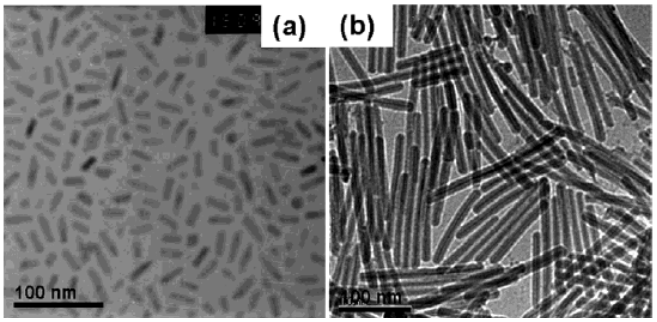

Figure: low-resolution conventional TEM images of 7 x 33 nm and 8 x1 40 nm sized MnO nanorods. Image from ref. 6

In 2005 Zitoun et al. reported a synthesis which started from Mn(II)-oleate and oleic acid in trioctylamine. Tuning the reaction time and the reagent amount they obtained pentapods and hexapods with elongated branches which are very homogeneous in size and shape.[12]

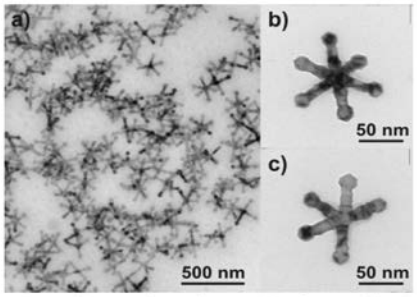

Figure: TEM image of an assembly of MnO multipods(a), a hexapod (b), and a pentapod (c). Image from ref. 12

Another example of anisotropic shape are the dumbbell MnO nanoparticles reported in 2006 by Zhong et al. They synthesized the dumbbell-like nanoparticles starting from the pyrolysis of manganese formate hydrate in oleic acid and trioctylamine. The dumbbells are homogeneous in size and morphology. It is clearly distinguishable two-arm dumbbells with the two arms align in a line; the three-arm dumbbells with a T-structure and four-arm dumbbells with a cross structure. The 1D growth route was explained by the orientation aggregation mechanism.[13]

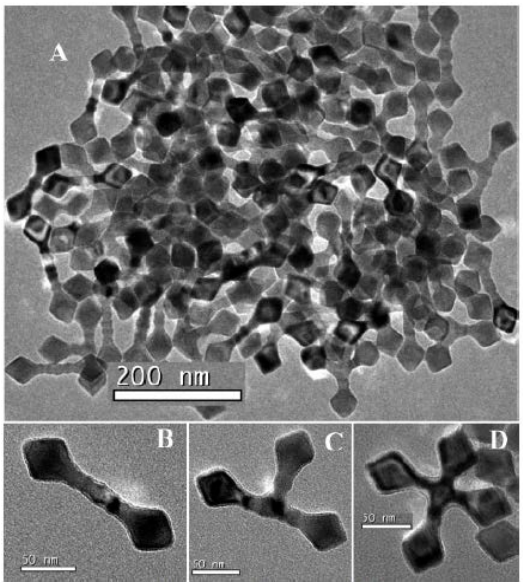

Figure: low-magnification TEM images of MnO dumbbells: (A) ensemble, (B) two arms, (C) three arms, (D) four arms. Image from ref. 13

Then Ould-Ely at al. in 2006 investigated different trioctylamine/oleic acid (or trioctylamine/stearic acid) and H_2O/Mn precursor molar ratios and obtained a progression of forms from squares to cross and multipods with defined jagged edges through progressive "etched" steps.[14]

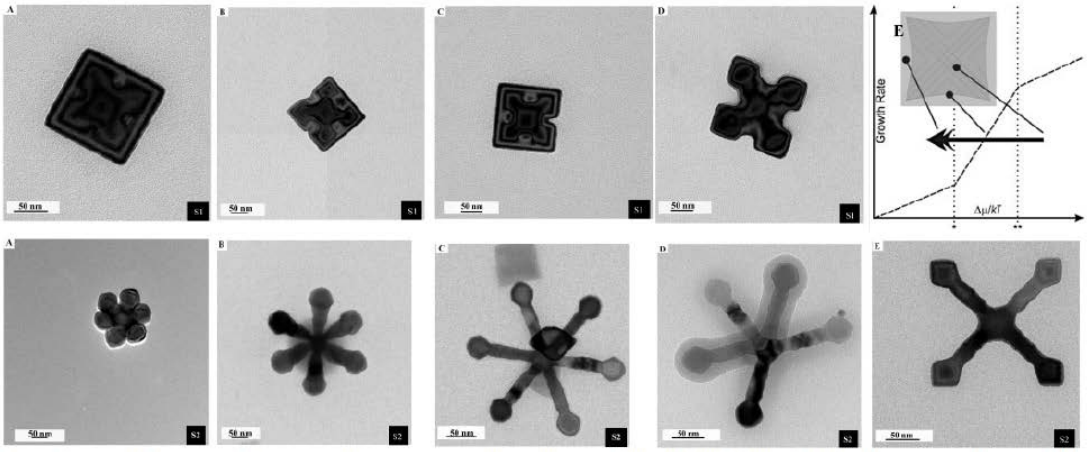

Figure: progression of forms ranging squares through partially "etched" squares to fully formed cross and their derivatives. Series 1 shows evolution of crystal growth conditions and texture of the evolving crystal. Series 2 is the progression of a hexapod nanoparticle to octahedral structures and derivatives. Image from ref. 14

In the following year, the same group[15] showed the conversion of the MnO NPs into a mixture of MnO and Mn_3O_4 nanoparticles with retention of the shape. The conversion is carried out by heating the nanoparticles in solvent (such as hexadecane) or exposing them to air (at high temperature or at room temperature suspended in hexane). The electron diffraction (ED) shows the formation of the Mn_3O_4 phase and exhibit moiré interference patterns due to the presence of two closely aligned and similar crystal structures which are.

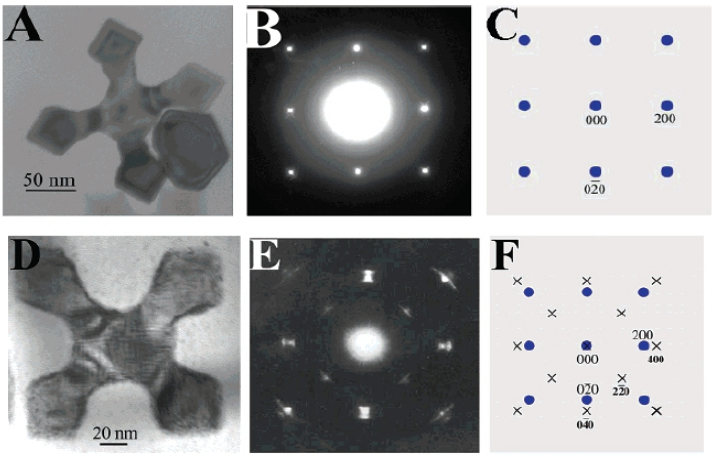

Figure: TEM images teken at [001] axes.(A) one fresh nanocross, (B-C) experimental and simulated SAED patterns confirming the fcc-MnO lattice. (D) an aged nanocross, (E-F) experimental and simulated SAED patterns showing two sets of distinct diffraction spots attributed to MnO and Mn_3O_4. Image from ref. 15

In 2007, Chen et al. starting from manganese(II) stearate in octadecene and varying temperature and surfactant nature (alcohol or carboxylic acid), obtained a fine control on the nanoparticles shape. Octadecanol seems to be an activation reagent while stearic acid an inhibitor when they are added prior to heating. The resulting shapes are: rice, rods, peanuts, needles, and dots.[16]

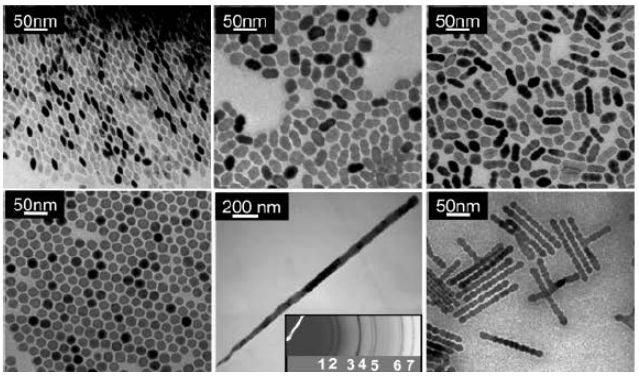

Figure: TEM images of differently shaped MnO nanocrystals. Spherical MnO were synthesized by $MnSt_2$ with excess 1-octadecanol. Rice-shaped and other elongated MnO nanocrystals were synthesized by $MnSt_2$ with stearic acid. Rice-shaped MnO nanocrystals appeared at a very early stage. Image from ref. 16

Xi-Guang and co-workers described the synthesis of six-horn-like branched MnO nanoparticles by thermal decomposition of $Mn(CH_3COO)_2$ in the presence of 1-octylamine and oleic acid. The microscopic characterization shows that the branches grew along the [100] direction with a bundle of nanorods. Experimental evidences demonstrated that the formation of branches can be divided into two steps: (i) formation of octahedral NPs with polar surfaces and (ii) following directional etching. It is likely that the solvent mixture with oleic acid and organic amines favors the formation of MnO octahedra, then the oleic acid becomes responsible for the etching process and the consequent evolution of six-horn-like MnO nanoparticles.[17]

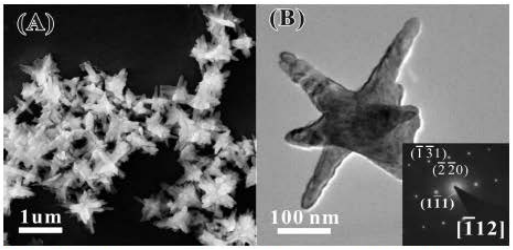

Figure: (A) low-magnification SEM image and (B) TEM image of a six-horn-like MnO nanostructure synthesized by refluxing octahedral MnO nanoparticles with oleic acid and 1-octylamine at 400°C for 30 minutes. Image from ref. 17

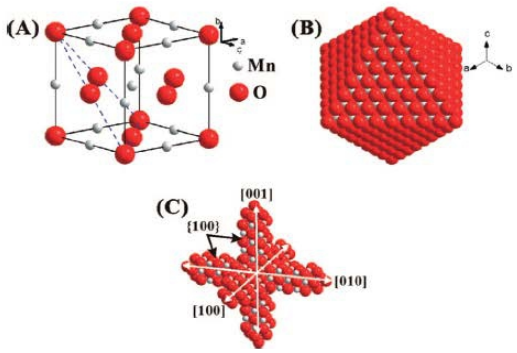

Figure: schematic model of (A) a MnO unit cell, (B) a MnO octahedron, and (C) a six-horn-like MnO. Image from ref. 17

In 2010, Puglisi et al. reported the synthesis of spherical and octahedral MnO nanoparticles starting from Mn(II) monooleate, Mn(II) dioleate or Mn(II) distearate. In particular, they described that in the same reaction it was possible to control the MnO vs. MnS nanoparticle formation changing the molar ratio between manganese precursor and elemental sulfur. On the other hand, it was possible to tune the size and shape of the MnO nanoparticles changing the type of manganese precursor or reaction time, temperature and heating rate. Some preliminary tests showed the possibility to obtain anisotropic nanoparticle shapes starting from Mn(II) stearate.[18]

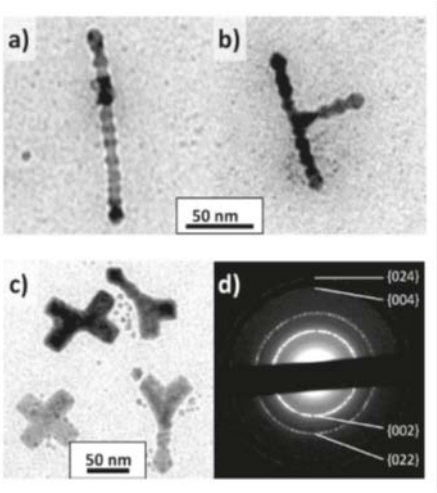

Figure: TEM images of alpha MnS and MnO nanoparticles with highly anisotropic shapes. (a) jagged-edge rods and (b) jagged-edge T-shape nanocrystals were obtained by manganese distearate as precursor. (c) Crosses and cross-rod NPs were synthesized by using high amount of oleic acid.(d) electron diffraction pattern. Image from ref. 18

Some years later (in 2012), An et al. described a solvothermal procedure to synthesize nanocubes, nanorods and tetrahedral nanoparticles controlling the final dimensions. 16 nm nanocubes were obtained decomposing manganese oleate in octadecene at 320 °C for 30 min. If the reaction mixture is heated for 1 hour, 29 nm nanocubes are formed. Replacing 1-octadecene with 1-hexadecene, octahedral nanoparticles were produced with an average edge length of 26 nm. Furthermore, by decomposing Mn(II) oleate in 1-hexadecene in the presence carboxylic acid as surfactant, spherical nanoparticles were obtained. In particular, the reaction mixture was heated for 2 h to reflux at 288 °C with a rate of 5 °C/min and spherical MnO nanocrystals with diameters of 3, 5, 11, and 13 nm were generated using behenic, stearic, myristic, and decanoic acid, respectively, as carboxylic acid surfactant. On the other hand, to synthesize rod shaped nanoparticles, the authors started from Mn(II) oleate in 1-hexadecene with myristic acid or decanoic acid, heated to 280 °C for 2 h with a rate of 2 °C/min. Tetrahedral nanoparticles were synthesized heating Mn(II) oleate in phenyl ether at 260 °C with a rate of 2°C/min. Furthermore, oleyl alcohol was added. Nanotetrahedra with edge lengths approximately of 6, 8, and 20 nm were prepared by changing the heating rate and reaction time.[7]

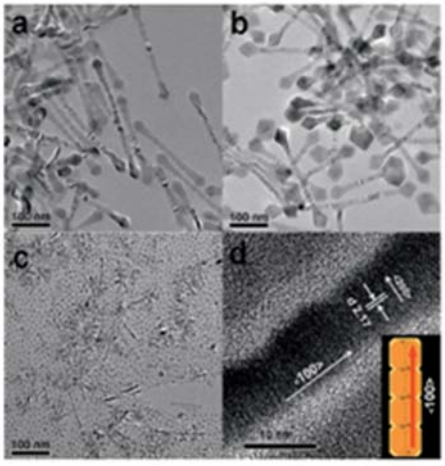

Figure: TEM images of (a) rod-shaped, (b) T-shaped MnO nanocrystals and (c) a mixture of spherical and anisotropic MnO NPs. (d) high-resolution TEM image of MnO rod nanocrystal with oriented attachment along the <100> direction. Image from ref. 7

Finally, F.J Douglas et al.[19] and A. Kim et al.[20] (2014) reported the synthesis of MnO octapod nanocrystals for biomedical and catalytic application, respectively. In the figure below, we can observe nano octapods synthesized by Douglas and co-workers starting from manganese acetate with oleic acid and oleylamine in 1-octadecene. Octapods show a high uniformity in size.[19]

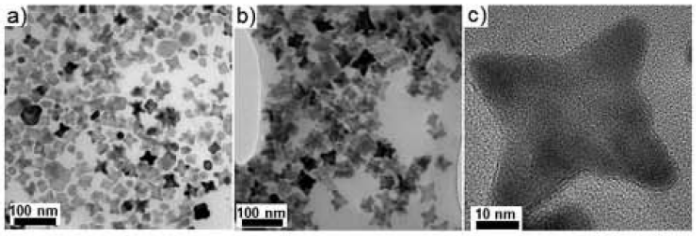

Figure: TEM images of octapods particles obtained from (a) manganese acetate and (b and c) [$Mn_3O(OAc)_6(Im)_3][OAc]$, the latterv showing an octapod viewed down the [100] zone axys. Image from ref. 19

3.1.2. MnS - types of synthesis

Similarly to the MnO oxide, MnS could be synthesized by a wide range of methods but the hydrothermal and the solvothermal methods are the most common considered. Differently to the MnO (which exists only in the rock-salt crystal structure), the sulphide present three crystallographic polymorphs: cubic α-MnS (rock-salt), cubic β-MnS (zincblende), and hexagonal γ-MnS (wurtzite).

In the majority of literature reports, the synthesis of MnS NCs led to structurally pure products. Different crystal phases show different physical properties, then it is useful to obtain pure polymorph sample. For MnS, the synthesis purposes involve not only the size and shape control, but also the control on the crystal structure. Accordingly, reaction temperature is a key physical parameter, since high temperature usually favors the chemical equilibrium and the formation of the most stable phase. One of the first MnS synthesis study described that heating Mn(II) diethyldithiocarbamate in hexadecylamine at low *T* (120-150 °C) gave multipods comprising γ-MnS arms stemming from a β-MnS core whereas 30 nm α-MnS cubes were obtained at 180 °C.[21] Then, a more detailed investigation in 2012 gave similar results for the reaction of Mn(II) chloride and thioacetamide in oleylamine, confirming the fundamental role of temperature.[22] These authors reported the β → α and γ → α phase transformation of MnS nanoparticles subjected to high pressure. The formation of α- *vs.* γ-MnS nanoparticles seem to depend also to the heating rate (15 °C/min: α-MnS; 25 and 35 °C/min: γ-MnS) when Mn(II) diethyldithiocarbamate was heated in octadecene at 320 °C in the presence of large excess of both oleic acid and oleylamine (100:1 with respect to Mn).[23] To summarize, only few examples of synthetic procedures reported are able to allow the synthesis of three (at least two) MnS polymorphs starting from the same solvothermal reaction and applying only small variations.

Some papers reported also the ability to tune nanoparticles size and shape by solvothermal reaction. In the previous example, starting from Mn(II) diethyldithiocarbamate or phenanthroline Mn(II) diethyldithiocarbamate as precursors, authors have been able to obtain hexapod, octahedral, and hexagonal α-MnS nanoparticles whereas the γ-MnS presented a pencil-shaped with size uniformity.[23] In a another paper published in 2011, the presence of oleic acid and oleylamine into the reaction mixture made by Mn(II) oleate, sulphur and octadecene could switch the nanoparticles shape from spherical to star-shaped.[24]

Polymorphism control could also be achieved by chemical means. α-MnS NCs were prepared by reacting Mn(II) chloride and thiourea in autoclave (T = 190 °C) for 12 h, using

water as solvent, whereas, when benzene was used as solvent γ-MnS rods (d = 40-100 nm, l = 250-700 nm nm) were obtained.[25] Mn(II) nitrate with elemental sulfur in octadecylamine at 200 °C lead to α-MnS hexagons approximately of 50 nm at high sulfur concentration whereas γ-MnS rods (d ≈ 50 nm) originated at low sulfur concentration.[26] Hydrothermal reaction starting from Mn(II) chloride and sodium sulfide at 180 °C gave 200 nm α-MnS octahedral nanoparticles but, when a large excess of hydrazine was added, γ-MnS rods were obtained (d = 200-300 nm, l = 1.0-1.5 μm).[27] Briefly, the crystal structure control of MnS nanoparticles was achieved either changing solvent and amount of sulfur or adding a reducing agent such as hydrazine. [23 24 25 27 28 29 30 31 32]

3.1.3. Core-shell MnO/FeOx NPs - types of synthesis

Core-shell are very promising structures due to their properties useful in different fields but their synthesis is challenging, above all when a good interface quality is required. In fact, in the last decade a wide range of papers have been published on metal-metal or metal metal oxide heterostructures, but the preparation of metal oxide – metal oxide heterostructures presents many difficulties and a fewer number of metal oxide-metal oxide core-shell NPs have been reported. In the field of magnetism, the coupling between two materials is a very good strategy to develop an exchange coupling between a ferromagnetic and an antiferromagnetic material. This type of coupling could be able to generate a bias field. One of the most popular antiferromagnetic oxide is the MnO which could be coupled to an iron ferromagnetic oxide to obtain nanoparticles with an enhanced magnetic stability. In literature, there are few example of heterostructures composed of MnO and iron oxide and rarely the synthesis of a proper core-shell MnO@FeOx structure was reported

In 2012 was published one of the first examples of MnO and iron oxide magnetic nanoplates synthesized by a hydrothermal method starting from $FeSO_4$*7 H_2O and $KMnO_4$ as metal precursors.[33] In 2013, Fe_3O_4/MnO hybrid nanocrystals were synthesized starting from preformed Fe_3O_4 nanoparticles with different sizes (5 nm, 11 nm, and 21 nm) with $Mn(CH_3CO_2)_2$ and oleic acid in trioctylamine at high temperature.[34] One of the most recent publications, reported in 2014 the synthesis of hybrid and dimeric MnO and Fe_2O_3 nanoparticles starting from preformed iron oxide or manganese oxide nuclei with manganese oleate or iron oleate respectively in 1-octadecene. The different nanoparticle structures depended on the use of cleaned or uncleaned nuclei, or else, depended on the concentration of oleic acid in the reaction medium.[35]

Moreover, another paper reported the formation of MnO@Fe_2O_3 and Fe_3O_4@MnO core-shell structures. Using a solvothermal strategy, authors started from Fe_3O_4 spherical nanoparticles and manganese (II) acetyl acetonate in dibenzyl ether with a mixture of oleic acid, oleylamine and 1,2-hexadecanediol to build Fe_3O_4@MnO nanocrystals. The same procedure was applied starting from MnO spherical nanoparticles and iron (III) acetyl acetonate in order to form the inverse MnO@Fe_2O_3 nanocrystals.[36] One of the most recent articles describes the synthesis of oleic acid-stabilized iron oxide/manganese oxide core/shell nanocrystals. A toluene dispersion of iron oxide preformed nanoparticles was added to oleylalcohol, then toluene was evaporated and manganese oleate precursor was hot-injected into the reaction mixture.[37]

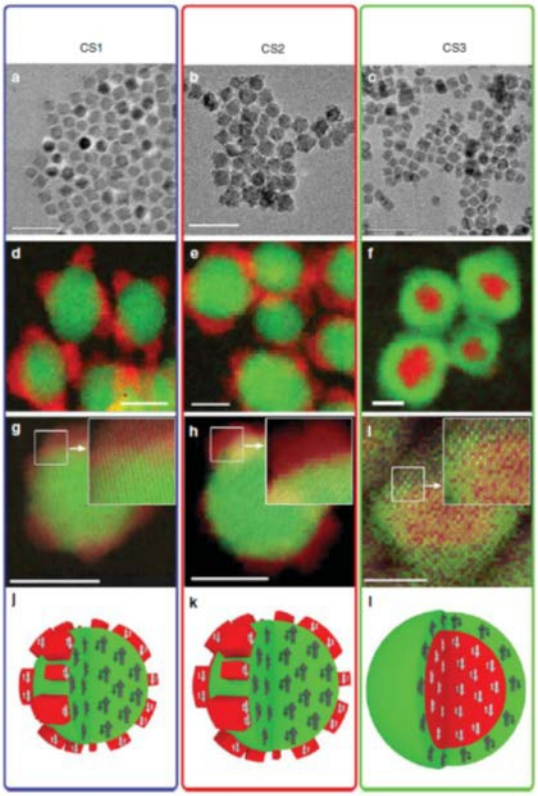

Figure: TEM images of the (a) Fe_3O_4@MnO NPs, *(b)* Fe_3O_4@MnO NPs *and (c)* MnO@Fe_2O_3 NPs *nanoparticles (scale bar = 50 nm). EELS-mapping of the (d)* Fe_3O_4@MnO NPs, *(e)* Fe_3O_4@MnO NPs *(scale bar = 10 nm) and (f)* MnO@Fe_2O_3 NPs *(scale bar = 5 nm) nanoparticles (where green corresponds to the Fe L signal and red to the Mn L edge, after background subtraction using a power law fit). High resolution-STEM annular dark field image overlaid with the EELS maps for the (g)* Fe_3O_4@MnO NPs, *(h)* Fe_3O_4@MnO NPs *(scale bar =10 nm) and (i)* MnO@Fe_2O_3 NPs *(scale bar = 5 nm) nanoparticles. Shown in the insets are enlarged views of the highlighted areas. Schematic representation of the morphological and magnetic structure for the (j,k) soft/hard and (l) hard/soft nanoparticles. Image from ref. 36*

3.1.4. Solvothermal synthesis and the role of the surfactants

As previously seen, the solvothermal synthesis is one of the most useful methods to synthesize metal oxide nanoparticles and the mostly used to build core-shell structure due to its capability of finely tune and control dimension, uniformity of size, shape and crystal structure of the nanoparticles. Solvothermal methods present some main reaction parameter which could be controlled and changed in order to obtain the desired products. These parameters are: the metal precursor (inorganic or organo metallic), the surfactants (the type of molecule and, possibly, a mixture of two or more surfactants), the solvent (polar or non-polar), the molar ratio between precursor, surfactants (and possibly other reagents), the reaction temperature (generally based on the solvent boiling point), the heating rate (slow or very fast) and the reaction time.

In literature, one of the most investigated parameter (that also in our work is the most deeply investigated) is the surfactant. Surfactant plays a fundamental role in the solvothermal process. At the beginning, it affects the metal ion availability during the nucleation (because the surfactant can coordinate the metal ion generating an intermediate precursor) and the crystal face reactivity during the nanocrystal growth. Finally, it is essential to disperse and stabilize the formed nanoparticles. Hence, the type of surfactant, its chemical nature and the metal-precursor : surfactant molar ratio are all key issues in a solvothermal reaction.

Many papers have already described the possibility to tune the nanoparticle shape, size and uniformity of size changing the type and the amount of surfactant. It was already demonstrated that ligands could affect the activity coefficient of the monomers in solution and control the relative nucleus concentration.[38]

If it is possible to achieve a reaction route where a relatively high monomer concentration and a low nucleus concentration are present in solution during the growth phase, thermodynamically unfavorable shapes (such as rods or branched shapes) could be formed due to the high monomer concentration which favor the non-equilibrium shapes. When the monomer concentration is gradually depleted and becomes too low, the non-equilibrium shapes disappear, because they are not stable, and evolve into equilibrium shapes (such as sphere) due to the ripening process.[38] Surfactants can strongly coordinate metal ions and a low concentration of free ions remains in the solution. A low reactivity rate of the metal ions clearly can separate the nucleation and the growth steps.[39] It also seems that a low monomer concentration is able to induce the Ostwald ripening process. We can deduce that an early stop of the reaction could end up with differently sized and/or shaped nanoparticles.

Moreover, the Ostwald ripening process could take place if surfactant were not present in the reaction solution. The surfactant concentration is one of the key points involved in the process.[38]

Other studies confirm the role of the surfactant on the crystal growth control, in particular their capability to generate a non-equilibrium state for the anisotropic shape formation.[40] When surfactants, which have different terminal groups such as carboxylic acids (e.g. oleic acid) and amines (e.g. oleylamine) are used, some crystal faces can be easily capped by the surfactant molecules while other non-passivate faces grow. Thus, some crystallographic faces are favored and an anisotropic growth is facilitated.[39] This phenomenon occurs due to the presence of different exposed atoms or different surface energies of the crystal faces. For example, the MnO rock-salt structure has {100} faces with an alternation of manganese and oxygen atoms, while the eight {111} faces comprise only manganese atoms (4 faces) or only oxygen atoms (4 faces). The different face structure corresponds to a different preference of the surfactant for a given face and thus to different surface energy. From experimental data, it seems that oleylamine preferentially interacts with the {111} faces the rock-salt crystal and poorly with {100} faces. Oleic acid does not have a marked preference and tends to decrease the energy and growth gaps between the faces.[41] Hence, oleic acid generally leads to isotropic shape nanoparticles and oleylamine leads to anisotropic growth.[24] Oleylamine favors the formation of the simplest and most common anisotropic shape that is the nanorod. When multipod or elongated branched shapes are obtained, it means that probably other factors such as the solubility, the diffusion rate and the reactivity of the reagent in the solvent have played an important role in the anisotropic growth. The supersaturation of the initial nuclei favors an increase in the growth rate and accordingly the development of anisotropic shapes.[42]

3.2. Applications

As previously described, the goal of our work is to synthesize antiferromagnetic/ferromagnetic core-shell NPs with both shape and exchange-coupling anisotropy in order to achieve an enhanced magnetic stability. This improved property, together with other characteristics derived from the coupling between AFM and FM materials at the nanoscale level, could find application in many fields as already reported in the recent literature.

3.2.1. Core-shell NPs

The applications of metal or metal oxide core-shell structures can be grouped into two main groups: technological and biomedical applications.

3.2.1.1. Technological Applications

3.2.1.1.1. Recording media[43]

In the field of recording media, the main goal is to increase the areal bit density and decrease the bit size. In order to conserve a good signal-to-noise ratio and high bit density, each single grain must overcome the superparamagnetic limit. Nevertheless, it is important that the thermal stability and the signal-to-noise ratio of the recording media are simultaneously balanced with the write-ability of a specific bit. A new generation of recording media needs to be studied to solve these problems. Good candidates seem to be the so-called “patterned media” where every bit is not made by several hundred magnetic grains but each bit is made by individual magnetic dots. A special type of this patterned media is made by self-assembled magnetic nanoparticles. In this case it is better to use a soft material with a tunable anisotropic constant antiferromagnetic materials, otherwise hard or high anisotropic constant material requires magnetic fields too high compared to the conventional write-head systems. An alternative strategy could be to decrease the effective hard material anisotropy by coupling to a soft material with a low anisotropic constant value, as in a core-shell structure. In this way,

the hard part preserves the thermal stability but the soft part allows to write the information reducing the switching field.

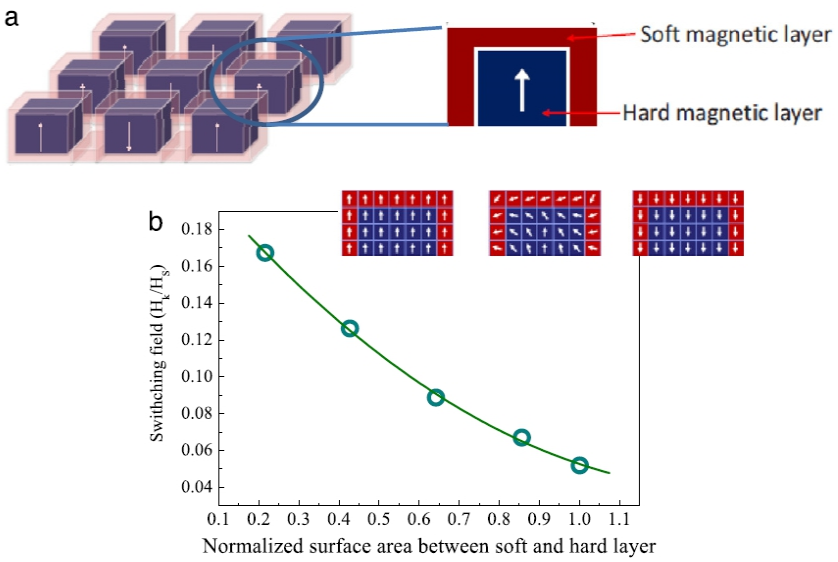

Figure: (a) nanostructured core/shell patterned media; (b) micromagnetic simulation of the dependence of the switching field on the normalized surface area between the soft and hard layer. Image from ref. 44

This approach is not a novelty, already in 1960 a first system made by an iron oxide core doped with cobalt and coated by a cobalt ferrite shell was studied as potential material for recording media. The system maintains the uniaxial anisotropy but increases its coercivity field. Until 1990, a new class of supports was developed in order to increase the coercivity field and minimize the size of the recording bit. Recent core-shell structure experiments seem to confirm their ability to allow particle size reduction and to obtain anyway a good signal-to-noise ratio and high thermal stability. However, the present trend for these systems involves the use of rare-earths for the hard part of the structure. All patented materials show a conventional interface hard/soft core-shell structure where the soft part is made of a metal or metal oxide. One example reported that FeRh was used as soft shell material, which at room temperature shows a transition from antiferromagnetic to soft-ferromagnetic. To slightly increase the temperature, it is possible to induce the transition and decrease the coercivity field in order to allow an easier recording of the material, then cooling the support, the shell returns to the antiferromagnetic state and the coercivity field and the thermal energy are increasing again for the stability. This process is known as heat-assisted magnetic recording.

Other core-shell characteristics that could be appealing for recording media applications are: i) to enhance the blocking temperature (it was already demonstrated that it could be achieved by adding an hard material surface layer on a soft nanoparticle material); ii) the switching field of a hard material that decreases when it is coupled to a soft material; iii) the possibility to organize nanoparticles in a self-assembled configuration; iv) the presence of an anisotropic gradient in the core-shell structure. However, from previous works it seems that the shell growth on a core could deteriorate the original nanoparticle and make a spontaneous nanoparticle self-assembly more difficult. Not only the quality of the core but, above all, the shell morphology are influent parameters in the formation of a regular and define array.

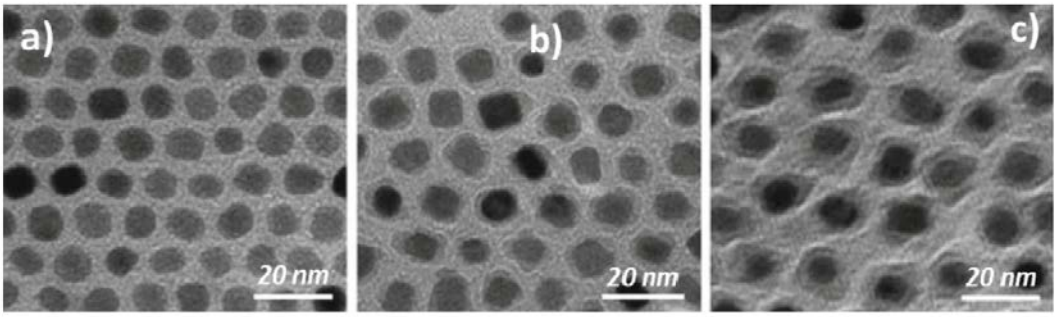

Figure: conventional TEM images of the as-synthesized FePt@Fe3O4 core-shell nanoparticles: (a) 7 nm FePt nanoparticles; (b) 7 nm FePt nanoparticles coated with 1 nm Fe3O4 shell; (c) 7 nm FePt nanoparticles coated with 3 nm Fe3O4 shell. Image from ref. 45

Core-shell nanoparticles are very promising materials for recording media but their conditions of use are more stringent compared to the permanent magnets. There are some rules that the core-shell nanoparticles have to follow: i) overall nanoparticles have to be single domain and show an out-of-plane magnetization; ii) a narrow switching field distribution is required; iii) exchange coupling between nanoparticles must not take place, thus nanoparticles should not to be in contact; iv) accidental recording of neighbor nanoparticles must not occur if the dipolar field are small enough; v) coercivity field has to be smaller than the writing field; vi) nanoparticles should have an high thermal stability and large saturation magnetization; vii) the self-assembly should be regular without defects and preferably in square array. This array is not simple to obtain because it is generally achieved with superparamagnetic nanoparticles at room temperature, magnetic nanoparticles tend to aggregate and destroy the 2D ordered array.

3.2.1.1.2. Catalytic, electronic and other applications[43]

Magnetic nanoparticle cores coated with an appropriate shell made of noble metal, semiconductor or metal oxide display improved physical and chemical properties (e.g. optical, catalytic, electrical, magnetic and thermal). In the catalysis field, there are some example of this behavior. Nanosized metal oxides are able to destroy the adsorption capacity of halogenated hydrocarbons and organophosphorous compounds, but with a transition metal oxide coating on the original metal oxide core, this destructive power is enhanced several fold.[46] [47] Another example regards the catalytic conversion from CO to CO_2 operated by iron oxide Au-coated nanoparticles supported on silica that is more efficient than that obtained with homogeneous gold nanoparticles on silica support.[48] Generally, metal cores (Fe, Ni, Co, Ru) improve their catalytic activity when coated with a silica shell which increases the core stability.[49] Many core-shell nanoparticles systems (e.g. Au/Pd, Au/Ag, Au/Pt, Pt/Pd and Co/Pt) are used as catalyst in a wide range of reactions.

Core-shell NPs having either core or shell made of metal or semiconductor are very important for electronics applications. In this way, it is possible to combine different materials, above all the conventional polymer materials (low dielectric constant, highly workable) with the ceramic materials (high dielectric constant, poorly workable) used in this field. Core-shell systems could show high capacitance; the shell prevents core photo-degradation and increases colloidal stability. The most common shell material in electronics application is silica. Silica has many good properties: it is inert and optically transparent, does not affect red-ox reactions of the core material, increases colloidal stability, prevents photocatalytic degradation of the core and can be engineered used to modulate the metal surface plasmon adsorption bands. Another commonly used coating is carbon. For example, carbon-coated iron oxide is used for the extraction of polycyclic aromatic hydrocarbons from environmental water samples.[50] Generally, the use of carbon on metal or metal oxide nanoparticles is aimed at increasing biocompatibility, non-toxicity and catalytic properties.[51] [52] Finally, nanoparticles with potential use in many fields such as the production of rubber, plastics, inks and so on, are organic/silica core-shell structures which combine the properties of both the materials.[53] [54]

3.2.1.2. Biomedical Applications[55]

Thanks to their peculiar structure, core-shell nanoparticles are excellent materials for biomedical applications. In particular, in the last decades some possible applications have been studied and others are presently being developed. The most important medical where core-shell nanoparticles can help innovation are: drug delivery, bioimaging, cell labelling, biosensors, and tissue engineering. Here, we limit ourselves to diagnostic contrast agents which are directly related to magnetic core-shell nanoparticles.

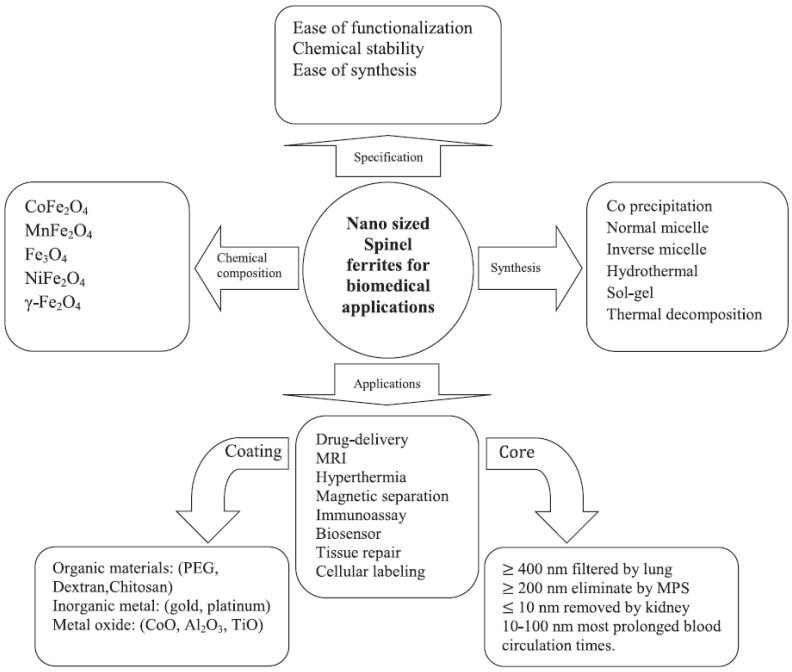

Image from ref. 56

3.2.1.2.1. Dual T_1 and T_2 contrast agents[57]

Single T_1 or T_2 contrast agent could create ambiguity in the analysis of medical MRI images, especially when the biological target is very small. Thus. the possibility to combine a T_1 and T_2 contrast agent could overcome such a problem, eliminating ambiguities and artifacts and producing more accurate images. However, when a T_1 and a T_2 material are very close, the T_1 spin-lattice relaxation process is strongly decreased. To solve this problem, a separating layer must be included between the two materials in order to modulate the magnetic coupling. Micellar structures, inorganic porous materials and block copolymers have been considered as possible frameworks.

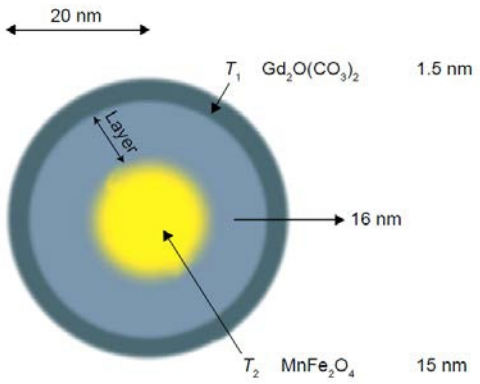

Figure: Scheme of core–shell dual-mode nanoparticle contrast agent [$MnFe_2O_4$@SiO_2@$Gd_2(CO_3)_2$]. The T_1 contrast material is positioned on the shell to have direct contact with the water for high T_1 contrast effects, and the superparamagnetic T_2 contrast material is located at the core, inducing a long-range magnetic field for the relaxation of water. Image from ref. 57

Another approach could be the addition of chelate Gd to the polymeric coating on a magnetic T_2 nanoparticle agent. This combination would allow one to simultaneously record T_1 and a T_2 images without the above described complications. Nevertheless, SPION (e.g. iron oxide) nanoparticles, due to their large surface area, could be able to cross the blood-brain barrier, but all the gadolinium complex are not able to cross it, thus preventing a CNS use of the dual agents.

3.2.2. MnO and MnS NPs

As described in the Thesis, the synthesis of MnO and MnS nanoparticles is a great challenge if a fine control over NP size and shape is desired. Thus, the effort to produce MnO and MnS nanoparticles is not only directed to prepare preformed nuclei for core-shell NPs, MnO and MnS nanoparticles themselves could find an important role in many applications.

3.2.3. MnO NPs

Similarly to the previously described applications of core-shell NPs, also applications of MnO nanoparticles can be divided into the groups of technological and biomedical applications.

3.2.3.1. Technological Applications

3.2.3.1.1. Lithium-ion battery[58 59]

In the last years, lithium-ion batteries had a great success as renewable and environmental friendly energy storage systems for applications such as electric vehicles and portable electronics. The primary advantages compared with the previous energy storage systems are: high energy power and density, low cost, safety and reliability, high capacity ,and long cycle life. Until now, graphitic carbon was the most frequently used anode material due to its stability and low cost but it shows a poor Li intercalation rate into its lattice crystal structure. Nowadays, nano-sized transition metal oxides are promising candidates for their high capacity, low cost and environmental friendly nature. In particular, MnO can store from two to eight Li ions per formula unit depending on its oxidation state and could give an energy density when coupled with specific cathodes. Furthermore, a carbon shell over the MnO nanoparticles could provide electronic conductivity (MnO is an insulator) and heteroatom doping of the carbon shell could increase the carbon conductivity. Thus, MnO@carbon composites seems to be an eligible material for lithium-ion battery application.

3.2.3.2. Biomedical Applications

Nowadays, nanoparticles are one of the most studied "devices" for diagnostic and therapeutic goals in medicine. The main advantage of the nanoparticles is the possibility to simultaneously combine many functionalities. A single nanoparticle could be used for drug delivery, MRI contrasting, bioimaging, and active targeting simultaneously.

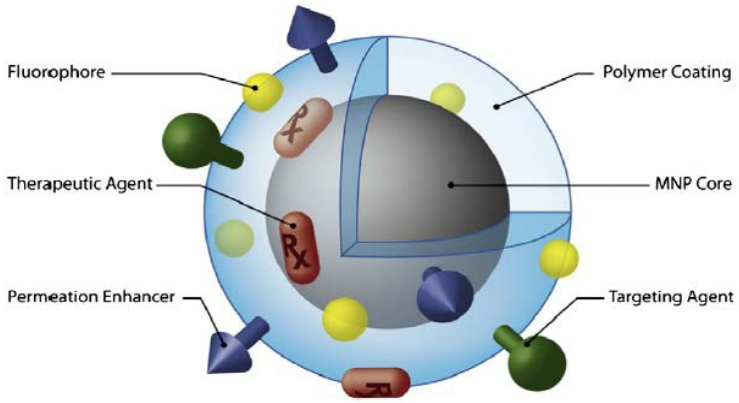

Nanaparticle possessing various ligands to enable multifunctionality in a single nanoparticle platform. Image from ref. 60

3.2.3.2.1. T1 contrast agent for MRI[61]

Magnetic resonance imaging is a very useful technique to study organisms and above all to provide detailed medical imaging. In particular this technique is employed to study: cancer tissues, gene expression, cell migration, angiogenesis and apoptosis and cardiovascular disease. It is well known that iron oxide nanoparticles (SPIONs) are the eligible material used as T_2 contrast agent.

Mn^{2+} is a cation very attractive as T_1 contrast agent thanks to its five unpaired electrons.[57]

The first use of Mn^{2+} in MRI dates back to 1979 in a study on cardiac infarction in dogs.[62]

Manganese ions could be used into two main classes of contrast agents: small molecules and nanoparticulate agents. The first type are complexes where a chelant agent coordinates a manganese ion. These small molecules could be also incorporated into lipidic bylayers to improve their biocompatibility. The second agent type are MnO, MnO_2 or Mn_3O_4 nanoparticles. When they are driven into cells, proteolytic degradation convert these nanoparticles from T_1 to T_2 contrast agents. The Mn^{2+} ability to pass through the calcium

channel can be exploited for neuroimaging, however, this application implies that vulnerable brain cells are exposed to manganese. The main limitation of the most used T_1 agents (above all the paramagnetic Gd chelant agents) is the progressive loss of efficacy at higher magnetic fields. Also, internalization into cells and accumulation of nanoparticles in low pH compartments leads to dissolution of oxide materials.[62] Furthermore, short blood circulation time, poor detection sensitivity and toxicity favored research on T_2 contrast agents over T_1 agents.[57]

Despite this, nanoparticles are able to give a very good quality contrast images when they are monodisperse, water soluble and highly crystalline.

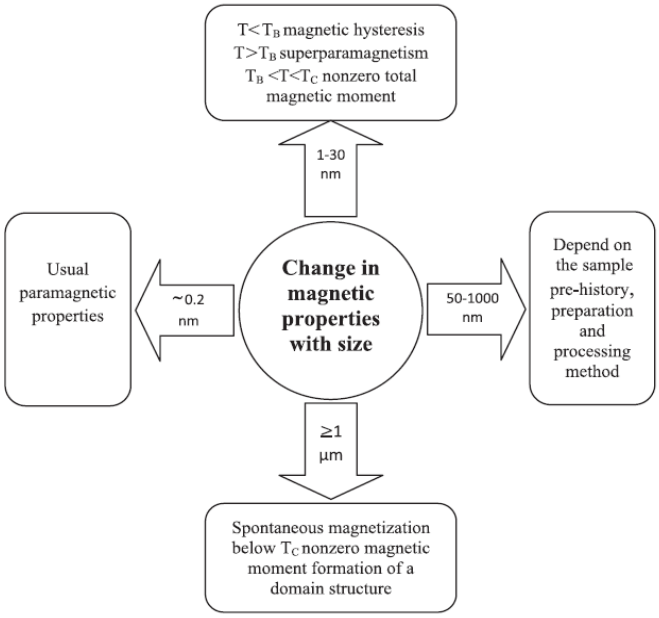

Image from ref. 60

For MRI applications, it could be useful to have paramagnetic or superparamagnetic nanoparticles that are able to acquire a significant magnetization also at low fields but that are also able to avoid interaction and aggregation when no field is applied.

Moreover, a suitable coating is fundamental for enhancing biocompatibility and decreasing toxicity. Capping agents could be important to add other functionalities such as fluorescent groups or specific active targeting. The presence of fluorescent groups allows one to have a dual signal and to detect the nanoparticle position also by optical techniques. Otherwise, the presence of a specific active targeting such as a monoclonal antibody allows a specific binding between nanoparticles and the target cells or tissues, to increase nanoparticle

concentration in the local site and enhance the pharmacological or diagnostic nanoparticle effects. If a targeting molecule is not loaded on the coating, nanoparticles are conveyed into the desired pathological or tumoral cells by the EPR effect (enhanced permeability and retention). The lacking/inefficient lymphatic system in the endothelial cancer tissues allows nanoparticles to permeate into the cells. The use of iron oxides, such as maghemite or magnetite, as T_2 contrast agents is very useful due to a positive dose-effect correlation, but T_2 contrast agent give a negative contrast image, while T_1 contrast agents are able to give a positive contrast image with an improved visibility of the site of interest. Several articles already reported the feasibility to use MnO as T_1 contrast agent in MRI. For example, Hyeon and coworkers prepared MnO nanoparticles coated by an amphiphilic phospholipid functionalized with Herceptin as a contrast agent for *in vivo* studies. Surprisingly, the nanoparticles do not show significant toxicity also after several weeks.[63] In another work, a mixture of SPIONs and MnO nanoparticles was found very useful to achieve a "double labeling" of different cells population thanks to the different positive and negative contrast.[64]

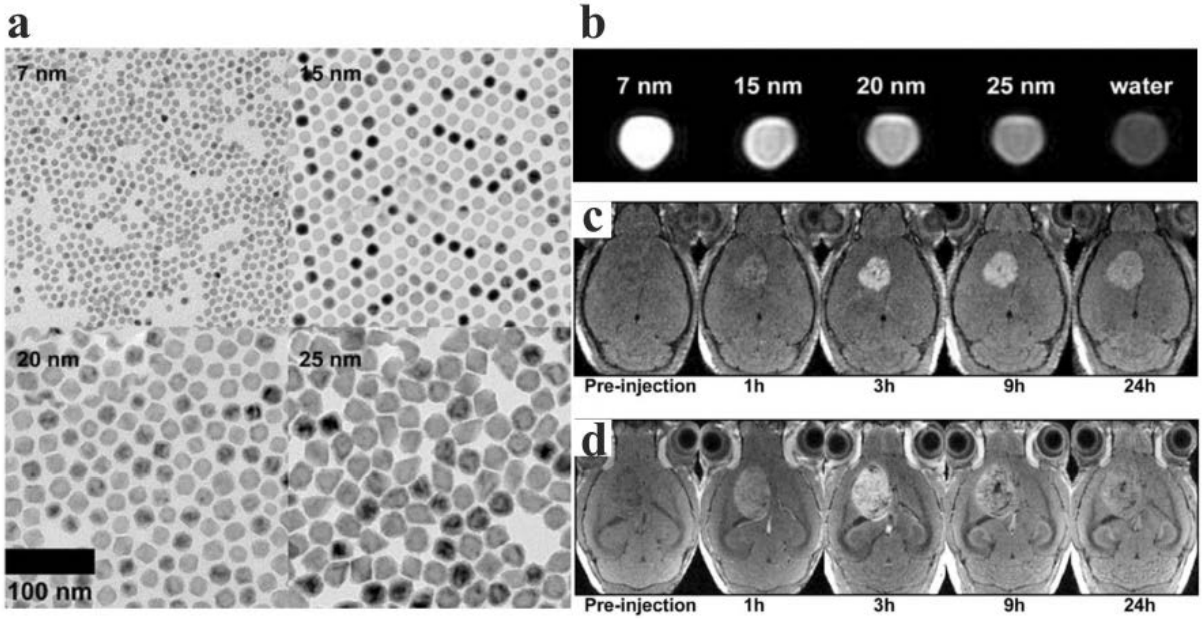

Figure: MnO NPs experiments to verify the feasibility as a T_1 contrast agents.
(a) conventional TEM images of monodisperse MnO NPs with different sizes;
(b) T_1 weighted images of MnO NP aqueous solutions;
(c) the contrast inside the tumor tissue is increased by MnO NPs with Herceptin;
(d) the contrast in the surrounding tissue is enhanced. Image from ref. 63

Aside from the MRI application, magnetic nanoparticles could be an interesting material as probes for multimodal imaging. In fact, combining different materials it is possible to simultaneously exploit their individual properties. For example, manganese ferrite where the biocompatible shell is loaded with I^{124} allows one to observe nanoparticle localization either with MRI and with PET (positron emission tomography).[65]

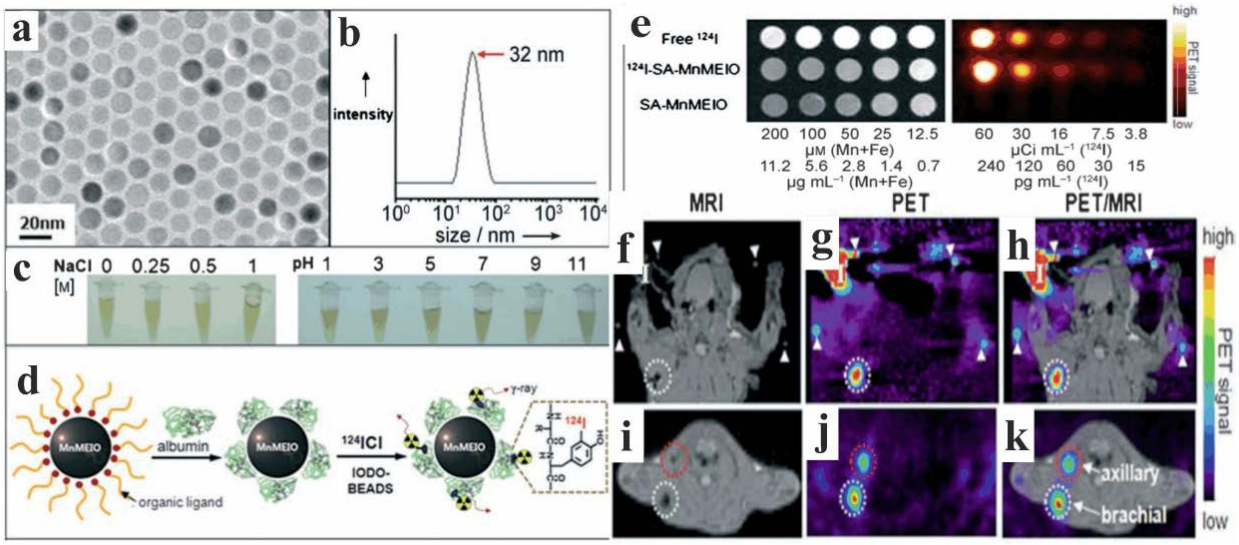

Figure: Bimodal imaging of manganese ferrite NPs conjugated with ^{124}I.

(a) conventional TEM image of monodisperse $MnFe_2O_3$ NPs.

(b) Hydrodynamic diameter of $MnFe_2O_3$ NPs.

(c) Aqueous solutions with different NaCl concentration and varying pH.

(d) Scheme representing the conjugation of ^{124}I onto $MnFe_2O_3$ NPs.

(e) MRI and PET images of free ^{124}I, $MnFe_2O_3$ NPs, and ^{124}I-conjugated $MnFe_2O_3$ NPs.

(f-k) In vivo MRI/PET images of a tumor rat after injection of ^{124}I-conjugated $MnFe_2O_3$ NPs.

Image from ref. 65

It was also reported that it is possible to combine MnO and gold in a bimodal system consisting of Au@MnO "nanoflowers".[66 67]

For these biological uses, it is important to evaluate the long-term nanoparticle toxicity due to the direct exposure to the human body. To study the compatibility and the possible toxicity, it is important to understand the behavior, the properties, the metabolism and the fate of the nanoparticles.

Despite *in vivo* studies are fundamental to investigate both kinetic processes and toxicological impact, most of the data derives from *in vitro* assays which are simpler, faster and less expensive experiments.[68] [69]

Generally, the common reaction to nanomaterials is an inflammatory response[70] and a possible release of reactive oxygen species (ROS) able to damage DNA.[71] Quantum-dots are very well-known inflammatory materials and ROS releases,[72] while gold and silver nanoparticles have size-dependent toxicity.[73] [74] About magnetic metal oxide nanoparticles, very high toxicity was observed when "naked" NPs were used, free of a safe and biocompatible coating. The high toxicity of "naked" NPs seems due to the cellular uptake and the ROS release caused by Fe-ion leaching.[75] MnO has also been investigated. Many papers reported that the dose used in biomedical applications involves a comparatively low toxicity.[64] In a comparison between MnO and Fe_3O_4 nanoparticles coated by hydrophilic micellar phospholipid shell, MnO showed a slightly higher toxicity than iron oxide.[76] Other publications report that free manganese ions are not harmful for the human body and manganese oxide nanoparticles could be applied for *in vivo* techniques because they are not subject to ion leaching.[77]

3.2.3.2.2. Nucleic acid delivery agent[78]

Manganese oxide could be the eligible material for this application due to its natural presence in cells and tissues of living organisms and to its ability to interact with nucleic acids and other biomolecules. MnO is a highly biocompatible material with no toxicity, as demonstrated by treating different cells with MnO nanorods. In addition, MnO seems to localize at the cell surface and it is thus well tolerated. Nucleic acids are used as therapeutic agents due to their specificity for the target and their influence on gene transcription and RNA processing. The direct treatment with nucleic acid only does not achieve a successful transporting across the cell membranes without destroying their structure and functions. The MnO nanorods could carry, e. g., short interfering RNA (siRNA), antisense and splice switching oligonucleotides (SSO), and DNA or RNA vaccines. MnO nanoparticles and nucleic acids are both negatively charged thus it is important to cover the nanoparticles with a suitable coating to provide for suitable interaction with the two components.

3.2.4. MnS NPs

In the last few decades, MnS and other semiconductor materials such as Bi_2S_3, PbS, CdS and CoS were investigated for their novel optical, electrical and magnetic properties. Among this wide family of semiconductors, nanostructured porous semiconductors have attracted particular attention for possible applications in catalysis, high-capacity anode materials, spin-valve devices, biosensor, luminescence, biofiltration gas storage, magnetic and heat dissipation. A combination of optical and magnetic effects could also be exploited. In particular MnS, which is an important VIIIB-VIA magnetic semiconductors, finds applications even in solar cells as window/buffer material, solar selective coatings, short-wavelength optoelectronic material, optical mass memory/storage and processing of information for electronic devices. However, MnS is still an relatively poorly studied material which could find new possible applications in the future.

3.3. Magnetic material[79]

To clarify the magnetic behavior and properties of the nanoparticles described in this thesis and to give a larger background of the magnetic properties in the metal and metal oxide nanoparticles field, here it is reported the brief description of the magnetic ordering types and the explanation of some magnetic effects such anisotropy and exchange-bias which are directly related to the MnO and MnO@Fe_2O_3 studied nanostructures.

3.3.1. Schematic summary of the magnetic ordering types

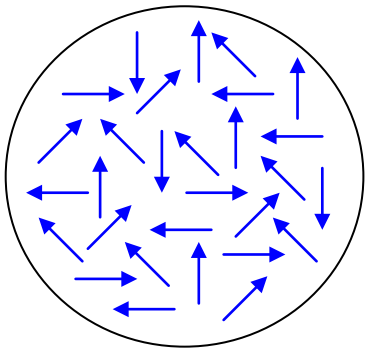

paramagnetic

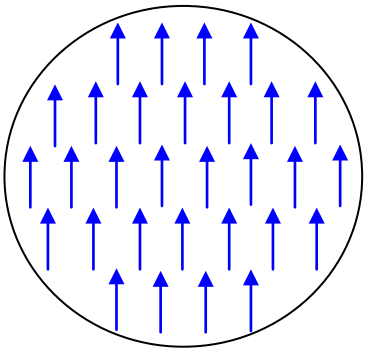

ferromagnetic

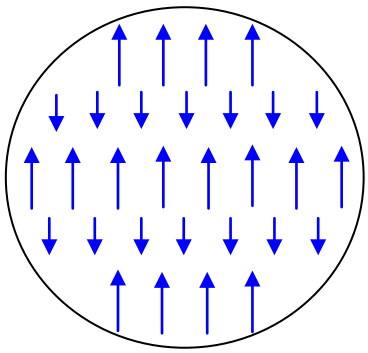

antiferromagnetic

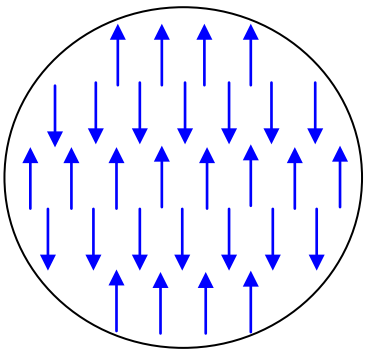

ferrimagnetic

3.3.2. Magnetic ordering hysteresis loop

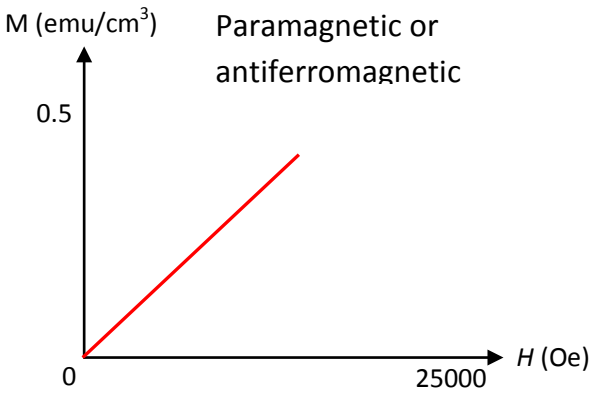

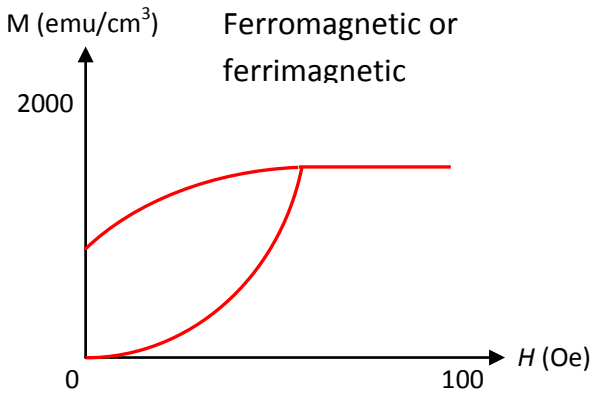

3.3.3. Diamagnetism

Diamagnetic is a material which has no unpaired electron and then no net magnetic moment without an external applied field *H*. Clearly, most substances are diamagnetic, e. g., water, sugar, table salt, gasoline, most organic substances, salts not involving transition metal ions, etc.

When A diamagnetic material is subjected to a magnetic field an extra current are generated in each atom by electromagnetic induction. According to the Lenz's law, the induced current flows as to create a magnetization *M* opposite to the applied field. When the magnetic field is turned off, the induced current does not flow anymore and the net magnetization vanishes . This explains why diamagnetic materials have no spontaneous magnetization. .

In a diamagnetic material, susceptibility $\chi = M / H$ is negative and magnetization decreases when the magnetic field increases. Since diamagnetism is not related to permanent atomic moments related to unpaired electrons, it is displayed by all substances. All materials exhibit a diamagnetic response but only the material which not show any other magnetic behavior are classified as diamagnetic. This happens when all atomic or molecular orbital are either completely filled or empty. For example all the noble gases are diamagnetic. Many atomic gases also are diamagnetic, because the electrons match in the molecular orbitals and no net magnetic moment is left.

3.3.4. Paramagnetism

Paramagnetic materials are materials containing unpaired electrons and, then, net atomic magnetic moment. These magnetic moments are weakly coupled to each other, so the thermal energy is able to produce a random alignment of the magnetic moments and no net magnetization is observed in the absence of an external field.. Transition-metal salts are a typical example of paramagnetic materials. In these salts, cations have a magnetic moment resulting from the partially filled d shell, and anions ensure the spatial separations between the cations. Therefore, interactions between magnetic moments on neighbors cations are weak. Also the rare-earth salts tend to be paramagnetic. Other examples of paramagnetic materials are metals, such as aluminium, or some gases, such as oxygen. Furthermore all ferromagnetic materials [see below] become paramagnetic above their Curie temperature at which thermal energy is high enough to destroy the magnetic moment order. (This is in general true for all magnetically-ordered materials, such as antiferromagnets and ferrimagnets, above their critical temperature) In a paramagnetic material susceptibility is about 10^{-3} – 10^{-5}. Paramagnetic susceptibility is approximately independent of the applied field when the field is not too large.. In many cases, paramagnetic susceptibility is inversely proportional to the temperature. In metallic paramagnets, susceptibility is independent of the temperature, (*Pauli paramagnets*). This behavior is due to the metal electrons which are able to wander through the lattice. In these materials, the susceptibility is nearly independent of temperature, it does not show the typical $1/T$ susceptibility dependence of Langevin paramagnets (see below).

The susceptibility dependence on the temperature is explained by the Langevin theory of paramagnetism which assumes that the non-interacting magnetic moments on the atomic sites are (i) randomly oriented as a result of the thermal agitation and (ii) aligned by the action of the applied field..

$$\boldsymbol{M} = Nm\left[\coth\left(\frac{mH}{k_{\mathrm{B}}T}\right) - \frac{k_{\mathrm{B}}T}{mH}\right] = NmL(\alpha)$$

where $\alpha = mH/k_{\mathrm{B}}T$, and $L(\alpha) = \coth(\alpha) - 1/\alpha$

The last equation is valid under the assumption that the atomic magnetic dipole moments can assume all the possible orientations with respect to the applied magnetic field. In reality, quantum theory allows magnetic moments to assume only discrete orientations because of spatial quantization. Then, considering this limitation, another function describes the quantum paramagnetic behavior the Brillouin function. In both cases, it can be shown that paramagnetic susceptibility is inversely proportional to temperature, $\chi = C/T$ (Curie law).

Many paramagnetic materials do not exactly obey to the Curie law but follow a more general temperature dependence described by the Curie-Weiss law:

$$\chi = \frac{C}{T - \theta}.$$

Paramagnetic materials which follow this law, below a critical temperature (the Curie temperature, T_c), undergo a spontaneous magnetic ordering and become ferromagnetic. This law considers that exist an internal interaction between the localized moments, called "molecular field". This is a mutual interaction between the electrons which tends to align the dipole moments parallel to each other. It was assumed also that the intensity ***Hw*** of the molecular field is directly proportional to the magnetization:

$$\boldsymbol{H}_{\mathrm{W}} = \gamma \boldsymbol{M}$$

Where γ is called the "molecular field costant". By this assumption and inserting the total field $H = H_{\mathrm{applied}} + H_{\mathrm{W}}$ in the Curie law, the Curie-Weiss can be derived:

$$\chi = \frac{\boldsymbol{M}}{\boldsymbol{H}} = \frac{C}{T - \theta}$$

where $\boldsymbol{T} = \theta$ corresponds to the phase transition to the spontaneously ordered phase.

When θ is positive, the molecular field follow the same direction of the applied field and force the magnetic moment to align each other in the same direction of the applied field. Ferromagnetic materials show this behavior above the ***Tc*** where thermal energy is high enough to destroy ferromagnetic order and the material displays paramagnetic behavior. .

3.3.5. Antiferromagnetism

In antiferromagnetic (AFM) materials, spins align in an antiparallel way to each other; in oxides (and higher chalchogenides) of transition metals, AFM arises from superexchange interaction between metal ions mediated by the intervening oxide anion. Under a critical temperature known as Néel temperature, the magnetic structure of AFM materials can be looked at as composed by two identical magnetic ion sublattices. Both lattices are spontaneously magnetized but in opposite directions. Antiferromagnetic materials have no net spontaneous magnetization and their behavior is similar to the paramagnetic materials when an external magnetic field is applied: magnetization is linear in weak applied field and the susceptibility is small and positive. Above the Néel temperature, susceptibility is dependent on the temperature and follows the Curie-Weiss law , while below the Néel temperature, the susceptibility decreases with temperature.

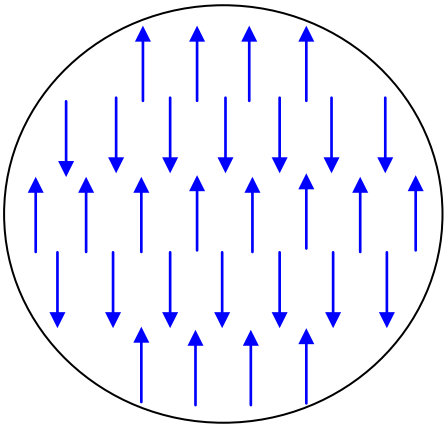

The first evidence of the above described antiferromagnetic structure was provided in 1949 with the study of manganese oxide (MnO). This crystal is composed by Mn^{2+} ions in two different sets one antiparallel to the other. Its crystal structure is a face-centre cubic rock-salt structure in which, below the Néel temperature, the magnetic moments in each (111) plane align parallel to each other and opposite with the magnetic moments in the neighboring (111) planes.

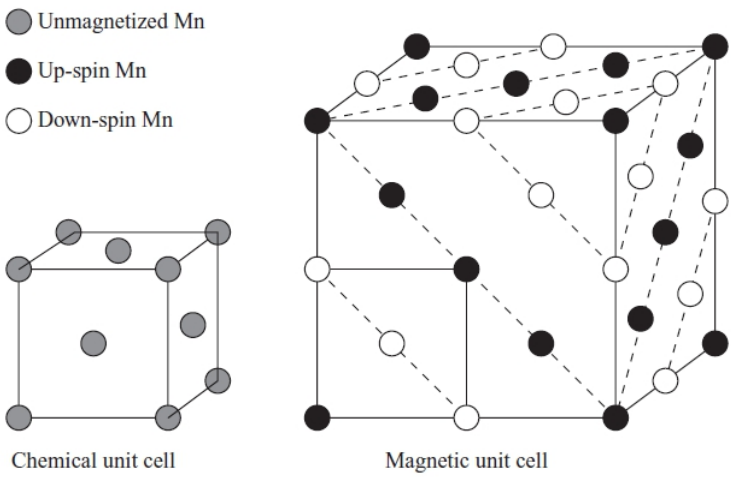

Figure: MnO structure above and below the Néel temperature. Image from ref. 79

Basically the Weiss theory works well also for the antiferromagnetic materials even if most antiferromagnet are ionic salts with localized magnetic moments. For these materials the susceptibility above the Néel temperature is:

$$\chi = \frac{C}{T - (-\theta)}$$

There is a Curie-Weiss susceptibility dependence where θ is negative. This negative value suggests the existence of a negative Weiss molecular field that produces the antiparallel alignment of the spins. According to the Curie-Weiss law, the Néel temperature $T_N = -\theta$, where θ is the value obtained from the plot of inverse susceptibility vs. temperature. This behavior derives from the interactions between the nearest magnetic atoms of the two sublattices. Below the Néel temperature each sublattice presents a spontaneous magnetization (with no external applied field) which is due to the molecular field created by the other sublattice, so that the net spontaneous magnetization is equal to zero.

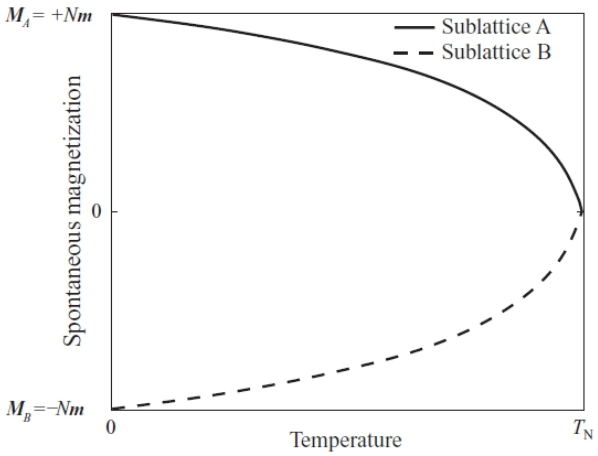

Figure: spontaneous magnetization of the two sublattices in an antiferromagnetic material. Image from ref. 79

The spontaneous magnetization of each sublattice often follows the Langevin (or Brillouin) law describing its dependence on temperature and applied magnetic field. When an external magnetic field is applied, there are two limit cases: the parallel and the perpendicular external field to the spontaneous magnetization direction.

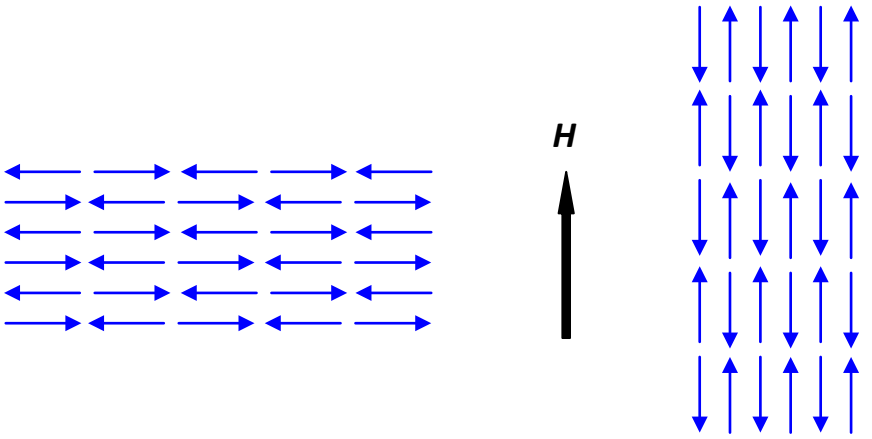

Figure: possible interaction between the applied field and the magnetization direction in an antiferromagnetic material.

So, below the Néel temperature, the susceptibility has a complex behavior since its value depends on the angle between the spontaneous sublattice magnetization and the externally applied magnetic field. If the external field is applied parallel to the sublattice A

magnetization, the A sublattice magnetization increases while the B sublattice magnetization decreases. The susceptibility is:

$$\chi_{\parallel} = \frac{2Nm^2 B'(J,\alpha)}{2k_B T + Nm^2 \gamma B'(J,\alpha)}$$

At 0 K, the susceptibility tends to zero because thermal fluctuations disappear and sublattices are perfectly aligned and no external field is able to torque their magnetic moments. The above susceptibility law it is the same as that followed by ferromagnetic materials below the Curie temperature, but in the latter case a change in magnetization under a very strong external field is anyway negligible with respect to the spontaneous ferromagnetic magnetization.

If the external field is applied perpendicular to the AFM magnetization axis, the magnetic moments are rotated by the applied field, so in this direction a net magnetization appears and a molecular field opposite to the magnetization is formed. The applied and molecular field perfectly balance to each other. The formula for susceptibility is:

$$\chi_{\perp} = \frac{\boldsymbol{M}}{\boldsymbol{H}} = \frac{1}{\gamma}$$

As anticipated, AFM order in transition metal oxides (and sulfides, etc.) is brought about by an inter-electronic interaction known as Superexchange. For example, let us consider the structure of MnO.

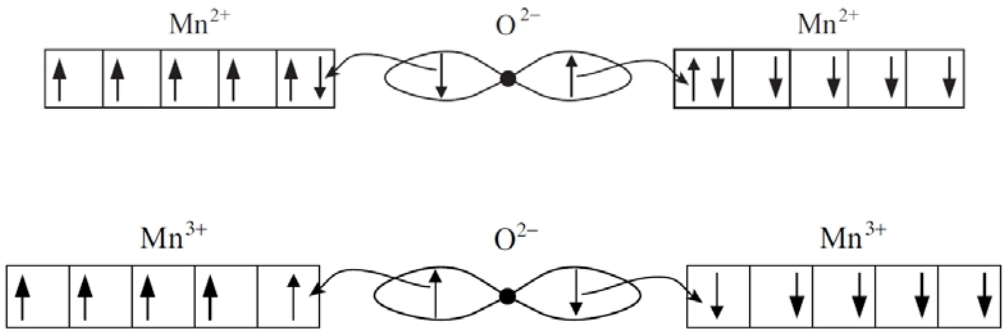

Figure: Superexchange in the Mn 3d orbitals generates a magnetic moment coupling. Image from ref. 79

The bonding in MnO is ionic and in the crystal linear chains of Mn^{2+} and O^{2-} can be found. Along each chain, the oxide anion has an occupied p orbital along the Mn-O-Mn direction, while manganese(II) has 5 electrons in the d orbitals, one electron in each orbitals, all with parallel spin.

Delocalization between manganese and oxygen can only occur when an O^{2-} ion donates electrons to the vacant orbitals of Mn^{2+}. When a manganese ion has spin-up electrons, it can only interact with a spin-down electron from the oxygen atom; the other electron in the oxygen p orbital is spin-up and can only interact with a manganese ion in which the 5 electron on d orbital are spin-down. In this way, the oxygen atom is able to mediate an energy-saving interaction which leads to antiferromagnetical order between the two manganese ions. In the case that the transition metal d orbitals are empty, oxygen is also able to induce an antiferromagnetic interaction acting as a ligand. Oxygen donates electron density to the d empty orbitals which then contain electrons with the same spin of the electrons in the filled transition metal d orbitals, because of Hund's rules.

Antiferromagnetic materials have not the wide range of applications possible for a ferromagnetic material but, in addition to being used as simple systems to test the theoretical models, they are increasingly important in the context of spintronics: for instance, they are critical components of spin valves thanks to phenomenon called exchange anisotropy or exchange bias coupling. Exchange anisotropy was observed for the first time in a single domain particle comprising a cobalt metal core and a cobalt oxide shell (Co@CoO). These particles had a normal hysteretic behavior when cooled in zero field but when field–cooled, they displayed a shifted hysteresis loop, coercivity was increased and its magnitude was different when the applied field was increased or decreased.

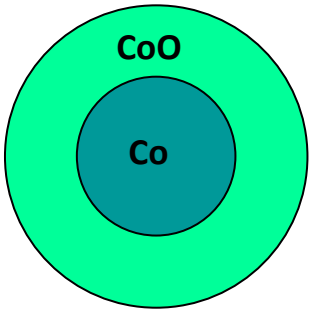

Figure: scheme of a core-shell particle where an antiferromagnetic and a ferromagnetic material are matched.

Antiferromagnetic materials are used in many application to pin the magnetic direction of the ferromagnetic layer. The pinned layer is generally coupled to a second ferromagnetic layer which can orient its magnetization in response to an applied magnetic field. The device resistance is higher when the two ferromagnetic layer are aligned in opposite direction. This kind of device could be used also as sensitive magnetic field sensor, such as a read-head for computer hard-disks..

3.3.6. Ferromagnetism

In ferromagnetic (FM) materials there is a strong interaction of electrostatic nature, i. e., the exchange interaction, which makes spins – and hence magnetic moments, also - line up and produce a large spontaneous magnetization despite the thermal effect. A property of the ferromagnetic material is that they become paramagnetic above the Curie temperature where their susceptibility follows the Curie-Weiss law. As to the Weiss theory, the molecular fields acts in the material below the Curie temperature and it is strong enough to magnetize the material even without an external magnetic field. Ferromagnetic materials can be thus seen as paramagnets with a very large internal molecular field. The spontaneous magnetization in ferromagnetic material can be explained combining the Langevin and Weiss theory. In fact both these physical law define a curve in the (α, *M*) plane and they are both valid – as it must be - at their intersection point. At temperature below T_C the FM material shows spontaneous magnetization M_{spont}.

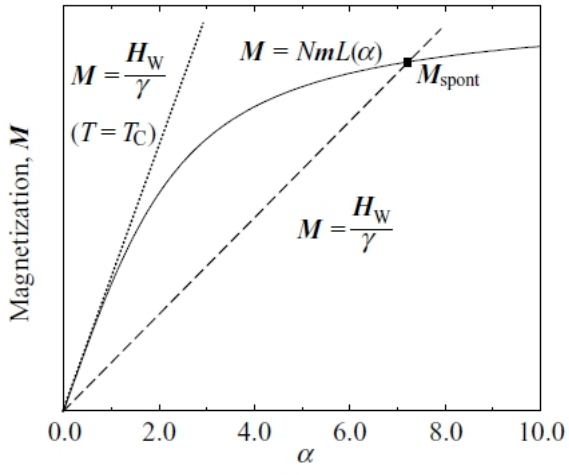

Figure: Graphical solution of FM Weiss and Langevin equations showing the spontaneous magnetization in a ferromagnetic material. Image from ref. 79

The slope of the $M = H_W / \gamma$ line is proportional to the temperature. When temperature increases, the slope increases and the line intersects the Langevin curve at points with smaller spontaneous magnetization. When the slope of the magnetization function equals that of the tangent to the Langevin function, the spontaneous magnetization becomes zero: this point corresponds to the Curie temperature. Magnetization decrease smoothly to zero near the Curie temperature, meaning that the transition from ferromagnetic to paramagnetic is a second-order transition. A large molecular field produce high Curie temperature. A larger thermal energy is required to destroy the magnetic order and induce the FM to PM transition in a material where a strong exchange interaction is active. A more accurate description of the spontaneous magnetization dependence on the temperature can be achieve using the Brillouin function instead of the Langevin function.

The Weiss molecular field is due to a quantum mechanical effect because there is an electrostatic energy saving which induces electron spins in neighbor atoms to orient parallel to each other. This interaction is direct consequence of the Pauli exclusion principle. If two electrons in an atom share the same atomic or molecular orbital they must have antiparallel spins, increasing the electrostatic Coulomb repulsion. Otherwise, if two electrons occupy different orbitals and have the same spin direction, their Coulomb repulsion is less unfavorable. Spin orientation affects the spatial part of the wave function and this affects the electrostatic Coulomb interaction between the electrons. This explains why small changes in the electron distribution can produce a significant effect on the total energy of an atom.

The localized-moment theory gives a good interpretation of the properties of ferromagnetic materials. However this theory present two important discrepancies from the experimental evidence. It was not experimentally observed that the magnetic moment per atom are the same in both FM and PM regions of a material and that the magnetic moment per atom corresponds to an integral number. In ferromagnetic transition metals such as Fe, Ni, and Co, the Fermi level is situated in a region of overlapping 3d and 4s bands. The transition metals of the first series do not show strongly difference in the structure of the 3d and 4s bands, so the difference in electronic structure are mainly due to changes in the Fermi levels. This approximation is the rigid-band model. Because of the overlap between 3d e 4s bands, the valence electrons partially occupy each of this level. The large number of electrons near the Fermi level reduces the energy necessary to re-oriented the spin. The s band has only one energy level for atom, so the band is narrow and the energy gap between require to promote an electron to the next level is high, on the other hand the d band has 5 orbitals per atom, the bands are broad and the energy gap to the next level is lower.

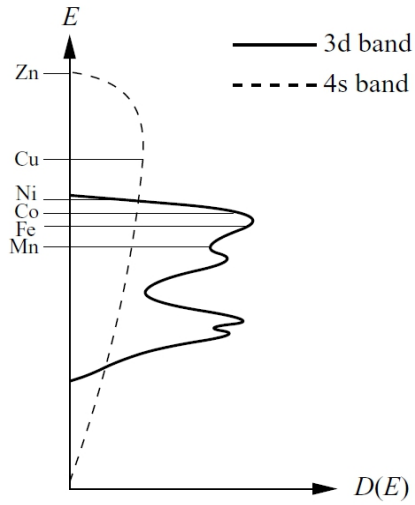

Figure: scheme of the Fermi levels positions in Zn, Cu, Ni, Co, Fe, and Mn. 3d and 4s densities of states in transition metals are shown. Image from ref. 79

The energy of the 3d band is shifted by the exchange interaction for electrons with one spin direction relative to the band for electrons with the opposite direction. If the Fermi level lies within 3d band many electrons are shifted to a lower-energy spin direction state and give a spontaneous magnetization in the ground state. The final structure is similar to a Pauli paramagnet into a magnetic field but in this case the exchange interaction induce an energy change and a spontaneous magnetization occurs also without an external field.

This model also agrees to the experimental evidence that the later transition metals such as Zn and Cu are not ferromagnetic, in fact in Cu the Fermi level lies above the 3d band and the 4s band has no exchange-splitting, while the Zn has both 3d and 4s orbitals filled and there is no contribution to net magnetization. In other transition metals, such as Cr or Mn, the exchange interaction is less strong, band energy larger and there is no ferromagnetic behavior. Rather, these metals have an antiferromagnetic spin arrangement.

3.3.7. Ferrimagnetism

Ferrimagnetic (FIM) materials have a very similar behavior to ferromagnetic materials which show a spontaneous magnetization below a critical temperature (Curie temperature) even when there is no magnetic field applied. The internal magnetic structure is however similar to the antiferromagnetic structure with two oppositely directed sublatttices but in this case the magnetization of one sublattice is greater than that of the other one, so the net magnetic moment is not equal to zero.

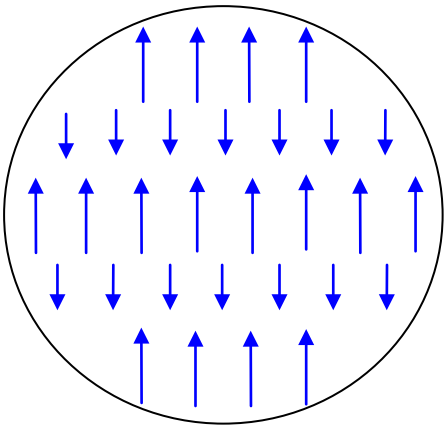

In ferrimagnetic materials, the sublattices are not structurally identical. To describe them properly, it is necessary to consider the interactions A-B between the spins of the both sublattices and the interactions A-A and B-B between the spins in the same sublattice. The A-B interactions are antiferromagnetic, while the A-A and B-B interactions are ferromagnetic. To apply the Weiss theory to this type of materials, it is important to assume that the Curie law works for each sublattices. It is possible derive the Curie-Weiss law that for ferrimagnetic materials is:

$$\chi = \frac{C}{T + (C/\chi_0)}$$

This equation is in a good agreement with experiments, except near the Curie point. The Curie point is the point at which theoretical and experimental susceptibility diverge and a spontaneous magnetization appears.

Below the Curie temperature, both sublattices are spontaneously magnetized with a $M(\alpha)$ curve very similar to the curve described by the Langevin/Brillouin law. The two magnetizations are not independent, the magnetization of sublattice A depends from

magnetization B and vice versa. Both sublattices must have the same Curie point because - otherwise - at some temperature one of the sublattices had no magnetization and would not be able to align the moments of the other sublattice. The A and B spontaneous magnetization curves shapes depends on the molecular fields and on the A and B type ions distribution, the resulting net magnetization is not necessary monotonically with the temperature. Generally the net magnetization increases with increasing temperature up to the Curie temperature, before which it quickly decays to zero. Some FIM materials show a zero net magnetization before the Curie point and beyond the Curie point magnetization returns to rise in the opposite direction. This temperature is called the *compensation point*. The magnetization of the sublattices is perfectly balanced and the net magnetization is zero.

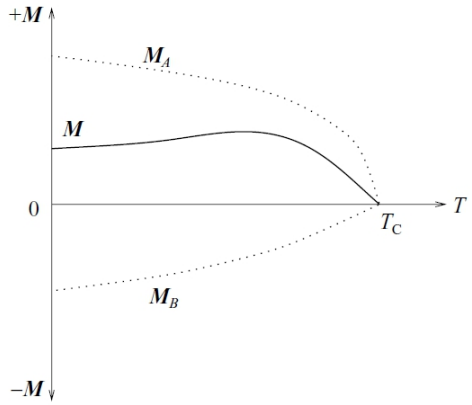

Figure: scheme of the spontaneous magnetization of the ferrimagnetic sublattices (dotted curves), and its resultant magnetization (solid curve),

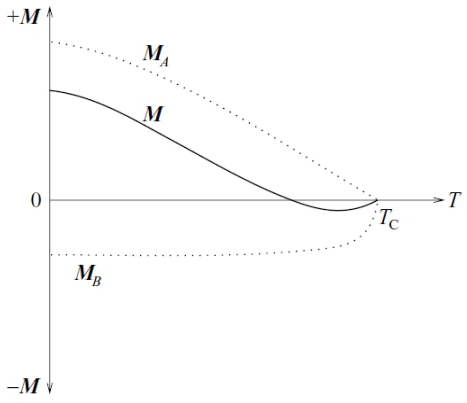

Figure: ferrimagnets unusual magnetization curves. Image from ref. 79

If the material is composed by more than two sublattices, the magnetization dependence on the temperature is very complicated but there is the possibility that exists a compensation point.

Actually, the most important ferrimagnetic material are the cubic ferrites which are electrically insulating mixed oxides, always containing iron . They are used in high-frequency applications because an applied field not induce undesired currents through the material. Ferrites fall in two main broad groups as to their crystal structure: cubic and hexagonal ferrites.

The cubic ferrites have the general formula $MO*Fe_2O_3$ in which M is a divalent metal, usually from the first transition, such as Mn^{2+}, Ni^{2+}, Fe^{2+} and Co^{2+}. The crystal structure of the cubic ferrites is the spinel structure in which oxygen are ordered in a face-centered cubic arrangement with two types of voids between the anions. There are tetrahedrally coordinated sites and octahedrally coordinated sites. In the spinel structure, only 1/8 of the tetrahedral sites and ½ of the octahedral sites are occupied.

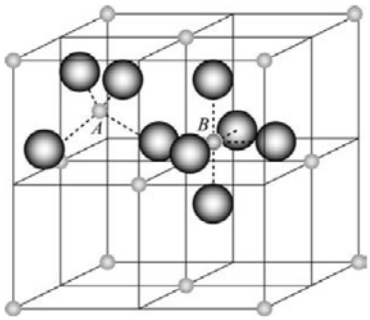

Figure: spinel structure scheme. The oxygen atoms (large sphere) are close-packed in 111 planes and create octahedral and tetrahedral sites occupied by A and B metal cations.
Image from ref. 79

In the (direct) spinel structure, all 2+ ions lie on the tetrahedral sites, while all 3+ ions lie on the octahedral sites. In the case of M = Zn^{2+} and Cd^{2+}, ions that have no magnetic moment, the ferrite is merely paramagnetic. Furthermore, the inverse spinel structure exists where the Fe^{3+} ions are equally distributed on the A and B sites with the divalent ions can be found on the remaining B sites. The Fe, Co and Ni ferrites have inverse structure and are ferrimagnetic. The antiferromagnetic A-B interaction is the predominant interaction and so Fe^{3+} ions in octahedral sites are anti-parallel aligned to the Fe^{3+} ions in tetrahedral sites. In this case the magnetic moments of the Fe^{3+} ions cancel out and their contribution to the net magnetization is zero However, the M^{2+} ions (Fe, Co, Ni) have magnetic moment aligned parallel one to another because of the ferromagnetic A-A and B-B interactions and it is their total moment that creates the net magnetization.

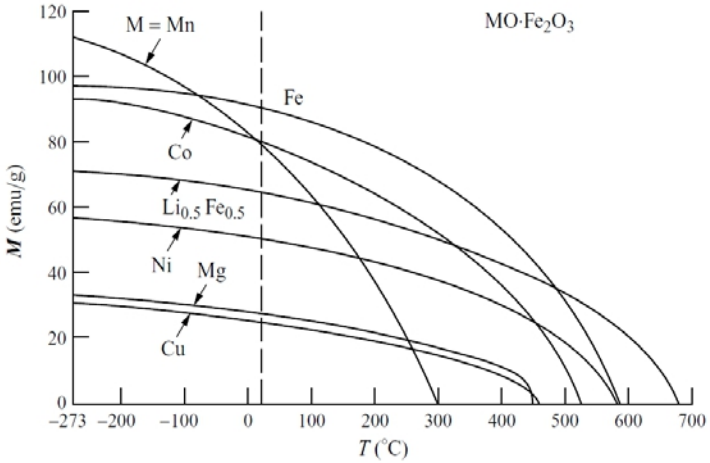

Figure: example of magnetization of some cubic ferrites. Image from ref. 79

Saturation magnetization and Curie temperature are very different in the cubic ferrites. For a specific application, ferrites properties could be tuned easily with solid solutions of mixed ferrites. Ferrites are magnetically soft materials, which are easy to magnetize and demagnetize. Their low electrical conductivity and high permeability made ferrites a good candidate for application as cores for induction coils operating at high frequencies. In the past, ferrites was an important material used as memories composed of a ferrite cores connected by a wire network. Ferrites were important for this application due to their square-shaped hysteresis loop.

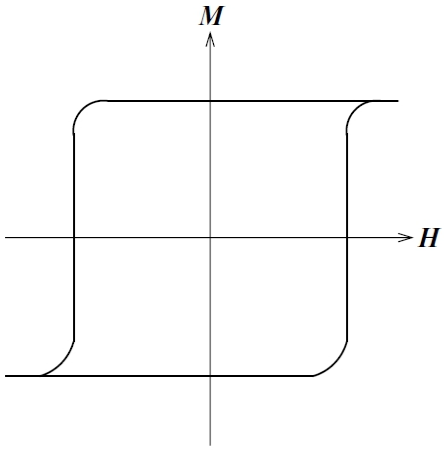

Figure: typical ferrite hysteresis loop. Image from ref. 79

This typical shape is induced by the large magnetocrystalline anisotropy. The remanence magnetization and saturation magnetization are very close to each other and a well-defined

applied field slightly greater than the coercive field is able to invert the magnetization direction.

Other important good feature of the cubic ferrites are: low magnetostriction, high Curie temperature, mechanical strength, and minimal temperature variation.

Hexagonal ferrites can be mostly represented by the $BaFe_{12}O_{19}$ barium ferrite whose hexagonal structure is known as magnetoplumbite.

In the unit cell, magnetoplumbite shows 10 oxygen layers. S and S* block are spinels with 6 Fe^{3+} ions, 4 of this are on octahedral sites and their spins are aligned to each other. S and S* are equivalent and rotate of 180° respect to each other. Otherwise R and R* blocks have 3 oxygen layers but in the middle layer one oxygen anion is replaced by a barium ion. R and R* respectively own 6 Fe^{3+} ions which are 5 of them in the octahedral sites (3 spin-up and 2 spin-down) and one spin-up coordinated by 5 O2- anions. Their main application of hexagonal ferrites is as permanent magnets. Hexagonal ferrites are hard magnetic material.

3.3.8. Anisotropy

Magnetic properties of crystalline materials are anisotropic because they assume different values depending on the direction along which they are measured. In particular, anisotropy can be intrinsic to the material or induced by an external circumstance. When it is intrinsic to the material, anisotropy is closely related to the crystal structure or the crystal shape. A typical example of intrinsic anisotropy is the magnetocrystalline anisotropy. This phenomenon explains why the magnetization tends to align itself along a preferential crystallographic direction. In other words, magnetocrystalline anisotropy is the energy difference per unit volume between the hard and easy magnetization axis. Starting from these considerations, it is easy to realize that different crystal cells show different preferential magnetic directions. For example the body-centered cubic Fe has the <100> direction as preferential axis, whereas the Ni face-centered cubic has the <111> face as easy axis. The preferential magnetic axis does not affect the magnetic saturation: it reaches the same value of magnetization regardless of the direction where the field is applied. Somewhat different value of field will be needed to achieve the saturation. The physical reasons to magnetocrystalline anisotropy are the coupling between the spin and orbital degrees of freedom of the electrons. In fact, when a magnetic external fields is applied, the spins are re-oriented and accordingly the spatial orbitals too need to be re-oriented. However, the orbitals are coupled to the lattice so they oppose to the re-orientation. In some materials the coupling between the orbitals and the spins is weak so the magneto-crystalline anisotropy is not strong. While in some other material this anisotropy is very strong and a very large field is required to invert the magnetization. A typical example of these latter materials are the rare-earth which are heavy elements with a very strong spin-orbital coupling. For this reason rare-earth-containing magnets are often used for applications as permanent magnet.

One example of rare-earth is terbium metal, which presents an hexagonal cell with the easy axis in the *c* plane. In this element the magneto-crystalline anisotropy is so strong that, also applying a very large magnetic field, only around the 80% of the magnetic saturation value could be achieved. This behavior is due to the resistance of the magnetization to move off the easy axis.

Obviously a polycrystalline material with no preferred orientation of its crystallites/domains does not show overall magneto-crystalline anisotropy. However, only a polycrystalline material with a perfectly spherical shape do not show any magnetic anisotropy, because an external magnetic field magnetize it equally in all directions. Non spherical samples are easier

to magnetize in a certain direction. This behavior is called shape anisotropy. In general, magnetization is along the direction where the sample has its largest size.

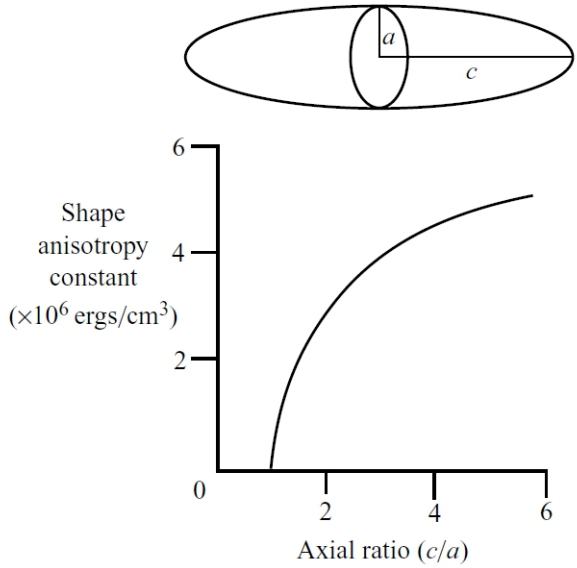

Figure: example of shape anisotropy constant trend in a spheroid cobalt structure.
Image from ref. 79

The shape anisotropy constant of ellipsoidal specimens strongly depends on the *c/a* ratio between the major and minor axes. The shape anisotropy constant increases with the axial ratio.

3.3.9. Exchange bias

The phenomenon called exchange bias was observed for the first time in 1956 studying Co/CoO nanoparticles which showed a shifted hysteresis loop. Exchange bias is a consequence of the coupling across a FM/AFM interface.

Exchange-bias has been studied in the last decades, in order to exploit it to beat the superparamagnetic limit of the materials used for applications that require a stable magnetization for long time such as recording media. These applications require a decrease in particle size – to increase the storage density - which involves a decrease also in the anisotropy energy per particle that becomes comparable to the thermal energy. In this way, thermal energy generates magnetization instability in the nanoparticles, this behavior is called "superparamagnetic limit". To remedy to this problem by enhancing the magnetic stability again and increasing the blocking temperature, it is possible to exploit the exchange coupling between a ferromagnetic and antiferromagnetic material.[80]

The exchange bias appears when a ferromagnetic/antiferromagnetic interface is cooled (through the Néel temperature of the AFM) in a magnetic field. The quality of the interface is very important on the magnetic final results.2 Generally the Curie temperature of the ferromagnet is above the Nèel antiferromagnet temperature, so the ferromagnetic spins are already align to the field direction. When the Néel temperature is reached during the cooling process, the antiferromagnetic moments align to the ferromagnetic ones because of the exchange coupling. When an exchange bias phenomenon occurs it is possible to see: i) a magnetic hysteresis loop shift of the ferromagnet below the antiferromagnetic Néel temperature, which can be related to an additional biasing field causing an unidirectional magnetic anisotropy and, ii) a broader hysteresis loop with an increased coercivity revealing induced uniaxial or multiaxial anisotropy.

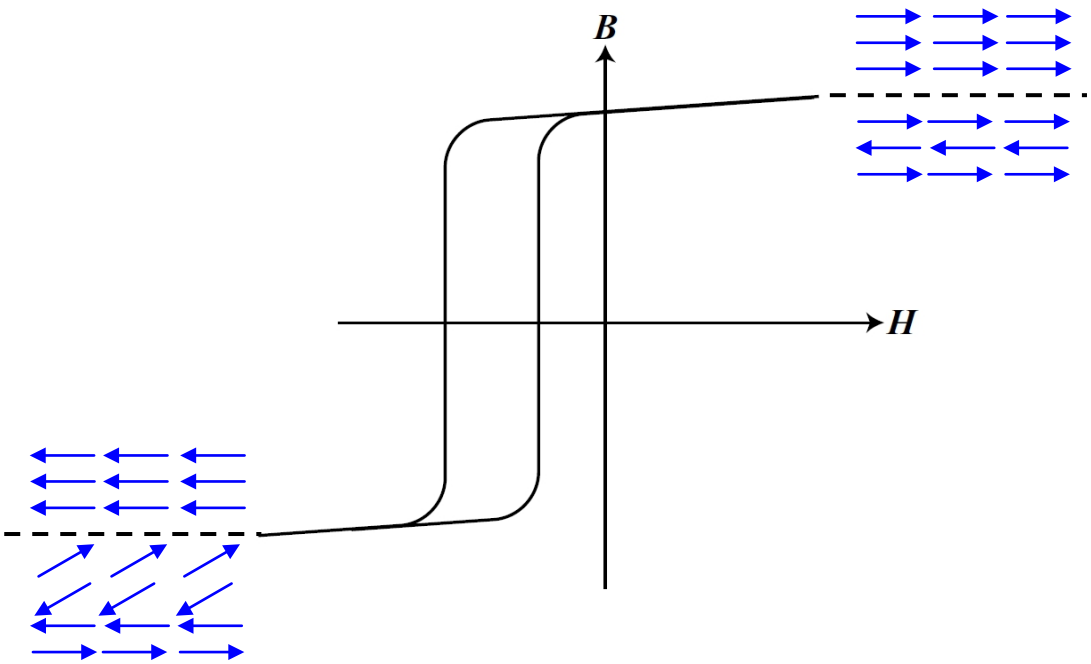

Figure: simplified representation of the exchange bias. Image from ref. 79

A simple description of the exchange bias phenomenon is as follows. Ferromagnetic spins are aligned parallel to the field that was applied during the cooling and AFM spins close to the surface are aligned parallel to the FM spins because of the exchange coupling.. When an oppositely directed field is applied, antiferromagnetic spins resist to the inversion of FM spins due to their large anisotropy. The AFM spins lying at the interface tend to pin the ferromagnetic moment in the same original direction taken during the cooling. This mechanism produces the need of a very large coercivity field to reverse the magnetization. It is important to stress that the aim of the field cooling is to give a single alignment direction to the sample. Without field cooling, the distribution of the easy axis becomes random.

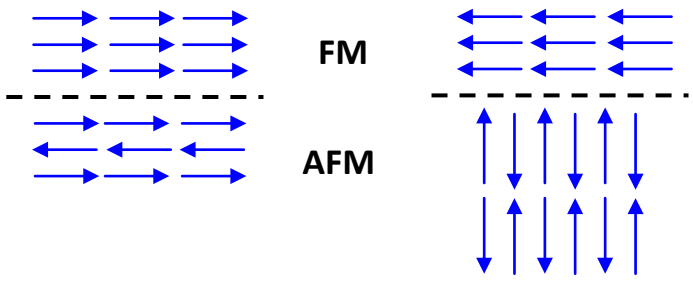

Figure: representation of uncompensated and compensated FM/AFM interface.
Image from ref. 79

This simple theoretical model is a simplification of the real physical behavior. In fact the expected amount of exchange bias is many order larger than the magnitude experimentally observed. The simplified model considers mainly: i) the interaction of the ferromagnet with the applied field, ii) the anisotropy energy in the antiferromagnet and, iii) the interface interaction between ferro- and antiferromagnet. A more detailed model could consider also: i) the thickness of the ferro- and the antiferromagnet, ii) the angle between the antiferromagnetic sublattice magnetization and anisotropy axis, iii) the angle between ferromagnetic magnetization and anisotropy axis and, iv) the angle between the applied field and the ferromagnetic anisotropy axis. The real sample is also affected by: i) the parallel or perpendicular orientation of the antiferromagnetic domain wall to the surface, ii) surface roughness, iii) the fraction of the interfacial spins significantly involved in the exchange interaction. Several experiments performed during the last decades shed lightly on the exchange bias phenomenon and increasingly complex models explained that the ordering in the antiferromagnetic material affects the resulting exchange bias and the mechanism for the coercivity increase is due to several causes, conversely to exchange bias. Finally, it was found that exchange bias is smaller in thin-film multilayer with a good quality deposition than in a polycrystalline sample. It means that defects are very important to exchange-bias. Probably the presence of defects has to be considered also when explaining both anisotropy and increased coercivity.

4. Summary of the results

My PhD research project concerns the synthesis and characterization of magnetic nanoparticles (NPs) of transition metal chalcogenides (oxides and sulfides) with controlled size, shape and composition. The final goal is to increase the NP magnetic anisotropy, *i. e.*, the energy barrier for the reversal of the nanoparticle magnetic moment, so that it is larger than the thermal energy at room temperature thus achieving a high magnetic stability. Products based on such NPs can have many applications, *e. g.*, in the field of magnetic memory devices.

Strategies to increase the magnetic anisotropy are either the synthesis of magnetic nanoparticles with anisotropic shapes or the synthesis of core-shell structures with exchange-bias deriving from the coupling between a ferromagnetic/ferrimagnetic (FM) and an antiferromagnetic (AFM) material. The novelty of my project lies in the implementation of *both* the above strategies in a single nanoparticle in order to achieve the desired improvement of magnetic stability. The main steps required are (i) the synthesis of AFM nanoparticles with anisotropic shape and (ii) the coating of such nanoparticles with a FM transition metal oxide. As to the AFM nanoparticles, I focused my attention on MnO and MnS (the latter having a higher Néel temperature T_N = 160 K than the T_N = 116 K of MnO) as antiferromagntic material for the synthesis of anisotropic nanoparticles, in order to exploit them as core in an AFM metal oxide/FM metal oxide core-shell structure. As a coating, I focussed on FM iron oxide FeOx (FeOx = $Fe_{3-x}O_{4-x}$, $0 \leq x \leq 1$) because of its high saturation magnetization and the large body of knowledge about the iron oxide nanochemistry. *Thus, the final product I aimed at are anisotropic MnO@FeOx core-shell NPs*. The synthetic investigation and characterization of MnO, MnS and MnO@FeOx NPs, aimed at achieving the desired size, shape and crystal structure, are described in detail in my Thesis.

Moreover, our interest for the core-shell structure was also directed on a magnetic investigation of thin-film assemblies of FM metal/AFM metal oxide core-shell NPs deposited on substrate. The magnetic behaviour of assemblies of Ni@NiO NPs prepared by different protocols and with different shell thickness was studied in our laboratories in the framework of a collaboration with the group led by Prof. D'Addato, Dr. Luches, and Prof. Valeri in Modena.

4.1. MnO nanoparticles

In my PhD research, MnO (and MnS) nanoparticles (NPs) were synthesized by a solvothermal method involving the high-temperature decomposition of a manganese(II) carboxylate precursor (oleate or stearate) in octadecene, in the presence of sulphur and (possibly) free fatty acid (oleic or stearic acid) as a surfactant:

$$(R_1COO)_2Mn \xrightarrow[\text{octadecene, } \Delta]{\text{S, } R_2COOH} \text{MnO NPs}$$

where R_1 and R_2 independently are oleic (R = Ol) or stearic (R = St) residues. Both precursors and surfactants have low environmental impact. I have investigated how the synthetic outcome, in particular the NP composition and shape, is affected by several parameters, such as the type of fatty acid present in the precursor or as a surfactant, the manganese/sulphur/surfactant molar ratio, and the growth temperature and time.

The study of the sulfur : manganese (S:Mn) molar ratio gave interesting results about the NP composition. It had already been demonstrated that, when the S:Mn molar ratio is ≤ 0.5, we only obtained MnO NPs and when S:Mn ≥ 2, MnS NPs were produced. I have found that the composition of the resulting NPs is also strongly affected by the surfactant : manganese (L:Mn) molar ratio, in addition to the S:Mn molar ratio. When plotting the NP composition in a plot with these two molar ratios on the axes, the boundary between the MnO and MnS regions is close to the plot diagonal.

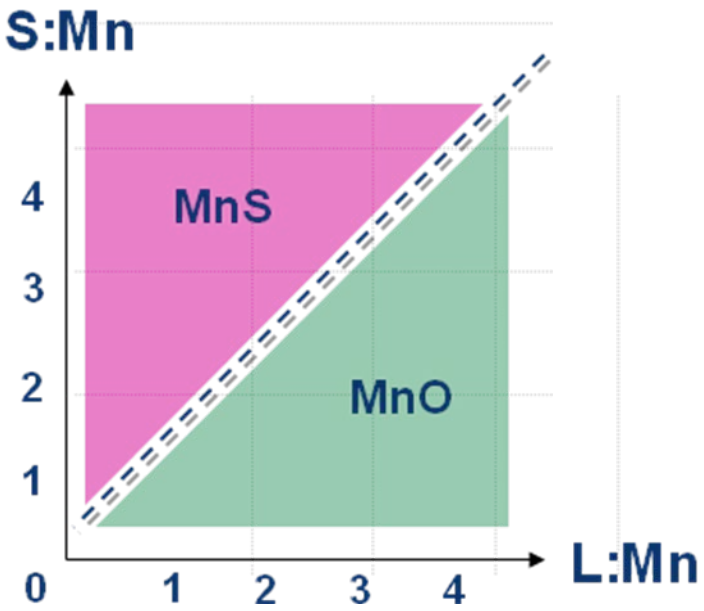

Accordingly, it was decided to always use S:Mn = 0.5 to synthesize MnO NPs and S:Mn = 2 to synthesize MnS NPs (see below). The reason why we used sulfur to prepare MnO NPs is that nicely anisotropic MnO NPs were produced when S was present in a small amount in the reaction mixture

I have then investigated the influence of using Mn oleate or Mn stearate as a precursor, often with the addition of the corresponding oleic and stearic acid ($R_1 = R_2$ = Ol and $R_1 = R_2$ = St), on the NP shape. A series of experiments has been carried out with fixed growth time and temperature and varying the L:Mn molar ratio. This ratio turned out to be critical in controlling the NP size and (above all) shape. When $R_1 = R_2$ = Ol, we obtained multipode NPs with *n* = 1 to 6 oval lobes, which have form factor = L/W = 1.6. When $R_1 = R_2$ = St, we again obtained multipode NPs but with features largely different from the $R_1 = R_2$ = Ol case. The NPs have more elongated branches with constant width and jagged edges. The NPs can have *n* = 2 (rods), 3 (T's), and 4 (crosses) branches with form factor = 3.6. No NP with *n* > 4 branches was observed. The size of the NPs is also a function of the L:Mn ratio. To analyze the size of the anisotropic NPs, I used conventional TEM images to measure: diagonals for octahedral NPs and NPs with *n* = 4 and 6; length and width for *n* = 3 NPs; length for *n* = 2 NPs; diameter for spherical and irregular NPs. It can be seen that the length of the lobe/branch is approximately equal irrespective of the value of *n*.

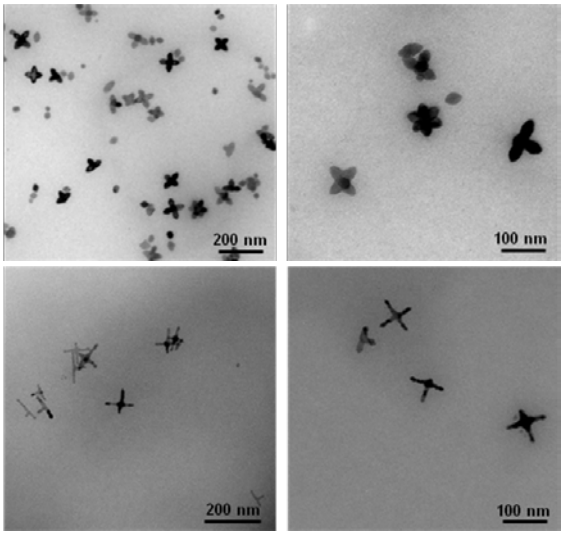

C*onventional-TEM images of selected MnO NPs. Top left: MnO multipods synthesized with* $R_1 = R_2$ *= Ol and L:Mn = 4:1. Bottom left: MnO multipods synthesized with* $R_1 = R_2$ *= St and L:Mn =1:1.*

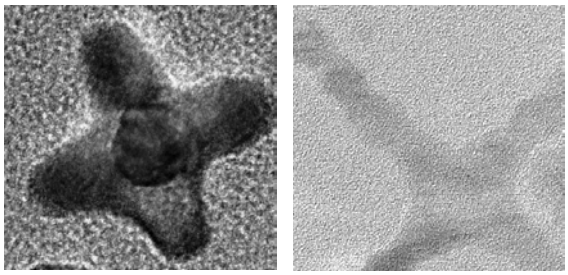

HRTEM images. Left: MnO multipods with $R_1 = R_2$ *= Ol and L:Mn 4:1; right) MnO multipods with* $R_1 = R_2$ *= St surf:prec 1:1 NPs are single crystals.*

In the case of $MnOl_2$ precursor, low (1-2) and high (7-8) L:Mn molar ratio gave oleate-coated MnO NPs (MnO@oleate) with isotropic and regular shapes, such as octahedral or ellipsoidal NPs, while using an intermediate molar ratio (3-6) gave multipods with a varying degree of shape development and definition. Conversely, in the MnO@stearate case of $MnSt_2$

precursor, the extreme L:Mn molar ratios (low: 0-2, high: 4) gave elongated-branch multipode NPs (with a varying degree of shape development), while the intermediate ratio (L:Mn = 3) gave a mixture of spherical, octahedral and elliptic NPs. Finally, I also used different acids in the precursor and as free surfactant ($R_1 \neq R_2$). It resulted that the overall NP shape (lobed *vs.* branched) is governed by R_1, the fatty carboxylate present in the precursor.

An accurate study of the NP crystal structure has been carried out by HR-TEM. In HRTEM images, crystal planes parallel to the electron beam cause the appearance of lattice fringes. We found that the majority of the MnO NPs are single crystals, grown as such from a single seed or developed by oriented attachment of smaller crystals. Some reactions, such as $R_1 = R_2$ = Ol with L:Mn = 3 and $R_1 = R_2$ = St with L:Mn = 2, gave MnO@oleate and MnO@stearate NPs in the early stage of anisotropy development with budding branches and lobes, which led us into supposing that anisotropic shape developed starting from initially isotropic seeds. This supports the first hypothesis of anisotropic growth from a single seed according with the HRTEM investigation.

To evaluate the NP magnetic properties, SQUID magnetometric measurements have been carried out on isotropic and both types of anisotropic NPs. The magnetic behaviour of the NPs was investigated by measuring the magnetization *M* as a function of the field *H* at 5 and 295 K (hysteresis loops) and both zero-field cooled (ZFC) and field cooled (FC) magnetization as a function of temperature between 295 and 5 K. Size and shape do not significantly affect the magnetic properties of the multipod NPs which show a magnetic behaviour similar to that of isotropic (spherical or octahedral) MnO nanoparticles. The small differences between the isotropic and the anisotropic NP samples are related to the surface effects (*e.g.*, the small exchange bias effect due to the coupling between the pinned-spin FM surface layer and the AFM internal part of the NP), the magnitude thereof depends on the surface/volume ratio of the NP, as expected.

In conclusion, I synthesized MnO NPs with highly anisotropic shape that retain their antiferromagnetic structure despite the peculiar shape. These NPs satisfy the requirements needed to be used as AFM core in core-shell NPs that exploit both their antiferromagnetism and shape to achieve an increased magnetic stability.

4.2. MnS nanoparticles

Building on the above described solvothermal reaction procedure, I further developed my protocol in order to also obtain a synthetic procedure for MnS NPs. At variance with (rock salt) MnO, MnS presents three different polymorphs, which possess different physical properties. Hence, it is critical to achieve control on the crystal structure of MnS NPs. The MnS polymorphs are: the thermodynamically stable α-MnS (rock salt structure) where Mn ions are octahedrally coordinated; the β-MnS (zinc blende structure) and γ-MnS (wurtzite structure) where Mn ions are tetrahedrally coordinated. As reported in the literature, up to now it was possible to control the MnS crystal phase by varying temperature and/or pressure. In this study, it was demonstrated that, in a solvothermal synthesis, the surfactant is able to act not only as a growth regulator/capping agent but also as a true reactant, which affects the nanocrystal structure at the seed-growth step.

According to the previous results, I decided to use S:Mn molar ratio equal to 2 in order to avoid the formation of MnO. The starting point of this investigation was a peculiar and reproducible result I observed when investigating how the formation of MnO *vs.* MnS NPs depended on the S:Mn and L:Mn ratios. The solvothermal reaction with S:Mn = 2 and L:Mn = 4 surprisingly gave MnS NPs despite under these conditions formation of MnO NPs is expected (see the figure above). Furthermore, this result was independent on the Mn precursor used. Thus, I was prompted to investigate which is the effect of the surfactant in this peculiar case by carrying out a series of syntheses using a set of long-chain aliphatic surfactants having different functional end-groups. The results are collected in the following Table.

Precursor: $MnSt_2$		**Precursor: $Mn_2(CO)_{10}$**	
Surfactant (L)	**Crystal phase**	**Surfactant (L)**	**Crystal phase**
Dodecylamine	γ-MnS	Oleylamine	α-MnS (γ-MnS)
Hexadecylamine	γ-MnS	Dodecylamine	α-MnS
Octadecylamine	γ-MnS	Hexadecylamine	α-MnS
Oleylamine	γ-MnS	Octadecylamine	α-MnS
OlAm/DdTh	γ-MnS	Stearic acid + Oleylamine	α-MnS
None	α-MnS	Stearic acid + Dodecylamine	γ-MnS

Oleylalcohol	α-MnS	Stearic acid + Hexadecylamine	γ-MnS
Dodecanethiol	α-MnS	Stearic acid + Octadecylamine	γ-MnS
Stearic acid	α-MnS/MnO	Oleic acid + Hexadecylamine	γ-MnS

When $MnSt_2$ is used as a precursor, the presence of an amine in the reaction mixture leads to γ-MnS nanoparticles, while α-MnS NPs are observed for all other surfactants. When the metal precursor is the surfactant-free manganese decacarbonyl, even amine surfactants yielded α-MnS NPs. However, when a surfactant mixture containing both carboxylic acid and amine (acid : amine = 1:2), the resulting MnS NPs have γ crystal structure. Therefore, pure γ-MnS NPs can be obtained when both carboxylic acid and amine are present, in particular a 1:2 mixture of stearic acid and C_{12}-C_{18} alkylamine. Conversely, when the surfactant comprises either a carboxylic acid or an amine only, α-MnS nanoparticles are obtained. It is also noteworthy that the presence of a sulfur-containing surfactant (dodecanethiol) does not affect the formation of γ-MnS nanoparticles.

In conclusion, I have developed a synthetic protocol which enables one to control the polymorphism of MnS NPs.

4.3. MnO@FeOx ($FeOx = Fe_{3-x}O_{4-x}$, $0 \leq x \leq 1$) core-shell nanoparticles

The final step towards anisotropic AFM/FM core-shell is the development of an effective protocol for the coating of (possibly anisotropic) MnO NPs with a shell of iron oxide of adequate quality (thickness, compactness) for the buildup of a strong exchange coupling between the AFM core and FM shell leading to increased magnetic stability. The main challenge in the synthesis of core-shell NPs starting from a pre-formed NP core is to find the conditions under which the shell precursor efficiently coats the core without nucleating homogeneous NPs. We investigated the synthetic conditions in order to obtain a significantly compact and thick shell of iron oxide on the MnO NPs and simultaneously avoid the nucleation and growth of homogeneous iron oxide NPs.

To begin with, I first set at developing a coating protocol using spherical MnO cores. When the formation of iron oxide coating on such NPs will be well controlled, I will refine the synthetic protocol for core-shell NPs using anisotropic MnO nanoparticles as substrate in

order to achieve my final goal of synthesizing anisotropic AFM/FM NPs with increased magnetic stability thanks to the synergic effect of shape anisotropy and exchange coupling.

I compared hydrothermal and solvothermal methods. The former method was not promising, probably due to the low reaction temperature, and therefore I focused on the solvothermal method. Two series of solvothermal reactions with different setups were compared. In the first series involved I used $Fe(CO)_{10}$ as a precursor, 1-octadecene as a solvent, and a low initial concentration of MnO cores in the reaction mixture. The iron pentacarbonyl precursor seemed not effective in the heterogeneous nucleation on the MnO surface and shell growth. The best outcome by this method were core-shell NPs free from iron oxide NPs from homogeneous nucleation, having MnO cores with unchanged size but with a very low iron content. In analytical ESI and EDX mapping with nanometre resolution, the signal from iron was very weak. It was not even clear whether iron oxide is present on the MnO surface or it had somehow diffused into the MnO core. Due to the low iron content, no iron-related crystal structure could be identified by electron diffraction and HRTEM. Actually, it is not even possible to discern whether iron is present as metal or oxide. A reaction series where the amount of iron was increased was carried out. Even when the iron precursor concentration was so high that the formation of homogeneous iron oxide NPs occurred, no increase in the iron oxide shell thickness was obtained.

Therefore, in the second series I resorted to iron (III) acetylacetonate as a precursor, dibenzyl ether as solvent, and a high initial concentration of MnO cores in the reaction mixture. This procedure using Fe(III) acetylacetonate as a metal precursor, which is based on a previous report by Nogués et al. published in 2013, showed to be promising. Improving on this procedure, we developed a reproducible 20 min long protocol that gives core-shell NPs with a 0.5-2 nm thick iron oxide shell and free from homogeneous iron oxide NPs. Holding that such thickness is too low to develop an exchange interaction strong enough to suppress the superparamagnetism of so small FeOx NPs, I considered to increase the shell thickness by sequentially performing several shell-growth steps onto the FeOx coated MnO cores. Different methods to stepwise increase the shell thickness were tested.

Regarding the treatment of the MnO core/core-shell NPs between the sequential additions of Fe precursor, the protocols can be classified as follows: i) protocols where the NPs were isolated between the shell-growth steps; ii) protocols where the reaction mixture was cooled but the NPs were not isolated and iii) protocols where the reaction mixture is maintained at high temperature throughout the whole multi-step procedure. The last procedure affords long multi-step reactions with many additions of Fe precursor (and possibly

surfactants). Core-shell NPs with suitably thick shell was prepared as follows. The standard 20 min protocol was carried out, then the reaction mixture was kept at 250 °C and every 20 min the same initial amount of Fe precursor and surfactants (dissolved in some mL of toluene) was added. Globally, the reaction lasted 4 hours. In these reactions, a large shell thickness (6-7 nm) was obtained but, unfortunately, independently-nucleated homogeneous FeOx NPs were always observed. At the moment, magnetic measurements are in progress to analyze the behaviour of these core-shell NPs and understand if they are able to generate an effective exchange coupling between MnO and FeOx.

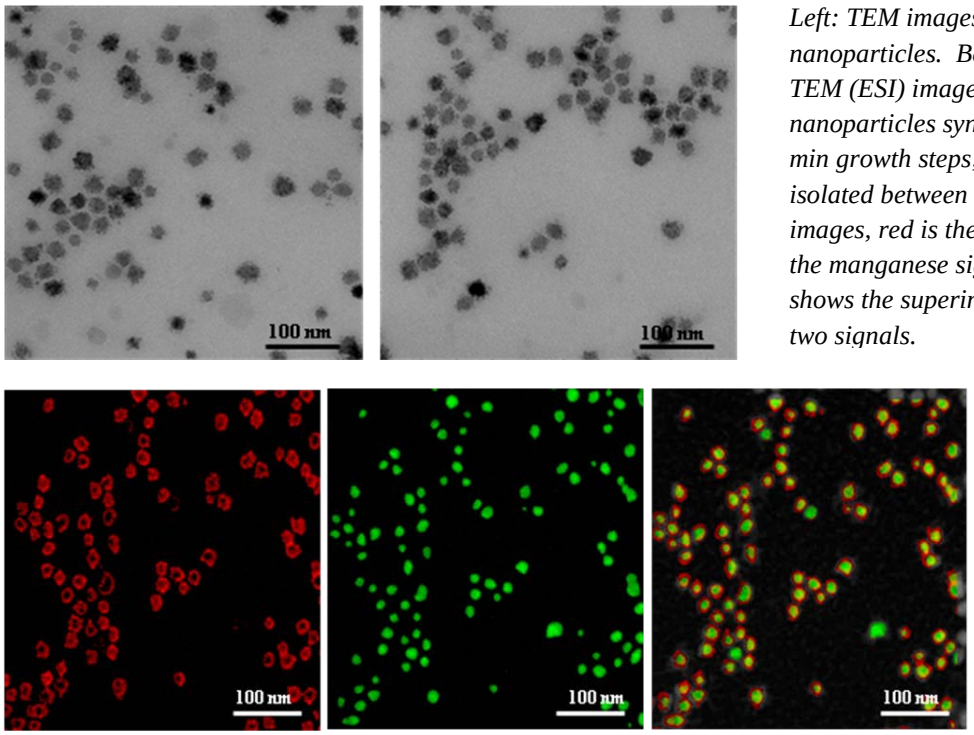

Left: TEM images of core-shell nanoparticles. Below: energy filtered TEM (ESI) images of core-shell nanoparticles synthesized with two 20 min growth steps; the nanoparticles were isolated between the two steps. In the images, red is the iron signal, green is the manganese signal and last image shows the superimposition between the two signals.

4.4. Ni@NiO core-shell nanoparticles

Shifting to another type of core-shell NPs prepared to achieve better magnetic stability, we performed a detailed study of thin-film assemblies of Ni@NiO core–shell nanoparticles (NP) prepared by the group of Prof. D'Addato, Dr. Luches, and Prof. Valeri in Modena using high-vacuum vapor deposition techniques. Magnetic measurements were performed to compare the magnetic behaviour of NPs where the shell had been prepared by different methods or NPs with different shell thickness were prepared by a single method.

In the first series of samples, several Ni@NiO core-shell NPs were obtained by oxidation of Ni NPs: in vacuum deposition (sample A and B, native oxide), deposition in

oxygen atmosphere (sample C), post-annealing in air (sample D); furthermore, these NPs were compared to Ni@NiO NPs obtained by sequential (reactive) deposition of a first NiO layer, a second layer of discrete Ni NPs, and a third NiO layer (sample E). Field-cooled/zero-field-cooled magnetization curves and field-cooled isothermal hysteresis cycles at T = 5 K were recorded by a SQUID magnetometer to study the relationships between magnetic properties and the morphology of the oxide shell. The exchange-bias (EB) field H_{bias} is negligible in samples where just native oxide is present (A and B, oxidation during in-vacuum deposition of metallic NPs) and samples where NiO is present as a few, small islands on the Ni NPs (C, exposure to air) despite that the NiO/Ni interface is of good quality. Heating Ni NPs in air at 250 °C produced a complete shell of NiO - at the expense of the Ni NP - and a substantial H_{bias} is observed. The tri-layer heterostructure NiO/Ni/NiO presents the strongest EB effects on the Ni NP magnetization and thus has the most effective exchange interaction at the NiO/Ni interface.

The strong EB effects observed and the possibility to accurately regulate the thickness of both NiO layers and the size of the Ni core of the tri-layer NiO/Ni NPs/NiO samples (with much better control and flexibility than in the case of preparation by oxidation) prompted us to investigate a series of tri-layer samples where NPs with different thickness of the third (NiO) layer t_s were compared. In the samples with the thinnest layer, NiO islands formed and enlarged on the Ni cores, and a complete shell was achieved only at t_s = 1.6 nm. In the sample with the thickest NiO shell, a discontinuous NiO matrix embedding the Ni cores was formed. These samples displayed a strong dependence of H_{bias} on the thickness of the third layer t_s, which however did not agree with the conventional Meiklejohn-Bean model. The variation of H_{bias} could be related to the thickness dependence of the NiO magnetic anisotropy constant. Tri-layers samples have lower H_{bias} than the annealed sample (at equal shell thickness) probably due to the lower quality of the interface and the different mutual arrangement of the Ni and NiO crystal lattice.

In conclusion, using tri-layers samples, it was possible to separately investigate the contributions to the exchange bias arising from the thickness and interface quality. Furthermore, it was possible to prepare magnetic NPs with tunable EB and magnetic stability by regulating a single morphological parameter (t_s). These results are a first, significant step towards the synthesis of magnetic nanoparticles with tunable magnetic properties.

References

1. Lin, C.-C., Chen, C.-J. & Chiang, R.-K. Facile synthesis of monodisperse MnO nanoparticles from bulk MnO. *J. Cryst. Growth* **338,** 152–156 (2012).

2. Baek, M. J. *et al.* Water-Soluble MnO Nanocolloid for a Molecular T_1 MR Imaging: A Facile One-Pot Synthesis, In vivo T_1 MR Images, and Account for Relaxivities. *ACS Appl. Mater. Interfaces* **2,** 2949–2955 (2010).

3. Kim, N. D., Yun, H. J., Kyu Song, I. & Yi, J. Preparation and characterization of nanostructured Mn oxide by an ethanol-based precipitation method for pseudocapacitor applications. *Scr. Mater.* **65,** 448–451 (2011).

4. Thota, S., Prasad, B. & Kumar, J. Formation and magnetic behaviour of manganese oxide nanoparticles. *Mater. Sci. Eng. B* **167,** 153–160 (2010).

5. Bastami, T. R. & Entezari, M. H. Synthesis of manganese oxide nanocrystal by ultrasonic bath: Effect of external magnetic field. *Ultrason. Sonochem.* **19,** 830–840 (2012).

6. Park, J. *et al.* Synthesis, characterization, and magnetic properties of uniform-sized MnO nanospheres and nanorods. *J. Phys. Chem. B* **108,** 13594–13598 (2004).

7. An, K. *et al.* Synthesis of Uniformly Sized Manganese Oxide Nanocrystals with Various Sizes and Shapes and Characterization of Their T1 Magnetic Resonance Relaxivity. *Eur. J. Inorg. Chem.* **2012,** 2148–2155 (2012).

8. Moya, C., Morales, M. D. P., Batlle, X. & Labarta, A. Tuning the magnetic properties of Co-ferrite nanoparticles through the 1,2-hexadecanediol concentration in the reaction mixture. *Phys. Chem. Chem. Phys.* **17,** 13143–13149 (2015).

9. Schladt, T. D. *et al.* Highly soluble multifunctional MnO nanoparticles for simultaneous optical and MRI imaging and cancer treatment using photodynamic therapy. *J. Mater. Chem.* **20,** 8297 (2010).

10. López-Ortega, A. *et al.* Size-dependent passivation shell and magnetic properties in antiferromagnetic/ferrimagnetic core/shell MnO nanoparticles. *J. Amer. Chem. Soc.* **132,** 9398–407 (2010).

11. Chen, H., Chu, P. K., He, J., Hu, T. & Yang, M. Porous magnetic manganese oxide nanostructures: Synthesis and their application in water treatment. *J. Colloid Interface Sci.* **359,** 68–74 (2011).

12. Zitoun, D., Pinna, N., Frolet, N. & Belin, C. Single crystal manganese oxide multipods by oriented attachment. *J. Am. Chem. Soc.* **127,** 15034–5 (2005).

13. Zhong, X., Xie, R., Sun, L., Lieberwirth, I. & Knoll, W. Synthesis of dumbbell-shaped manganese oxide nanocrystals. *J. Phys. Chem. B* **110,** 2–4 (2006).

14. Ould-Ely, T. *et al.* Manganese(II) oxide nanohexapods: Insight into controlling the form of nanocrystals. *Chem. Mater.* **18,** 1821–1829 (2006).

15. Irene Rusakova , Teyeb Ould-Ely , Cristina Hofmann , Darío Prieto-Centurión , Carly S. Levin , Naomi J. Halas , Andreas Lüttge, and K. H. W. Nanoparticle Shape Conservation in the Conversion of MnO Nanocrosses into Mn3O4. *Chem. Mater* **19,** 1369–1375 (2007).

16. Chen, Y., Johnson, E. & Peng, X. Formation of monodisperse and shape-controlled MnO nanocrystals in non-injection synthesis: Self-focusing via ripening. *J. Am. Chem. Soc.* **129,** 10937–10947 (2007).

17. Xi-Guang, H. *et al.* Directional etching formation of single-crystalline branched nanostructures: A case of six-horn-like manganese oxide. *J. Phys. Chem. C* **113,** 2867–2872 (2009).

18. Puglisi, A. *et al.* Monodisperse Octahedral alpha -MnS and MnO Nanoparticles by the Decomposition of Manganese Oleate in the Presence of Sulfur. *Chem. Mater.* 2804–2813 (2010).

19. Douglas, F. J. *et al.* Formation of octapod MnO nanoparticles with enhanced magnetic properties through kinetically- manganese complexes †. *Nanoscale* **6,** 172–176 (2014).

20. Kim, A. *et al.* Facile Synthesis of Multipodal MnO Nanocrystals and Their Catalytic Performance. *Eur. J. Inorg. Chem.* **2014,** 1279–1283 (2014).

21. Jun, Y., Jung, Y. & Cheon, J. Architectural control of magnetic semiconductor nanocrystals. *J. Am. Chem. Soc.* **124,** 615–619 (2002).

22. Yang, X. *et al.* Polymorphism and formation mechanism of nanobipods in manganese sulfide nanocrystals induced by temperature or pressure. *J. Phys. Chem. C* **116,** 3292–3297 (2012).

23. Peng, L., Shen, S., Zhang, Y., Xu, H. & Wang, Q. Controllable synthesis of MnS nanocrystals from a single-source precursor. *J. Colloid Interface Sci.* **377,** 13–17 (2012).

24. Zhang, Y., Lu, J., Shen, S., Xu, H. & Wang, Q. Ultralarge single crystal SnS rectangular nanosheets. *Chem. Commun.* **47,** 5226–5228 (2011).

25. Mu, J. *et al.* Phase and shape controlling of MnS nanocrystals in the solvothermal process. *J. Nanoparticle Res.* **10,** 197–201 (2008).

26. Wang, D. S.; Zheng, W.; Hao, C. H.; Peng, Q.; Li, Y. D. A Synthetic Method for Transition-Metal Chalcogenide Nanocrystals. *Chem. Eur. J.* **15,** 1870–1875 (2009).

27. Gui, Y., Qian, L. & Qian, X. Hydrothermal synthesis of uniform rock salt (α-) MnS transformation from wurtzite (γ-) MnS. *Mater. Chem. Phys.* **125,** 698–703 (2011).

28. Yang, X. *et al.* Size-controlled synthesis of bifunctional magnetic and ultraviolet optical rock-salt mns nanocube superlattices. *Langmuir* **28,** 17811–17816 (2012).

29. Biswas, S., Kar, S. & Chaudhuri, S. Effect of the precursors and solvents on the size, shape and crystal structure of manganese sulfide crystals in solvothermal synthesis. *Mater. Sci. Eng. B* **142,** 69–77 (2007).

30. Ma, D., Huang, S. & Zhang, L. One-pot synthesis and magnetic, electrical properties of single-crystalline α-MnS nanobelts. *Chem. Phys. Lett.* **462,** 96–99 (2008).

31. An, C. *et al.* Hydrothermal preparation of α-MnS nanorods from elements. *J. Cryst. Growth* **252,** 575–580 (2003).

32. Biswas, S., Kar, S. & Chaudhuri, S. Solvothermal synthesis of α-MnS single crystals. *J. Cryst. Growth* **284,** 129–135 (2005).

33. Zhao, Z. & Liu, J. One pot synthesis of tunable Fe3O4–MnO2 core–shell nanoplates and their applications for water purification. *J. Mater. Chem.* **22,** 9052 (2012).

34. Im, G. H. *et al.* Fe3O4/MnO hybrid nanocrystals as a dual contrast agent for both T1- and T2-weighted liver MRI. *Biomaterials* **34,** 2069–2076 (2013).

35. Ullrich, A., Hohenberger, S., Özden, A. & Horn, S. Synthesis of iron oxide/manganese oxide composite particles and their magnetic properties. *J. Nanoparticle Res.* **16,** 2580 (2014).

36. Estrader, M. *et al.* Robust antiferromagnetic coupling in hard-soft bi-magnetic core/shell nanoparticles. *Nat. Commun.* **4,** 1–8 (2013).

37. Ito, D., Yokoyama, S., Zaikova, T., Masuko, K. & Hutchison, J. E. Synthesis of ligand-stabilized metal oxide nanocrystals and epitaxial core/shell nanocrystals via a lower-temperature esterification process. *ACS Nano* **8,** 64–75 (2014).

38. Chen, Y., Kim, M., Lian, G., Johnson, M. B. & Peng, X. Side reactions in controlling the quality, yield, and stability of high quality colloidal nanocrystals. *J. Am. Chem. Soc.* **127,** 13331–13337 (2005).

39. Liu, Z. *et al.* Complex-Surfactant-Assisted Hydrothermal Route to Ferromagnetic Nickel Nanobelts. *Adv. Mater.* **15,** 1946–1948 (2003).

40. Kim, D. S.; Lee, J. Y.; Na, C. W.; Yoon, S. W.; Kim, S. Y.; Park, J.; Jo, Y.; Jung, M. H. Synthesis and Photoluminescence of Cd-doped α-MnS Nanowires. *J. Phys. Chem. B* **110,** 18262–18266 (2006).

41. Tian, Q. *et al.* Large-scaled star-shaped a -MnS nanocrystals with novel magnetic properties. *ChemComm* 8100–8102 (2011).

42. Ren, Y., Gao, L., Sun, J., Liu, Y. & Xie, X. Facile synthesis of gamma-MnS hierarchical nanostructures with high photoluminescence. *Ceram. Int.* **38,** 875–881 (2012).

43. López-Ortega, A., Estrader, M., Salazar-Alvarez, G., Roca, A. G. & Nogués, J. Applications of exchange coupled bi-magnetic hard/soft and soft/hard magnetic core/shell nanoparticles. *Phys. Rep.* **553,** 1–32 (2015).

44. Goh, Chi-Keong; Yuan, Zhi-min; Liu, B. Magnetization reversal in enclosed composite pattern media structure. *J. Appl. Phys.* **105,** 083920–083920–3 (2009).

45. Vikas Nandwana, Girija S. Chaubey, Kazuaki Yano, C. R. and J. P. L. Bimagnetic nanoparticles with enhanced exchange coupling and energy products. *J. Appl. Phys.* **105,** 014303 (2009).

46. Klabunde, C. L. C. and K. J. Unique Chemical Reactivities of Nanocrystalline Metal Oxides toward Hydrogen Sulfide. *Chem. Mater.* **14,** 1806–1811 (2002).

47. Schneider, J. J. Magnetic Core/Shell and Quantum-Confined Semiconductor Nanoparticles via Chimie Douce Organometallic Synthesis. *Adv. Mater.* **13,** 529–533 (2001).

48. Hongfeng Yin, Zhen Ma, Miaofang Chi, S. D. eterostructured catalysts prepared by dispersing Au@Fe2O3 core–shell structures on supports and their performance in CO oxidation. *Catal. today* **160,** 87–95 (2011).

49. L.H. Yao, Y.X. Li, J. Zhao, W.J. Ji, C. T. A. Core–shell structured nanoparticles (M@SiO2, Al2O3, MgO; M = Fe, Co, Ni, Ru) and their application in COx-free H2 production via NH3 decomposition. *Catal. today* **158,** 401–408 (2010).

50. Xin-Bo Zhang, Jun-Min Yan, Song Han, H. S. and Q. X. Magnetically Recyclable Fe@Pt Core−Shell Nanoparticles and Their Use as Electrocatalysts for Ammonia Borane Oxidation: The Role of Crystallinity of the Core. *J. Am. Chem. Soc.* **131,** 2778–2779 (2009).

51. Yu Wang, Hui Juan Zhang, Li Lu, Ludger Paul Stubbs, C. C. W. and J. L. Designed Functional Systems from Peapod-like Co@Carbon to Co3O4@Carbon Nanocomposites. *ACS Nano* **4,** 4753–4761 (2010).

52. V. R. Galakhov, A. S. Shkvarin, A. S. Semenova, M. A. Uimin, A. A. Mysik, N. N. Shchegoleva, A. Ye. Yermakov, and E. Z. K. Characterization of Carbon-Encapsulated Nickel and Iron Nanoparticles by Means of X-ray Absorption and Photoelectron Spectroscopy. *J. Phys. Chem. C* **114,** 22413–22416 (2010).

53. John J. Fitzgerald, Christine J. T. Landry, J. M. P. Dynamic studies of the molecular relaxations and interactions in microcomposites prepared by in-situ polymerization of silicon alkoxides. *Macromolecules* **25,** 3715–3722 (1992).

54. Tomoki Ogoshi , Hideaki Itoh , Kyung-Min Kim, and Y. C. Synthesis of Organic−Inorganic Polymer Hybrids Having Interpenetrating Polymer Network Structure by Formation of Ruthenium−Bipyridyl Complex. *Macromolecules* **35,** 334–338 (2002).

55. Paria, R. G. C. and S. Core/Shell Nanoparticles: Classes, Properties, Synthesis Mechanisms, Characterization, and Applications. *Chem. Rev.* **112,** 2373–2433 (2012).

56. Z. Karimi, L. Karimi, H. S. Nano-magnetic particles used in biomedicine: Core and coating materials. *Mater. Sci. Eng. C* **33,** 2465–2475 (2013).

57. Estelrich J, Sánchez-Martín MJ, B. M. Nanoparticles in magnetic resonance imaging: from simple to dual contrast agents. *Int. J. Nanomedicine* **10,** 1727–1741 (2015).

58. Hongyeol Park, Dae Hoon Yeom, Jaegyeong Kim, J. K. L. MnO/C nanocomposite prepared by one-pot hydrothermal reaction for high performance lithium-ion battery anodes. *Korean J. Chem. Eng.* **32,** 178–183 (2015).

59. Hao Liu, Zhenghui Li, Yeru Liang, Ruowen Fu, D. W. Facile synthesis of MnO multi-core@nitrogen-doped carbon shell nanoparticles for high performance lithium-ion battery anodes. *Carbon N. Y.* **84,** 419–425 (2015).

60. Z. Karimi, L. Karimi, H. S. Nano-magnetic particles used in biomedicine: Core and coating materials. *Mater. Sci. Eng. C* **33,** 2465–3084 (2013).

61. *Design of Multifunctional Magnetic Nanomaterials for Biomedical Applications, Dissertation zur Erlangung des Grades 'Doktor der Naturwissenschaften' dem Fachbereich Chemie, Pharmazie und Geowissenschaften der Johannes-Gutenberg-Universität Mainz vorgelegt*. (2010).

62. Margaret F. Bennewitz, Tricia L. Lobo, Michael K. Nkansah, Gözde Ulas, Gary W. Brudvig, and E. M. S. Biocompatible and pH-Sensitive PLGA Encapsulated MnO Nanocrystals for Molecular and Cellular MRI. *ACS Nano* **5,** 3438–3446 (2011).

63. Hyon Bin Na, Jung Hee Lee Prof., Kwangjin An, Yong Il Park, Mihyun Park, In Su Lee Prof., Do-Hyun Nam Prof., Sung Tae Kim Prof.1, Seung-Hoon Kim Prof., Sang-Wook Kim Prof., Keun-Ho Lim, Ki-Soo Kim Prof., S.-O. K. D. andTaeghwan H. P. Development of a T1 Contrast Agent for Magnetic Resonance Imaging Using MnO Nanoparticle. *Angew. Chemie Int. Ed.* **46,** 5397–5401 (2007).

64. Assaf A. Gilad, Piotr Walczak, Michael T. McMahon, Hyon Bin Na, Jung Hee Lee, Kwangjin An, Taegwhan Hyeon, P. C. M. van Z. and J. W. M. B. MR tracking of transplanted cells with 'positive contrast' using manganese oxide nanoparticles (pages 1–7). *Magn. Reson. Med.* **60,** 1–7 (2008).

65. Jin-sil Choi, Jeong Chan Park, Hyunsoo Nah, Seungtae Woo, Jieun Oh, Kyeong Min Kim Dr., Gi Jeong Cheon Dr., Yongmin Chang Prof., J. Y. P. andJinwoo C. P. A Hybrid Nanoparticle Probe for Dual-Modality Positron Emission Tomography and Magnetic Resonance Imaging. *Angew. Chemie Int. Ed.* **47,** 6259–6262 (2008).

66. Thomas D. Schladt, Mohammed Ibrahim Shukoor Dr., Kerstin Schneider, Muhammad Nawaz Tahir Dr., Filipe Natalio, Irene Ament, Jan Becker, Florian D. Jochum, Stefan Weber, Oskar Köhler, Patrick Theato Dr., Laura Maria Schreiber Prof. Dr., Carsten Sönnichsen P, W. E. G. M. P. D. andWolfgang T. P. Au@MnO-'Nanoblumen' – Hybrid-Nanokomposite zur selektiven dualen Funktionalisierung und Bildgebung. *Angew. Chemie Int. Ed.* **122,** 4068–4072 (2010).

67. Thomas D. Schladt, Mohammed Ibrahim Shukoor Dr., Kerstin Schneider, Muhammad Nawaz Tahir Dr., Filipe Natalio, Irene Ament, Jan Becker, Florian D. Jochum, Stefan Weber, Oskar Köhler, Patrick Theato Dr., Laura Maria Schreiber Prof. Dr., Carsten Sönnichsen P, W. E. G. M. P. D. andWolfgang T. P. D. Au@MnO Nanoflowers:

Hybrid Nanocomposites for Selective Dual Functionalization and Imaging. *Angew. Chemie Int. Ed.* **49,** 3976–3980 (2010).

68. Valerian E. Kagan, Hülya Bayir, A. A. S. Nanomedicine and nanotoxicology: two sides of the same coin. *nanomedicine* **1,** 313–316 (2005).

69. Lewinski N, Colvin V, D. R. Cytotoxicity of nanoparticles. *Small* **4,** :26–49 (2008).

70. Andre E. Nel, Lutz Mädler, Darrell Velegol, Tian Xia, Eric M. V. Hoek, Ponisseril Somasundaran, Fred Klaessig, V. C. & M. T. Understanding biophysicochemical interactions at the nano–bio interface. *Nat. Mater.* **9,** 543 – 557 (2008).

71. Brian C. Schanen, Ajay S. Karakoti, Sudipta Seal, Donald R. Drake III, W. L. W. and W. T. S. Exposure to Titanium Dioxide Nanomaterials Provokes Inflammation of an in Vitro Human Immune Construct. *ACS Nano* **3,** 2523–2532 (2009).

72. Andre Nel, Tian Xia, Lutz Mädler, N. L. Toxic Potential of Materials at the Nanolevel. *Science (80-.).* **311,** 622–627 (2006).

73. C. Carlson, S. M. Hussain, A. M. Schrand, L. K. Braydich-Stolle, K. L. Hess, R. L. J. and J. J. S. Unique Cellular Interaction of Silver Nanoparticles: Size-Dependent Generation of Reactive Oxygen Species. *J. Phys. Chem. B* **112,** 13608–13619 (2008).

74. Pan Y, Neuss S, Leifert A, Fischler M, Wen F, Simon U, Schmid G, Brandau W, J.-D. W. Size-dependent cytotoxicity of gold nanoparticles. *Small* **3,** 1941–1949 (2007).

75. eixiong Hu, Koon Gee Neoh, Lian Cen, and E.-T. K. Cellular Response to Magnetic Nanoparticles 'PEGylated' via Surface-Initiated Atom Transfer Radical Polymerization. *Biomacromolecules* **7,** 809–816 (2006).

76. Jong Young Choi, Su Hee Lee, Hyon Bin Na, Kwangjin An, Taeghwan Hyeon, T. S. S. In vitro cytotoxicity screening of water-dispersible metal oxide nanoparticles in human cell lines. *Bioprocess Biosyst. Eng.* **33,** 21–30 (2010).

77. SCHULZE, ERIC MD, PhD; FERRUCCI, JOSEPH T. Jr. BA; POSS, KIRTLAND BA; LAPOINTE, LARRY BS; BOGDANOVA, ANNA PhD; WEISSLEDER, RALPH MD, P. Cellular Uptake and Trafficking of a Prototypical Magnetic Iron Oxide Label In Vitro. *Invest. Radiol.* **30,** 611–620 (1995).

78. Brooke Parker-Esquivel, Kristin J. Flores, Daniel Louiselle, Michael Craig, Lifeng Dong, Richard Garrad, Kartik Ghosh, Adam Wanekaya, Garry Glaspell, and R. K. D. Association of Poly I:C RNA and Plasmid DNA onto MnO Nanorods Mediated by PAMAM. *Langmuir* **28,** 3860–3870 (2012).

79. Spaldin, N. *magnetic materials - fundamentals and applications - II ed.* (2010).

80. J. Nogues, I. K. S. Exchange bias. *J. Magn. Magn. Mater.* **192,** 203–232 (1999).

5. Synthesis of MnO nanoparticles

5.1. Introduction

Bulk manganese(II) oxide MnO is a well known material that exhibits antiferromagnetic behavior below the Néel temperature T_N = 116 K. MnO is also a model compound to study and understand antiferromagnetism.[1] MnO oxide occurs in a single crystal structure, *i. e.*, the rock-salt fcc structure.[2] The MnO mineral manganosite is a black mineral discovered in Germany in 1817 and later also found in Nordmark, Sweden, United States, and Burkina Faso.[3]

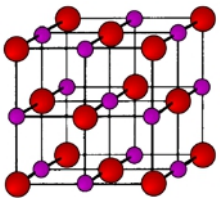

rock-salt structure

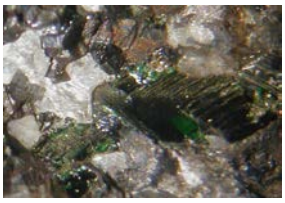

manganosite

Figures: manganese oxide mineral

MnO has particular properties at the nanoscale where it usually acquires a partial ferromagnetic behavior.[2] This peculiar characteristic makes MnO nanoparticles an excellent candidate for application such as spintronic devices,[4] and energy-storage lithium-ion battery.[5]

memory device

lithium-ion battery

Figures: some examples of possible MnO nanoparticles applications

Nanoscale MnO retains an antiferromagnetic order[5] but the surface spins are uncompensated and are responsible for a ferromagnetic-like response. The antiferromagnetism of MnO makes it useful as a material for nanoscale AFM-FM exchange-coupled systems with enhanced magnetic stability thanks to the unidirectional anisotropy arising from exchange coupling. This enhanced stability could be further improved by taking advantage of shape anisotropy. For this reason, in this work we searched for solvothermal synthetic procedures to obtain MnO nanoparticles with anisotropic shape. Using such anisotropic NPs as a scaffold for the growth of a FM metal oxide layer, one could prepare anisotropic AFM-FM core-shell NPs with *two* additional anisotropies with respect to isotropic FM NPs that would synergically increase the energy barrier for the reversal of the NP magnetization. Anisotropic growth is well-known in materials such as TiO, ZnO, CdTe and PbSe that show an oriented growth induced by dipole-dipole interaction, but it is unexpected for the rock-salt cubic MnO structure.[1] However, in the last years some authors reported experimental reaction conditions able to give anisotropic MnO NPs. We aim at finding a controlled and reproducible procedure for the synthesis of anisotropic antiferromagnetic MnO NPs.

In our work a series of environmental friendly precursors and surfactants have been used to study the development of the MnO NP shape from octahedral to multipodal; several differently-shaped NPs were subsequently characterized as to their magnetic properties. The solvothermal synthesis of MnO NPs (carried out in 1-octadecene) involved also a small amount of sulfur as a reagent, which favors the formation of anisotropic shapes over isotropic ones. In a previous work of ours,[6] it was already demonstrated that small amounts of sulfur are able to induce the development of some crystal faces with respect to other ones, without introducing any significant amount of sulfur in the MnO crystal lattice. The role and the mechanism of sulfur in the nucleation and crystal growth is not clear yet. The correlation between reaction conditions and NP size, shape and crystal structure and the influence of the anisotropic NP shape on the MnO magnetic properties have been investigated in this work.

5.2. Results and discussion

5.2.1. Manganese precursors: manganese dioleate and manganese distearate

MnO nanoparticles were synthesized by a solvothermal process starting from manganese dioleate and manganese distearate since size- and shape-uniform nanoparticles are obtained by solvothermal decomposition of metal-oleate complexes in a "heat-up process".[7] Manganese dioleate and manganese distearate precursors were prepared as pure as possible. The precursor (and other reagents) were chosen because they were environmental friendly and able to give high-quality nanocrystals.[1]

Precursor synthesis is a very critical point because is not possible to completely purify the products from the corresponding free acid by filtration, crystallization or chromatography on silica gel.[6] This could cause a different concentration of free fatty acid in the reaction mixture. Infrared spectra analysis was carried out to verify the presence of free fatty acid and to have an indication about the precursor purity. Precursor purity is very important because free fatty acid impurity could decrease the nominal precursor : surfactant molar ratio.

5.2.2. MnO vs. MnS nanoparticles: the role of sulfur

In previous work carried out in our laboratory,[6] it was noticed that starting from the same solvothermal reaction setup, it was possible to modulate the formation of MnO or MnS NPs by changing the sulfur : metal precursor molar ratio. A wide range of sulfur : metal precursor molar ratio (between 0 and 4) was investigated and it was observed that a stoichiometric amount of sulfur led to a mixture of MnO and α-MnS nanocrystals (no nanoparticle containing with both oxide and sulfide anions was observed) when $MnOl_2$ is decomposed in octadecene at 320 °C. Pure batches of α-MnS NCs were obtained using a S:Mn molar ratio ≥ 2 whereas pure MnO NCs could be obtained using S:Mn ≤ 0.6. These results are detailed in the MnS chapter below (chapter 7).

As expected the sulfur amount present in the reaction mixture directly affects the final NP composition. However, in the previously mentioned work it emerged the feasibility to obtain anisotropic MnO nanoparticles. In particular, some preliminary results demonstrated that, when the S: Mn molar ratio is about 0.5, Mn oleate with oleic acid gave concave shapes at

L:Mn = 4 and Mn stearate with stearic acid gave branched nanoparticles at L:Mn = 0.5 and 1.2.[6]

In the present study we observed that a S: Mn molar ratio between 0.4 and 0.6 (which leads to the formation of pure MnO NPs) is also able to affect the NPs final shape. Comparing equal reaction conditions, concave and anisotropic shapes were observed when sulfur was present, whereas conventional shapes were formed without sulfur. The role of the sulfur on the crystal growth is not clear yet, but a large number of experimental data confirm the importance of sulfur to synthesize anisotropic NPs.

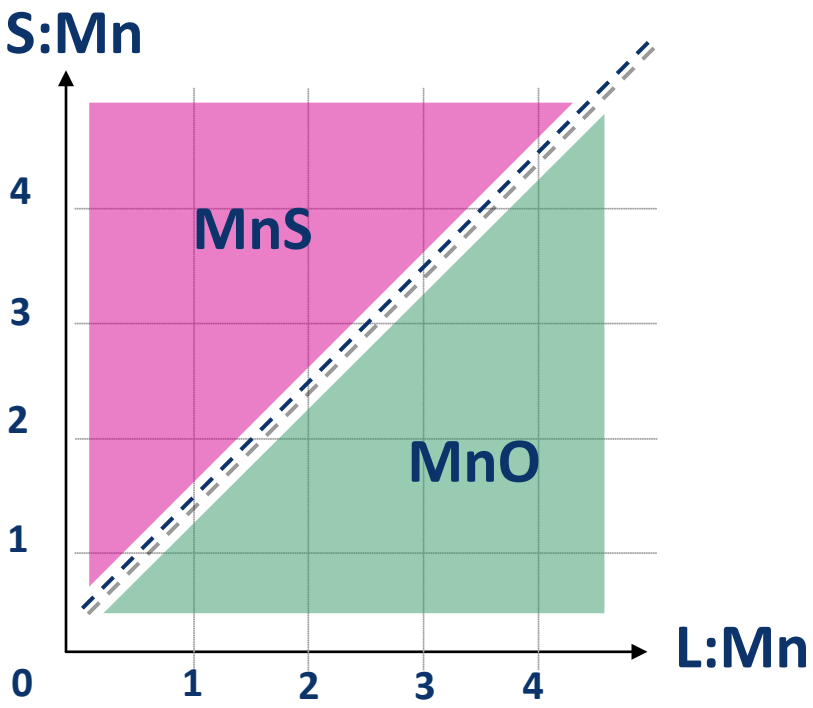

Figure 1: Schematic representation of the reaction conditions for MnS vs. MnO formation

To anticipate the main results, we consider a coordinate plane with axes representing the L:Mn (L = surfactant) and S:Mn molar ratios in the reaction mixture. The green (purple) triangle represents the region where MnO (α-MnS) nanocrystals form. The boundary between the α-MnS and MnO regions runs diagonal in an approximately linear way. In the case of $MnSt_2$, it bisects the plot ($S:L_{free}$ = 1:1), when $MnOl_2$ is used, the boundary is shifted towards the left side by about one unit [$S:(L_{free}+1)$ = 1:1]. This suggests that the oleate anion plays a role in favoring the formation of MnO NCs. $MnSt_2$ is less efficient at that and a pure α-MnS NC batch is formed under the same conditions that lead to MnS/MnO NC mixtures with the

di-oleate precursors. A S:Mn molar ratio about 0.5 was always used in all reactions because adding sulfur to the reaction mixture bears two advantages:

- a better size dispersion for isotropic nanoparticles (spheres or octahedral)
- well-defined shape and higher aspect ratio for anisotropic nanoparticles.[6]

Anisotropic shapes (with their negative curvature surfaces) increase the surface-volume ratio and enhance the nanoparticle magnetic stability and low-temperature magnetization.[7] To summarize, the sulfur : precursor molar ratio is the key to control the composition of the nanoparticles while, as we will soon see, the nanoparticle size and the shape are mainly driven by the surfactant : precursor molar ratio. Nanocrystals properties depend on their size and shape, thus a good control on the nanocrystal characteristics is strongly desired.[7]

5.2.3. Anisotropic MnO nanoparticles

Many reactions were performed to study the correlation between the manganese precursor : surfactants molar ratio and morphological features of the resulting nanoparticle, keeping all the other reaction parameter fixed. The main results are reported in the following tables:

MnO@Oleate

Reaction	Surf : Prec	Shape	Size (nm)	Dev. Std. (nm)
E196	0:1	irregular NPs	45	12
E11	1:1	octahedron	45	7
E47	2:1	spheroid	20	2.8
E16	3:1	4-flower (budding)	54	13
		3-flower (budding)	53x47	12x12
		octahedron (rare)	53	12
E14	4:1	4-flower	80	16
		3-flower	80x55	16x16
		6-flower (rare)	77	16
E51	6:1	sphere	23	18
		flower-like (rare)	71x70	19x22
E53	7:1	ellipsoid	83x21	10.5x10.5
E23	8:1	sphere (rare)	12	3

MnO@Stearate

Reaction	Surf : Prec	Shape	Size (nm)	Dev. Std. (nm)
E54	0:1	irregular NPs	55	9
E63	0.8:1	crosses	98	28
		T-shape	105x60	27x27
		rods (rare)	114	28
E46	1:1	crosses	80	24
		T-shape	79x46	24x24
		rods (rare)	73	21
		sphere	20	4
E56	2:1	sphere	39	24
		T-shape (budding)	81x63	24x24
		rods (budding)	81	25
E58	3:1	octahedron	24	6
		sphere	26	7
E48	4:1	crosses	78	24
		T-shape	75x75	24x24
		rods (rare)	73	23

Table 1 and 2: Average size of NPs. Below there is A schematic representation of the different NP shapes can be found below; the red segments show how size was measured in each case.

For each shape, the reported size values correspond to:

- sphere: diameter

- octahedral: diagonal and axis

- ellipse: minor and major axis

- rod: length

- T-shape and crosses: branch length

- multipods: diagonals

From the experimental data reported in tables *1* and *2*, we could notice that NPs with different shapes belonging to the same sample show similar size. Moreover, budding shapes are smaller or sometimes similar to the corresponding well-defined shape. This means that all nanoparticles in a single reaction have the same rate growth and perhaps are not due to oriented attachment. Besides, in the case of stearate samples (where different samples show the same anisotropic shapes such as crosses, T-shape and rods), rods are in all the samples less frequent than crosses and T-shape NPs.

Reaction	**Average aspect ratio**
Mn oleate multipods	1.65
Mn stearate multi-branched	3.57

Table 3: Average aspect ratio the oleate (L:Mn = 4 which shows the well-defined shapes) and stearate samples (L:Mn = 1, which is very similar also to L:Mn = 4 sample and little smaller that L:Mn = 0.8 sample). As expected, the aspect ratio of the stearate sample is higher due to the elongated branches, whereas oleate multipods comprise oval lobes.

5.2.4. Type of shapes – legend

sphere

ellipse

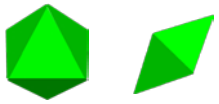

octahedron

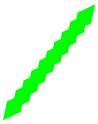

rod

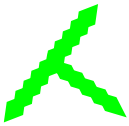

3-branch multipod (T-shape)

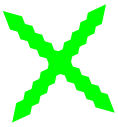

4-branch multipod (cross)

6-oval lobe multipod
6-flower

5(or 6)-oval lobe multipod
[5(or 6)-flower]

4(or 5)-oval lobe multipod
[4(or 5)-flower]

5.2.5. MnO@Oleate NPs conventional TEM images

Surf: oleate; L:Mn = 0:1

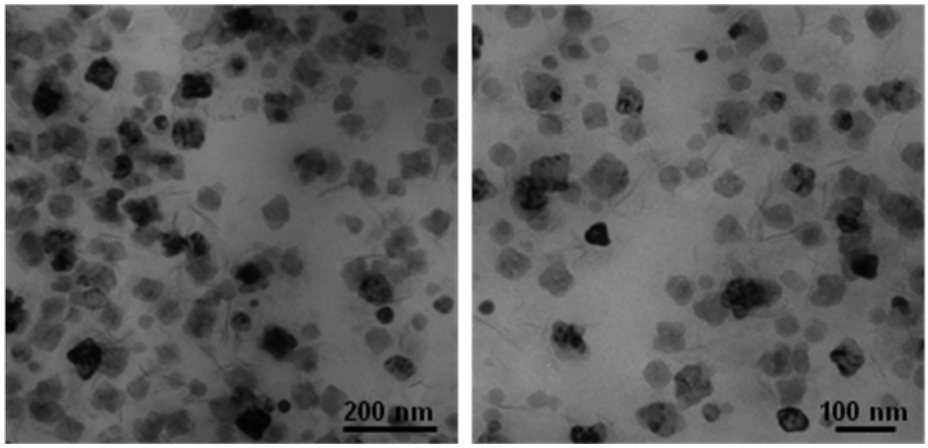

Surf: oleate; L:Mn = 1:1

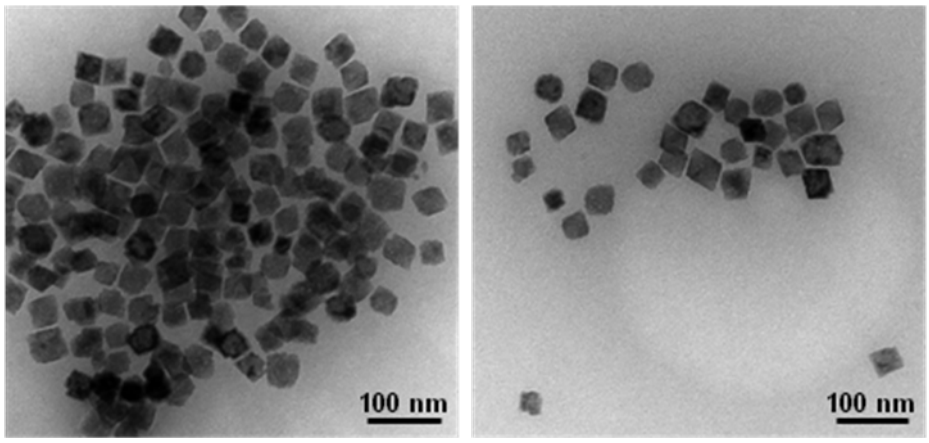

Surf: oleate; L:Mn = 2:1

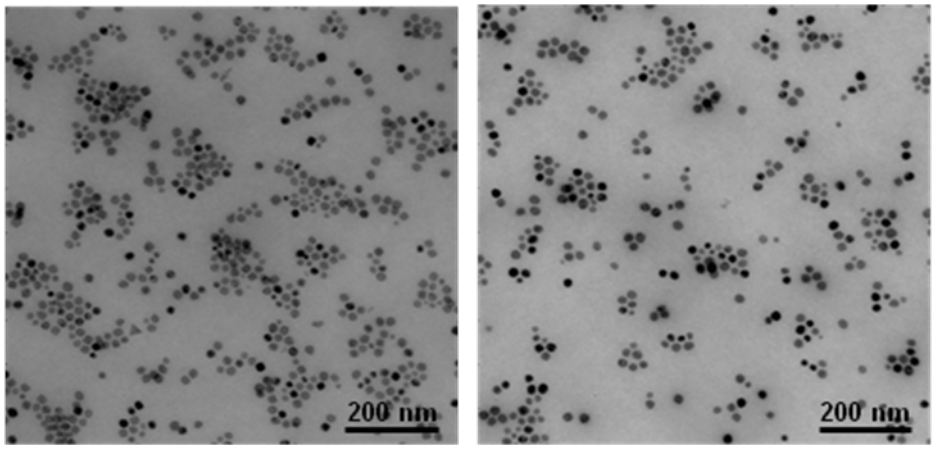

Surf: oleate; L:Mn = 3:1

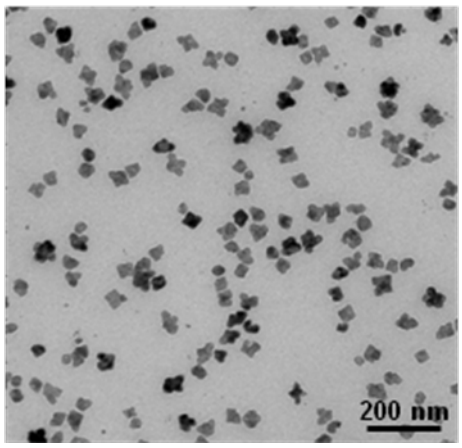

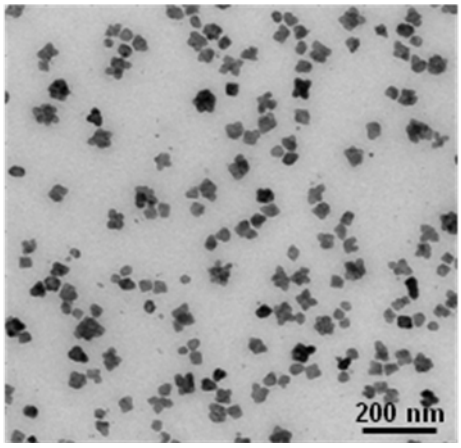

Surf: oleate; L:Mn = 4:1

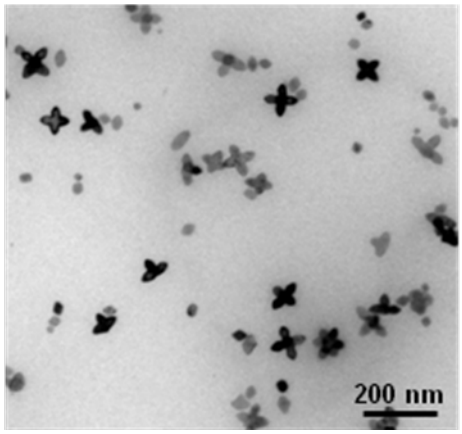

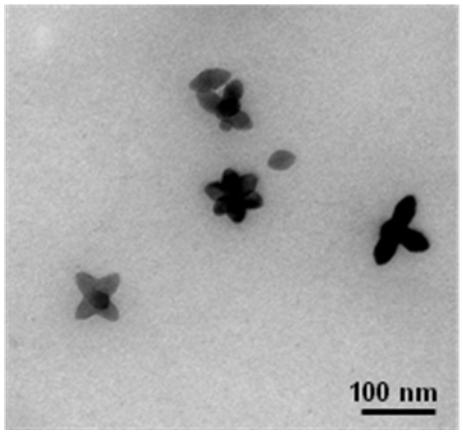

Surf: oleate; L:Mn = 5:1

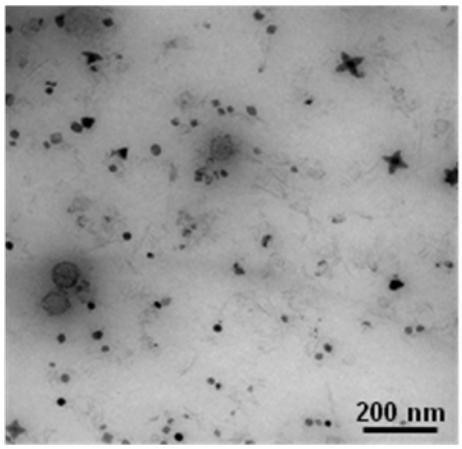

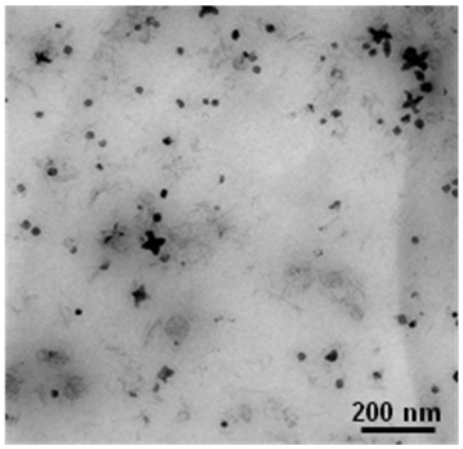

Surf: oleate; L:Mn = 6:1

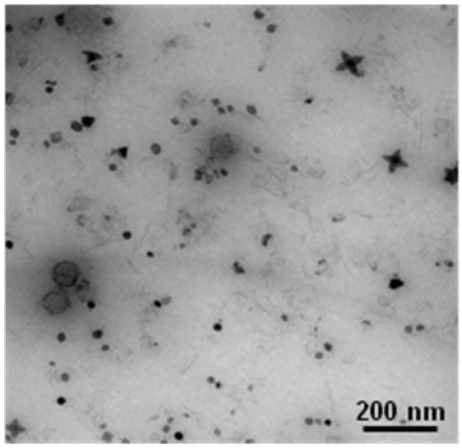

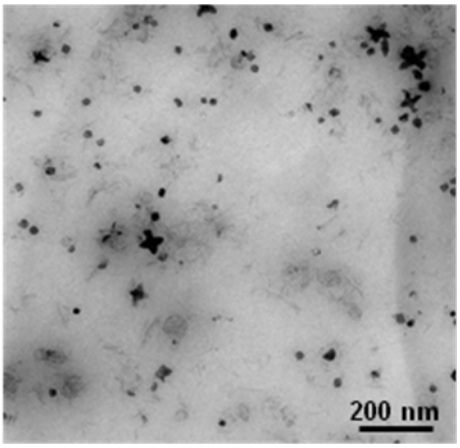

Surf: oleate; L:Mn = 7:1

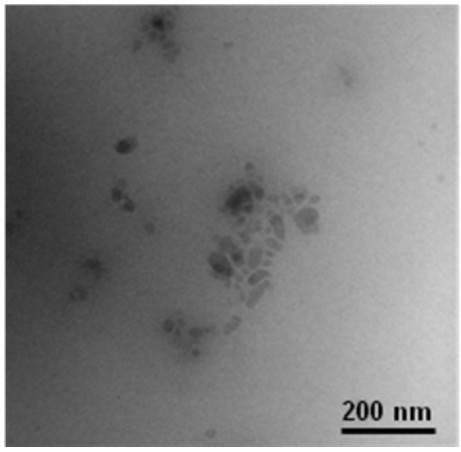

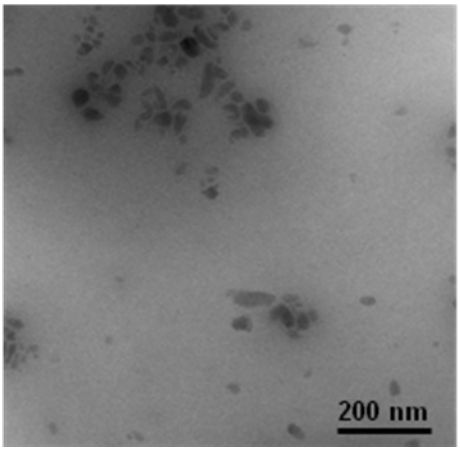

Surf: oleate; L:Mn = 8:1

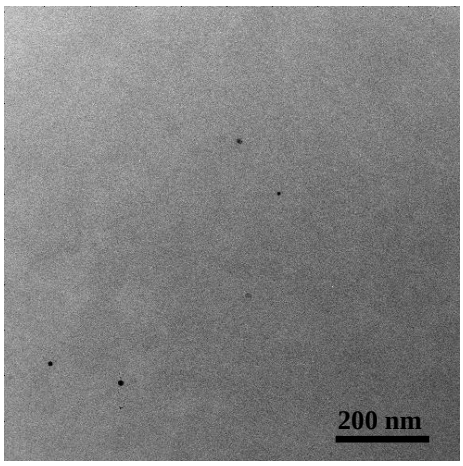

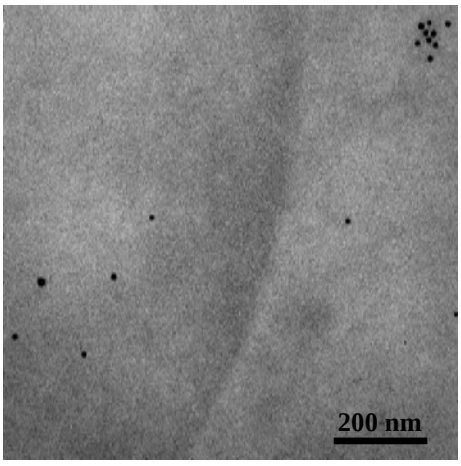

5.2.6. MnO@Stearate NPs conventional TEM images

Surf: stearate; L:Mn = 0:1

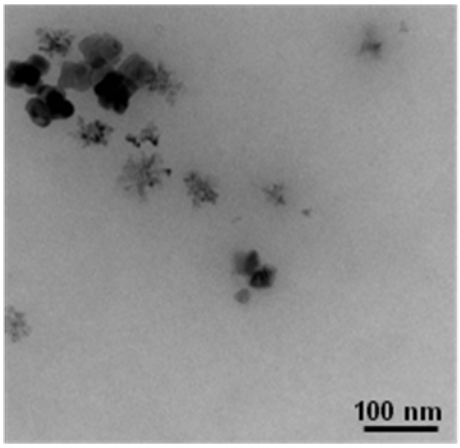

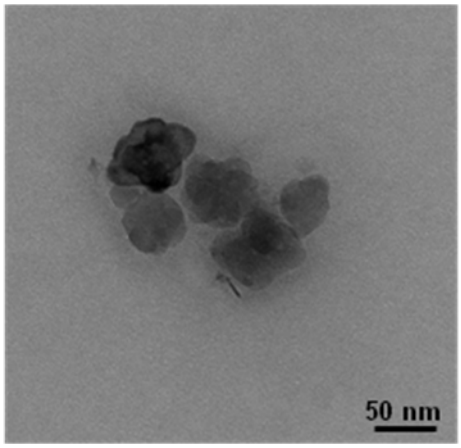

Surf: stearate; L:Mn = 0.8:1

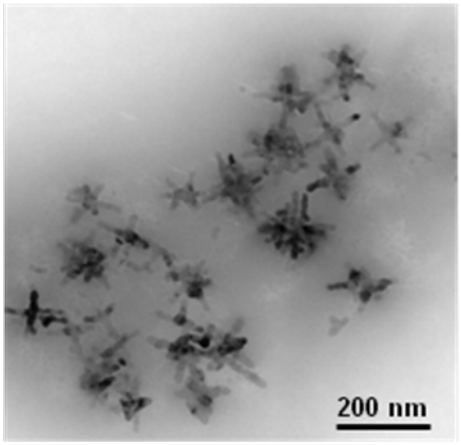

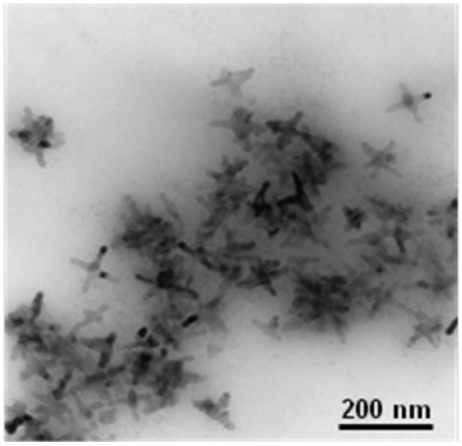

Surf: stearate; L:Mn = 1:1

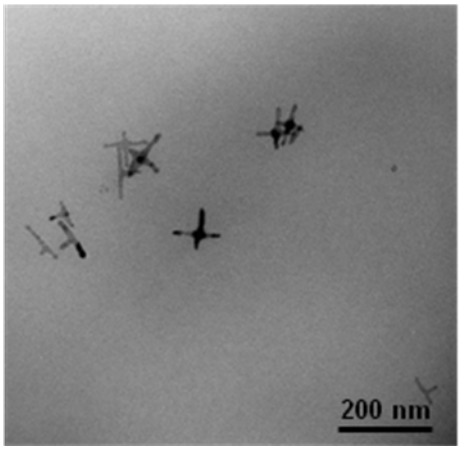

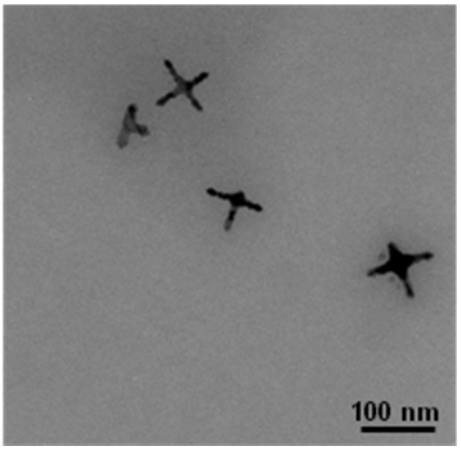

Surf: stearate; L:Mn = 2:1

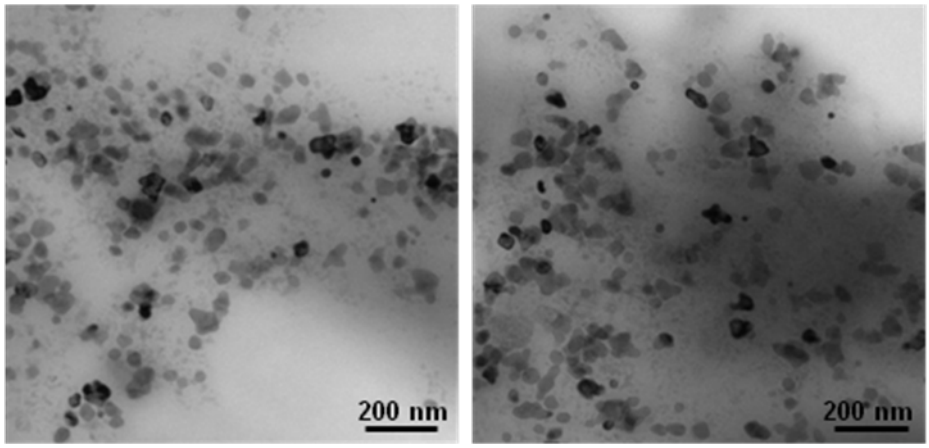

Surf: stearate; L:Mn = 3:1

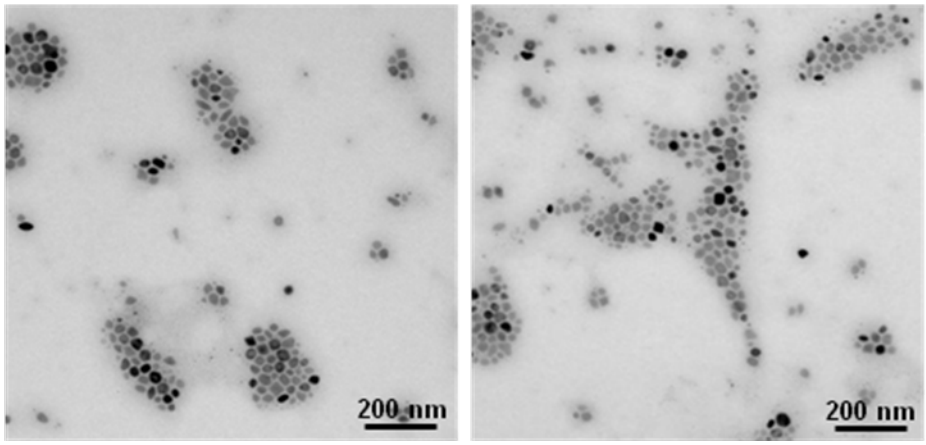

Surf: stearate; L:Mn = 4:1

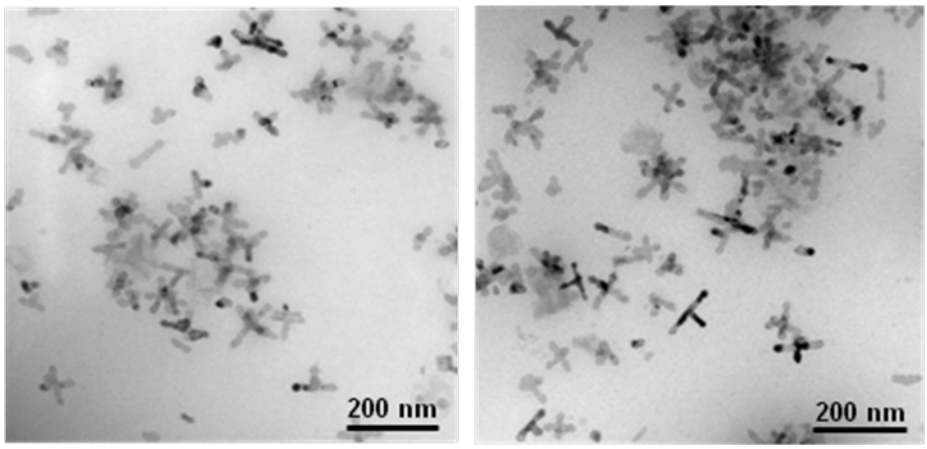

Curiously, the two manganese precursors shows different behavior upon changing the molar ratio between the free fatty acid used as a surfactant and the manganese carboxylate compounds used as a precursor. How the shape of the MnO NPs changes with the L:Mn ratio can be pictorially represented as follows:

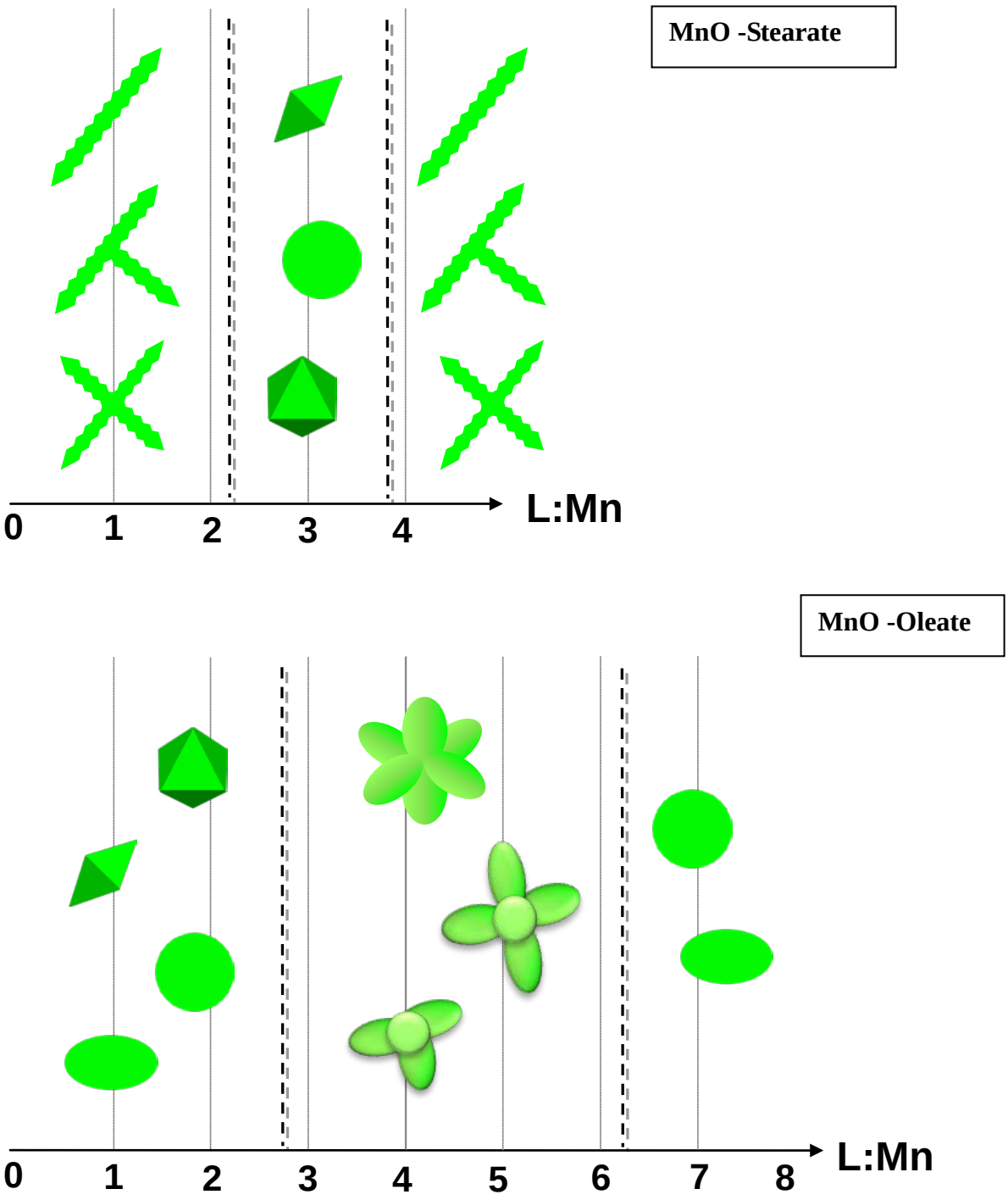

Figure 2: Schematic representation of the NPs shape as a function of the L:Mn molar ratio

Different factors are important during the nucleation and growth steps in order to control nanoparticle size and shape.[8]

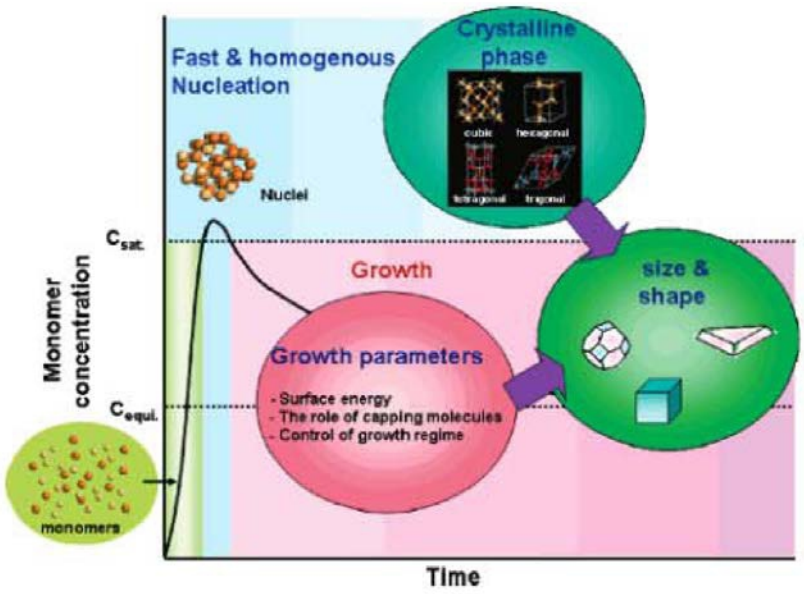

Image from ref. 8

After the initial seed formation with a certain crystal structure, three quantities could affect the NP growth phase: i) the intrinsic surface energy of the different crystal faces; ii) surfactants that could cap different surfaces, and iii) the type of regime (kinetic or thermodynamic). Of course, the initial seed crystal structure also plays a major role in the growth phase. Isotropic (i.e., cubic) crystal structures mostly induce isotropic growth, while uniaxial crystal structures naturally lead to anisotropic growth.[8]

The surfactant terminal group has a primary importance to determine the capped and the free crystal faces. Non-capped faces have higher surface energy than capped ones. Different surface energies induce different growth rates for non-equivalent crystal faces. Surface energy can control the growth rate and favor some crystal faces over other ones.[8] Many papers reported on the ability of carboxylic acid and amine to selectively block the growth of some crystal faces.[8] In our work, we decided to always use carboxylic acids and study how the amount of these capping agents affects the NP shape.

In the thermodynamic regime the surface energy is always minimized and NCs have convex shape. In case of non-equilibrium condition and kinetic control, negatively-curved and concave NC surfaces can be observed. In this regime, both selective etching and selective growth mechanisms are involved.[9] Cubic, octahedral and spherical shapes are obtained under thermodynamically control whereas multipodal shapes are kinetically controlled.[7] A paper

about iron oxide NP synthesis reported that, when the oleic acid to iron oleate molar ratio was decreased, the NP shape changed from sphere to star-like. These authors proposed that, at short decomposition times, the nanoparticle growth is kinetically controlled, leading to the formation of star-shaped NPs.[10]

Temperature is not the only parameter to determine the kinetic or thermodynamic conditions, monomer concentration also has a primary importance in the determination. The balance between these two regimes controls the isotropic or anisotropic growth of the nanoparticles. At a given temperature, a low monomer concentration leads to a thermodynamic regime, while a high concentration favors a kinetic regime. Indeed, it was already observed that low monomer concentrations and high temperature yield spherical nanoparticles. Spherical NPs derive from equal growth of all faces to form a unique and continuous surface.[8] In a paper about the synthesis of PbS NPs, it is stated that low temperature and high monomer concentration favor the kinetic regime, while, increasing the temperature, all crystal faces have equal growth rate.[11] In another paper, repeated precursor injections are used as a strategy to maintain a high monomer concentration in order to synthesize nanorods.[12]

5.2.7. Anisotropic MnO nanoparticles from manganese dioleate precursor

Analyzing our experimental results we found that, in the case of Mn oleate precursor with oleic acid surfactant, anisotropic shapes appear in the molar ratio range $3 \leq L{:}Mn \leq 6$. In particular, at L:Mn = 4 the concave shapes are well developed with outgrowth and elongation of the oval lobes. In the case L:Mn = 6, the product comprises a vast majority of spherical nanoparticles and some rare cross-shaped nanoparticles, whereas in the case L:Mn = 3, the NPs display the same lobed shape observed in L:Mn = 4 case but at the budding stage (where "budding" means that a concave shape is not well-developed yet and the anisotropic NPs are in the early stage of shape development with short lobes/branches and low aspect ratio). The well-defined anisotropic NPs obtained starting from Mn(II) oleate comprise n = 1 to 6 oval lobes. The lobes have aspect ratio = L/W = 1.6 and the angle between adjacent lobes is 90°. The lobes are arranged as to point to the vertices of an octahedron, irrespective of their number. These features clearly mirror the cubic crystal structure of MnO.

Starting from low L:Mn molar ratio, the concave shapes progressively develop upon increasing the surfactant concentration, yielding well-defined shapes at intermediate L:Mn.

Before the intermediate range, conventional isotropic shapes such as octahedral, spherical and elliptic are observed, while at high L:Mn ratio only spherical or elliptic nanoparticles are formed. The high molar ratio results (L:Mn ≥ 6) agree with a previous paper, where it was reported that adding a strongly coordinating carboxylic acid surfactant produced spherical NPs. The reaction with L:Mn = 8:1 shows rare spherical nanoparticles because the high oleic acid amount hinders the Mn precursor degradation and very few nanoparticles are formed.

In the literature it is reported that, in general, the decomposition of Mn oleate precursor in a non-coordinating hydrocarbon solvent gives conventional and thermodynamically stable shapes. The high surfactant concentration reduces the surface energy and inhibits differences in face growth rate leading to spherical shape.[7] Traces of water and oxygen in the solvothermal reaction mixture could affect not only the crystal structure and the crystallinity of the nanoparticles but also their size and shape uniformity.[7]

It is puzzling why the overall habit of these NPs can have symmetry lower than cubic ($n < 6$) despite the isotropic reaction environment. It was earlier noticed that etching processes of MnO NPs caused by oleic acid are more effective in the <111> directions but the {111} faces are very resistant so the six apices of the these faces are preferentially etched out.[13] Further previously-described octapods derived from cubic NPs by preferential etching of {100} faces and a rapid growth of {111} faces. There is no evidence of anisotropic etching but a very quick precursor decomposition could induce anisotropic growth.[13]

5.2.8. Anisotropic MnO nanoparticles from manganese distearate precursor

In the case of Mn stearate precursor with stearic acid surfactant, the intermediate range of L;Mn ratio produces isotropic (octahedral and spherical nanoparticles), whereas for L:Mn ≤ 2 or L:Mn = 4 formation of anisotropic NPs is observed. In particular, the L:Mn = 0.8, 1 and 4 cases gave well-defined and highly-developed anisotropic shapes whereas the L:Mn = 2 gave similar, budding anisotropic shapes, that is, cross- and T-shaped nanoparticles with short, low aspect-ratio branches, which strongly hint at an early development stage of well-developed anisotropic NPs. In comparison with the oleate case, the anisotropic NPs are multipods with elongated branches; the branches have jagged edges (instead of smooth surface) and higher aspect ratio. NPs are fairly monodisperse, even among different shape. This not surprising because it has been already noticed that it is easier to achieve NPs monodispersion for anisotropic than for more symmetric shapes.[1]

In the present case of Mn stearate precursor, the nanoparticles have elongated branches with aspect ratio = 3.6 and constant length (ca. 80-100 nm). The nanoparticles can have $n = 2$ (rods), 3 (T's), and 4 (crosses) branches. The angle between adjacent branches is 90°. The branches are arranged like the diagonals of a square. No NP with $n > 4$ branches was observed. All NPs appear as 'flat' shapes, *i. e.,* the branches lie on a common plane. As in the previous Mn oleate precursor case, the overall NP shape is related to the cubic MnO structure but in the present case it always has lower symmetry than cubic. Interestingly, in these samples the relative population of $n = 2$, 3, and 4 nanoparticles is about 1: 2 : 2. In a previous work, different T-shapes was observed when myristic acid was used in large excess as a surfactant at low temperature (280°). In that case, anisotropic NP shape was attributed to oriented attachment rather than anisotropic growth.[7]

To summarize, tuning the surfactant : precursor molar ratio in this type of solvothermal synthesis is an effective strategy to obtain nanoparticles with the desired shape and size, with good reproducibility. However, the shape of both MnO@oleate and MnO@stearate NPs shows a cyclical trend as a function of the L:Mn molar ratio. Moreover, comparing NPs from reaction involving the same L:Mn molar ratio, the shape trends are opposite for oleate and stearate precursors. This behavior is very peculiar because is beyond the explicatory ability of conventional thermodynamic and kinetic arguments so even a tentative explanation has not been found yet.

5.2.9. TEM of tilted MnO@oleate multipod NPs

Up to now we have described the MnO@oleate NPs prepared from Mn oleate with L:Mn = 4 : 1 as a containing three NP populations with different shape:

- 6-lobe multipods
- 4-lobe multipods
- 3-lobe multipods

However, it is important to remember that conventional TEM images are just a planar projection of the true tridimensional NP shape. Thus, the tridimensional shape that we deduct from TEM images could be a not completely faithful reconstruction of the true NP shape. For instance, the vertically projected TEM image could conceal upright details. To better understand the true NP shape, multipods were also imaged after tilting the sample. Three images taken with different tilt angle are shown below (the tilt axis is approximately parallel

to the top/bottom image sides). It can be easily appreciated how the shape of the NP projection changes with tilt angle. Often, NPs seem to have 3, 4 or 6 oval lobes depending on the tilt angle (some NPs are highlighted by red boxes as an example). Thus, the multipod NPs in the sample may comprise more lobes than their projection might show in a conventional TEM image. Four instance, a 4-flower could be a 5-flower with an upright lobe which is scarcely recognizable as such in the conventional TEM image.

Hence, we can speculate that the multipod NP sample is more homogeneous as to both size and shape.

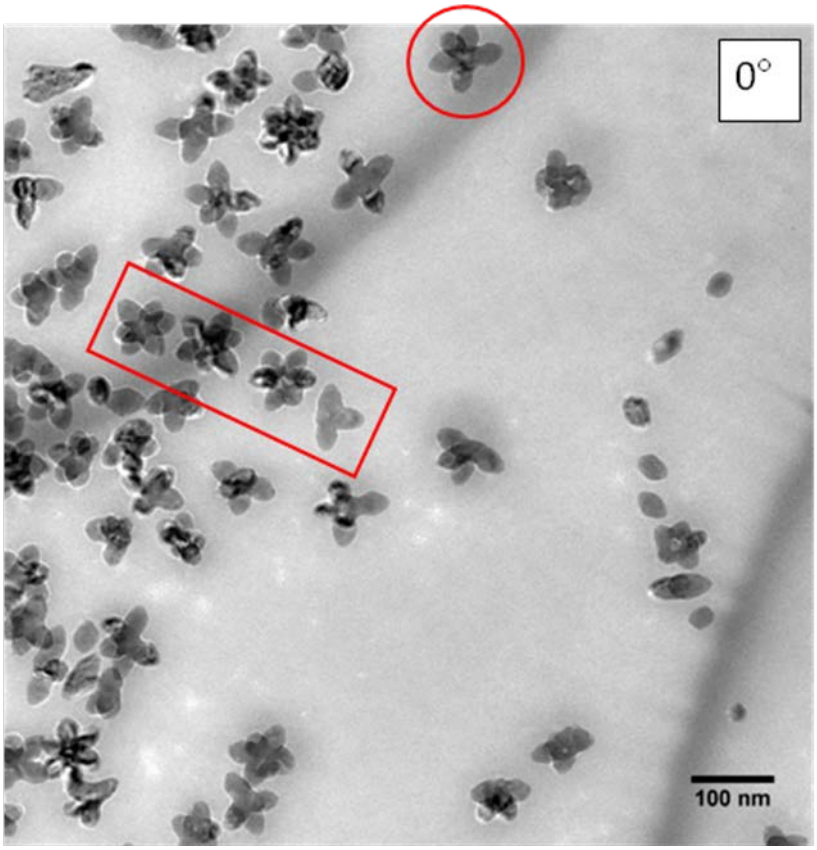

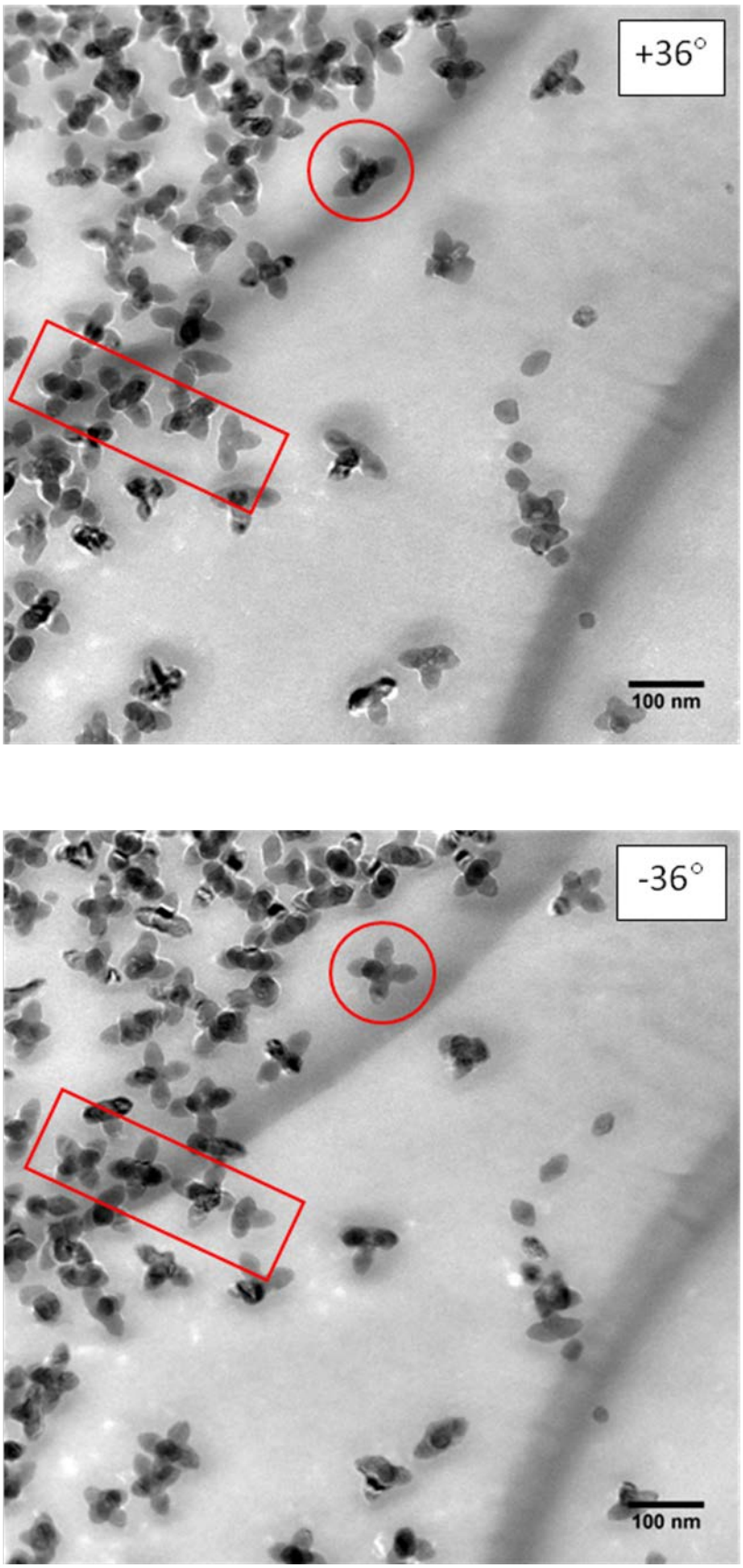

Figure 3: Tilted MnO@oleate NPs images. The images of the multipod NPs taken from 3 different angles (0°, +36° and -36°) show that probably most of the NPs have 6 oval lobs.

5.2.10. High resolution TEM (HR-TEM) of MnO@oleate nanoparticles[14] [15]

To investigate the crystal structure of anisotropic MnO NPs and the relationship between crystal structure and shape, some MnO@oleate samples have been studied by high resolution TEM (HR-TEM). The high resolution images show the crystal planes parallel to the electron beam as lattice fringes. However, the image is not a simple representation of the structure. The HR-TEM image of a crystalline NP may show several lattice fringes. Each lattice fringe observed in the HR-TEM image is due to the interference of three beams, the forward scattered beam and the two beams scattered by a given crystal plane with conjugated +**g** and –**g** scattering vectors. It is important to remember that the position of the fringes in the images does not correspond to the position of atomic planes. The intensity of the lattice fringes is affected to different extents by dynamical scattering. To appreciate these effects and understand the contributions due the specimen structure, it is best to separately analyze each lattice fringe present in the image. To achieve this, the Fourier Transform is useful to understand the HR-TEM images. However, the interpretation of HR-TEM images is very difficult when the NPs have varying thickness – as is always the case with NPs - and have imperfect crystal structure exhibiting interfaces, defects, lattice distortions or variations in chemistry. In Fourier theory, the HR-TEM image of a perfect crystal with uniform thickness can be considered as the sum of sinusoidal lattice fringes with constant amplitude and phase , each corresponding to a family of equivalent scattering planes.

Every HR-TEM image can be characterized by the local value of the amplitude and phase of each lattice fringe visible in the image. The amplitude is the contrast (in a particular image position) of a lattice fringe and amplitude variations can be caused by changes in the specimen thickness, chemical composition or imaging conditions (*e. g.* lens aberrations). The phase of a lattice fringe is less sensitive to specimen thickness and imaging conditions and is often more useful to investigate crystal interfaces of defects. Both amplitude and phase images obtained by Fourier analysis of the HR-TEM images are affected by the size and shape of the mask in Fourier space used to single out the scattering from a particular plane family.

The high resolution TEM images of MnO@oleate samples have been analyzed in order to investigate the NPs thickness from the amplitude images and the crystal structure continuity from the phase images.

The most simple case are octahedral NPs obtained when the precursor is Mn oleate and L:Mn = 1:1. Octahedral NPs have convex shape and expected to be single crystals. The

homogeneity observable in both phase and amplitude images show a homogeneous crystal structure and orientation and, hence, octahedral MnO NPs are single crystals.

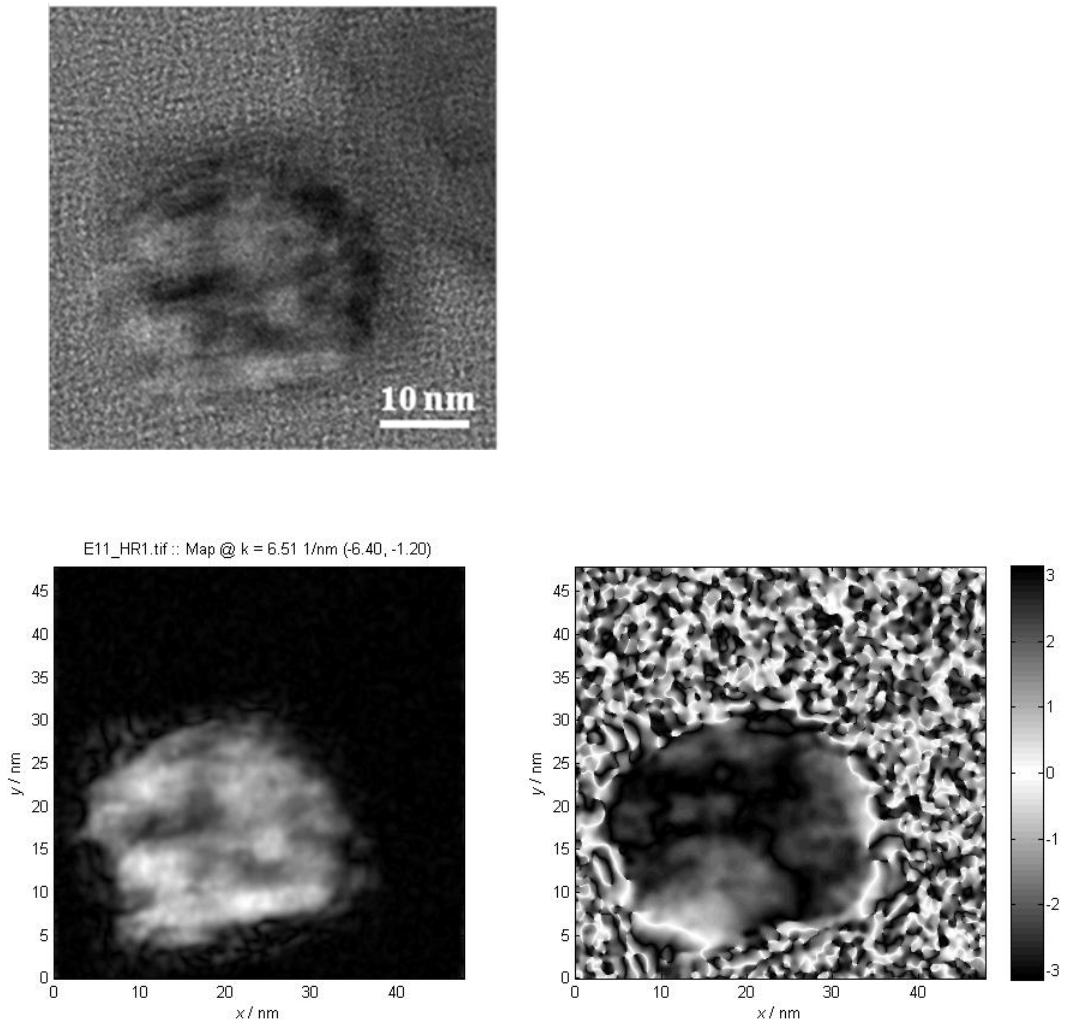

Figure 4: HR-TEM of an octahedral MnO NP prepared by L:Mn = 1:1 molar ratio. HR-TEM (top); amplitude (left) and phase (right) of the {220} lattice fring . The homogeneous aspect of the images corresponds to a single crystal NP.

In the case of multipod MnO NPs with oval lobes, synthesized from Mn oleate when L:Mn = 4:1, the images are more difficult to interpret because of the complex shape, large thickness (comparable or large than typical extinction coefficients of MnO), and the presence of defects and boundaries that generate discontinuities in the NP crystal structure. Here are reported two anisotropic MnO NPs as an example of two shapes present in the NP sample: the 5- and 6-lobe multipod. In the images of a single lobe of a 5-lobe multipod, [figure *5*] both amplitude

and phase are homogeneous. Amplitude homogeneity means constant NP thickness and composition, while phase homogeneity is an indication of the lobe being a single crystal. The NP edges are clearly visible as an abrupt change in the phase images. The lobe in the figure *5* has partial phase continuity at the intersection with the other lobes (at the bottom of the image).

Observing the amplitude and the phase images of a whole 5-lobe multipod, all the lobes can be considered homogeneous in amplitude and phase but the central circular phase discontinuity could be interpreted as a discontinuity or – at least – a misalignment of each lobe with respect to the other ones (including the central vertical lobe). As before, the NP edges which are easily seen as abrupt phase changes.

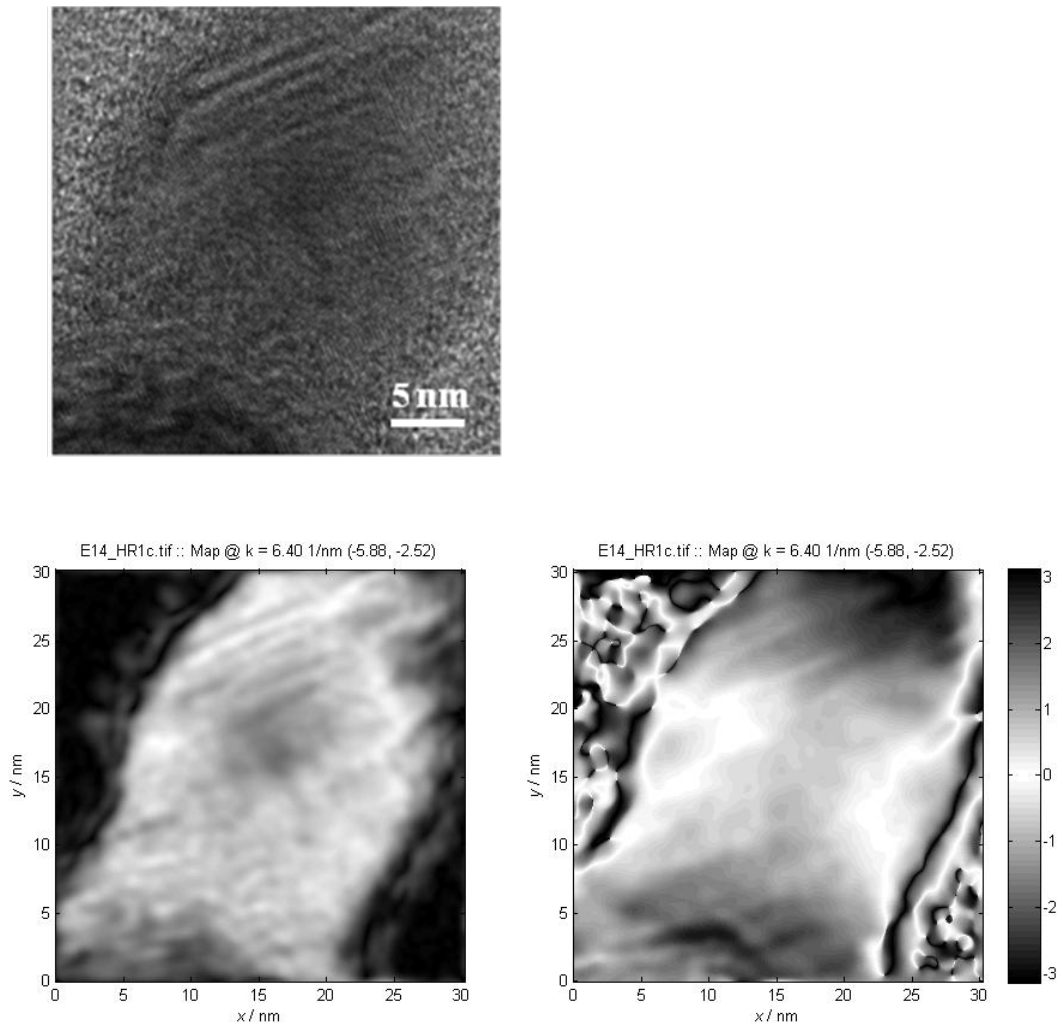

Figure 5: HR-TEM of a single lobe of a 5-flower NP. HR-TEM (top); amplitude (left) and phase (right) images of the {220} lattice fringe. Both amplitude and phase images are homogeneous and each lobe can be considered a single crystal.

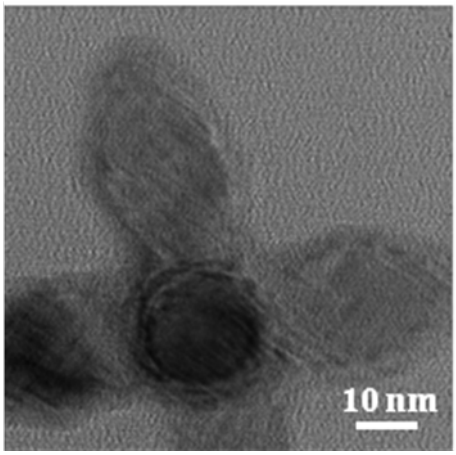

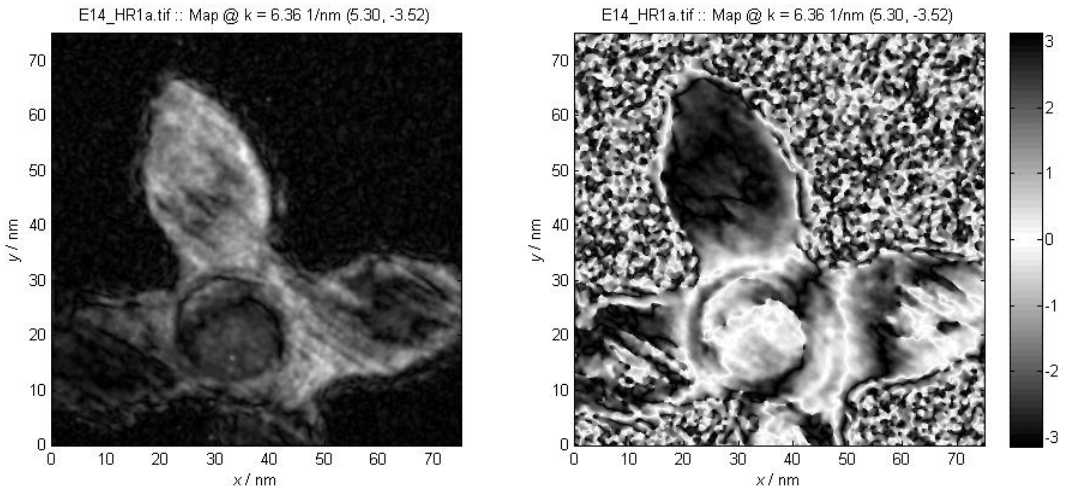

Figure 6: HR-TEM of a 5-flower NP. HR-TEM (top); amplitude (left) and phase (right) images of the {220} lattice fringe.. All lobes are homogeneous in amplitude and phase; and the central circular phase discontinuity can be due to the boundary of the central (vertical) lobe with the four side (horizontal) lobes.

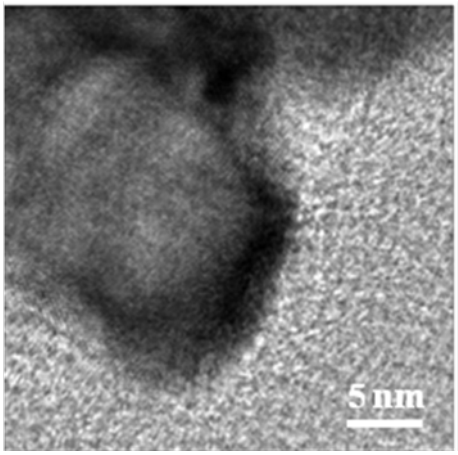

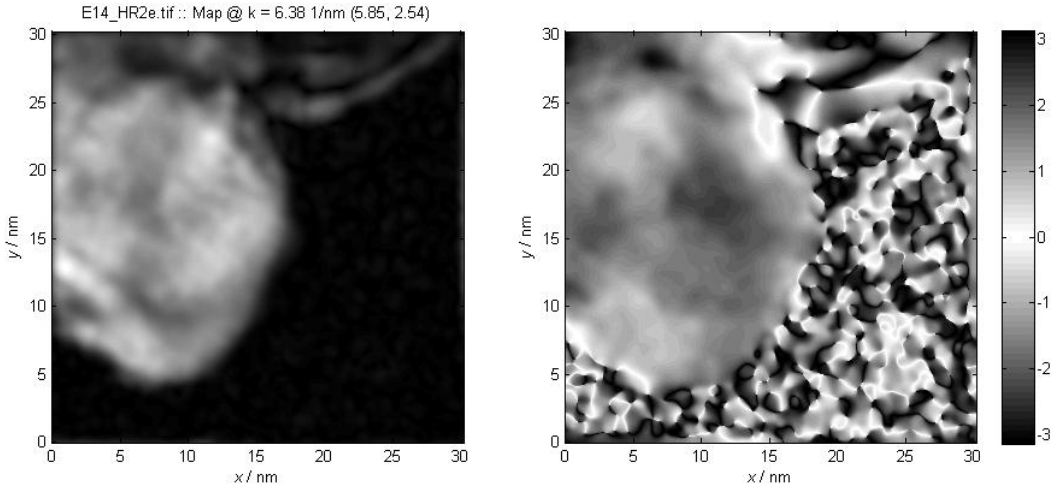

Figure 7: HR-TEM of a single lobe of a 6-flower NP. HR-TEM (top); amplitude (left) and phase (right) images of the {220} lattice fringe. Images show one single lob which seems to be homogeneous in amplitude and phase and appears as a single crystal.

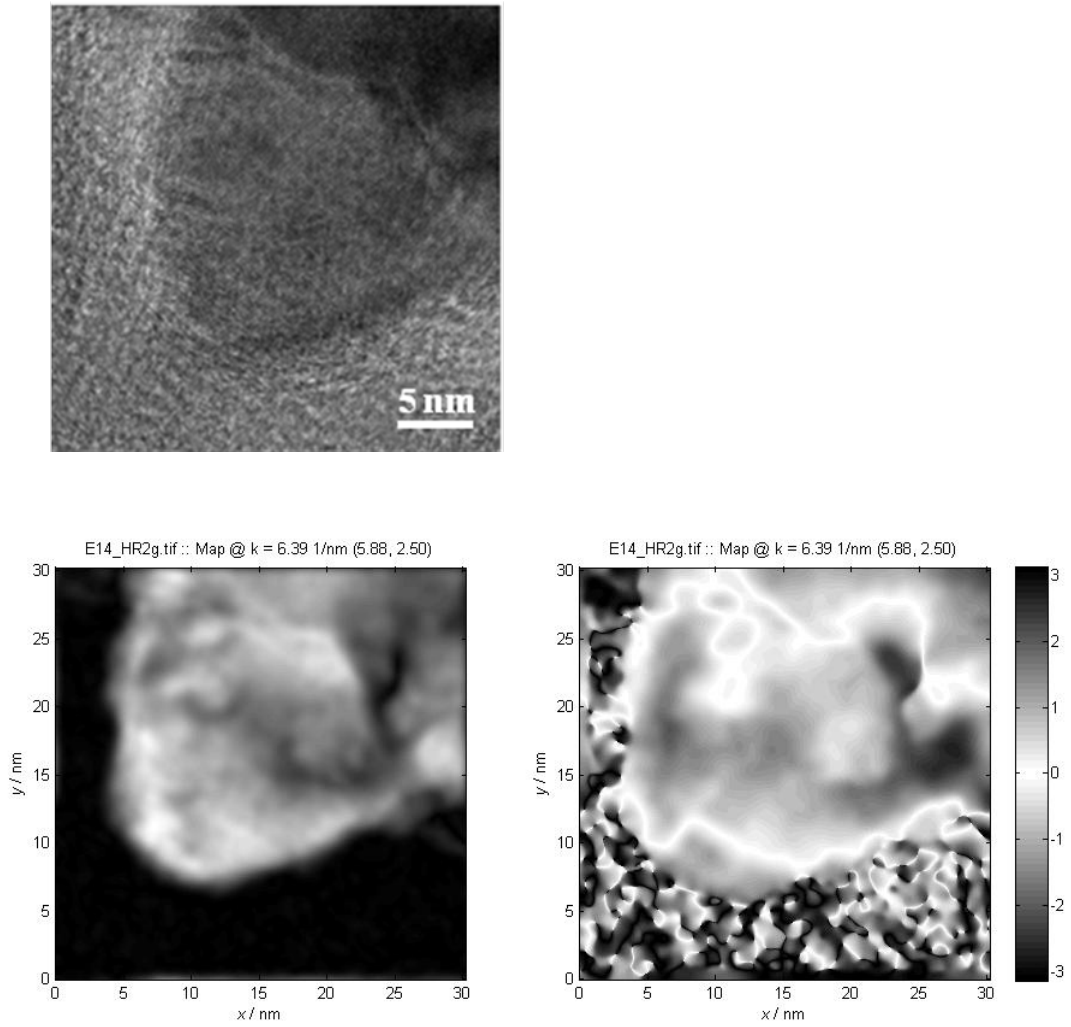

Figure 8: HR-TEM of a single lobe of a 6-flower NP. HR-TEM (top); amplitude (left) and phase (right) images of the {220} lattice fringe. Images show another single lob which seems to be homogeneous in amplitude and phase and appears as a single crystal.

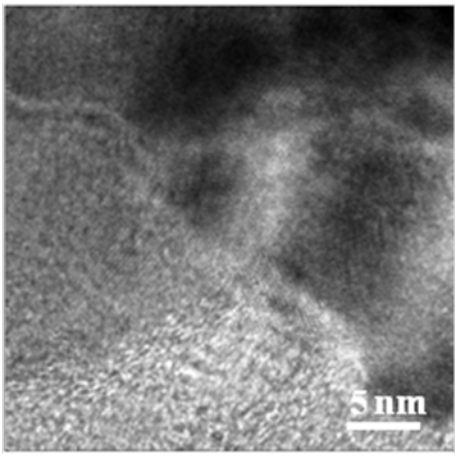

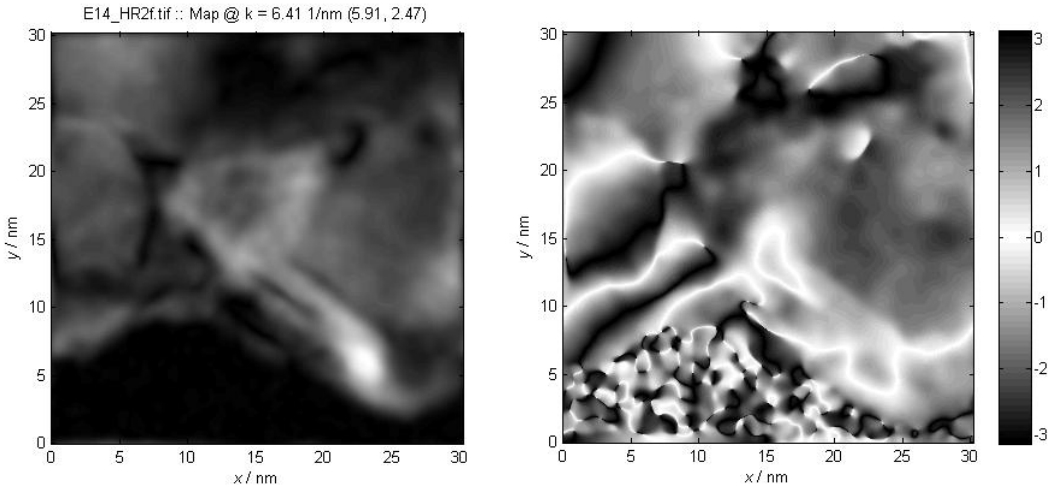

Figure 9: HR-TEM of a single lobe of a 6-flower NP. HR-TEM (top); amplitude (left) and phase (right) images of the {220} lattice fringe. Images show the intersection between two lobs that seems not present discontinuity along the junction. Little phase discontinuities can be due to the boundary of the crystal.

In the case of 6-lobe multipods, the amplitude and phase images of single NP lobs confirm the homogeneity in composition, thickness and crystal structure for each lobe. [figures *7* and *8*] The amplitude and phase images show discontinuity where the lobe overlap with a neighboring lobe. In the bottom images, where two adjacent lobes are partially shown, one can appreciate that the {220} lattice fringe is present with similar intensity in different lobes while the phase image shows that different lobes are slightly misaligned (the lobe at the right side has constant phase while that at the left side has linearly varying phase). In figure *10* a

whole 6-lobe multipod is imaged at high resolution. This amplitude image is difficult to interpret since the lobes are partially overlapping. Though the different lobes have different amplitude (gray level), it is clear that the {220} lattice fringe is present throughout the NP. The phase image is even more difficult to interpret due to overlapping lobes.

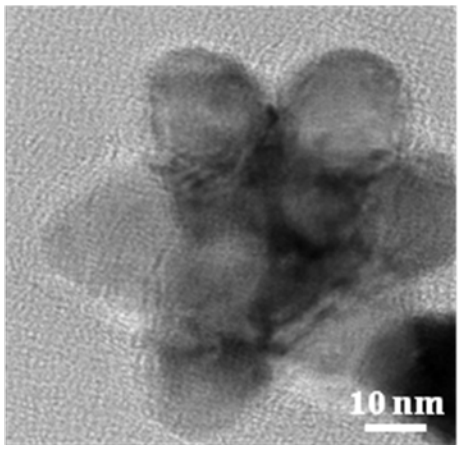

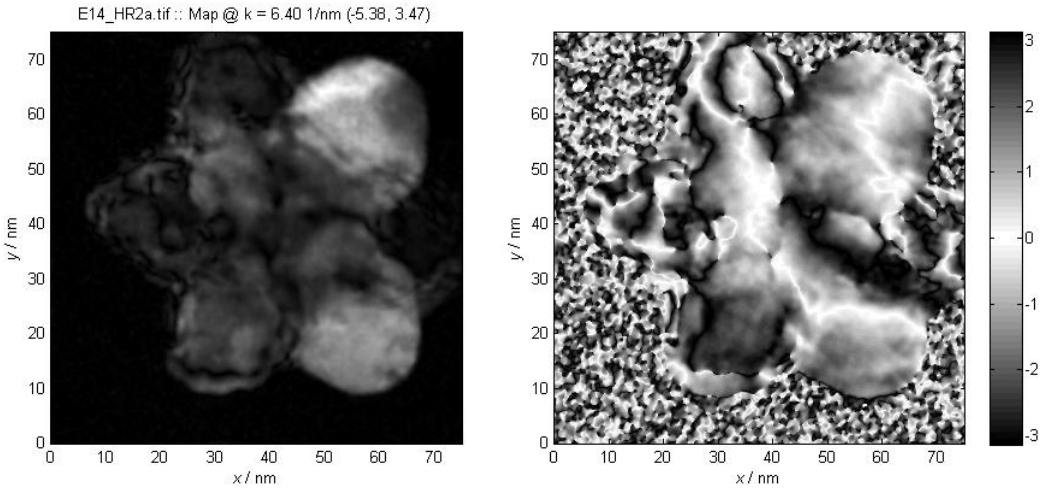

Figure 10: HR-TEM of a single lobe of a 6-flower NP. HR-TEM (top); amplitude (left) and phase (right) images of the {220} lattice fringe Clearly visible amplitude and phase discontinuities are probably due to a discontinuity in the NP thickness.

A previous article already reported on single-crystal MnO multipods, describing MnO size-uniform and single-crystal multipodal nanoparticles.[13] Other researchers reported on MnO octapods which appeared to be single-crystals that originated from oriented attachment. This mechanism often produces polycrystalline structures, but some exceptions were described.[7] Even when the crystal planes across different NP lobes or branches are perfectly aligned, it is

possible that the NPs are aggregates resulting from an oriented attachment process.[16] However, when anisotropic NPs are not produced by oriented attachment, initial seeds could be recovered that had the same shape of the final nanoparticles and the relationship between these two NPs had already been proved in a large variety of noble meta NPs.[16]

Similarly to this, the MnO@oleate NPs from the L:Mn = 3 case have early-stage underdeveloped concave shapes very similar to the well-defined anisotropic shapes of the NPs obtained using L:Mn = 4. This could be evidence of anisotropic seed growth mechanism. Moreover, inspecting the conventional TEM images of the NPs from the L:Mn = 3 reaction, it is noteworthy that the octahedral NPs and the budding 4- and 3-flower NPs have similar size, about 50 nm. This could be another piece of evidence that both isotropic and anisotropic NPs simultaneously grow. Hence, the anisotropic concave NPs are not the result of an oriented attachment because the simultaneously present octahedral or ellipsoidal nanoparticles (which should attach to each other to form the final anisotropic structure) are much larger than the lobes constituting the anisotropic NPs A further proof of a seed growth mechanism, are the size and shape of nanoparticles aged for a shorter time than the usual 60 min. MnO@stearate NPs were prepared from Mn distearate using L:Mn = 1 and aged just for 10 min. The conventional TEM images of this early stage reaction [figure *11*] display the same rods, T-shapes and crosses present in the 1 hour reaction but in this case the NPs branches are longer (cross branch ≅ 130 nm and T-shape ≅ 130 x 70 nm) than the branches of NPs aged for 1 hour.

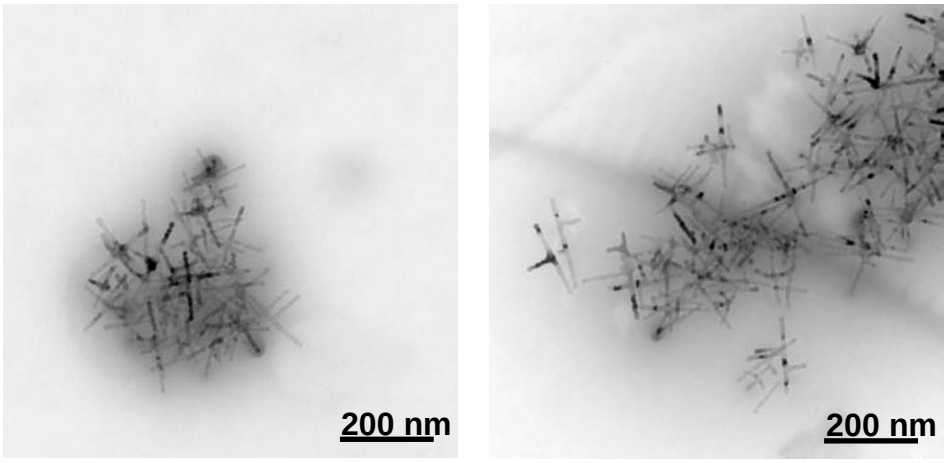

Figure 11: conventional TEM images of MnO@stearate NPs prepared from Mn distearate using L:Mn = 1 and aged just for 10 min. Nanoparticle shapes are the same observed for the NPs aged for 1 hour but in this case the NPs branches are longer.

5.2.11. Precursor vs. surfactant role on the crystal growth

The dramatically different reaction outcome observed when using Mn@oleate or Mn@stearate NPs requires some comment since these carboxylic acids just differ by the double bond between C_9 and C_{10}. First, we wanted to clarify whether the difference is due to the precursor or surfactant. We performed reactions where precursor and surfactant were different carboxylic acids (Mn oleate precursor was decomposed in the presence of stearic acid as a free surfactant and Mn stearate precursor was decomposed in the presence of oleic acid as surfactant). The size and shape of the NPs were similar to those synthesized with the same precursor. Then, the nanoparticle shape (lobed *vs.* branched) is governed by the type of fatty acid in the precursor. The reason of this behavior could be the greater influence of the $[R_1COOMn]^+$ and $(R_1COO)_2Mn$ species in the seed formation and in the initial growth and (at most) minor involvement of free R_2COOH.

It is well-known that surfactants such as oleylamine and oleic acid play an important role in the growth mechanism but cannot be the only explanation to the anisotropic nanoparticle formation since carboxylic acids were employed as surfactants in all cases. Probably, precursor decomposition is the main mechanism involved in the anisotropic growth.[7] After decomposition, the metal centres could affect the kinetic nanoparticle seed formation. The organic molecules introduced by the precursor fragmentation could also influence the nanoparticle morphology and manipulate the growth by perturbing the metal ligation sphere.[7]

5.2.12. Surfactant : Mn-precursor molar ratio effects

Observing the schematic representation of the reaction outcomes [figure *2*] there are some evidence that could be immediately noticed:

- the surfactant : precursor molar ratio strongly affects the resulting NPs shape;
- the anisotropic shapes produced by reacting oleate and stearate precursors are different;
- the isotropic shapes given by the two precursor are always spheroidal or octahedral nanoparticles with similar size (e.g. both spherical MnO@oleate NPs L:Mn = 2 and MnO@stearate NPs L:Mn = 3 have diameter ≈ 20 nm);
- the NP shapes seems to appear with a cyclical trend;

- the conditions under which anisotropic vs. isotropic occur are opposite for oleate and stearate precursor.

Thus, we can state that the surfactant : precursor molar ratio is a key point to control the synthetic outcome and obtain NPs with the desired characteristics. However, we are not yet able to explain why so markedly different anisotropic shapes are produced using two long-chain aliphatic carboxylic acids which differ only for a double bond in the middle of the chain. It is a very strange behavior, especially because this difference is not so chemically relevant due to the fact that a double bond is also present in the solvent aliphatic chain. Many previous papers reported that using different terminal groups (such as carboxylic acid *vs*. amine) the crystal growth is affected by the selective ability of the surfactants to preferentially cap some crystal faces and favor the growth of the remaining free faces. However, in our case both the surfactants are carboxylic acids so a very similar behavior could be expected. The main morphological differences are the NP overall shape, aspect ratio, and edges, which are smooth for oleate and jagged for stearate. Nevertheless, both precursors are able to generate complex shapes with multiple lobes or branches stemming from the NP center. No sample contained rod-like NPs only. Moreover, it is also curious that the relationship between the precursor : surfactant molar ratio and the NP shape seems to be cyclic in the precursor concentration for both precursors. The trend is complex to explain and it is also peculiar that the oleate and stearate cyclical trends are almost exactly ”out of phase”.

5.2.13. Magnetic properties of MnO@oleate and MnO@stearate NPs

The magnetic properties of both MnO@oleate and MnO@stearate NPs were investigated by SQUID magnetometry. For each sample, magnetic properties were investigated by measuring the magnetization *M* as a function of the field *H* at 5 and 295 K and the zero-field cooled (ZFC) and field cooled (FC) magnetization as a function of temperature between 295 and 5 K In the following table the main magnetic properties are reported.

MnO@oleate samples

Magnetic	MnO Samples (L:Mn)			
parameters	**1:1**	**2:1**	**3:1**	**4:1**
T_{max} (K)	2	2	290	2
M_{2000}(emu/g)	2.650	2.201	0.658	0.907
M_{rem}(emu/g)	0.225	0.157	0.087	0.087
M_{rem}/ M_{2000}	0.08	0.07	0.13	0.10
H_c (kOe)	1.493	1.035	2.752	2.367
H_{cr} (kOe)	14.280	16.763	17.337	16.008
H_{bias} (Oe)	944	882	1936	1600

MnO@stearate samples

Magnetic	MnO Samples (L:Mn)						Mn_3O_4
parameters	**0:1**	**0.8:1**	**1:1**	**2:1**	**3:1**	**4:1**	**1:1**
T_{max} (K)	5	5	5	5	5	5	15
M_{2000}(emu/g)	1.254	3.136	0.166	2.185	1.636	2.305	2.244
M_{rem}(emu/g)	0.031	0.190	0.020	0.135	0.048	0.126	0.817
M_{rem}/ M_{2000}	0.02	0.06	0.12	0.06	0.03	0.05	0.36
H_c (kOe)	0.217	1.302	2.823	1.218	1.013	1.472	5.878
H_{cr} (kOe)	6.488	14.711	16.625	14.147	15.967	16.589	8.350
H_{bias} (Oe)	79	619	1721	605	674	1029	659

First, we consider the MnO@oleate samples. The L:Mn=1:1 and L:Mn=2:1 NPs show narrow hysteresis loops with a large contribution which is difficult to saturate almost linear, as expected from their regular convex shapes. The loop is typical trend of antiferromagnetic nanomaterials. In both samples the coercivity is high. The bias field is measurable due to the surface effect where the spins are not completely compensated. In both ZFC curves the characteristic antiferromagnetic peak is not detectable whereas the FC curves are different, for only L:Mn=1:1 NPs display a low temperature jump characteristic of ferro- or ferri- magnetic materials. In the case of L:Mn=3:1 and L:Mn=4:1 samples, which comprise multipod nanoparticles, the hysteresis loop is open. In both these samples, the coercivity and the bias field are very high due to the surface effect that are very important for the increase of the surface/volume ratio compared to the previous L:Mn=1:1 and L:Mn=2:1 samples. The ZFC curve of L:Mn=4:1 sample present a very weak antiferromagnetic peak around 25K and FC curve shows a strong ferro/i-magnetic jump.

We now shift to the MnO@stearate samples. Six samples were analyzed from L:Mn=0:1 to L:Mn=4:1 (namely, L = 0, 0.8, 1, 2, 3, 4). Sample L:Mn=0:1, comprising irregular concave NPs, shows a very narrow hysteresis loop. ZFC and FC magnetizations describe a curve typical of antiferromagnetic behavior. Samples L:Mn=0.8:1, L:Mn=2:1 and L:Mn=3:1 have narrow hysteresis loops. Samples L:Mn=0.8:1 and L:Mn=3:1 FC curves describe a small ferro/i-magnetic jump and ZFC curves show a very small peak that could be interpreted as the antiferromagnetic peak. On the other hand the L:Mn=2:1 sample has a FC curve similar to the previous ones but a ZFC curve with a visible antiferromagnetic peak. Finally, L:Mn=1:1 and L:Mn=4:1 samples (which are anisotropic nanoparticles with elongated jagged-edge branches) show very large hysteresis loops and FC curves where the ferro/i-magnetic jump is clear observable. The antiferromagntic peak in the ZFC curve is evident for L:Mn=1:1 but is not detectable for the L:Mn=4:1 sample.

These MnO samples could be compared with a Mn_3O_4@stearate with L:Mn=1:1 where the size and shape of the nanoparticles are very similar to those of L:Mn=1:1 MnO@stearate nanoparticles. The Mn_3O_4@stearate sample was obtained by slow oxidation of a MnO@stearate sample which was kept under air. The Mn_3O_4 sample has a very wide hysteresis loop, bias field and coercivity are well measurable. The ZFC curve, as expected, has no antiferromagnetic peak and the FC curve has a very high ferro/i-magnetic jump.

The magnetic properties of anisotropic MnO NPs are in agreement with what expected for a nanoscale antiferromagnetic material such as MnO.[1] Size and shape effects are not significant for the multipod structures. Multipods display a magnetic behavior similar to that of MnO spherical nanoparticles despite the elongation of the arms. The small differences between the isotropic NPs and the anisotropic NPs could be ascribed to the surface effect where the pinned spins form a FM-like layer that generates a small exchange bias interacting with the antiferromagnetic core of the nanoparticle. In the anisotropic NPs, where the surface/volume ratio is higher than for isotropic NPs, the surface effect are slightly more pronounced and the exchange bias field is a little higher than that of isotropic NPs. Hence, these anisotropic MnO nanoparticles preserved their antiferromagnetic structure despite the peculiar shape with high surface/volume ratio and also showed their ability to create a significant exchange coupling at the core-(surface layer) interface. Therefore, it is not only possible but even promising to use these anisotropic MnO NPs as a backbone to grow a FM shell onto that has an highly anisotropic shape. So, we will exploit both the anisotropic shape and the antiferromagnetic order to build a core-shell structure with an AFM MnO core and a FM shell made of a soft magnetic material such an iron oxide. In this core-shell structure, the interaction between the two oxides at the interface could generate a strong exchange bias. Hence, the ability to synthesize AFM nanoparticles with anisotropic shapes is an important step towards core-shell NPs synergically stabilized by two magnetic anisotropies. The larger surface/volume ratio of the anisotropic AFM core (compared to a spherical cores) has the additional bonus of providing a strong exchange coupling using less material.

5.2.14. Procedure for the quantitative determination of manganese oxide nanoparticle dispersions by UV-VIS spectroscopy[17] [18]

5.2.14.1. Introduction

Since no method is available for the direct quantitative determination of manganese oxide nanoparticles, we resorted to two-step procedures comprising the digestion of nanoparticles in acid followed by the determination of Mn^{2+} ions in the ensuing aqueous solution. ICP-OES is a good method for the determination of Mn concentration but, for practical reasons (cost, speed, availability) we decided to resort to Uv-Vis quantification methods. In the literature, examples of specific manganese determination by UV detection of coloured Mn complexes are not available. Some authors described different ligands which can coordinate transition metals to form coloured complexes but no ligand was specific for manganese(II) ions. Despite this, we tried to complex Mn^{2+} ions with generic metal transition ligands. In particular, we tested xylenol orange and PAR as coordination ligands. In both cases, ligands coordinate the metal but formation of the coloured complex was not proportional to the manganese concentration in solution. Thus, the quantification of coloured Mn^{2+} complexes by UV-VIS spectroscopy is not a suitable technique to quantify the manganese concentration. Thus, starting from the techniques used for the determination of impurities in steels, we thought to measure permanganate ion concentration after oxidation of the Mn^{2+} ions released by the acid treatment. In this way, the manganese content of nanoparticle dispersions could be measured by the well-known method[17] based on the spectrophotometric detection of the permanganate anion in aqueous solution. However, the full release of Mn from organic components and complete oxidation of the manganese ions (possibly in both 2+ or 4+ oxidation states) into permanganate anion MnO_4^- (7+) are two key steps. We developed a reliable and accurate method to effectively carry out these two steps.

5.2.14.2. Procedure

A sample of oleic-acid coated MnO nanoparticle dispersion in hexane (500 μL) was evaporated in a glass vial by heating at 200 °C for 20 minutes. Then, low-metal-content conc. HNO_3 (69%, 3 mL) was added and a clear yellowish solution was obtained, which was left

standing at room temperature for 48/72 hours. The solution was then heated at 80-85 °C for 2/3 hours under magnetic stirring before adding milliQ water (3 mL) and $K_2S_2O_8$ (≈ 500 mg). The mixture was then held at 80-85 °C for 2 hours under magnetic stirring. The treatment with $K_2S_2O_8$ carried out the oxidative degradation of the organic part of the sample (oleic acid, residual solvent, etc.) that could decrease the method accuracy by, e. g., complexation of manganese ions and interference with the following oxidation step. Next, KIO_4 (≈ 100 mg) was added to the solution at 80-85 °C under magnetic stirring. The second oxidative treatment converted the manganese ions present in the sample into the permanganate anion. Just after the addition of KIO_4, the solution turned purple. Two minutes after the appearance of the purple color, the solution was cooled at room temperature and diluted to 10 mL with milliQ water in a flask. A few mg of KIO_4 were added to stabilize the solution. Further dilutions were made when needed.

During the method development, we changed some parameters in each step to find the better conditions. For example, sulphuric and hydrochloric acid were also used to degrade organic components but only using nitric acid (a strong oxidant) organic interferences could be completely eliminated. Acidic mixtures also were not as effective as pure nitric acid.

A large number of tests showed that complete oxidation and subsequent stability of the permanganate solution could only be achieved when the whole degradation/oxidation process is carried out in a narrow temperature range (80-85°C). It was observed that when the temperature is lower than 80 °C, the oxidation is much slower and incomplete. Otherwise, when the temperature is higher than 85 °C, the permanganate solution is unstable: after a short time at room temperature, precipitation of a pink powder and concomitant discoloration of the solution occur.

The quantity of oxidant salts used in this procedure was the highest possible allowed by solubility. The length of the time interval the sample was left in acid solution to degrade organic components was the minimum required to obtain a complete manganese release. When the starting sample solution is expected to be highly concentrated, it is better to extend the time for the acidic degradation.

This procedure required to prepare the sample for quantification by UV-VIS spectroscopy was validated by ICP-OES quantification. Specimens from the same sample were degraded in acidic solution, then heated and added with $K_2S_2O_8$. At this point each specimen was divided in two sub-specimens. One was ready for ICP analysis (diluted only if necessary) and the other was added with KIO_4 for the oxidation to permanganate ion and then diluted and

analysed by UV-VIS spectroscopy. Here, we report two examples of comparison between ICP-OES and UV-VIS spectroscopy quantification results.

	Concentration by ICP-OES		Concentration by UV-vis		Relative Difference
Sample	M	g/l	M	g/l	
MnO@oleate (E28b)	0.0189	1.04	0.0171	0.939	-10%
MnO@oleate (E226)	0.168	9.24	0.179	9.84	+6%

Table 4: Comparison of Mn determination by ICP-OES and our UV-Vis method. UV-VIS quantification values are acceptable considering that the accuracy of ICP-OES is about 5%. We reported two examples of sample quantifications. The first sample was a very diluted solution poor in organic compounds, while the second one was a concentrated solution very rich in organic surfactant. To improve the effectiveness of the acidic degradation in the latter case, the digestion in nitric acid at room temperature was 4 days long.

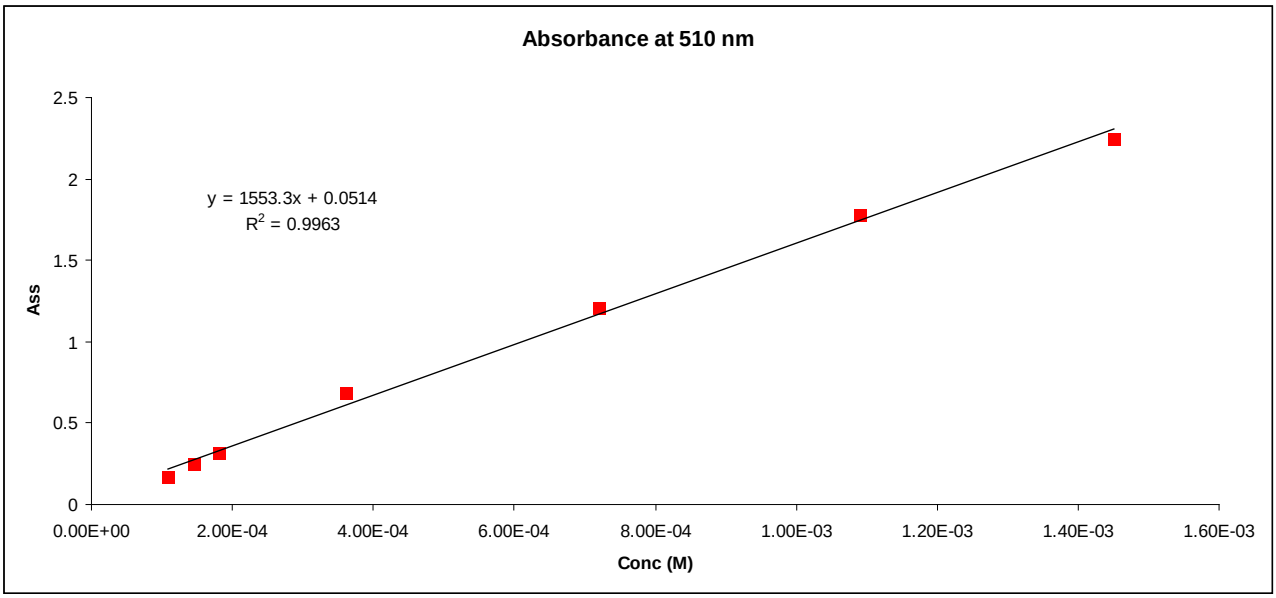

Figure 12: Calibration line obtained from a series of samples prepared from a standard Mn^{2+} solution. The standard solution (1 M) was diluted in order to prepare samples in a range concentration for UV-Vis detection between 10^{-4} and 1.5 10^{-3} M. Then the solutions were oxidized as described in the procedure using $K_2S_2O_8$ and KIO_4 at 80-85°C. Calibration lines were obtained by measuring absorbance at three characteristic permanganate absorbance peaks: 510, 525 and 545 nm. The best calibration line was that obtained at 510 nm (see plot).

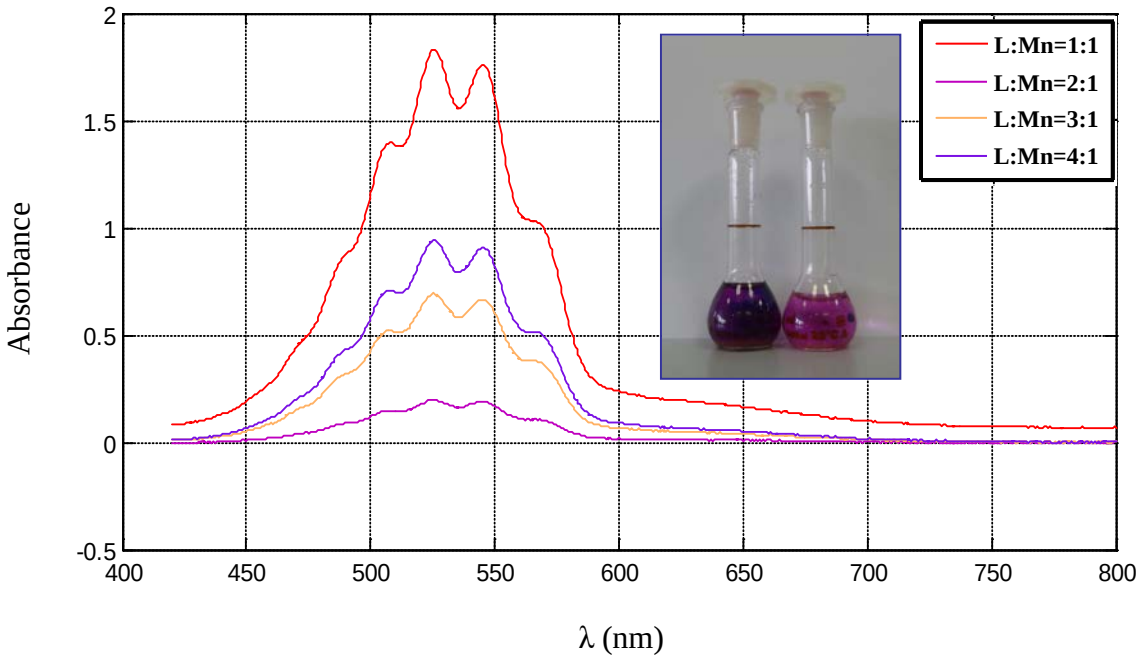

Figure 13: Typical UV-Vis spectra of the final solution obtained after (i) acidic digestion of MnO@oleate nanoparticles, (ii) oxidation of the organic species, and (iii) oxidation of the Mn ions to permanganate. In the inset, one of the final solutions (left) and the corresponding diluted solution (right) suitable for the spectroscopic analysis.

5.3. Conclusion

We can briefly summarize that MnO@oleate and MnO@stearate NPs have been synthesized by a shape-controlling solvothermal procedure. Among the synthetic conditions, the L:Mn molar ratio is easily tunable in order to control the NP size and shape. Our synthetic assays demonstrated that it is possible to synthesize concave and anisotropic MnO NPs, which have size suitable for our magnetic purposes. Magnetic investigation of both MnO@oleate and MnO@stearate nanoparticles showed similar results. All MnO NPs demonstrated a good antiferromagnetic behavior, as desired. Thus, they are suitable NPs that can be used as starting seeds to build antiferromagnetic / ferromagnetic core-shell structures. In this way we want to exploit a synergic effect between the exchange coupling generated at the AFM-FM core-shell interface and the shape anisotropic endowed by the anisotropic shape of the MnO core. Furthermore, to evaluate the reaction yield and measure the Mn concentration in the final hexanic dispersion of MnO NPs, we successfully developed a simple and cheap UV-Vis procedure to quantify the NP concentration.

5.4. Experimental section

5.4.1. Manganese carboxylate precursors synthesis

5.4.1.1. Synthesis of manganese(II) dioleate $[Mn(Ol)_2]$[6]

Materials

Anhydrous manganese(II) chloride (reagent grade ≥ 99%), tetramethylammonium hydroxide pentahydrate, sulphur powder (99.98%), oleic acid (reagent grade, 90%), methanol (≥ 99.8%) were purchased from Sigma-Aldrich and used as received without further purification.

Procedure

In a three-necked flask a clear solution of of tetramethylammonium hydroxide pentahydrate (4.55 g, 50 mmol) and oleic acid (15.75 mL, 50 mmol) in methanol (175 mL) was prepared and stirred under argon for 1 hour at room temperature.

Then the mixture was cooled to 0 °C using an ice bath and a solution of anhydrous $MnCl_2$ (3.15 g, 25 mmol) in methanol (100 mL) was slowly added. A white precipitate immediately formed, which was collected by filtration using a Buchner funnel previously cooled to –20 °C and washed with methanol (3 x 10 mL). Drying under vacuum gave a white powder.

IR (KBr pellet), ν (cm^{-1}): 3005, 2925, 2853, 1711, 1578, 1465, 1410, 1306, 722, 610.

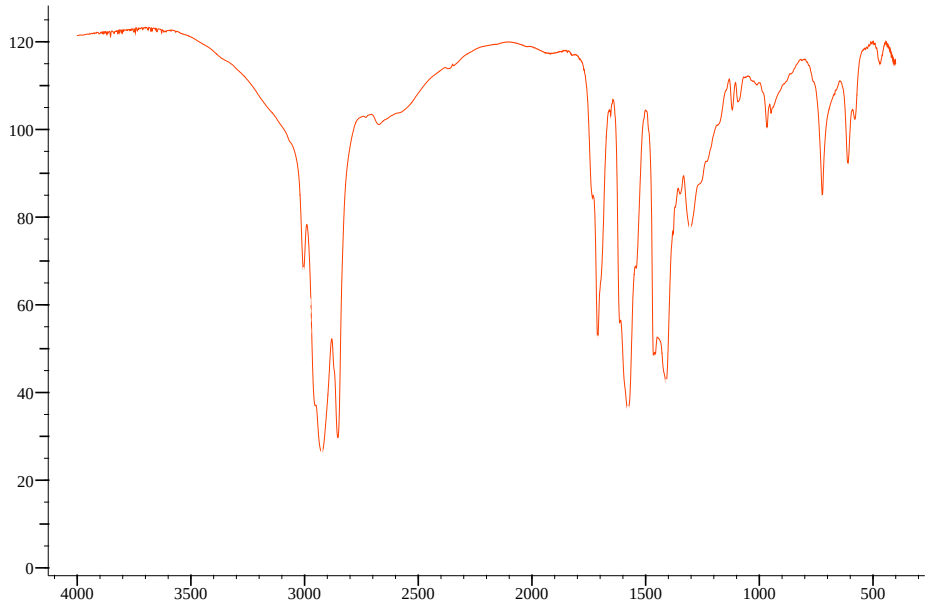

5.4.1.2. Synthesis of manganese(II) distearate $[Mn(St)_2]$[6]

Materials

Anhydrous manganese(II) chloride (99+%), tetramethylammonium hydroxide pentahydrate, sulfur powder (99.98%), stearic acid (reagent grade, 99%), methanol (≥ 99.8%) were purchased from Sigma-Aldrich and used as received without further purification.

Procedure

In a three-necked flask a clear solution of of tetramethylammonium hydroxide pentahydrate (4.55 g, 50 mmol) and stearic acid (14.2 g, 50 mmol) in methanol (175 mL) was prepared and stirred under argon for 1 hour at room temperature.

Then the mixture was cooled to 0 °C using an ice bath and a solution of anhydrous $MnCl_2$ (3.15 g, 25 mmol) in methanol (100 mL) was slowly added. A white precipitate immediately formed, which was collected by filtration using a Buchner funnel previously cooled to -20 °C and washed with methanol (3 x 10 mL). Drying under vacuum gave a white powder.

IR (KBr pellet), ν (cm^{-1}): 2955, 2917, 2849, 1552, 1468, 1440, 1320, 1113, 949, 721.

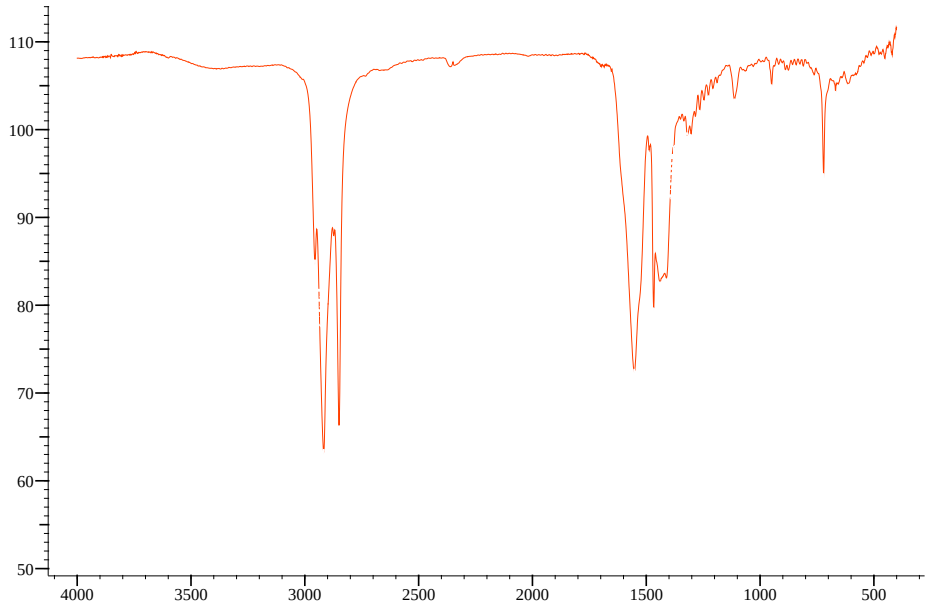

5.4.1.3. Synthesis of manganese(II) monooleate [Mn(OH)Ol][6]

Materials

Anhydrous manganese(II) chloride (reagent grade ≥ 99%), sodium oleate (reagent grade, 99%), ethanol (≥ 99.8%), hexane (≥ 97.0%), were purchased from Sigma-Aldrich and used as received without further purification.

Procedure

In a three-necked flask a clear solution of sodium oleate (2.45 g, 8 mmol) and manganese chloride (1 g, 8 mmol) in ethanol (12 mL), hexane (21 mL) and distilled water (9 mL) was stirred under argon for 5 hour at 75 °C.

Then the mixture was cooled to room temperature and stirred again for 12 hours. The solution was washed with a mixture of water and ethanol (1:1) in a separating funnel. Then the hexane was separated and evaporated. The dry product is brown.

IR (KBr pellet), ν (cm^{-1}): 3078, 2956, 2926, 1640, 1612, 1570, 1380, 1300, 992, 910, 719, 633.

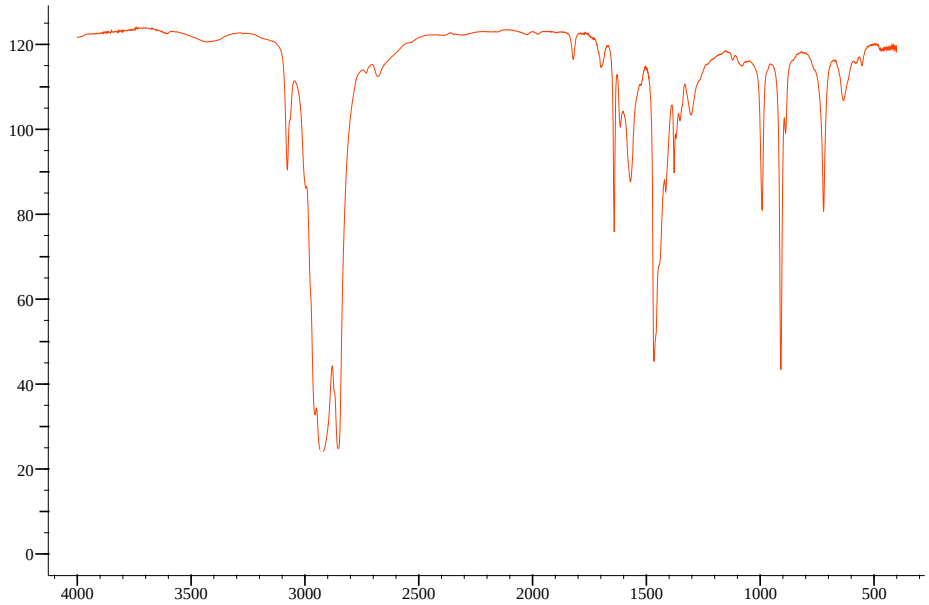

5.4.2. MnO nanoparticle synthesis

5.4.2.1. Synthesis of MnO nanoparticles starting from Mn oleate(II) as a precursor [6]

Materials

Manganese(II) dioleate, sulfur powder (99.98%), oleic acid (reagent grade, 90%) and octadecene (purum ≥ 95.0%) were purchased from Sigma-Aldrich and used as received without further purification.

Procedure

The procedure to prepare MnO nanoparticles is as follows. In a two-necked flask, the precursor manganese(II) dioleate (0.26 mmol) was dissolved in octadecene giving a 0.25 M solution of the manganese precursor. Then, sulfur (0.13 mmol) was added to the solution (Mn:S molar ratio = 1:0.5). Oleic acid (OlAc) was added to the solution in different amounts ranging from 0.26 mmol (Mn:OlAc = 1:1) to 2.08 mmol (Mn:OlAc = 1:8) to investigate how the Mn:OlAc molar ratio affects the synthetic outcome.

The resulting mixture was heated to 320 °C with heating rate 10 °C/min under nitrogen with magnetic stirring. At this temperature the solution changed from pink to dark brown and was aged for 1 hour at this temperature. Afterwards, the reaction mixture solution wad cooled to room temperature. Nanoparticles were precipitated by adding the reaction crude with a large excess of ethanol and then collected by centrifugation at 6000 rpm for 10 minutes. The nanoparticles were washed with ethanol and collected by centrifugation (three times) and then washed with acetone and collected by centrifugation (three times). The precipitate was finally redispersed in 5-10 mL of hexane by sonication (ultrasonic bath, 1 h, RT). The obtained nanoparticle dispersion are stable for several months.

5.4.2.2. Synthesis of MnO nanoparticles starting from Mn stearate(II) as precursor[6]

Materials

Manganese(II) distearate, sulfur powder (99.98%), stearic acid (reagent grade ≥ 99%) and octadecene (purum ≥ 95.0%) were purchased from Sigma-Aldrich and used as received without further purification.

Procedure

The procedure to prepare MnO nanoparticles is as follows. In a two-necked flask, the precursor manganese(II) distearate (0.26 mmol) was dissolved in octadecene giving a 0.25 M solution of the manganese precursor. Then, sulphur (0.13 mmol) was added to the solution (Mn:S molar ratio = 1:0.5). Stearic acid (StAc) was added to the solution in different amounts ranging from 0.26 mmol (Mn:StAc = 1:1) to 1.56 mmol (Mn:StAc = 1:6) to investigate how the Mn:StAc molar ratio affects the synthetic outcome.

The resulting mixture was heated to 320 °C with heating rate 10 °C/min under nitrogen with magnetic stirring. At this temperature the solution changed from grey-white to dark brown and was aged for 1 hour at this temperature. Afterwards, the reaction mixture solution wad cooled to room temperature. Nanoparticles were precipitated by adding the reaction crude with a large excess of ethanol and then collected by centrifugation at 6000 rpm for 10 minutes. The nanoparticles were washed with ethanol and collected by centrifugation (three times) and then washed with acetone and collected by centrifugation (three times). The precipitate was finally redispersed in 5-10 mL of hexane by sonication (ultrasonic bath, 1 h, RT). The obtained nanoparticles dispersion are stable for several months.

5.4.3. SQUID measurements

5.4.3.1. MnO@oleate samples

E11		E14		E16		E47	
L:Mn = 1:1		L:Mn = 2:1		L:Mn = 3:1		L:Mn = 4:1	
peso campione	3.71	peso campione	4.72	peso campione	7.31	peso campione	1.54
peso teflon	4.2	peso teflon	3.45	peso teflon	14.63	peso teflon	4.76
peso capsula	-	peso capsula	14.26	peso capsula	15.41	peso capsula	14.52

ZFC curves

E11

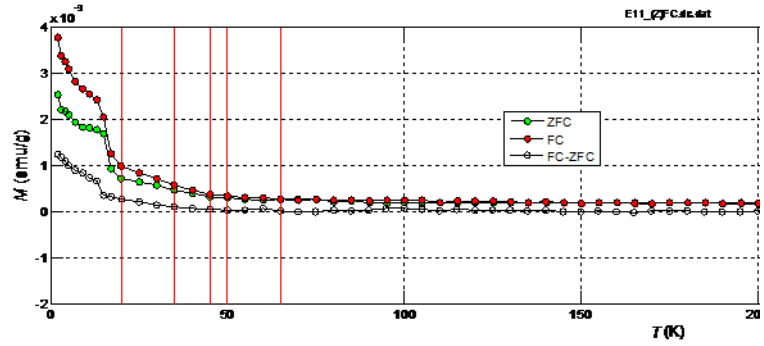

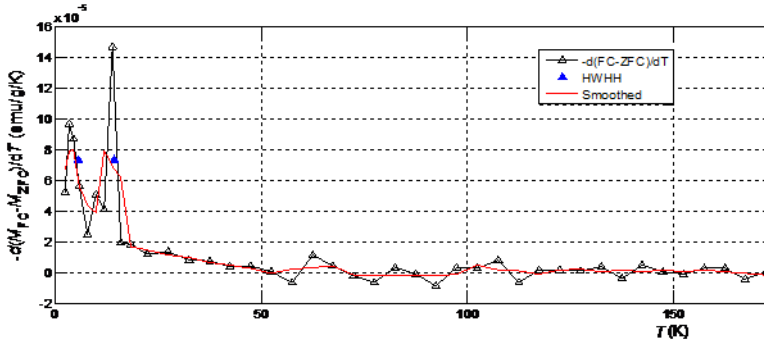

E14

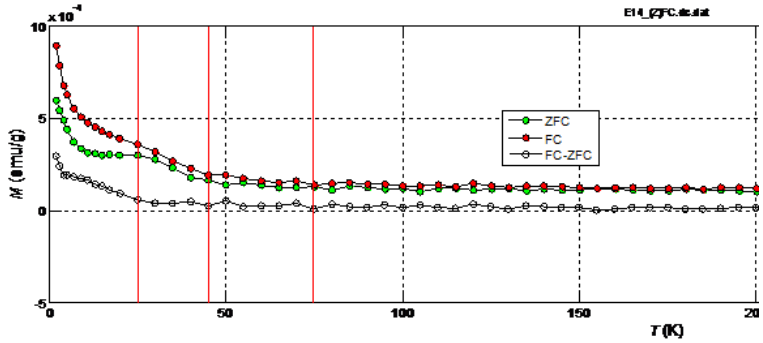
E14_ZFC.dc.dat
ZFC
FC
FC-ZFC
M (emu/g)
T (K)

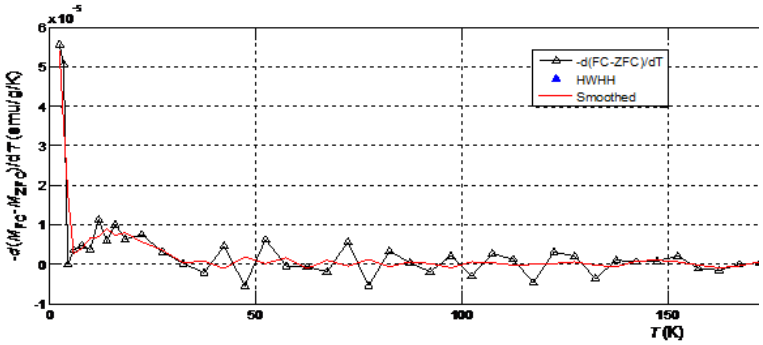
-d(FC-ZFC)/dT
HWHH
Smoothed
T (K)

E16

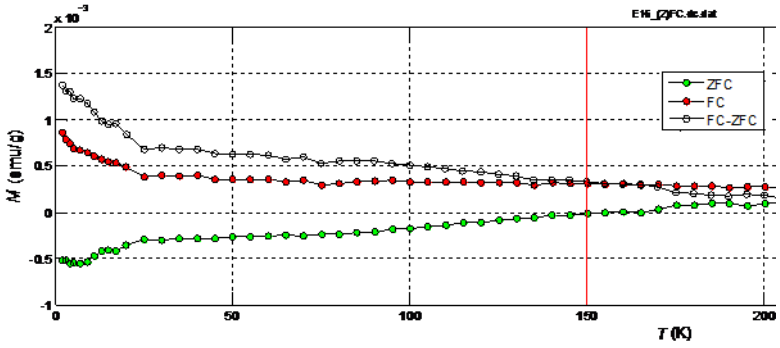
E16_ZFC.dc.dat
ZFC
FC
FC-ZFC
M (emu/g)
T (K)

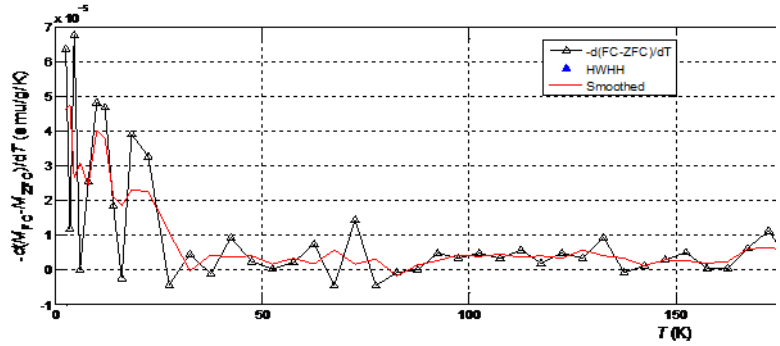
-d(FC-ZFC)/dT
HWHH
Smoothed
T (K)

E47

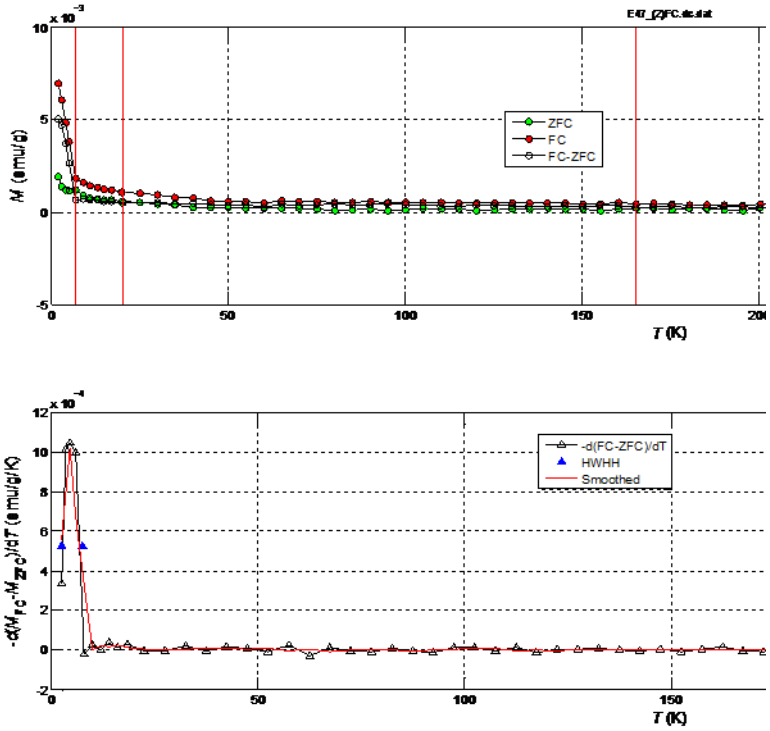
ZFC
FC
FC-ZFC
M (emu/g)
T (K)
-d(M_FC-M_ZFC)/dT (emu/g/K)
-d(FC-ZFC)/dT
HWHH
Smoothed
T (K)

FC hysteresis

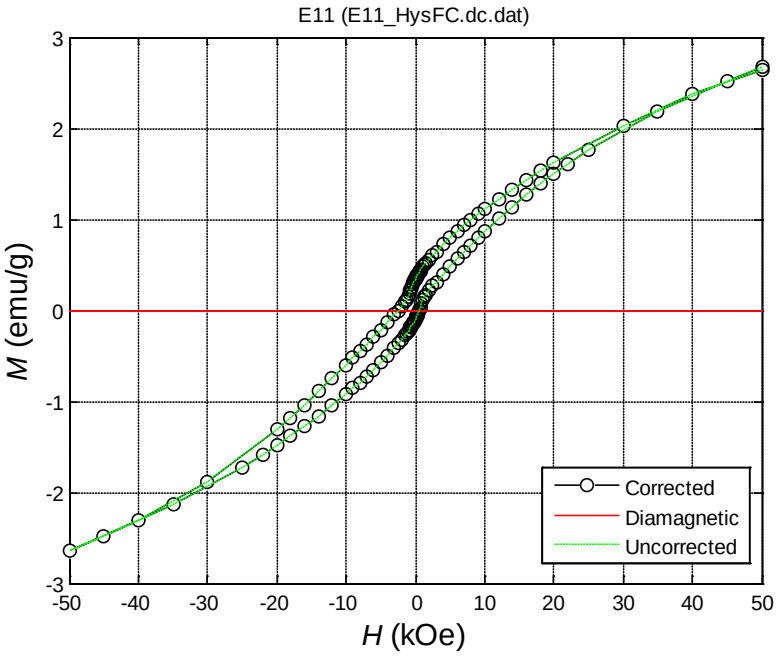

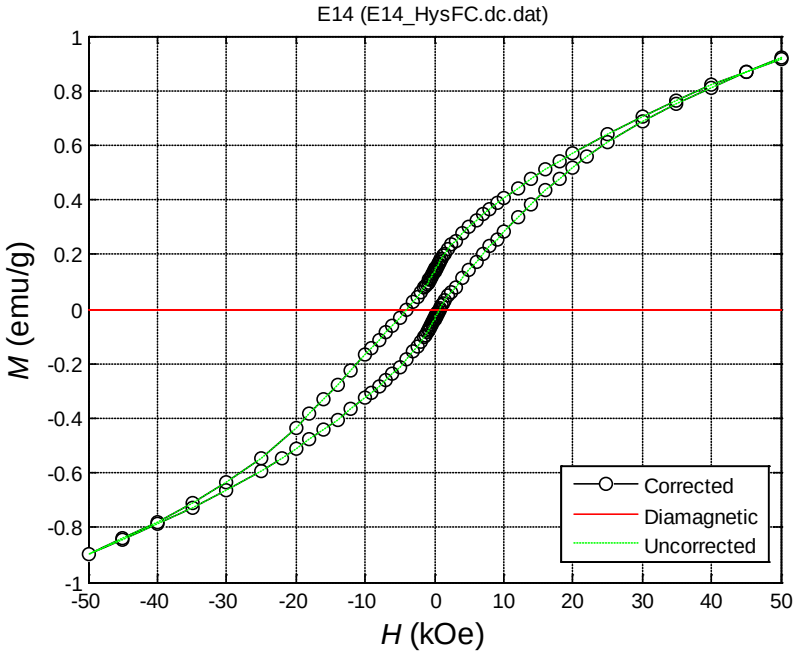

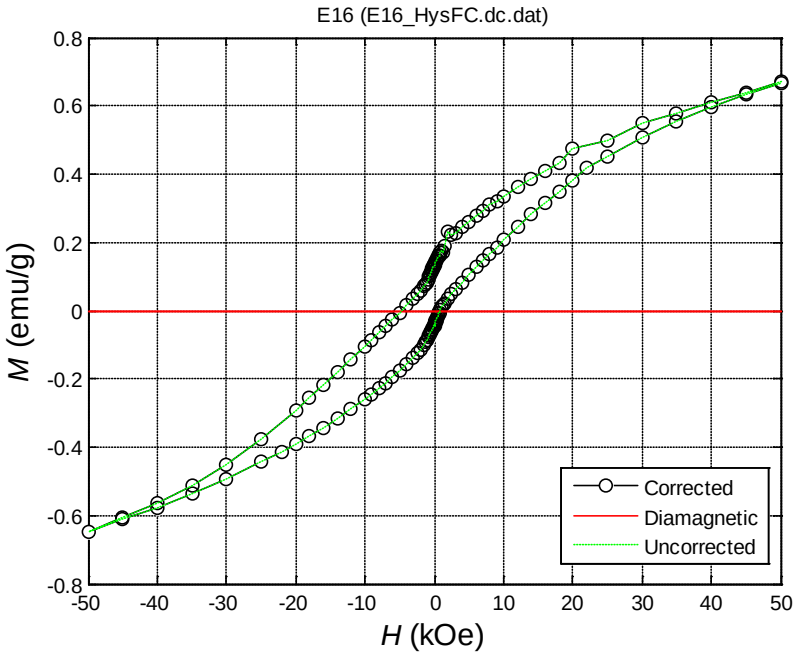
E16 (E16_HysFC.dc.dat)
M (emu/g)
H (kOe)
Corrected
Diamagnetic
Uncorrected

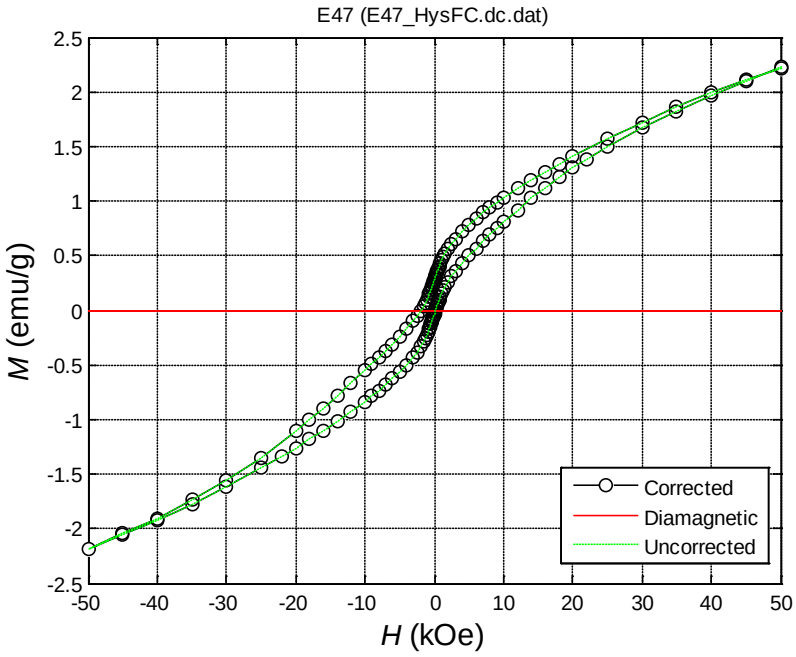
E47 (E47_HysFC.dc.dat)
M (emu/g)
H (kOe)
Corrected
Diamagnetic
Uncorrected

5.4.3.2. MnO@stearate samples

E54	E63	E46	E56	E58	E48
L:Mn = 0:1	L:Mn = 0.8:1	L:Mn = 1:1	L:Mn = 2:1	L:Mn = 3:1	L:Mn = 4:1
peso campione 2,8	peso campione 5,1	peso campione 14,8	peso campione 5,1	peso campione 8,8	peso campione 6,5
peso teflon 10,0	peso teflon 12,4	peso teflon 14,6	peso teflon 12,5	peso teflon 13,4	peso teflon 10,2

ZFC curves

E54

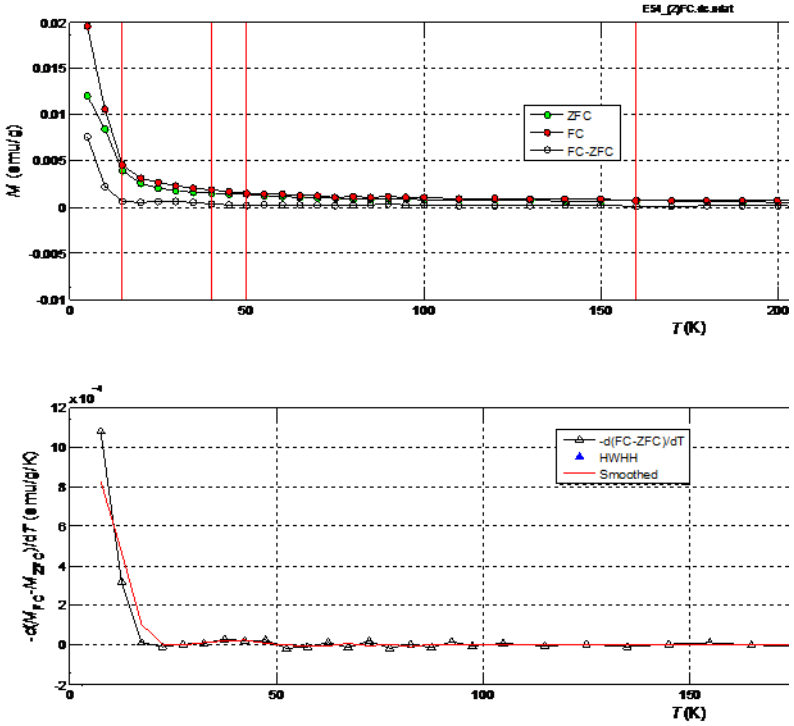

E63

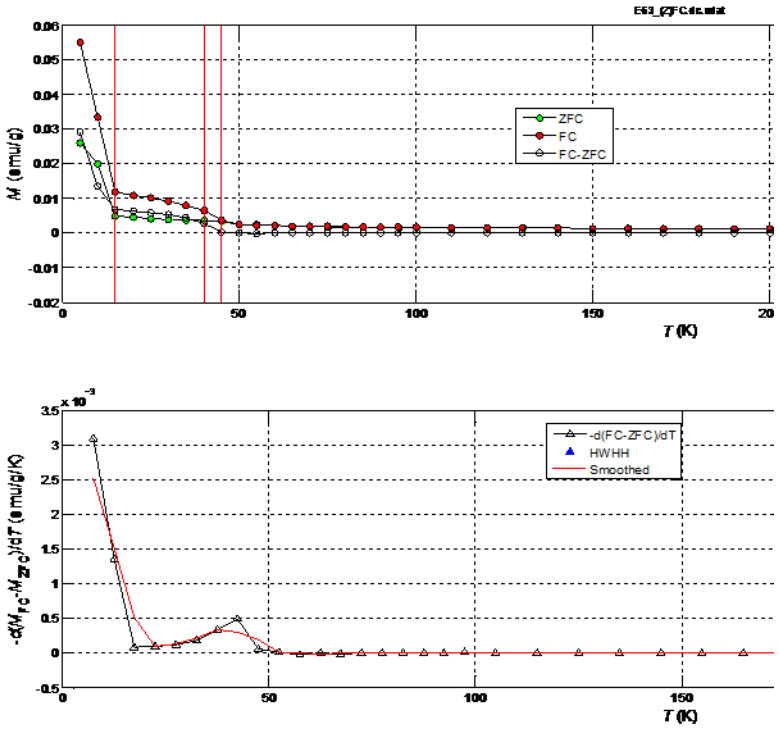
ZFC
FC
FC-ZFC
M (emu/g)
T (K)
-d(FC-ZFC)/dT
HWHH
Smoothed

E46

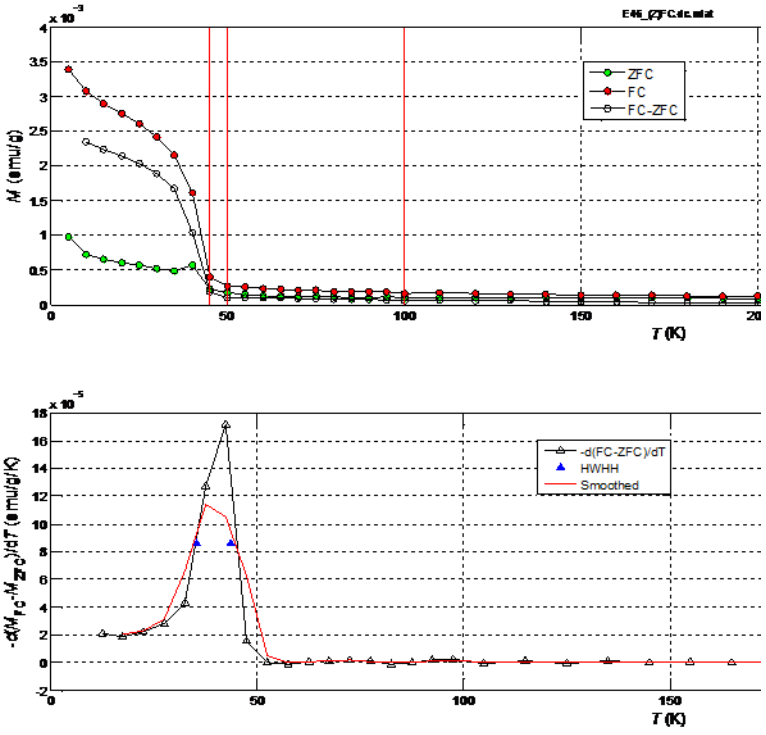
ZFC
FC
FC-ZFC
M (emu/g)
T (K)
-d(FC-ZFC)/dT
HWHH
Smoothed

E56

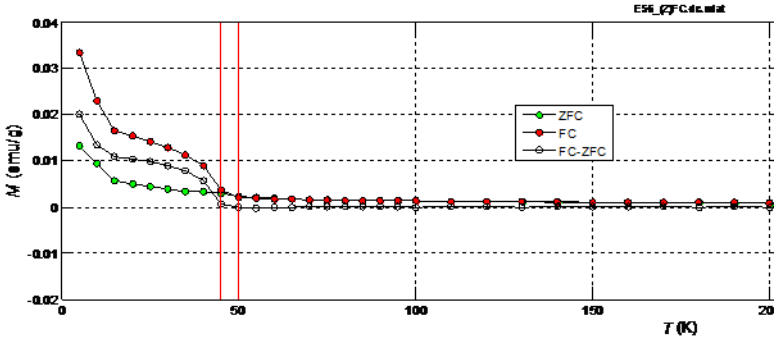
E56_(Z)FC.dc.mlst
ZFC
FC
FC-ZFC
M (emu/g)
T (K)

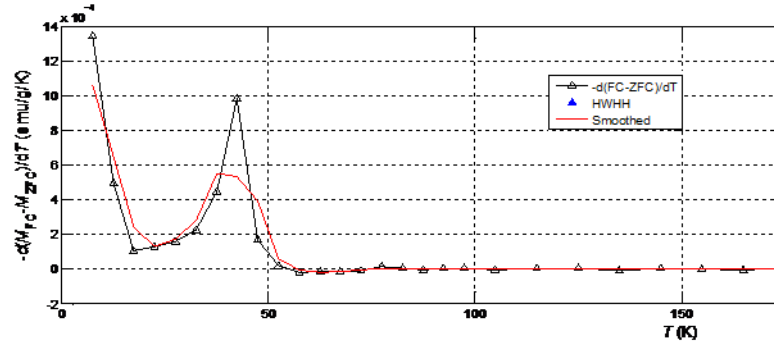
-d(MFC-MZFC)/dT (emu/g/K)
-d(FC-ZFC)/dT
HWHH
Smoothed
T (K)

E58

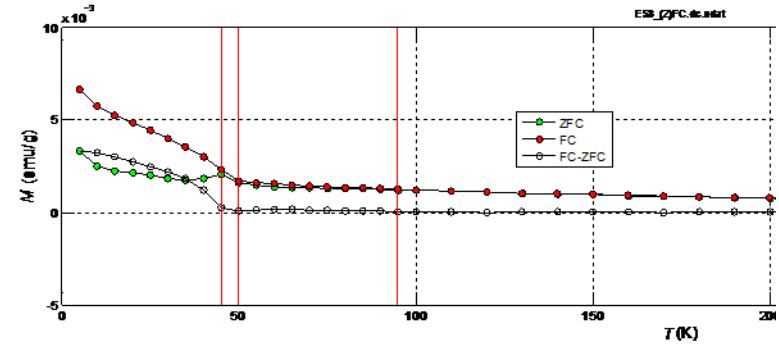
E58_(Z)FC.dc.mlst
ZFC
FC
FC-ZFC
M (emu/g)
T (K)

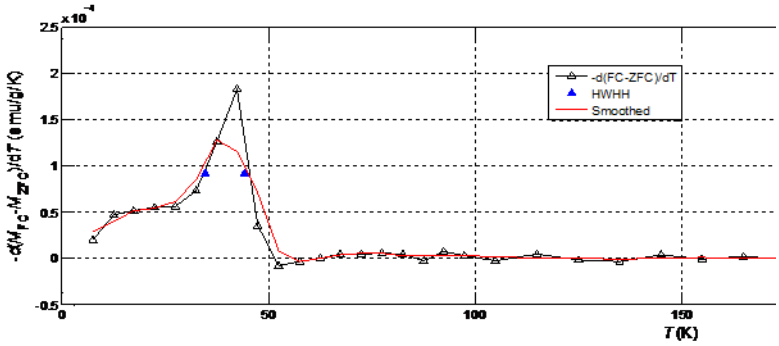
-d(MFC-MZFC)/dT (emu/g/K)
-d(FC-ZFC)/dT
HWHH
Smoothed
T (K)

E48

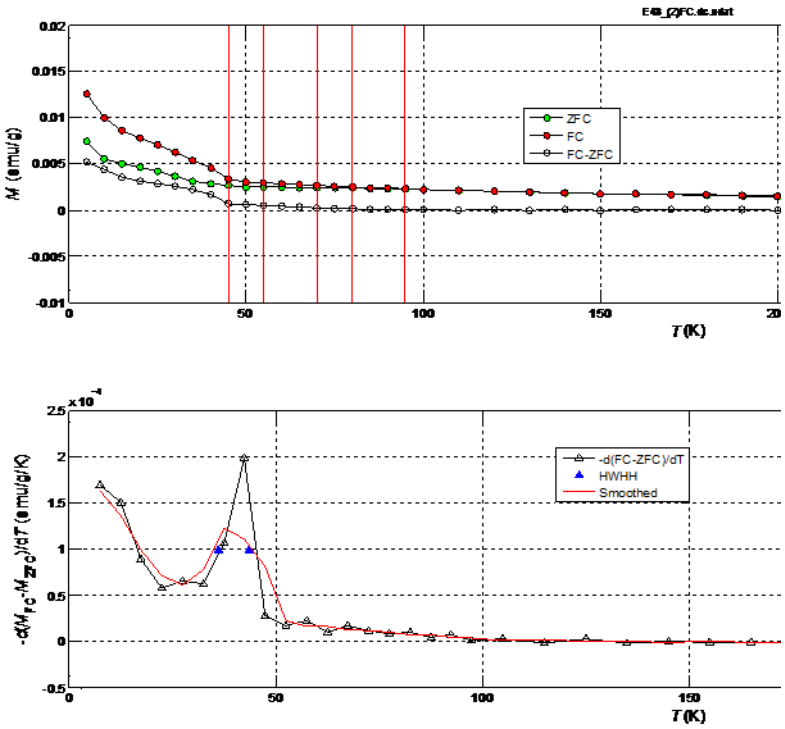
ZFC
FC
FC-ZFC
M (emu/g)
T (K)
-d(FC-ZFC)/dT
HWHH
Smoothed
-d(M_FC-M_ZFC)/dT (emu/g/K)

E55

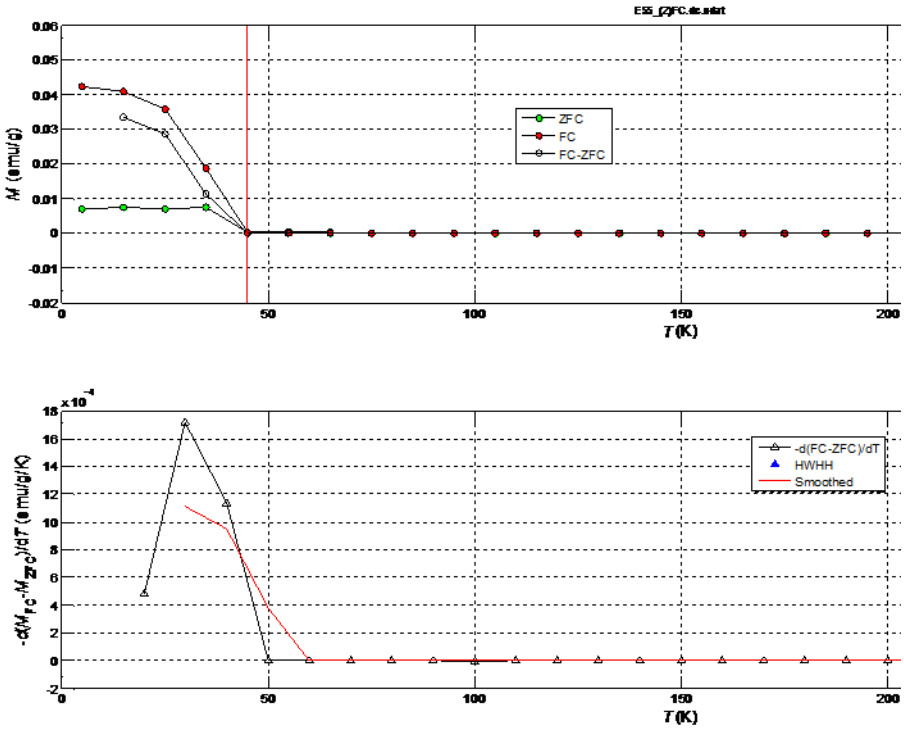
ZFC
FC
FC-ZFC
M (emu/g)
T (K)
-d(FC-ZFC)/dT
HWHH
Smoothed
-d(M_FC-M_ZFC)/dT (emu/g/K)

FC hysteresis

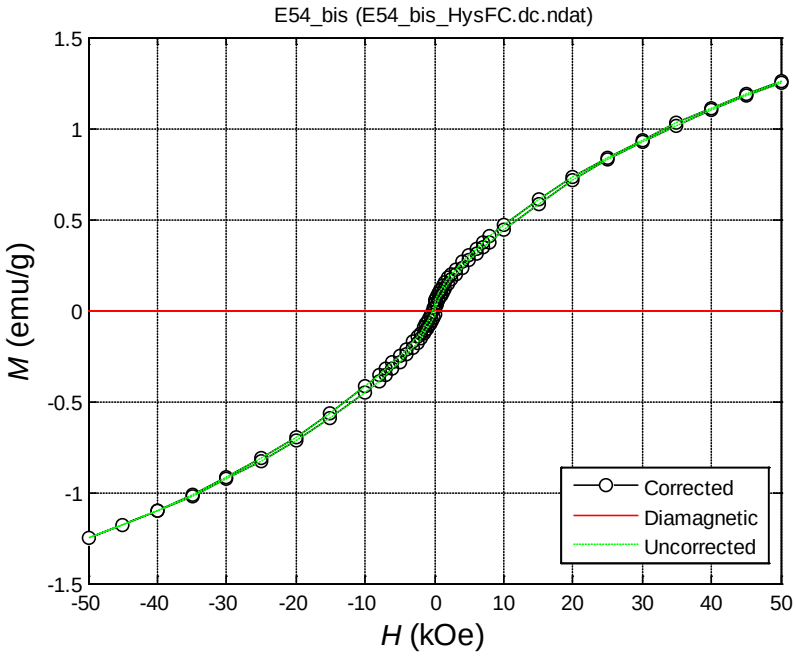

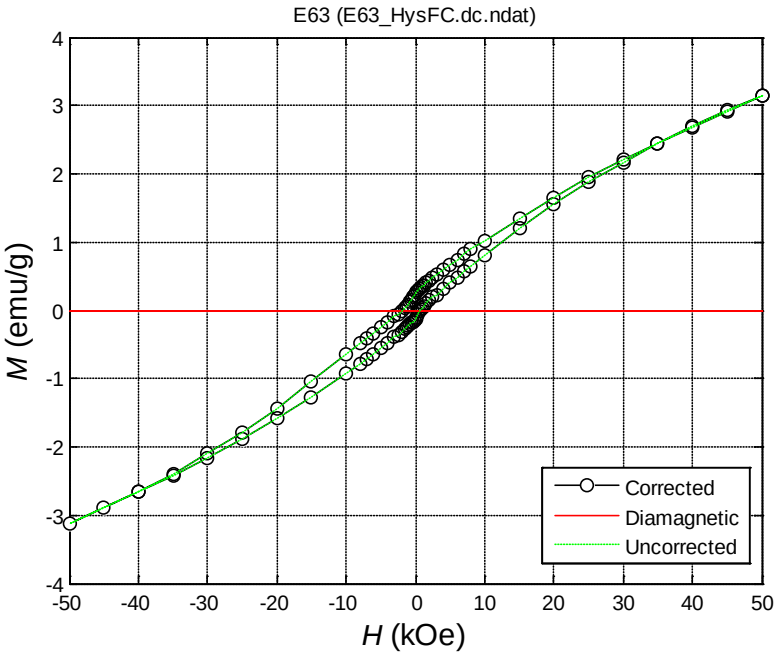

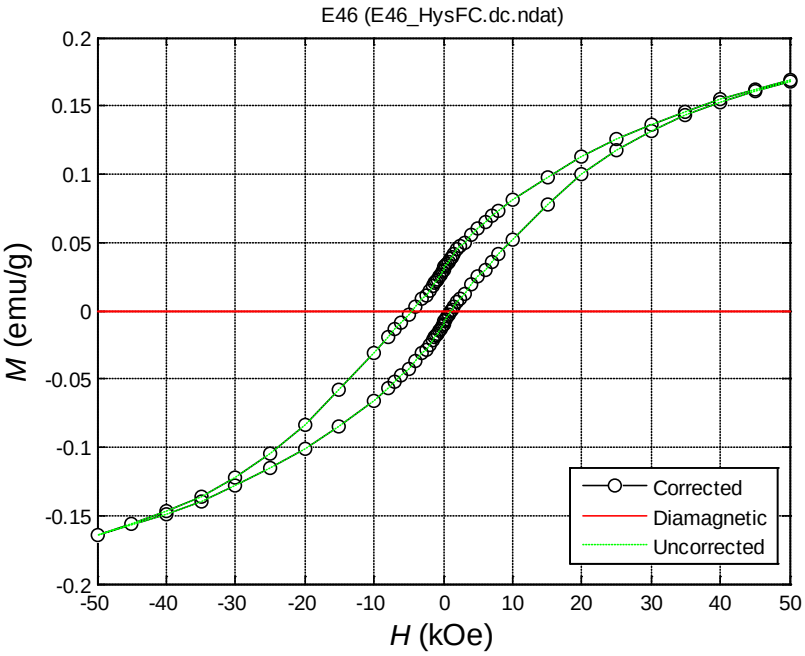
E46 (E46_HysFC.dc.ndat)
M (emu/g)
H (kOe)
Corrected
Diamagnetic
Uncorrected

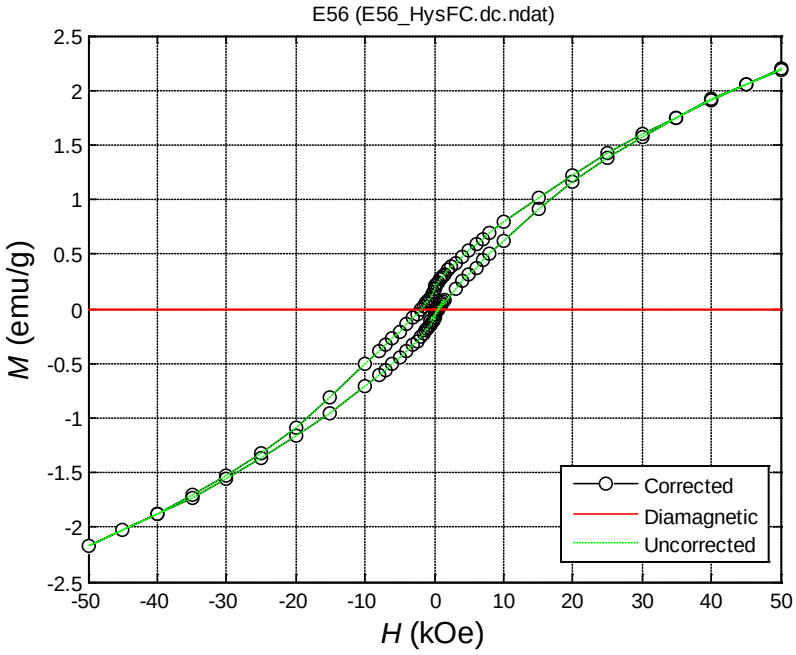
E56 (E56_HysFC.dc.ndat)
M (emu/g)
H (kOe)
Corrected
Diamagnetic
Uncorrected

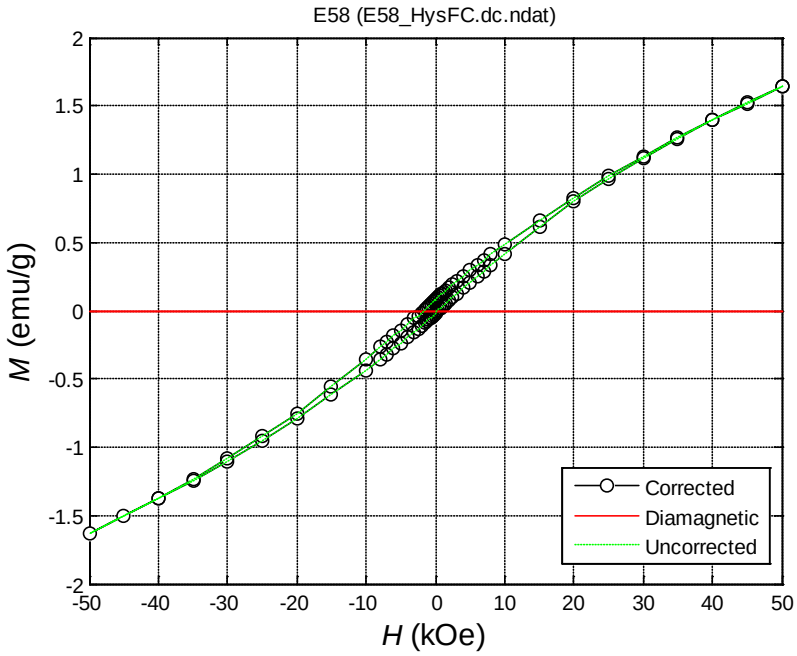
E58 (E58_HysFC.dc.ndat)
M (emu/g)
H (kOe)
Corrected
Diamagnetic
Uncorrected

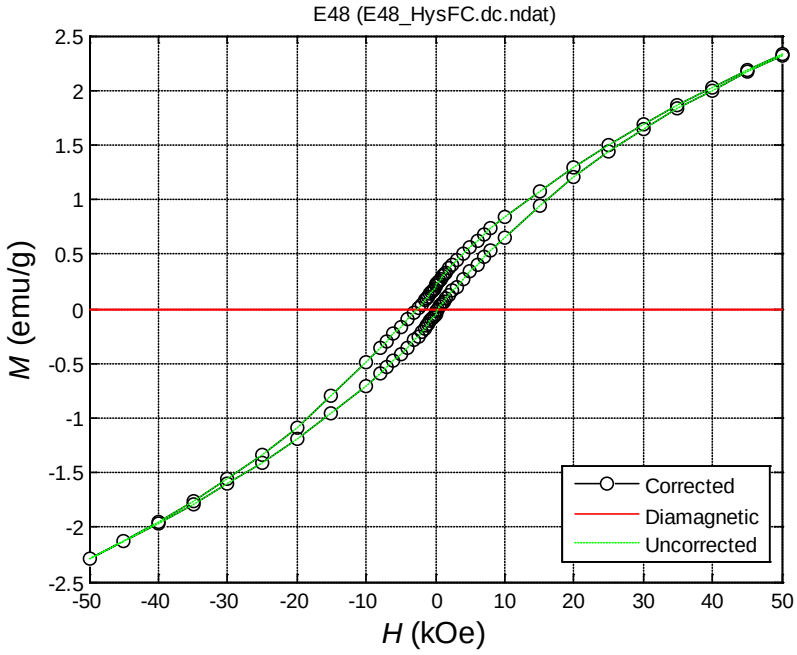
E48 (E48_HysFC.dc.ndat)
M (emu/g)
H (kOe)
Corrected
Diamagnetic
Uncorrected

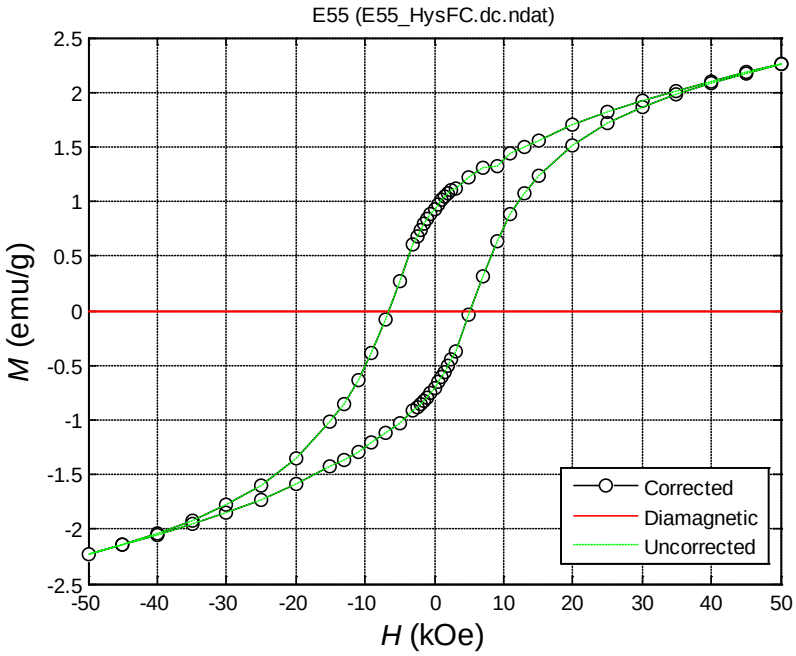
E55 (E55_HysFC.dc.ndat)
M (emu/g)
H (kOe)
Corrected
Diamagnetic
Uncorrected

6. MnO electrochemical study

6.1. Introduction

In literature has been reported that MnO_2 (Mn oxidation state +4) and Mn_2O_3 (Mn oxidation state +3) nanoparticles are able to catalyze the water splitting reaction. In particular, Mn_2O_3 has a high catalytic activity for the oxygen evolution reaction (OER) but a poor activity for the oxygen reduction reaction (ORR), while MnO_2 was demonstrated to be a very good catalyst for both reactions.[19] In principle, also MnO, where Mn is present as 2+ ion, could be used to catalyze the water splitting reaction. Recent preliminary studies reported that MnO is also active in the oxygen evolution reaction (OER) but it has poor activity in the oxygen reduction reaction (ORR). By now, preliminary studies involve films or spherical MnO nanoparticles. Our MnO nanoparticles could allow one to deeply investigate the MnO catalytic activity and discern if nanoparticle shape and dimensions affect the catalytic activity or if some crystal face has better activity than other faces for OER catalysis. Indeed, MnO has rock salt structure (reported in the figure at left) and we obtained NPs which preferentially developed the characteristic crystal faces {111}, {200}, and {220}. At present, the electrochemical experiments are in progress, but we here describe the procedure developed in order to remove the surfactant coating from the nanoparticles, a required step to perform accurate electrochemical measurements and achieve catalytic activity.

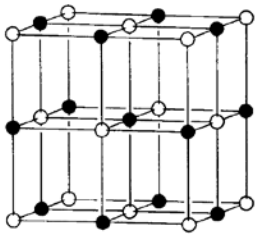

6.2. Result and discussion

Since it is required to work with a free metal oxide surface, we first set at eliminating all unbound fatty acid from MnO NPs. The samples are washed in order to eliminate the large excess of free surfactant still present in the final hexane dispersion. The coating of sample MnO@oleate (surfactant – precursor molar ratio = 1:1) was monitored by FT-IR spectroscopy in each surfactant removal step to verify the effectiveness of the procedure. After three precipitations with acetone followed by centrifugation, the FT-IR spectrum of the nanoparticles shows the disappearance of the characteristic peak of the free carboxylic acids about 1700 cm^{-1}. Hence, the excess of the surfactant not anchored to the nanoparticle surface

but only loosely bound within the first surfactant monolayer could be eliminated in a simple way.

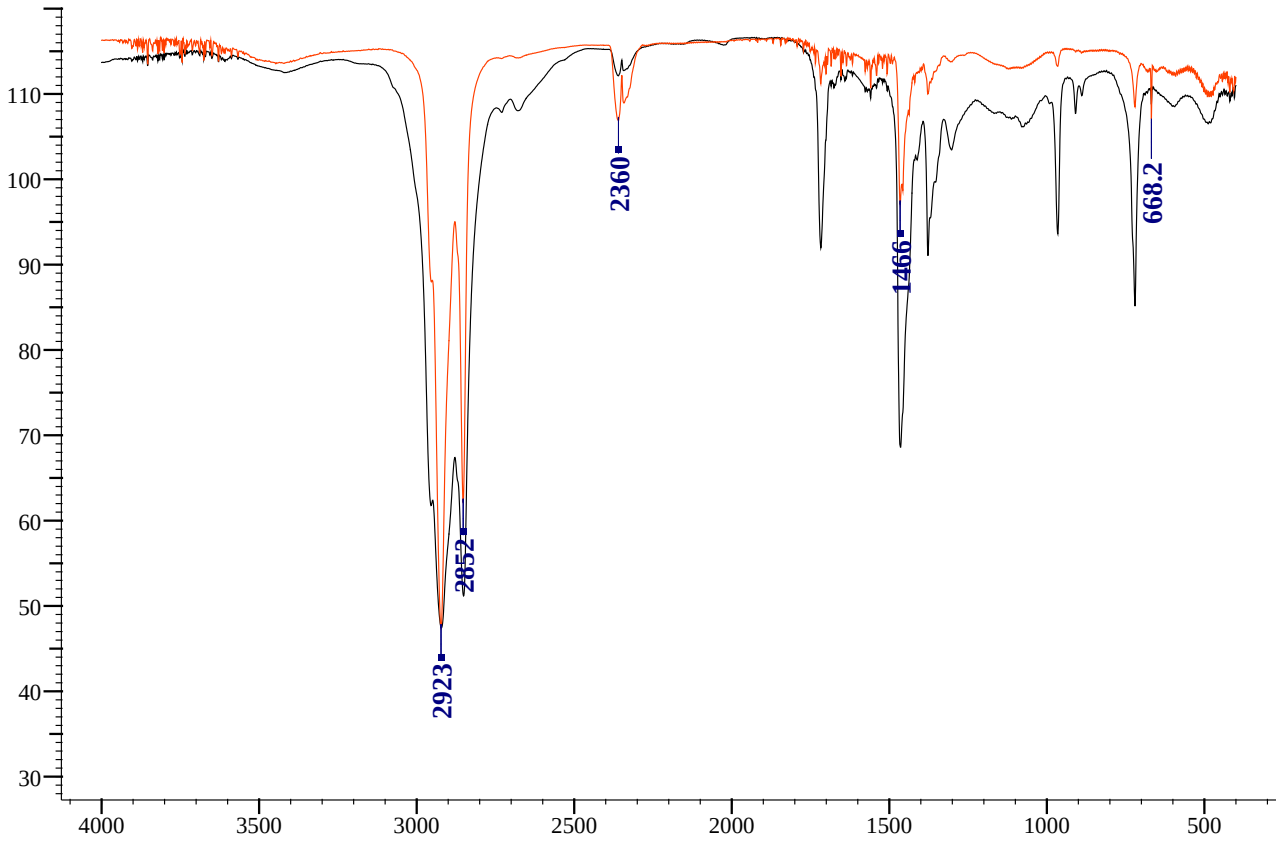

Figure 14: FT-IR spectra of MnO@stearate NPs. Black: before the washing treatment; red: after the washing treatment. The intensity of the peak at approximately 1700 cm^{-1}, due to carboxylic acid molecules not bound to the MnO surface, is largely decreased in the red spectrum

.

Next, the MnO nanoparticles were treated with lithium triethylborohydride ($LiEt_3BH$) in order to remove by reduction the stearate ligands anchored to the surface and achieve an uncapped surface for the electrochemical measurements. $LiEt_3BH$ is able to reduce the $–COO^-$ group to $–CH_2OH$ thus eliminating the interaction of the surfactant with the MnO surface. As expected from literature reports, a small amount of stearate remains also after the reduction, but the most part of the surface is now free and suitable for catalysis. The surfactant removal was verified by FT-IR spectroscopy and by elemental (CHN) analysis. We report the elemental analysis of the sample before and after the surfactant removal:

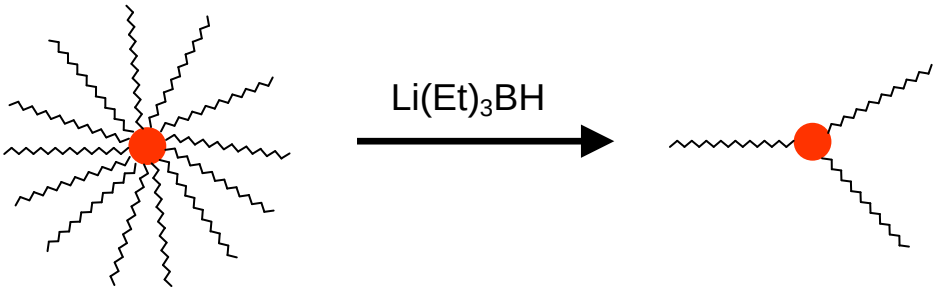

Figure 15: schematic representation of the surfactant removal by chemical method.

Elemental analysis

before reduction with $LiEt_3BH$: C: 82,62% H: 13,56%

after reduction with $LiEt_3BH$: C: 17,83% H: 3,07%

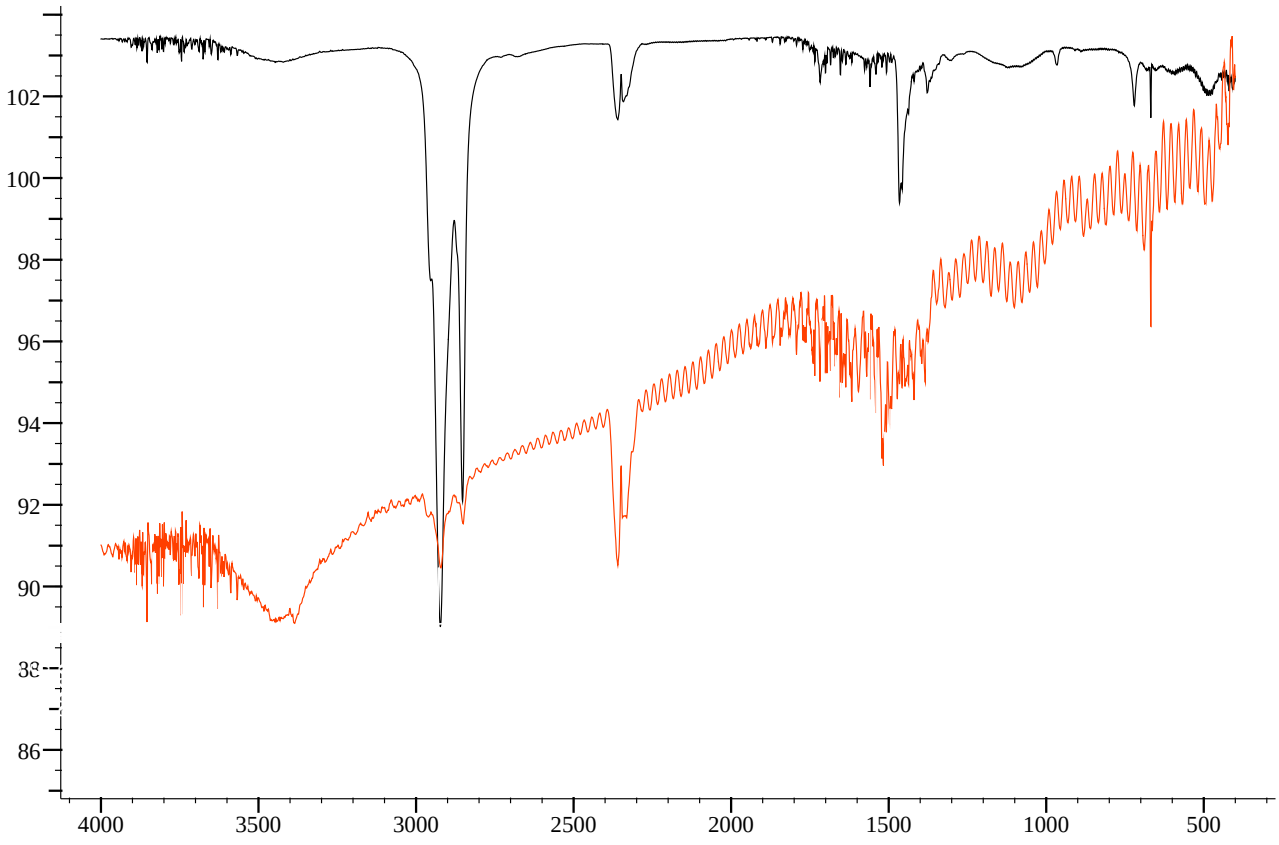

Figure 16: FT-IR spectra of a sample of MnO@oleate nanoparticles after the washing treatment (black) and after washing treatment and reduction with $LiEt_3BH$ (red).

Despite a wide number of repeated measurements, the FT-IR spectrum of nanoparticles treated with $LiEt_3BH$ shows a rolling baseline. If we compare the relative intensity of the characteristic peaks of the C-H stretching of the fatty chain (for example at 2923 and 2854 cm^{-1}), a significant reduction can be clearly seen. The aspect and behaviour of the nanoparticles are a further evidence of the surfactant removal. Until the treatment, dry nanoparticles appear like a wax that is easily dispersible in non-polar solvent, whereas after the treatment dry nanoparticles are like a black powder which quickly precipitated in non-polar solvent.

6.3. Experimental section

6.3.1. Surfactant removal from the MnO nanoparticle surface[20]

Some milligrams of a previously purified MnO nanoparticle sample were further washed with acetone and centrifuged at 6000 rpm for 10 min. The procedure was repeated 3 times. Then, the nanoparticles were dried in vacuum and treated with 5-6 mL of a 1 M solution of $LiEt_3BH$ in THF. The reaction was carried out under argon and magnetic stirring at room temperature for approximately 72 hours. It was found important, at the end of the treatment, to meticulously wash the sample with acetone, dichloromethane, water and acetone again. Each washing step was followed by centrifugation at 6000 rpm for 10 min. Finally, the nanoparticles were dried in vacuum overnight and conserved under argon in order to prevent the oxidation of MnO to Mn_3O_4.

6.3.2. Nanoparticles morphologies tested during the experiments

Sphere

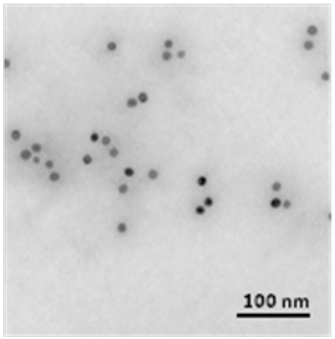

Octahedra

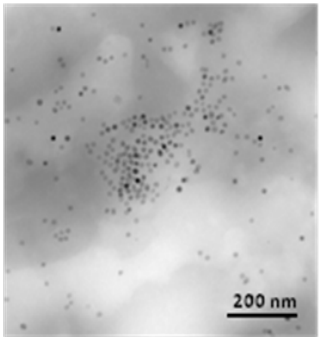

Sphere + octahedra

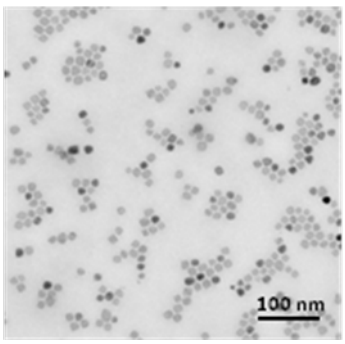

anisotropic shapes

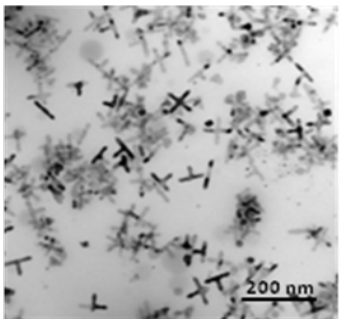

References

1. Zitoun, D., Pinna, N., Frolet, N. & Belin, C. Single crystal manganese oxide multipods by oriented attachment. *J. Am. Chem. Soc.* **127,** 15034–5 (2005).

2. Thomas D. Schladt, T. G. and W. T. Synthesis and Characterization of Monodisperse Manganese Oxide Nanoparticles−Evaluation of the Nucleation and Growth Mechanism. *chem mater* **21,** 3183–3190 (2009).

3. manganosite. *From Wikipedia, the free encyclopedia* (2013).

4. López-Ortega, A. *et al.* Size-dependent passivation shell and magnetic properties in antiferromagnetic/ferrimagnetic core/shell MnO nanoparticles. *J. Amer. Chem. Soc.* **132,** 9398–407 (2010).

5. Wang, C. H. *et al.* Antiferromagnetic order in MnO spherical nanoparticles. *Phys. Rev. B* **83,** 214418 (2011).

6. Puglisi, A. *et al.* Monodisperse Octahedral alpha -MnS and MnO Nanoparticles by the Decomposition of Manganese Oleate in the Presence of Sulfur. *Chem. Mater.* 2804–2813 (2010).

7. An, K. *et al.* Synthesis of Uniformly Sized Manganese Oxide Nanocrystals with Various Sizes and Shapes and Characterization of Their T1 Magnetic Resonance Relaxivity. *Eur. J. Inorg. Chem.* **2012,** 2148–2155 (2012).

8. Jun, Y., Lee, J.-H., Choi, J. & Cheon, J. Symmetry-controlled colloidal nanocrystals: nonhydrolytic chemical synthesis and shape determining parameters. *The journal of physical chemistry. B* **109,** 14795–806 (2005).

9. Douglas, F. J. *et al.* Formation of octapod MnO nanoparticles with enhanced magnetic properties through kinetically- manganese complexes †. *Nanoscale* **6,** 172–176 (2014).

10. Bau, J. a. *et al.* Nickel/Iron Oxide Nanocrystals with a Nonequilibrium Phase: Controlling Size, Shape, and Composition. *Chem. Mater.* **26,** 4796–4804 (2014).

11. Sang-Min Lee , Young-wook Jun , Sung-Nam Cho, and J. C. Single-Crystalline Star-Shaped Nanocrystals and Their Evolution: Programming the Geometry of Nano-Building Blocks. *J. Am. Chem. Soc.* **124,** 11244–11245 (2002).

12. Liberato Manna , Erik C. Scher, and A. P. A. Synthesis of Soluble and Processable Rod-, Arrow-, Teardrop-, and Tetrapod-Shaped CdSe Nanocrystals. *J. Am. Chem. Soc.* **122,** 12700–12706 (2000).

13. Kim, A. *et al.* Facile Synthesis of Multipodal MnO Nanocrystals and Their Catalytic Performance. *Eur. J. Inorg. Chem.* **2014,** 1279–1283 (2014).

14. Hÿtch, M. J.; Snoeck, E.; Kilaas, R. Quantitative measurement of displacement and strain Þelds from HREM micrographs. *Ultramicroscopy* **74,** 131–146 (1998).

15. Martin, J. Analysis of Variations in Structure from High Resolution Electron Microscope Images by Combining Real Space and Fourier Space Information H00FFtch Hg (k). *microsc. microanal. microstruct.* **8,** 41–57 (1997).

16. Polarz, S. Shape Matters: Anisotropy of the Morphology of Inorganic Colloidal Particles - Synthesis and Function. *Adv. Funct. Mater.* **21,** 3214–3230 (2011).

17. Willard, H. H. & Greathouse, L. H. the Colorimetric Determination of Manganese By Oxidation With Periodate. *J. Am. Chem. Soc.* **39,** 2366–2377 (1917).

18. Kolthoff, Sandell, Meehan, B. *Analisi chimica quantitativa - vol. II, Piccin editore, Padova*. (1974).

19. Pickrahn, K. L. *et al.* Active MnOx Electrocatalysts Prepared by Atomic Layer Deposition for Oxygen Evolution and Oxygen Reduction Reactions. *Adv. energy Mater.* **2,** 1269–1277 (2012).

20. Arienzo, M. D. *et al.* Photogenerated Defects in Shape-Controlled TiO 2 Anatase Nanocrystals : A Probe To Evaluate the Role of Crystal Facets in Photocatalytic Processes. *J. Am. Chem. Soc.* **133,** 17652–17661 (2011).

7. Synthesis of MnS nanoparticles

7.1. Introduction

In addition to MnO, another important antiferromagnetic semiconductor in the chalcogenide series is manganese(II) sulfide MnS. MnS crystallizes in three distinct structures: cubic α-MnS (rock-salt), cubic β-MnS (zinc-blende), and hexagonal γ-MnS (wurtzite). In α-MnS, manganese cations form a fcc lattice and the sulfide anions fill all of the octahedral voids. β-MnS also has a fcc lattice of Mn^{2+} ions but the sulfide anions occupy half of the tetrahedral voids. In hexagonal γ-MnS, the Mn^{2+} ions form a hcp lattice and the S^{2-} ions again occupy half of the tetrahedral voids.

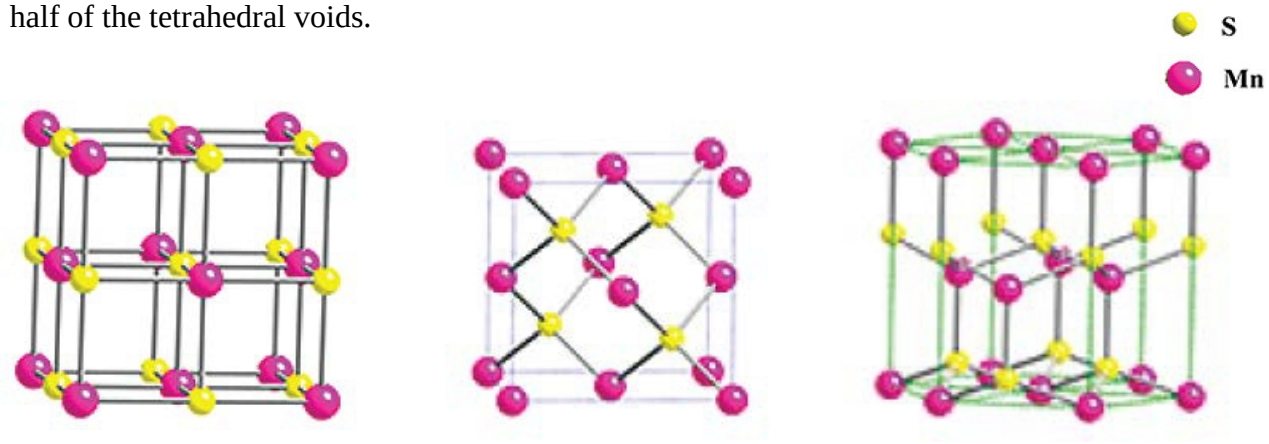

alpha beta gamma

Figures: manganese sulfide polymorphs. Images from ref. 1

Similar to isomorphic MnO, α-MnS has AF-II antiferromagnetic order, with ferromagnetic order within {111} Mn^{2+} sheets, which are antiferromagnetically coupled to each other, due to the predominance of next nearest neighbor interactions. In the zinc-blende form of β-MnS, where the Mn ions have the same spatial arrangement as in the rocksalt structure, the alignment of spins in {210} ferromagnetic sheets is parallel to that of one of its two neighboring planes, and antiparallel to the other. The hexagonal wurtzite form of γ-MnS, is more complicated than the cubic polymorphs and neutron diffraction studies indicate that the magnetic unit cell is four times that determined from x-ray crystallography.[2] Within the two metastable forms, β-MnS will form at lower temperature rather than the more stable γ MnS because the β MnS phase has the smallest free formation energy. [1]

α-MnS is the thermodynamically stable and the corresponding mineral is known since the

XIX century as alabandite.[4] The γ-MnS mineral is named rambergite has been discovered in 1996 in Sweden[5] while β-MnS browneite was found in a meteorite collected in Poland.[6] All MnS polymorphs display antiferromagnetic order[7] with Néel temperatures of approximately 100 K (β-MnS), 80 K (γ-MnS), and 154 K (α-MnS).[8]

alabandite

rambergite

Figures: manganese sulfide minerals

MnS is a very useful and versatile material due to its physical properties and could be used in many fields (medical or technological) for different applications such as photoluminescent components,[9] photoreduction catalysts,[10] anode material in lithium-ion batteries,[11] and supercapacitor materials.[12]

memory device

solar cell

lithium-ion battery

Figures: some examples of possible MnS nanoparticles applications

Since nanoparticle properties (such as magnetic and optical properties) are closely correlated to nanoparticle structure, size and surface, it is clear that a primarychallenge is to achieve a synthesis control in order to produce the desired MnS crystal phase. In particular magnetic properties, which are significant for many applications (e.g. recording media), have been reported in the literature only for α-MnS while β- and γ-MnS are still poorly characterized. Thus, it could be very useful to synthesize β- and γ-MnS nanoparticles in order to explore

their magnetic properties.

MnS NCs have been synthesized by different procedures, including chemical vapor deposition[13 14 15] and hydrothermal[16 17 18] methods, but we want to focus on NCs synthesized by solvothermal methods, which usually allow high experimental flexibility and finest NC control. Whereas reports on the solvothermal synthesis of β-MnS NCs are very rare,[19] a large number of syntheses of α-MnS[1 3 20 21 22 23 24 25 26 27] and γ-MnS[3 28 29] NCs have been illustrated.

In the procedures to synthesize manganese sulfide NCs, different reagents were used to introduce sulfur in the reaction mixture: Mn- complexes containing sulfur and organic (e.g. thiourea,[18] thioacetamide,[1] bistrimethylsilylsulfide,[24] dodecylthiol[30] or inorganic (sulfur,[20 21 27 28] ammonium sulfide[29]) compounds.

Exploring the examples in literature, very different S:Mn molar ratios were used, ranging from (1/3):1 to 4:1, but in most cases S:Mn ≥ 1. Curiously, S:Mn < 1 was successful when carboxylic acids were not present in the reaction mixture.

In a previous investigation of the MnS NCs solvothermal synthesis starting from manganese dioleate,[20] it was noticed that in the absence of free surfactants, an excess of sulfur (S:Mn ≥ 2) is needed to avoid the formation of MnO and to obtain MnS NCs.

Generally in literature, the aim of the synthesis is to obtain structurally pure products , *i. e.*, α- or β- or γ-MnS NCs to exploit their different physical properties.

Since the α phase is the thermodynamically stable phase and β and γ are metastable and kinetically favored phases, it is possible to find a correlation between the physical reaction conditions and the resulting crystal phase, for example, high temperature usually favors the achievement of chemical equilibrium and the most stable phase.

The effect of temperature is described in a paper where heating of Mn(II) diethyldithiocarbamate in hexadecylamine at low *T* (120-150 °C) gave multipods comprising γ-MnS arms stemming from a β-MnS core whereas 30 nm α-MnS cubes were obtained at 180 °C.[3] Furthermore, a more detailed investigation gave similar results for the reaction of Mn(II) chloride and thioacetamide in oleylamine.[1]

This report also described the β → α and γ → α phase transformation of MnS under high pressure. The formation of α- *vs.* γ-MnS NCs could also depend on the heating rate (15 °C/min: α-MnS; 25 and 35 °C/min: γ-MnS) when Mn(II) diethyldithiocarbamate was heated in octadecene at 320 °C with a large excess of both oleic acid and oleylamine.[23]

Chemical reaction parameters could also allow to achieve MnS polymorphism control. By reacting Mn(II) chloride and thiourea in autoclave (*T* = 190 °C) for 12 h, 30 nm α-MnS NCs

were prepared using water as solvent whereas when solvent was benzene γ-MnS rods (d = 40-100 nm, l = 250-700 nm) were obtained.[18] In another case, reaction of Mn(II) nitrate with elemental S in octadecylamine at 200 °C gave 50 nm α-MnS hexagons at high S concentration whereas γ-MnS rods ($d \approx 50$ nm) resulted at low S concentration.[27] Some examples of chemical control were also reported for hydrothermal synthesis, such as a reaction where Mn(II) chloride with sodium sulfide at 180 °C yielded 200 nm α-MnS octahedral NCs but γ-MnS rods (d = 200-300 nm, l = 1.0-1.5 μm) were obtained when a large excess of hydrazine was added.[17]

To briefly summarize, up to now the MnS nanoparticle polymorphism could also be controlled by chemical means. By reacting Mn(II) chloride and thiourea (T = 190 °C) for 12 h in autoclave, 30 nm α-MnS NCs were synthetized using water as solvent whereas when benzene was used as solvent γ-MnS rods (d = 40-100 nm, l = 250-700 nm) were obtained.[18] Reaction of Mn(II) nitrate with elemental S in octadecylamine at 200 °C formed 50 nm α-MnS hexagons at high S concentration whereas low S concentration gave γ-MnS rods ($d \approx 50$ nm).[27] Hydrothermal reaction of Mn(II) chloride with sodium sulfide at 180 °C gave 200 nm α-MnS octahedral NCs but when a large excess of hydrazine was added γ-MnS rods (d = 200-300 nm, l = 1.0-1.5 μm) were obtained.[17] In summary, MnS NCs crystal structure control was achieved changing the solvent, the amount of sulfur, or adding a reducing agent such as hydrazine. At the best of our knowledge, the effect of surfactant nature on the MnS NCs crystal phase has not been studied yet.

Starting from these considerations, in our work we decided to study the dependence of the polymorphism on the type of surfactant in a solvothermal synthesis, namely, the decomposition of (sulfur-free) manganese precursors in the presence of elemental sulfur and long-chain surfactants.

In particular, the focus of our work is on two issues: (i) how sulfur and surfactant affect on the formation of either MnO or MnS NCs and (ii) how the surfactant affects the polymorphism of MnS NCs.

As to the first point, we demonstrated (starting from a previous observation)[20] the importance of the Mn:S molar ratio in the reaction mixture in order to control the formation of MnS *vs.* MnO NCs. As to the second point, we showed that using a mixture of long-chain amine and carboxylic acid γ-MnS NCs formed whereas α-MnS NCs were synthesized whenever a single surfactant is used irrespective of its polar functional group.

7.2. Results and discussion

7.2.1. MnO vs. MnS: The role of sulfur and surfactant

Starting from the above described work on MnO nanoparticles, we set out to synthesize other manganese chalcogenide nanoparticles, in particular MnS NCs. Manganese stearate was chosen as precursor and the manganese : sulfur molar ratio became the focal point to obtain pure MnS NCs. We borrowed many synthetic conditions from the MnO work, such as solvent, heating rate, and ageing temperature and time.

A previous work[20] reported that a stoichiometric amount of sulfur gives a mixture of MnO and α-MnS nanoparticles when the manganese precursor is decomposed in octadecene. Different type of precursor such as Mn(OH)Ol, $MnOl_2$, and $MnSt_2$ gave the same results in relation to the molar ratio. Also, the use of an inorganic precursor like the $Mn_2(CO)_{10}$ in presence of stearic acid is able to form MnO or MnS NCs and its behavior is very close to the behavior of carboxylate precursors. The general trend could be summarized as follows: α-MnS NCs could be achieved using a S:Mn molar ratio ≥ 2 whereas pure MnO NCs were obtained using S:Mn ≤ 0.6. In the range between 0.6 and 2 a mixture of both MnO and α-MnS NCs is generally obtained. Curiously, no reaction shows the formation of mixed MnO_xS_{1-x} nanoparticles despite they have the same rock-salt structure. Probably, this was prevented by the largely different ionic radius of hexacoordinated O^{2-} (0.126 nm) and S^{2-} (0.170 nm).[31] Transmission electron microscopy (TEM) images and electron diffraction (ED) patterns of representative NCs are reported in [Figure *1*]. All ED patterns could be assigned to MnO or α-MnS NCs (or represent a mixture of both).

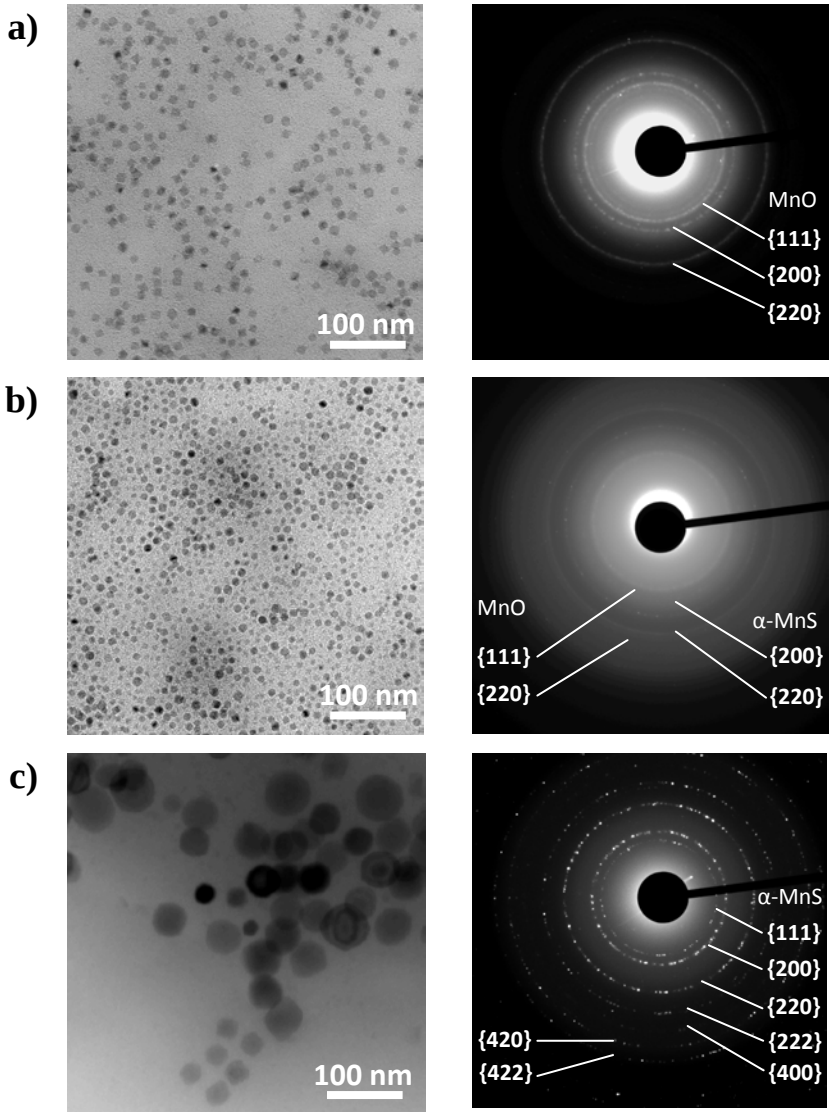

Figure 1: TEM images (left) and electron diffraction patterns (right) of NCs obtained by high temperature decomposition of $Mn_2(CO)_{10}$ with StAc:Mn = 2 and varying amounts of sulfur. a) S:Mn = 1, MnO NCs; b) S:Mn = 2, mixture of MnO and α-MnS NCs; c) S:Mn = 4, α-MnS NCs.

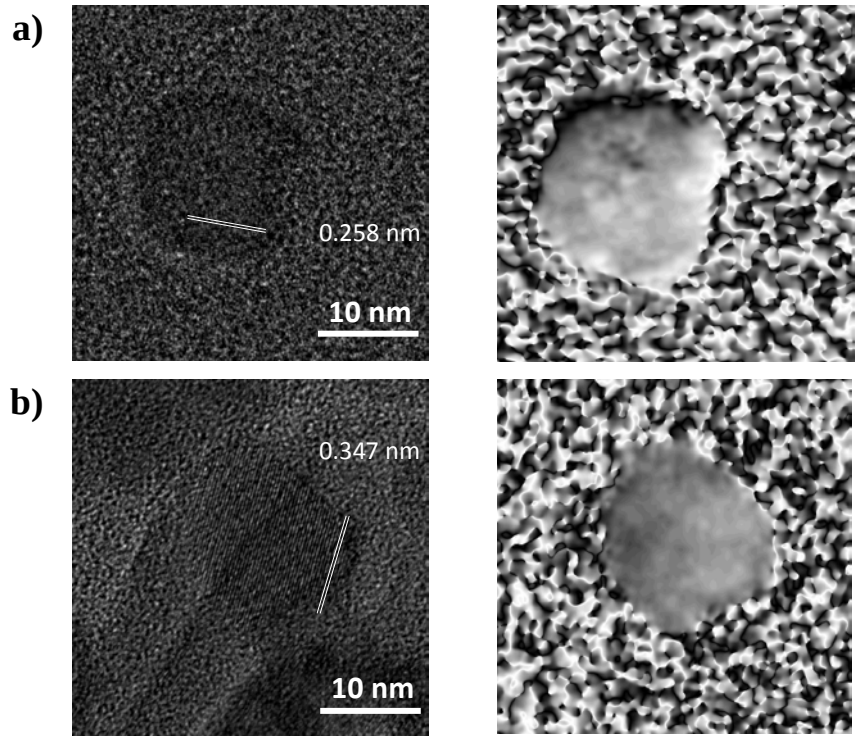

Figure 2: HRTEM images (left) and geometric phase analysis (GPA, right) of α-MnS and γ-MnS NCs. a) α-MnS NC prepared from $Mn_2(CO)_{10}$ in the presence of StAc (Mn:S:StAc = 1:4:2) displaying 0.258 nm lattice fringes corresponding to {200} planes. b) γ-MnS NC prepared from $MnSt_2$ in the presence of HdAm (Mn:S:StAc = 1:4:2) displaying 0.347 nm lattice fringes corresponding to {100} planes.

Geometric phase analysis (GPA)[32] *showed that the NCs are single crystallites, almost free from lattice defects.*

As expected, the S:Mn molar ratio between sulphur and metal precursor is a significant driving force affecting the nanocrystal nature but also the L:Mn molar ratio between metal precursor and surfactant (L) plays a role in the nanocrystals formation as significant as that of S:Mn. Thus, the experimental results are best graphically summarized in a plot with the S: Mn and L : Mn molar ratios as axes.

Hollow or solid colour squares indicate that MnO (MnS) NCs were obtained, and half-filled squares represent a MnO/MnS NC mixture. The color indicates the type of precursor. These results confirmed that a mixture of MnO and α-MnS NCs is observed when a stoichiometric S:Mn = 1:1 ratio[1] is used. A wide range of ageing times (30 – 180 min) was studied. The

[1] The resulting product comprised a mixture of MnO and α-MnS NCs. Electron diffraction gave no evidence that MnO_xS_{1-x} NCs formed despite both MnO and α-MnS have rock salt structure. This was probably prevented by the largely different ionic radius of hexacoordinated O^{2-} (0.126 nm) and S^{2-} (0.170 nm). [R. D. Shannon, *Acta Cryst.*, **A32** (1976) 751-767]

interconversion of MnO and α-MnS NCs during ageing never occurs. When decomposed in the absence of free StAc, $MnSt_2$ gave α-MnS NCs already for S:Mn = 1:1.

In the case of $Mn_2(CO)_{10}$, free StAc was added. From the plot, it is clear that a NC mixture is obtained when the molar amount of S and L were equal. Pure MnO NCs were given when the amount of S was lower than the L amount. Otherwise, when the amount of S was higher than that of L, α-MnS NCs are observed. In the case of Mn organic precursors, the added surfactant was the corresponding carboxylic acid, *i. e.*, OlAc for Mn(OH)Ol or $MnOl_2$ and StAc for $MnSt_2$. Generally, pure α-MnS NCs were obtained when the sulfur amount is high while pure MnO NCs when the ligand amount is high. Reactions prepared using high S:Mn *and* L:Mn ratios often did not yield nanocrystals.

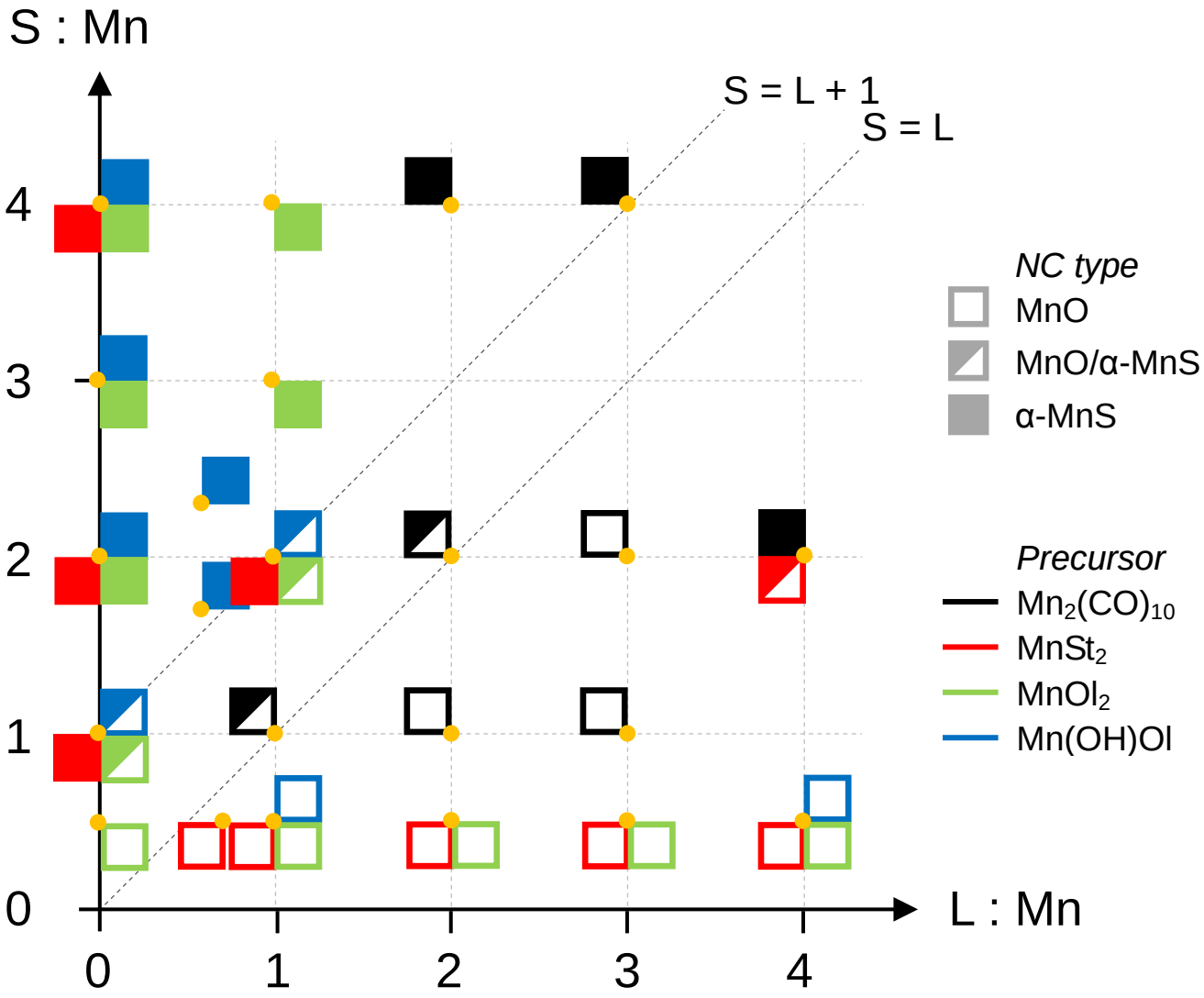

Figure 3: Pictorial representation of the NC outcome from the solvothermal synthesis involving the decomposition of different Mn precursors as a function of the L:Mn and S:Mn molar ratio. Each orange dot represents a synthesis at the corresponding values of L:Mn and

S:Mn. One to four squares are arranged about each dot to represent the resulting NCs when using different Mn precursors. The type of NC is encoded as follows: open squares: MnO NCs; half-filled squares: mixture of MnO and α-MnS NCs; solid squares: α-MnS NCs. Precursors are color coded as follows (counterclockwise from top left): black: $Mn_2(CO)_{10}$, red: $MnSt_2$, green: $MnOl_2$, blue: Mn(OH)Ol. The free surfactant L was StAc for $Mn_2(CO)_{10}$ and $MnSt_2$, and OlAc for Mn(OH)Ol and $MnOl_2$. Data for Mn(OH)Ol and $MnOl_2$ are in part taken from our previous work.[20]

It can be clearly seen that for $MnSt_2$ or $Mn_2(CO)_{10}$ in the presence of stearic acid, the boundary between MnO and α-MnS regions lies on the S:L = 1:1 line and it bisects the plot, whereas for Mn(OH)Ol or $MnOl_2$, the boundary is a straight line shifted towards the left side by about one unit [$S:(L_{free}+1) = 1:1$]. Mono-oleate precursors acts as the di-oleate despite the latter contains twice as oleate than the former. Accordingly, MnO formation is favored in the case of oleate precursors while stearate precursor tends to promote the α-MnS NCs. Generally, in both cases it is possible to state that pure α-MnS NCs were formed in sulfur-rich reactions (top-left of the plot) and pure MnO NCs in surfactant-rich reactions (bottom-right).

It was previously seen that the relatively stable *cyclo*-S_8 molecule (elemental sulfur) reacts at 180 °C with 1-octadecene to produce the more reactive specie H_2S (yield ≅ 2/3), which reacts with Cd-oleate to give CdS NCs.[33] It is reasonable to speculate that H_2S is the real sulfur source in the present case, too. Whereas, in CdS case it was established that the carboxylic acid did not react with H_2S, in our case the sulfur availability tends to decrease and surfactant concentration tends to increase. This behavior, suggests that reaction between RCOOH and H_2S occurs. For instance, it has been known that H_2S is able to convert RCOOH into the corresponding thioacid RC(O)SH.[34] This reaction would explain that the product does not significantly reacts with the Mn precursor. This idea also agrees with the slightly different behavior of StAc and OlAc [Figure *3*]. Since $MnSt_2$ decomposes at higher temperature (310-360 °C)[35] than Mn(II) oleate (250-320 °C)[36], it can be said that at the temperature of 320 °C, $MnSt_2$ decomposes and releases StAc more slowly than Mn(II) oleates so that an higher amount of sulfur is available for the formation of MnS NCs. Our synthesis is made at higher temperature (320 °C) and sulfur concentration (up to 1 M) than that of CdS reaction (180 °C, [S] = 0.01 M), which may favor the reaction of H_2S and RCCOH. Moreover, the possible catalytic activity of a d^5 such as Mn(II), in comparison to d^{10} Cd(II), should not be neglected.

Precursor	S:Mn	L:Mn [a]	NC type	Shape [b]	Median diameter (nm) [c]	Diameter std.deviation (nm) [c]
$Mn_2(CO)_{10}$						
	1:1	1:1	MnO / α-MnS	octahedron	12	1.7
		2:1	MnO	octahedron	12	1.4
		3:1	MnO	octahedron	17	3.1
	2:1	2:1	MnO / α-MnS	octahedron	10	1.8
		3:1	MnO	octahedron	12	1.8
		4:1	α-MnS	octahedron	23	3.8
				sphere	8	1.2
	4:1	2:1	α-MnS	sphere	40	8.9
		3:1	α-MnS	sphere	28	3.3
Mn(OH)Ol [d]						
	0:5	1:1	MnO	IRC	63 × 10	31.4 × 5.8
		4:1	MnO	octahedron	25	6.7
	1.7 :1	0.6:1	α-MnS	sphere	14	2.3
	2:1	0:1	α-MnS	sphere	17.5	2.3
	2.3 :1	0.6:1	α-MnS	sphere	14.7	2.7
		1:1	MnO / α-MnS	sphere	20	4.9
				octahedron	25	6
	3:1	0:1	α-MnS	sphere	18	2.4
	4:1	0:1	α-MnS	sphere	16	2.8
$MnOl_2$						
	0:1	3:1	MnO	spheroidal	6	1.8
		4:1	MnO	octahedron	72	19
	0.5:1	0:1	MnO	IRC	45	12.2
		1:1	MnO	octahedron	46	7.2
		2:1	MnO	quasi-sphere	20	2.8
		3:1	MnO	4-flower	54	12.8
				octahedron	53	12.3
				T-shape	53 × 47	12.3 × 12.2
		4:1	MnO	crosses	80	16.4
				T-shape	82 × 56	16.1 × 16.1
				6-flower	77	16
		6:1	MnO	sphere	23	18
				T-shape	71 × 43	22.5 ×22.3
				flower-like	71	19.1
		7:1	MnO	quasi-sphere	34 × 21	10.6 ×10.5
		8:1	MnO	sphere	12	2.8
	2:1	0:1	α-MnS	sphere	19	2.5
		1:1	MnO/α-MnS	sphere	24	2.0
	3:1	0:1	α-MnS	sphere	21.6	2.9
		1:1	MnO/α-MnS	sphere	7	0.7
				sphere	22	6.9
				octahedron	21.5	4.3
	4:1	0:1	α-MnS	sphere	21.5	3.6
		1:1	α-MnS	sphere	21.9	3.0

Precursor	S:Mn	L:Mn [a]	NC type	Shape [b]	Median diameter (nm) [c]	Diameter std.deviation (nm) [c]
MnSt2						
	0:5	0:1	MnO	IRC	55	9.2
		0:8	MnO	crosses	98	28.4
				T-shape	105 × 60	27.4 × 27.2
				rod	114	28.2
		1:1	MnO	crosses	80	24.3
				T-shape	79 × 45	24.5 × 24.4
				rod	73	21.7
		2:1	MnO	quasi-sphere	39	24.0
				T-shape	81 × 63	24.8 × 24.7
				rod	81	25.2
		3:1	MnO	IRC	25	5.9
		4:1	MnO	crosses	78	24
				T-shape	75 × 75	23.6 × 23.6
				rod	73	23.6
	2:1	0:1	α-MnS	quasi-sphere	65	9.9
				IRC	12 × 8	4 × 2
		1:1	α-MnS	quasi-sphere	7	1.2
		4:1	MnO/α-MnS	ellipse	31 × 23	4 × 3
	4:1	0:1	α-MnS	octahedron	29	8.7

[a] For $Mn_2(CO)_{10}$ and $MnSt_2$, L = stearic acid; for Mn(OH)Ol and $MnOl_2$, L = oleic acid.
[b] IRC = irregular, rounded, convex shape; quasi-sphere = shape very close to spherical.
[c] Both maximum and minimum values are shown for anisotropic shapes.
[d] Data are in part taken from our previous work.[20]

Table 1: Properties of NCs synthesized by the thermal decomposition of a manganese precursor in octadecene using different amounts of sulfur (S) and stearic acid (L).

The aim of this research is to study in detail the effect of the reagent type and concentration on the composition and above all polymorphism of the resulting NCs, and thus it was required that reactions be carried out using the same synthetic procedure. No effort was spent to investigate the NC size and shape because NC morphology was not the focus of our investigation. However, NC size and shape remain quantities of fundamental importance. Some preliminary synthesis of MnS NCs using different Mn : L molar ratios did not give interesting nanocrystals shapes.

An accurate description of the NC size and morphology is reported in the table [table

1]. Here, we can briefly summarize that MnO NCs (10-20 nm, dispersity 10-20%) usually show octahedral shape; α-MnS NCs are larger (10-65 nm), with higher dispersion (15-35%) and irregular convex shape.

Inspecting figure *3*, it is clear that the reaction with S:Mn = 2:1 and L:Mn = 4:1 yielded α-MnS NCs or a mixture of α-MnS and MnO NCs when using $Mn_2(CO)_{10}$ or $MnSt_2$, respectively. These results deviate from the previous diagonal boundary separating α-MnS and MnO regions. Thus, it was decided to further investigate the S:L:Mn = 2:4:1 reaction in detail selecting L from a wide set of long-chain aliphatic surfactants with different terminal groups.

7.2.2. How the free surfactant (L) directs the crystal structure of MnS NCs

Reaction parameters as temperature, time, solvent and molar ratio between reagents were fixed. In particular the reaction was carried out with S:Mn = 2:1 and L_{free}:Mn = 4:1, where L_{free} stands for a surfactant added to the reaction mixture. In a first series of reactions $MnSt_2$ was used as precursor and a wide range of long-chain aliphatic molecules with different terminal functional groups were employed to understand how basicity or nucleophilicity could affect the synthetic outcome. All results are summarized in the following table [table *2*] and selected ED patterns and TEM images are next displayed in figure [figure *4*]. Crystal structure of the MnS NCs was confirmed by HRTEM images [figure *2*].

The table shows that functionalities such as carboxylic acid, thiol and alcohol give α-MnS NCs, conversely several long-chain alkyl amines are all able to produce metastable γ-MnS NCs. Interestingly, also the reaction where a mixture of oleylamine and dodecanethiol (1:1 molar ratio) was used as surfactant, was able to produce γ-MnS nanoparticles.

The amine effect on the crystal structure, not sensitive to the amine chain length and insaturation, but could to be related to the basicity of amines, which is highest in our surfactant set.[37] On the other hand, nucleophilicity can be excluded because alkyl amines are less nucleophilic than sulfur compounds, such as dodecanethiol, that in our experiments induced the stable α-MnS crystals.[33] Similarly, the ability to undergo condensation reaction with carboxylic acids is probably not involved in the crystal control. In fact, oleylalcohol could also react with stearic acid to give the corresponding ester, as observed when long-chain ω-hydroxy carboxylic acids were used in similar conditions.[34] Regarding the size and shape of the γ NCs it is possible to summarize that they have irregular, rounded, convex (IRC) shape

with an aspect ratio of 1.4-1.5 for saturated amines with different sizes but, in the case of oleylamine, they can be described as 25 nm, almost spherical NCs. The mixed surfactant thiol/amine gave very broadly size-dispersed γ-MnS NCs.

L	NC type	Shape [a]	Size (nm) [b]	Std. dev. (nm)
Dodecylamine	γ-MnS	IRC	42 × 29	7 × 11
Hexadecylamine	γ-MnS	IRC	55 × 38	15 × 10
Octadecylamine	γ-MnS	IRC	55 × 38	12 × 9
Oleylamine	γ-MnS	IRC	27 × 20	10 × 8
OlAm/DdTh [c]	γ-MnS	IRC	10 - 200	large
None [d]	α-MnS	Spherical	65	10
		IRC	12 × 8	4 × 2
Oleylalcohol	α-MnS	IRC	12 × 8	3 × 2
Dodecanethiol	α-MnS	Octahedral	12	2
Stearic acid [d,e]	α-MnS	Spherical	7	1
	MnO	IRC	31 × 23	4 × 3

[a] IRC = irregular, rounded, convex shape
[b] Mean size; in the case of ellipsoidal NCs, the mean size of the major and minor axis are reported.
[c] Oleylamine : dodecanethiol mixture (1:1 mol/mol).
[d] Two morphological classes observed in TEM images.
[e] This sample also contains rare concave-shaped NCs.

Table 2: Properties of NCs synthesized by the thermal decomposition of $MnSt_2$ with S:Mn = 2 and L_{free}:Mn = 4

α-MnS NCs are in general smaller and with more regular shape than γ-MnS NCs. The octahedral shape of α-MnS NCs synthesized using L = DdTh is nicely confirmed by the intensity of the electron diffraction rings [figure *4*]: the anomalously intense 220 ring is evidence of the crystal texture produced by the octahedral NC shape.[20]

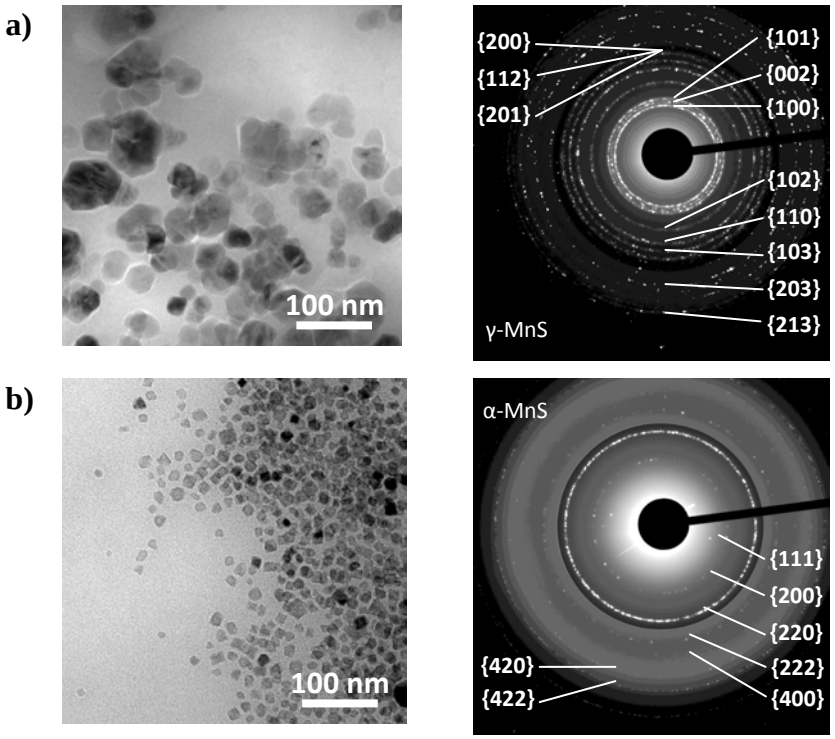

Figure 4: TEM images (left) and electron diffraction patterns (right) of NCs obtained by high temperature decomposition of $MnSt_2$ with S:Mn = 2 and L:Mn = 4. a) γ-MnS NCs synthesized using L = HdAm; b) α-MnS NCs synthesized using L = DdTh. The contrast of the outer part of both diffraction patterns was digitally increased to show high-index rings.

7.2.3. Role of stearate ligand in the precursor molecule

To understand these results, we deemed important to investigate the role of the stearate anion present in the precursor. Synthetic experiments similar to those reported in the previous table were carried out using $Mn_2(CO)_{10}$ as inorganic precursor and amines as free surfactants. Unexpectedly, only α-MnS NCs were obtained in all cases (few γ-MnS NCs were intermixed with a large amount of α-MnS NCs, when oleylamine was used as surfactant).

The γ-directing effect of amines on the crystal structure, observed with $MnSt_2$, vanished when $Mn_2(CO)_{10}$ was used instead of the carboxylate precursor. The role of the stearate contained in the precursor seems to be critical to achieve the γ-MnS NCs. The NCs produced from $Mn_2(CO)_{10}$ were smaller and with a lower aspect ratio than the corresponding ones from $MnSt_2$.

L	NC type	Shape [a]	Size (nm)	Std. dev. (nm)
Oleylamine	α-MnS (γ-MnS)	IRC	27 × 20	9 × 6
Dodecylamine	α-MnS	IRC	18 × 14	6 × 4
Hexadecylamine	α-MnS	IRC	22 × 16	4 × 3
Octadecylamine	α-MnS	IRC	20 × 14	4 × 3

[a] IRC = irregular, rounded, convex shape

Table 3: properties of NCs synthesized by the thermal decomposition of $Mn_2(CO)_{10}$ with S:Mn = 2 and L_{free}:Mn = 4

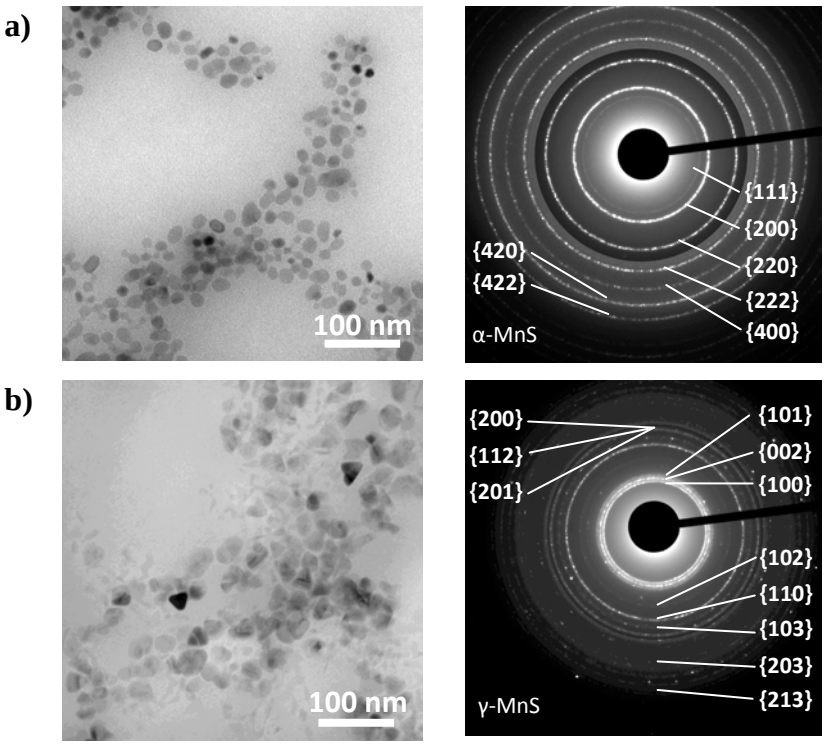

Figure 5: TEM images (left) and electron diffraction patterns (right) of NCs obtained by high temperature decomposition of $Mn_2(CO)_{10}$ with S:Mn = 2. a) α-MnS NCs synthesized using HdAm (L:Mn = 4); b) γ-MnS NCs synthesized using a mixture of StAc (L_{acid}:Mn = 2:1) and HdAm (L_{amine}:Mn = 4). The contrast of the outer part of both diffraction patterns was digitally increased to show the high-index rings.

To further investigate the role of stearate, we carried out a series of reactions where $Mn_2(CO)_{10}$ was decomposed using a mixture of free surfactants including, as above, an amine (L_{amine}:Mn = 4:1, L_{amine} = OlAm, DdAm, HdAm, OdAm) and a carboxylic acid in L_{acid}:Mn = 2:1 molar ratio (L_{acid} = StAc, OlAc). The S:Mn ratio was 2 as before. These reactions

mimicked the synthesis carried out using $MnSt_2$ in Subsection 7.2.2 despite that StAc here is present as free surfactant, not as carboxylate anion bound to the metal ion. The results are collected in the table *4* and TEM images and ED patterns are reported in figure *5*. γ-MnS NCs were produced when saturated amines were used as a surfactant. This demonstrates that both amine and stearic acid are required to direct the synthetic outcome towards γ-MnS NCs. The irregularly-shaped γ-MnS NCs are smaller than those prepared from $MnSt_2$ but have a similar aspect ratio (1.35 – 1.45).

L_{acid}	L_{amine}	NC type	Shape [a]	Size (nm)	Dev. Std. (nm)
Stearic acid	Oleylamine [b]	α-MnS	Spherical	33	6
			IRC	15 × 11	4 × 3
Stearic acid	Dodecylamine	γ-MnS	IRC	24 × 18	9 × 7
Stearic acid	Hexadecylamine	γ-MnS	IRC	30 × 21	7 × 5
Stearic acid	Octadecylamine	γ-MnS	IRC	35 × 24	10 × 7
Oleic acid	Hexadecylamine[b]	γ-MnS	Spherical	11	2
			Spherical	28	7

[a] IRC = irregular, rounded, convex shape
[b] Two morphological classes observed in TEM images.

Table 4: properties of NCs synthesized by the thermal decomposition of $Mn_2(CO)_{10}$ with S:Mn = 2 and using both amine and carboxylic-acid as a free surfactant ($L_{free,amine}$:Mn = 4:1, $L_{free,acid}$:Mn = 2:1)

In table [table *4*], oleylamine shows a peculiar behavior which could be due to the double bond present in its structure. A reaction with oleic acid and hexadecylamine was carried out to study the effect of the double bond on the carboxylic chain that could prevent the formation of a closely packaged coating. This reaction gave again γ-MnS NCs. The formation of the γ-MnS phase is related to the presence of both the functionalities, carboxylic acid and amine, like in the first series of reactions where stearic was present instead of the oleic acid used in this case. The particular behavior of oleylamine reported in the previous tables [table *3* and table *4*], could be due to the poor purity of commercially available OlAm (at best, technical grade 70%).[38]

From these data, it is clear that to prepare γ-MnS NCs starting from a solvothermal synthesis in 1-octadecene with elemental sulfur and a manganese carboxylate precursor, it is required

that both a carboxylic acid and a long chain aliphatic amine are present as surfactants, at least with molar ratio: $Mn:S:L_{free,acid}:L_{free,amine} = 1:2:2:4$. In all other tested cases only α-MnS NCs were formed. It is immaterial whether the carboxylic acid is added to the reaction as free surfactant or coordinated to the metal in the carboxylate precursor.

7.2.4. Attenuated Total Reflectance Infrared (ATR-IR) spectroscopy of MnS NCs

In order to obtain insight into the surfactant influence on the crystal polymorphism, ATR-IR spectra have been recorded from the most relevant samples. In particular, nanocrystals from the reactions using both $MnSt_2$ (L = HdAm, OlAm, DdTh, DdTh/OlAm, and StAc) and $Mn_2(CO)_{10}$ (L = HdAm, OlAm, StAc/HdAm, and StAc/OlAm) as a precursor have been tested.

We begin considering from reaction using $MnSt_2$ as a precursor. Both StAc and DdTh as precursors gave α-MnS NCs and their spectra are very similar. It is easy to see two $\nu_{as}(C=O)$ and $\nu_s(C=O)$ doublets of the carboxylate moiety located at 1564, 1552 and 1471, 1462 cm^{-1}, respectively and a $\nu(C=O)$ doublet of COOH group located at 1705 and 1699 cm^{-1}. These peaks indicate the presence of both stearate and StAc. Bands located at 1462 and 1564 cm^{-1} could be attributed to the M^{2+} stearates. The presence of a splitting of $\nu(C=O)$ bands of StAc and stearates is closely similar the so called Davydov splitting occurring in highly ordered structures such as Langmuir Blodgett films[39] and suggests that ordered layers formed on the NC surface. Some StAc molecules remained strongly adsorbed on the metal sulfide surface, despite several washing cycles. This behavior is in agreement with previous papers, e.g., Hironaka et al. reported on the ability of StAc to adsorb more strongly on sulfides nanoparticles (for example) FeS, rather than on oxides surfaces.[40] In NCs prepared by decomposing $MnSt_2$ with free DdTh, the presence of DdTh could be excluded by the absence of the characteristic peaks ascribable to DdTh. Moreover this spectrum is strongly similar to that of the NCs prepared in the presence of free StAc.

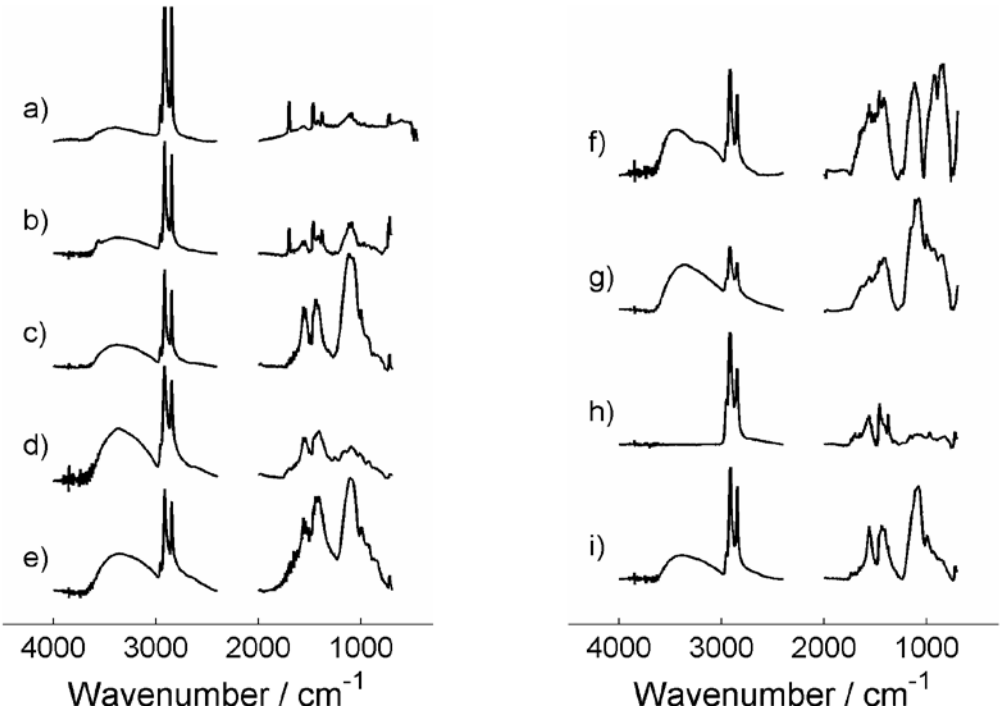

Figure 6: FTIR-ATR spectra of MnS NCs. Left: spectra of NCs prepared using $MnSt_2$ as a precursor with S:Mn = 2 and L:Mn = 4; L = StAc (a), DdTh (b), HdAm (c), OlAm (d), OlAm:DdTh 1:1 mixture (e). Right: spectra of NCs prepared using $Mn_2(CO)_{10}$ as a precursor with S:Mn = 2. Spectra (f) and (g) correspond to NCs prepared with amine surfactant only (L:Mn) = 4); L = HdAm (f), OlAm (g). Spectra (h) and (i) correspond to NCs prepared using a mixture of StAc (L_{acid}:Mn = 2:1) and amine surfactant (L_{amine}:Mn = 4); L_{amine} = HdAm (h), OlAm (i).

NCs synthesized from $MnSt_2$ using a free amine as a surfactant (yielding γ-MnS NCs) gave similar spectra where bands corresponding to both stearate and amine can be discerned. When OlAm or HdAm were used [figure *6*], the amines presence can be evidenced by the band located at 720 cm^{-1} due to the $\gamma_w(NH_2)$ wagging vibration,[41] while stearate produces two broad bands at 1551 and 1433 cm^{-1} due to ν_s and $\nu_{as}(C=O)$ of the carboxylate group. NCs appear to be coated with both surfactants. The presence of oleylammonium or hexadecylammonium stearate salts cannot be excluded though we were not able to find positive evidence. Furthermore, the spectrum of γ-MnS NCs prepared using a DdTh/OlAm mixture as surfactant is similar to that of NCs prepared using OlAm: peaks corresponding to

DdTh could not be detected. The thiol is not able to coat these nanocrystals when carboxylate is present.

NCs prepared using $Mn_2(CO)_{10}$ as a precursor have also been studied by ATR-IR.

The inorganic precursor decomposition in the presence of either HdAm or OlAm unexpectedly gave α-MnS NCs [figure *5*]. These samples show intense bands at 2955, 2920 and 2850 cm^{-1}, due to the by $\nu_{s,as}$ (C-H) vibrations of aliphatic CH_2 and CH_3 groups, and two complex system of bands located between 800-1200 and 1300-1700 cm^{-1}, respectively. These bands call the 1600-1300 cm^{-1} spectral region of pure OlAm and HdAm (1467: C-H bending, 1379: C-C deformation). Conversely, the 800-1200 region is not easily attributable to any vibration of pure amines. As predicted, these NCs are coated with the corresponding amine. The spectra of the nanocrystals synthesized from $Mn_2(CO)_{10}$ using the mixture StAc/HdAm (γ-MnS NCs) or StAc/OlAm (α-MnS NCs) [figure *6*] almost matched those observed for γ-MnS NCs prepared using $MnSt_2$ with HdAm or OlAm, respectively, in particular the spectral region between 1300-1600 cm^{-1}. When NCs were prepared with a mixture of stearate and amines, the formation of ammonium salts could not be excluded. It also is noteworthy that there is no clear difference between the final coating of α-MnS and γ-MnS NCs.

These spectroscopic results confirm that the presence of stearic acid as free surfactant or bound in the Mn precursor does not affect the resulting NC structure.

Curiously, even in the presence of insaturated compounds only, the C-H stretching of vinyl protons was not observed in the nanocrystal spectra. [figure *6*] This behavior has been already noticed, mainly when OlAc is involved. Probably it is due the disappearance of the C=C bond. Environmental effects that generate the shifting/broadening of the peak, can be ruled out since the vinyl C-H stretching could be detected in close-packed OlAc monolayers.[42]

ATR-IR spectroscopy gave some information about the ligands stably adsorbed on the NC surface. To summarize, NCs synthesized without amines show the presence of both stearic acid and stearate. Whereas, when stearic acid and an aliphatic amine were added in the reaction mixture, both stearates and amines could be detected. This is noteworthy since carboxylic acids (in the form of carboxylate anion) are usually able to remove amines from the surface of metal oxides and sulfides NCs. Unfortunately, despite these analysis, it is not evident a clear relationship between adsorbed species and polymorphism.

7.3. Conclusions

In this chapter it has been shown that the nature and the concentration of the surfactant and sulfur could affect the outcome of the final NC i.e., whether MnO or MnS NCs are obtained. The chemical composition (MnO *vs.* MnS) could be predicted depending on the S:Mn and L:Mn molar ratios. In particular, MnS is obtained when S:Mn is larger than L:Mn. Furthermore, an appropriate choice of the surfactant nature could allow for polymorphism control of the MnS NCs. When no or a single surfactant is present, α-MnS NCs are observed otherwise, when a 2:1 aliphatic amine : stearic acid mixture is used, γ-MnS NCs are obtained. No surfactant able to give β-MnS NCs was found. The α vs. γ crystal structure control is not affected by the details of the chemical structure of amine and carboxylic acid and whether the carboxylic acid is added as free surfactant or as bounded into the metal precursor is immaterial. The critical role of the amine seems to be related to its basicity. ATR-IR gave some information about the surfactants capping the final NCs. When NCs are prepared in absence of amines, they are capped by both stearic acid and stearate whereas, when an amine is added to the reaction mixture, both stearates and amines could be detected. To summarize, two main conclusions can be drawn: first, the carboxylic acid is equally effective when it is present as either carboxylate ligand in the precursor or free carboxylic acid. Indeed, when $Mn_2(CO)_{10}$ is heated in the presence of StAc, it is probable that the formation of a manganese stearate intermediate occurs, similarly to $Fe(CO)_5$ and oleic acid giving iron oleate intermediate in the solvothermal synthesis of iron oxide NCs.[43] Second, γ-MnS formation (that only occurs when a carboxylic acid is also present in the reaction mixture) seems to be related to the amine basicity. This suggests that monoalkylammonium carboxylate salts (R^1-NH_3^+ R^2-COO^-), (which are generated even in an apolar solvent such as cyclohexane)[41] may play an important role in the crystal structure control.

Unfortunately, ATR-IR could not confirm (nor exclude) that some long-chain ammonium stearates could be present on the final NC surface.

7.4. Experimental section

7.4.1. Synthesis of MnS nanoparticles[20]

Materials

Manganese(II) distearate, sulfur powder (99.98%), manganese decacarbonyl (98%), oleic acid (reagent grade, 90%), stearic acid (99%), oleylamine (technical grade 70%), dodecylamine (98%), hexadecylamine (90%), octadecylamine (≥99%), dodecanthiol (98%), oleylalcohol (≥ 85%), tryoctylphosphine (97%), and octadecene (purum ≥ 95.0%) were purchased from Sigma-Aldrich. Stearic acid (99%) was purchased from Calbiochem. All chemicals were used as received without further purification.

Procedure

The procedure to prepare MnS nanoparticles is as follows. In a two-necked flask, the precursor (0.26 mmol), was dissolved in octadecene giving a 0.25 M solution of the manganese precursor. Sulfur (0.52 mmol, 2 eq.), and a surfactant (1.04 mmol, 4 eq.) were added to the solution. The solution was heated to 320 °C (heating rate 10 °C/min) under nitrogen and magnetic stirring. After 1 hour, the reaction mixture was cooled to room temperature. The nanoparticles were precipitated by adding the reaction crude with a fivefold excess of ethanol and then collected by centrifugation (6000 rpm, 10 min). Next, the nanoparticles were washed with ethanol and collected by centrifugation (three times) and then washed with acetone and collected by centrifugation (three times). The precipitate was finally dispersed in hexane (5-10 mL) by sonication (ultrasonic bath, 1 h, RT). The obtained nanoparticles dispersions are stable for several months.

Several variants of this procedure were carried out by changing:

(i) the manganese precursor [$MnSt_2$ or $Mn_2(CO)_{10}$];

(ii) the sulfur:manganese S:Mn molar ratio (from 2:1 to 4:1);

(iii) the surfactant [L = stearic acid (StAc), oleic acid (OlAc), hexadecylamine (HdAm), dodecylamine (DdAm), octadecylamine (OdAm), oleylamine (OlAm), dodecanethiol (DdTh), trioctylphosphine (TOP), and oleylalcohol (OlAl)]; and

(iv) the surfactant:manganese L:Mn molar ratio (from 1:0 to 1:4).

Characterization

Conventional (medium resolution) transmission electron microscopy (TEM) images, high resolution TEM (HRTEM) images and electron diffraction (ED) patterns were recorded by a Zeiss LIBRA 200FE-HR TEM. Samples for microscopy were prepared by evaporating a drop of the nanoparticles dispersion in hexane on a carbon-coated TEM grid. Fourier-transform infrared (FTIR) spectra were collected by a Nexus Nicolet spectrometer. The FTIR spectra of NCs and solid surfactants were recorded using KBr pellets (sample:KBr *ca.* 1:100 w/w); for liquid surfactants, a drop of surfactant solution in hexane was deposited and evaporated on a pre-formed KBr pellet. Attenuated total reflectance - Fourier-transform infrared (ATR-FTIR) spectra (4 cm^{-1} resolution, 50 scans) were collected using an ATR platform (Golden Gate, Specac) mounted in a spectrophotometer (FTS-40, Biorad) equipped with a KBr beamsplitter and a MCT detector operating between 400 and 4000 cm^{-1}. In this case, the NCs were washed additional two times.

7.4.2. MnS nanoparticles conventional TEM images

TEM images and ED patterns of NCs prepared by thermal decomposition of manganese(II) distearate ($MnSt_2$) in the presence of sulfur (S) and different surfactants (L) with S:Mn = 2 and L:Mn = 4. Cfr. Table 2 in the main text.

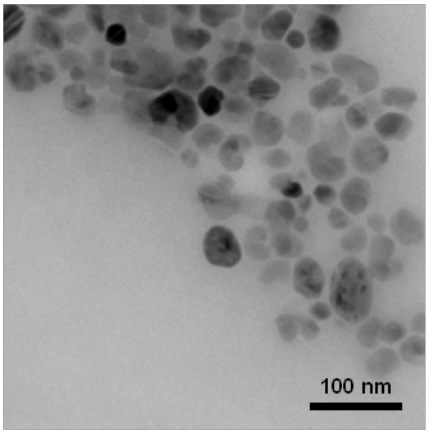

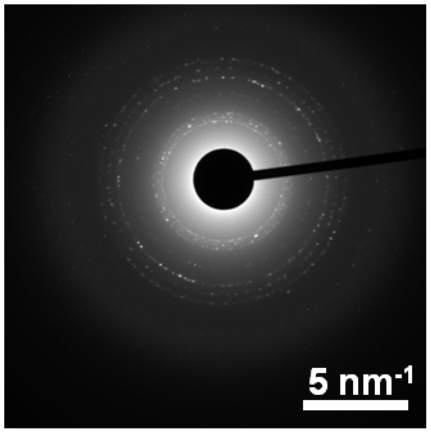

L = DdAm; outcome: γ-MnS NCs.

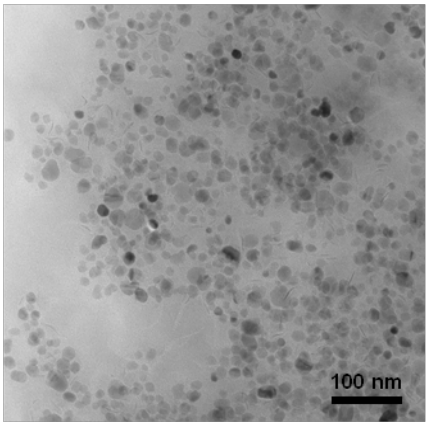

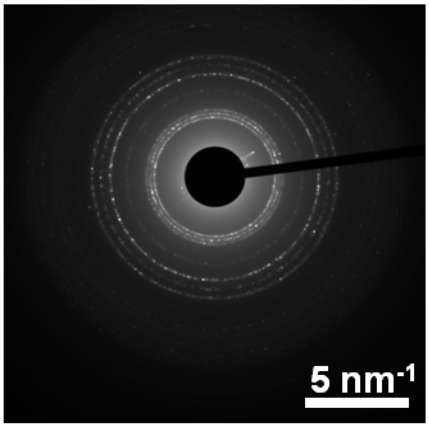

L = HdAm; outcome: γ-MnS NCs.

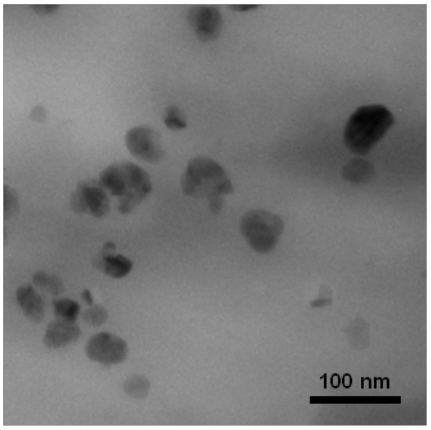

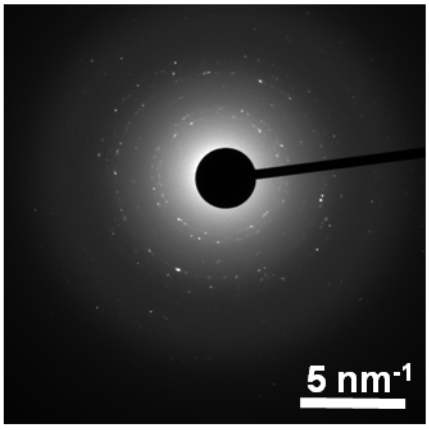

L = OdAm; outcome: γ-MnS NCs.

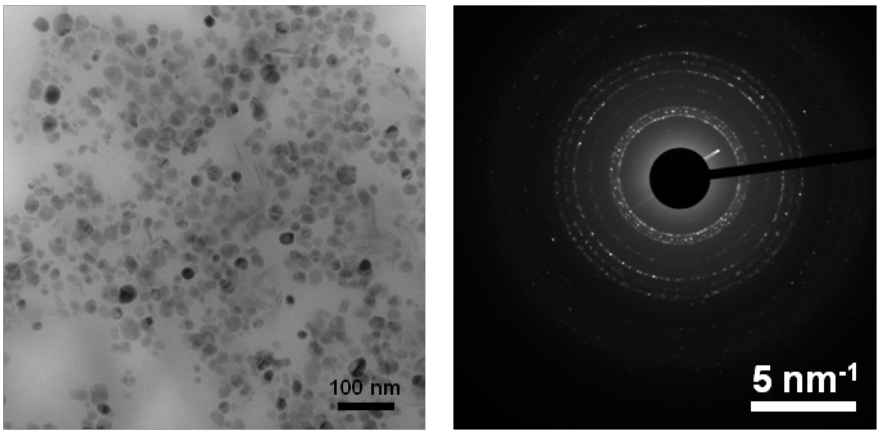

L = OlAm; outcome: γ-MnS NCs.

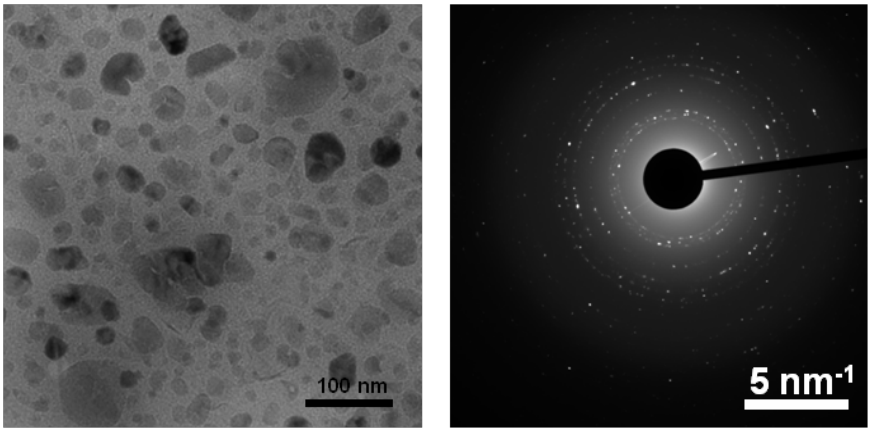

L = OlAm+ DdTh; outcome: γ-MnS NCs.

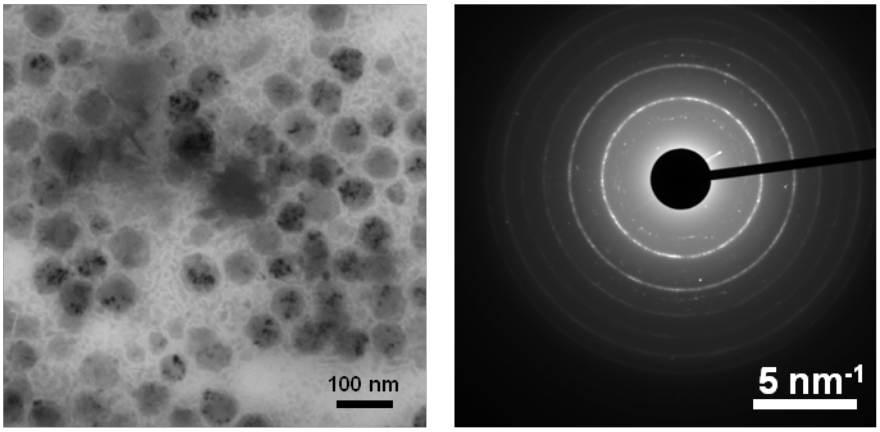

L = none; outcome: α-MnS NCs.

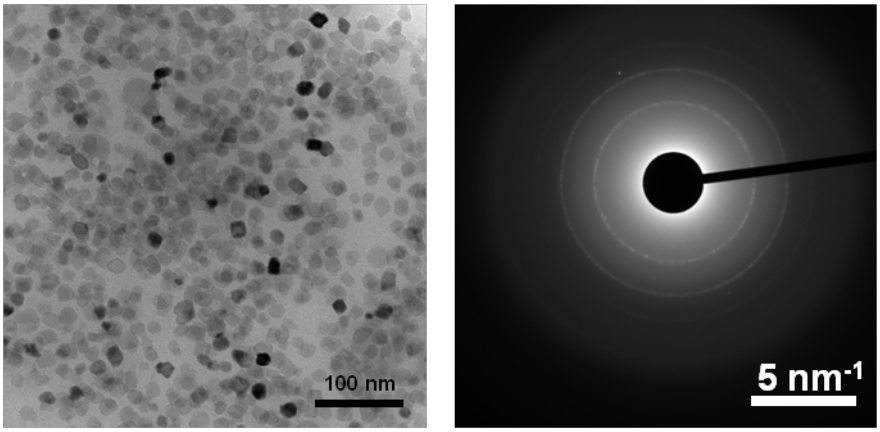

L = OlAlc; outcome: α-MnS NCs.

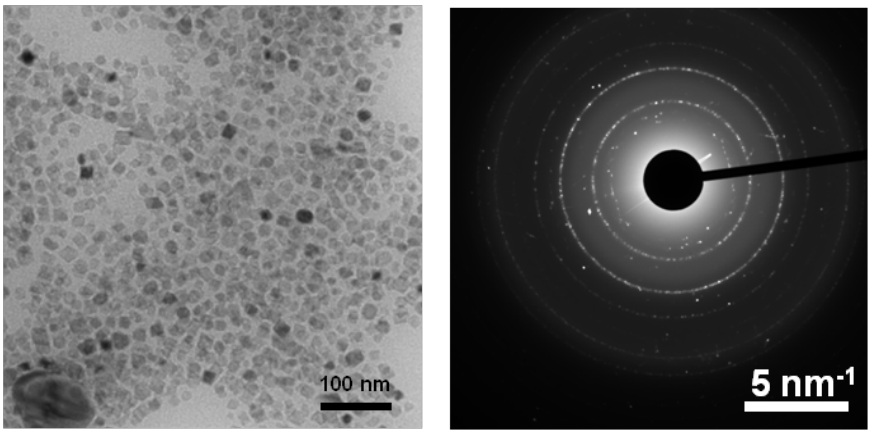

L = DdTh; outcome: α-MnS NCs.

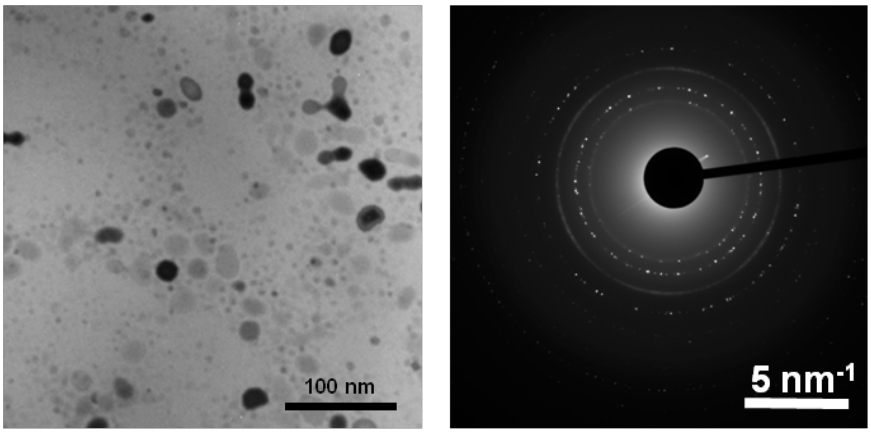

L = StAc; outcome: α-MnS NCs.

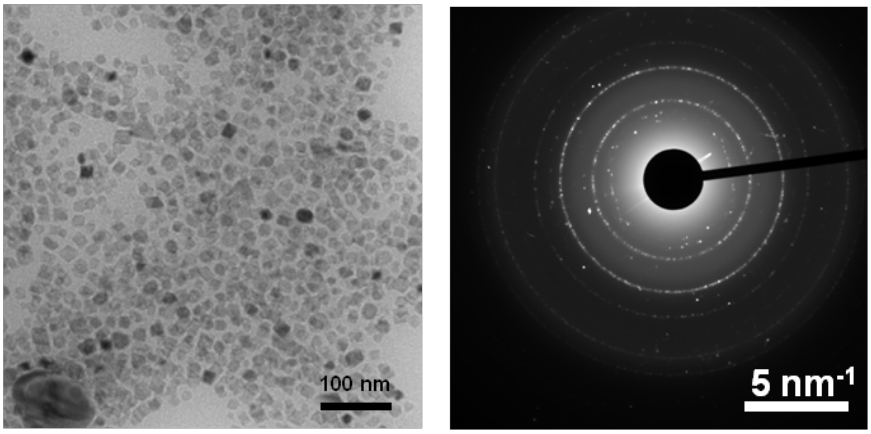

L = DdTh; outcome: α-MnS NCs.

TEM images and ED patterns of NCs prepared by thermal decomposition of manganese decacarbonyl [$Mn_2(CO)_{10}$] in the presence of sulfur (S) and different amine surfactants (L) with S:Mn = 2 and L:Mn = 4. Cfr. Table 3 in the main text.

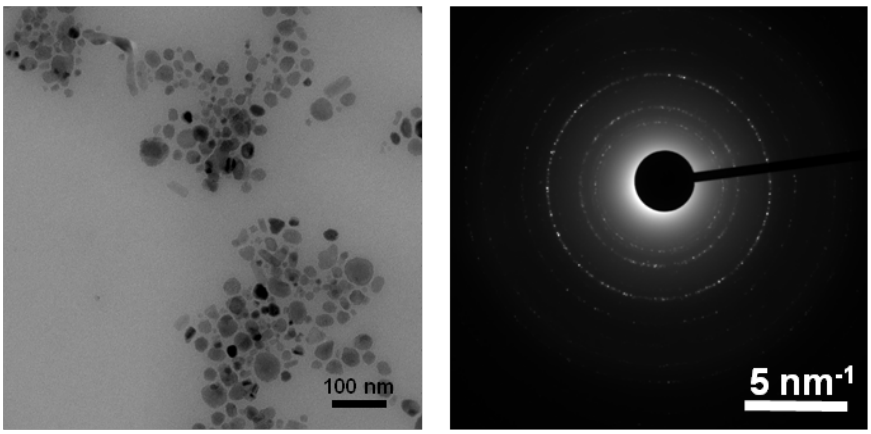

L = OlAm; outcome: α-MnS NCs.

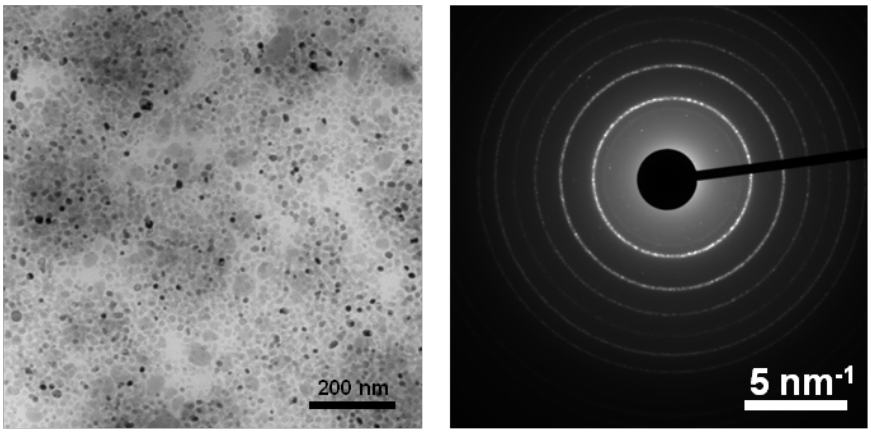

L = DdAm; outcome: α-MnS NCs.

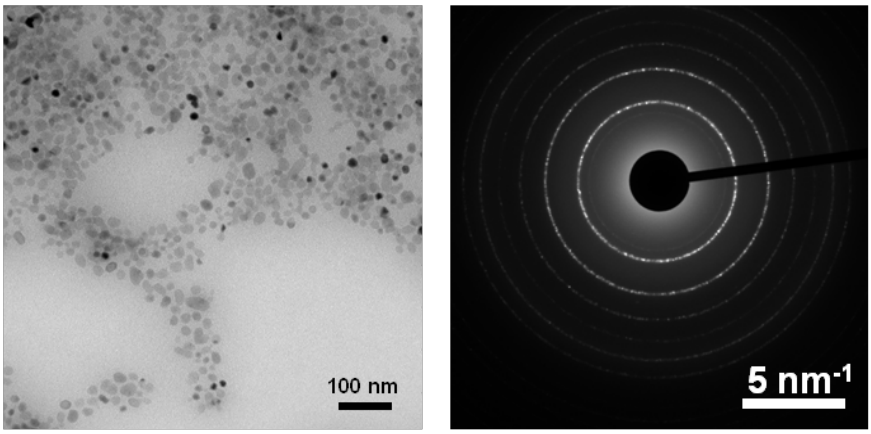

L = HdAm; outcome: α-MnS NCs.

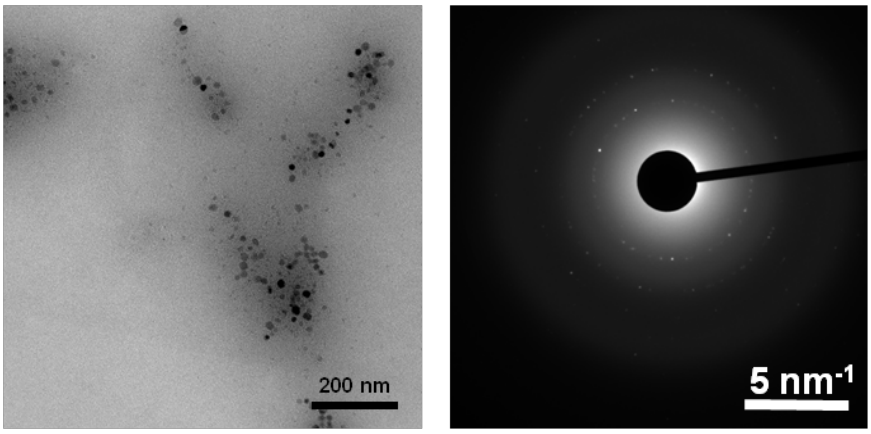

L = OdAm; outcome: α-MnS NCs.

TEM images and ED patterns of NCs prepared by thermal decomposition of manganese decacarbonyl [$Mn_2(CO)_{10}$] in the presence of sulfur (S) and a mixture of carboxylic acid (L_{acid}) and amine (L_{amine}) surfactants with S:Mn = 2, L_{acid}:Mn = 2 and L_{amine}:Mn = 4. Cfr. Table 4 in the main text.

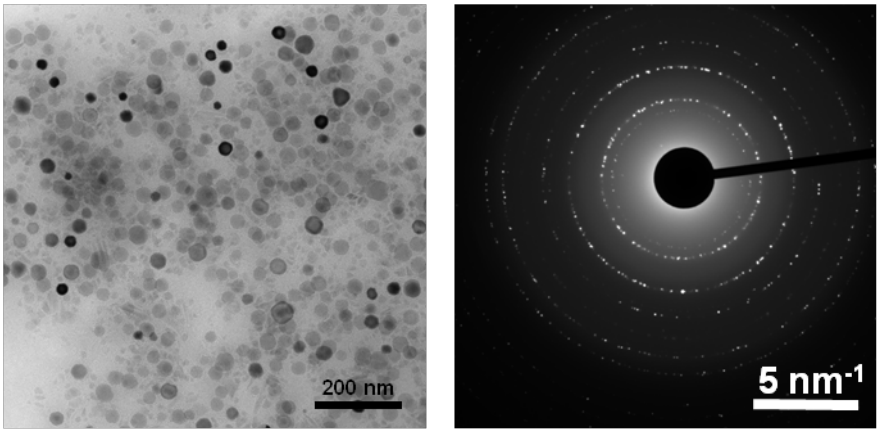

L_{amine} = OlAm, L_{acid} = StAc; outcome: γ-MnS NCs.

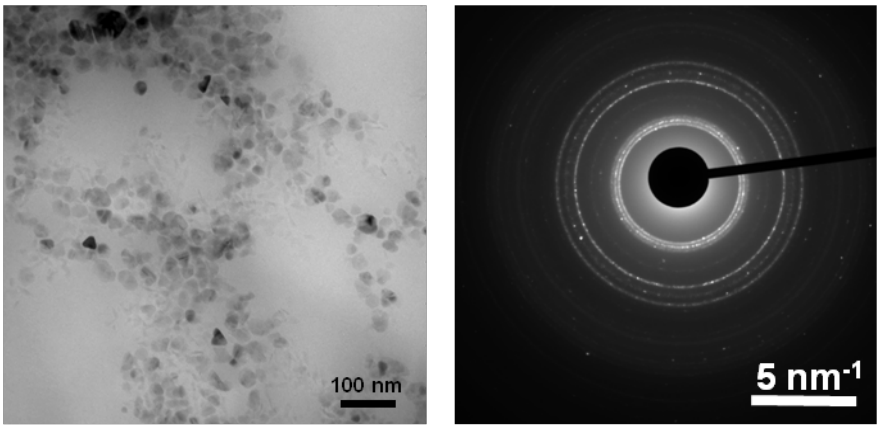

L_{amine} = HdAm, L_{acid} = StAc; outcome: γ-MnS NCs.

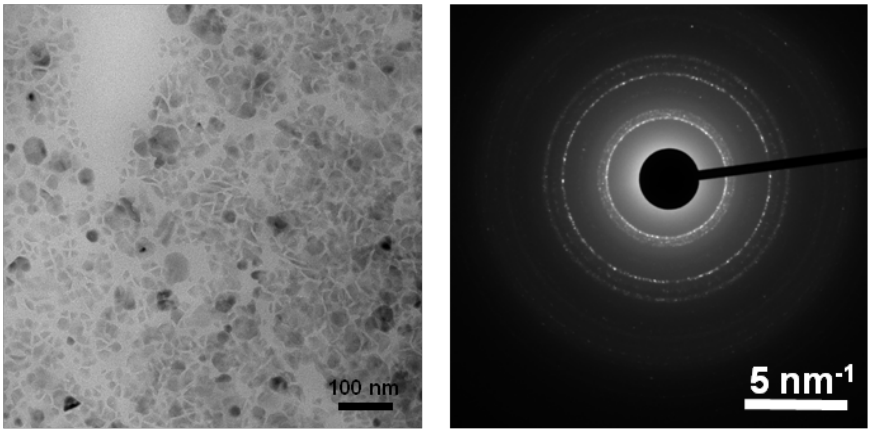

L_{amine} = DdAm, L_{acid} = StAc; outcome: γ-MnS NCs.

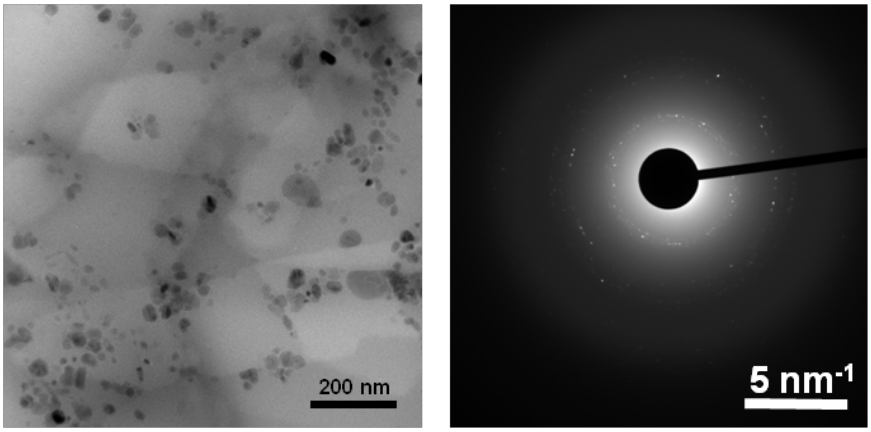

L_{amine} = OdAm, L_{acid} = StAc; outcome: γ-MnS NCs.

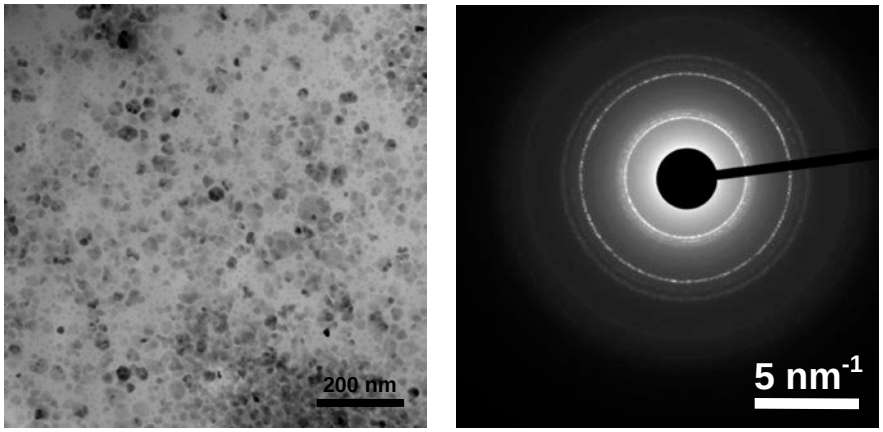

L_{amine} = HdAm, L_{acid} = OlAc; outcome: γ-MnS NCs.

7.4.3. MnS nanoparticles ATR spectra

Prec: $MnSt_2$ Surf: StAc

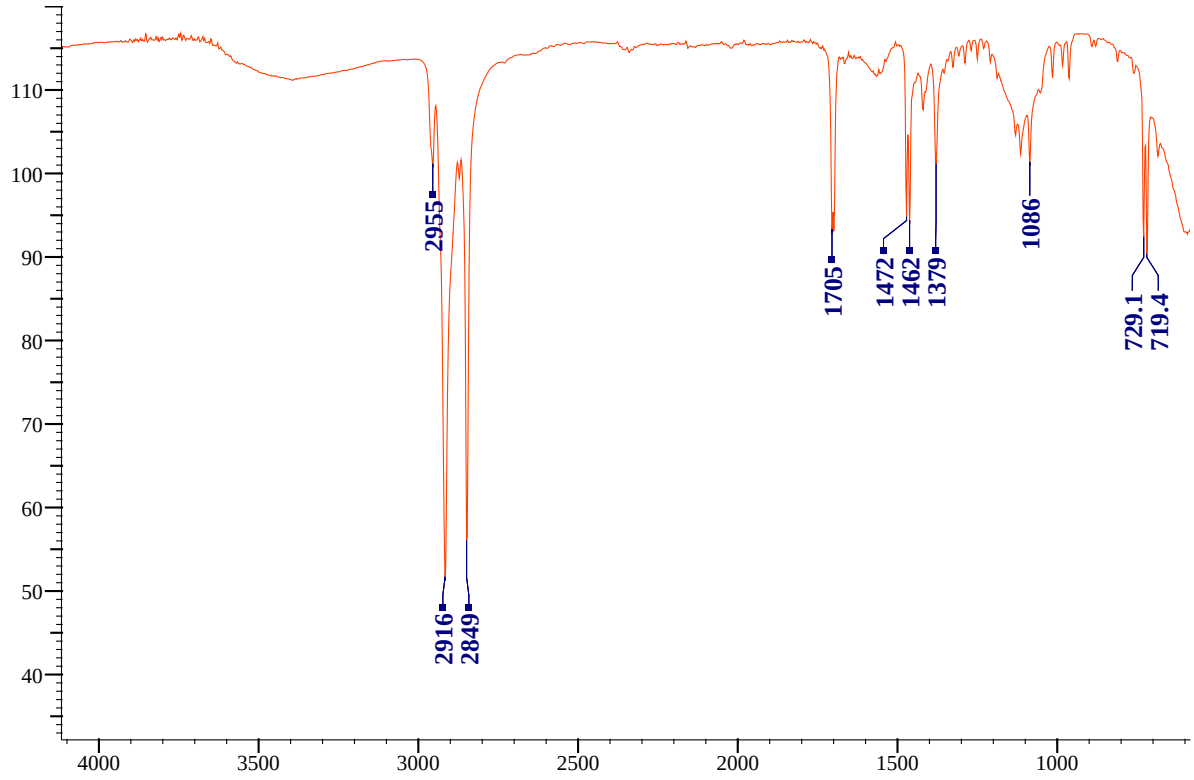

Prec: $MnSt_2$ Surf: OlAm

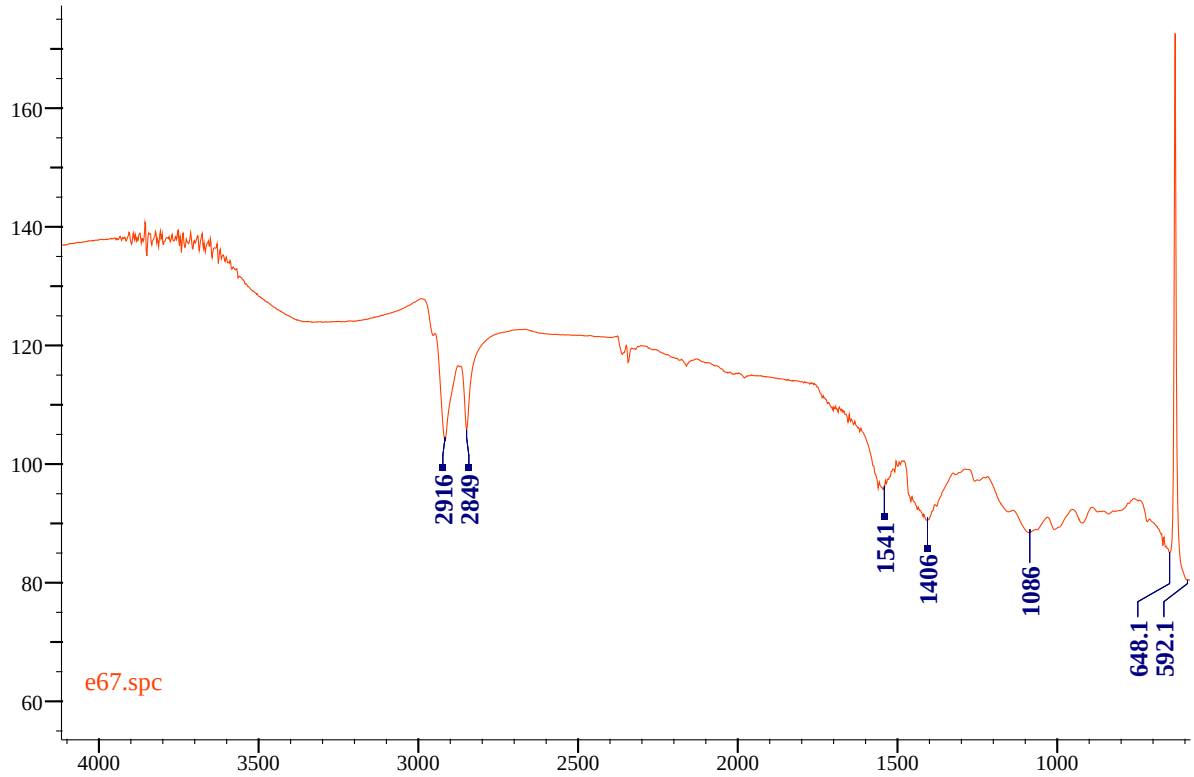

Prec: $MnSt_2$ Surf: HdAm

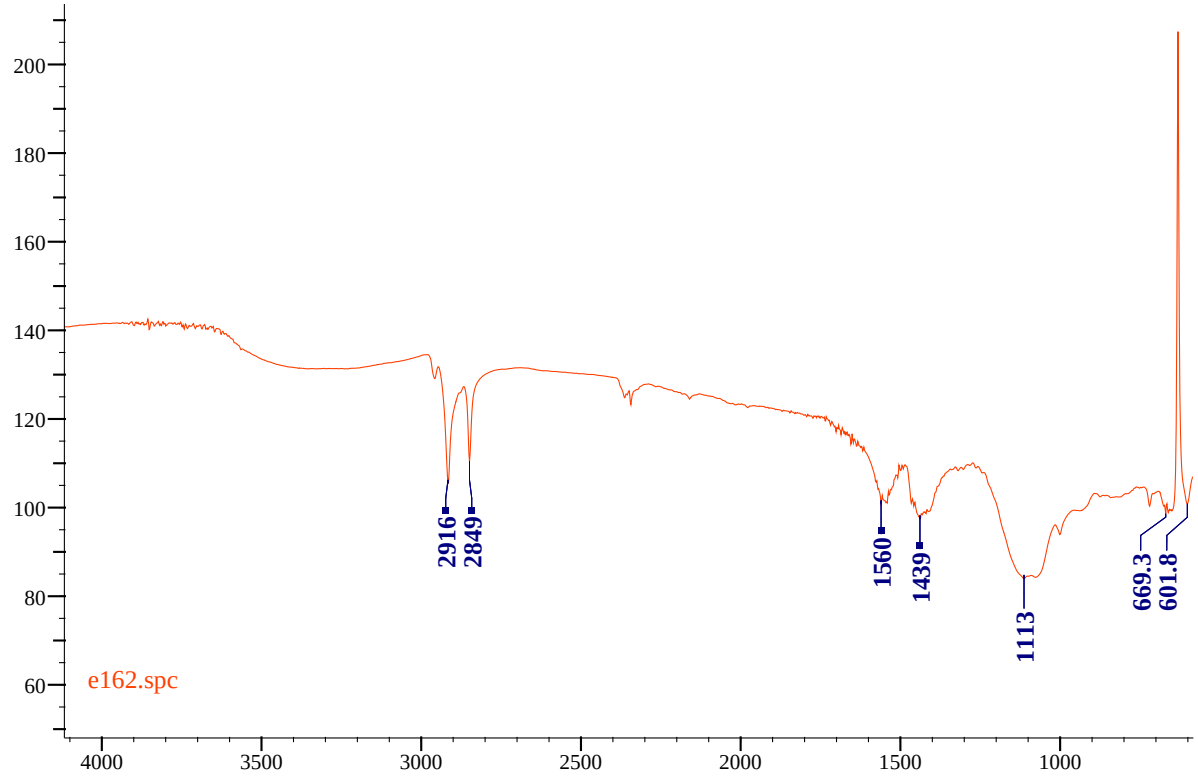

Prec: $MnSt_2$ Surf: DdTh

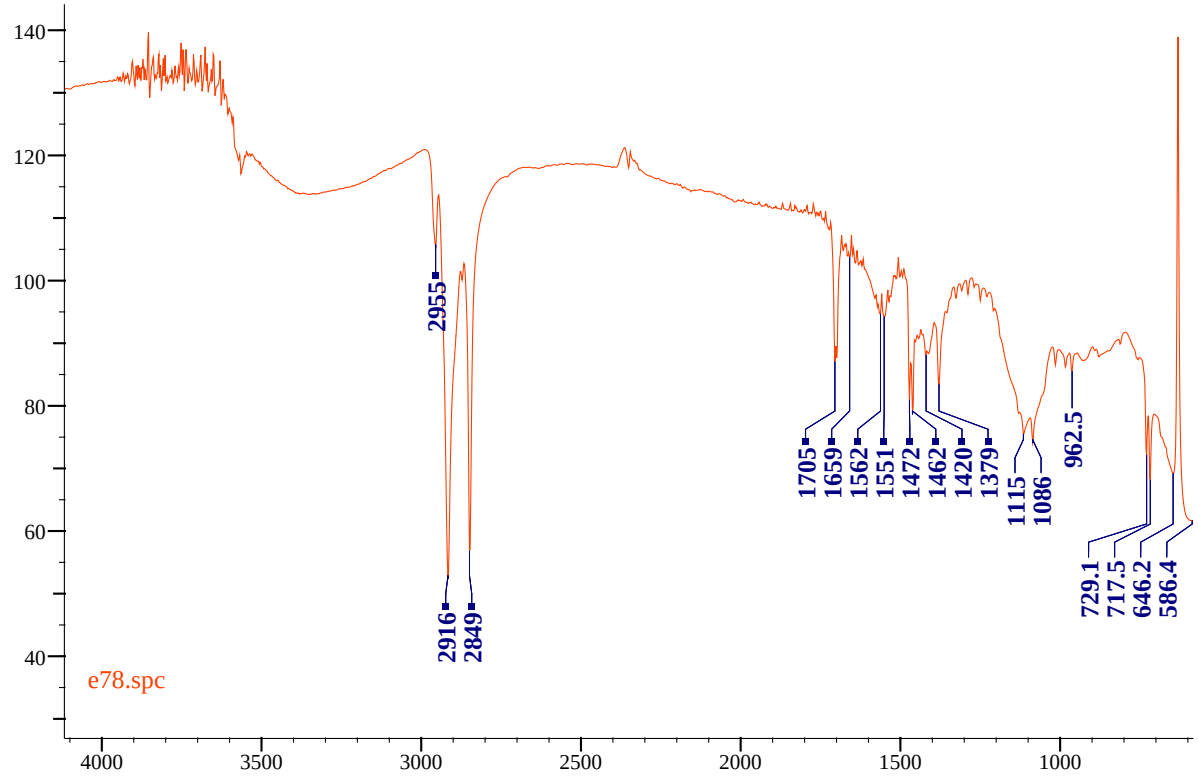

Prec: $MnSt_2$ Surf: OlAm + Ddth

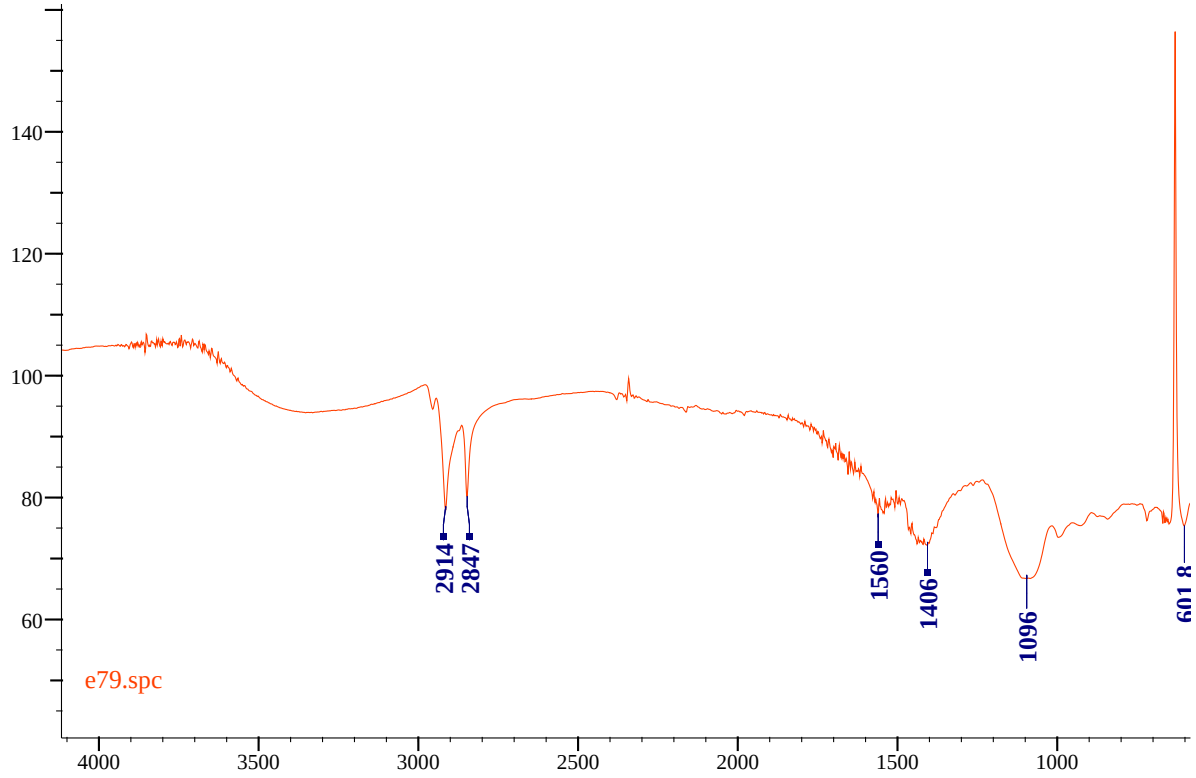

Prec: $MnSt_2$ Surf: OlAlc

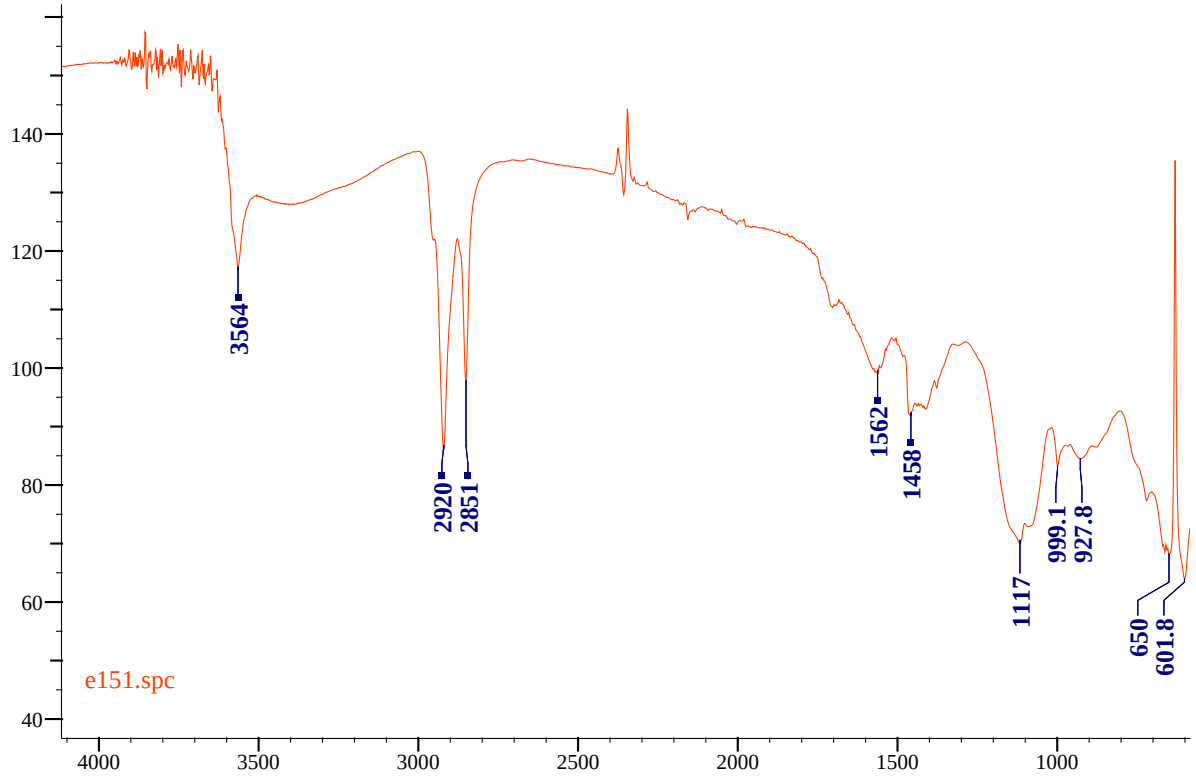

Prec: $Mn_2(CO)_{10}$ Surf: HdAm

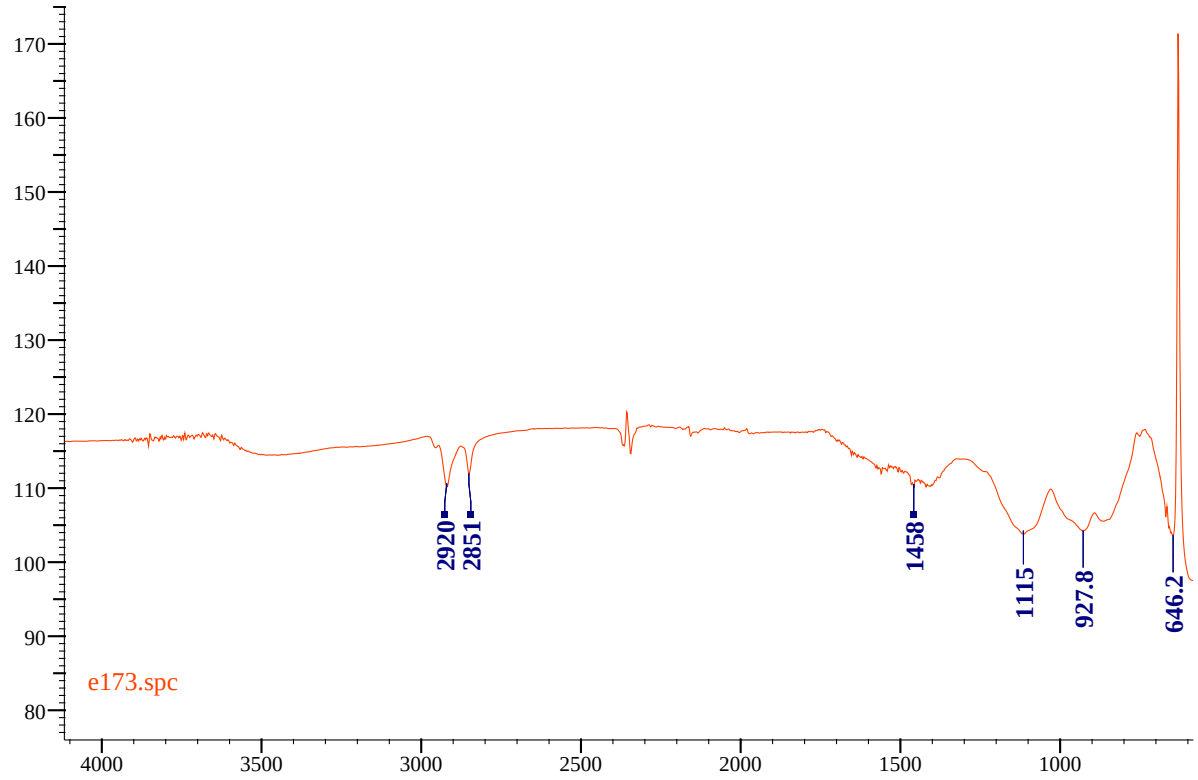

Prec: $Mn_2(CO)_{10}$ Surf: OlAm

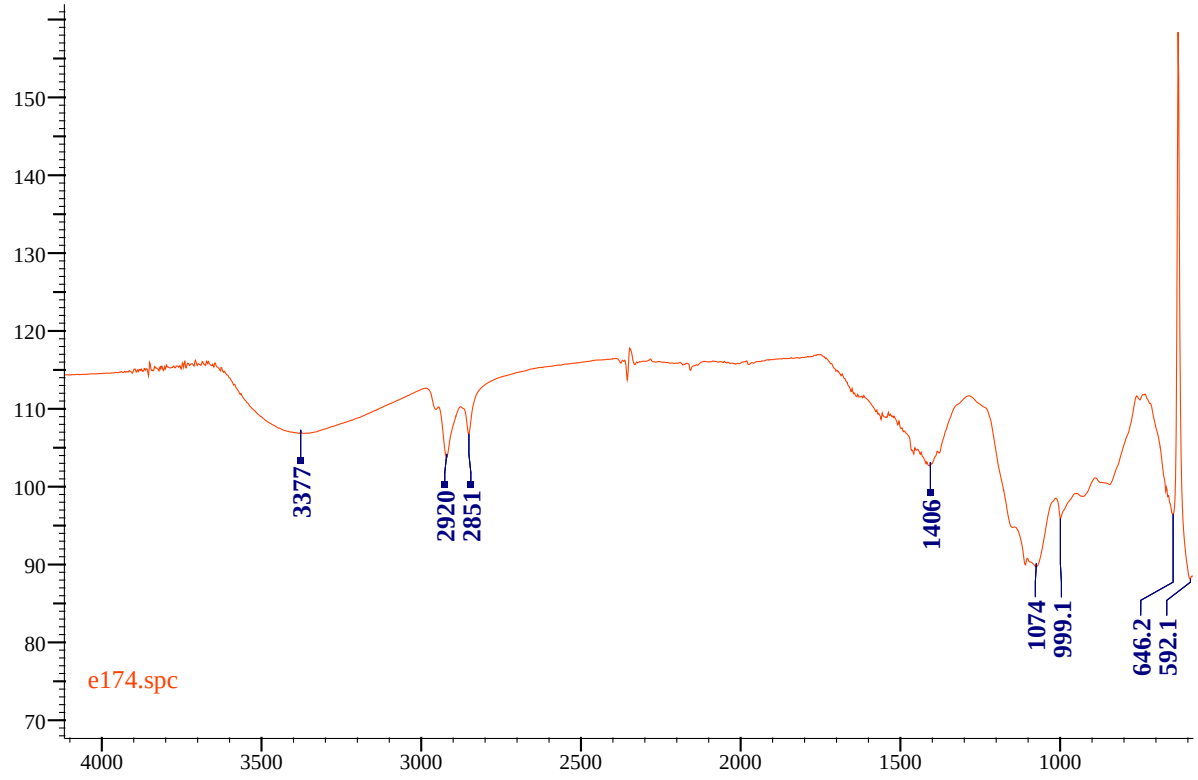

Prec: $Mn_2(CO)_{10}$ Surf: HdAm + StAc

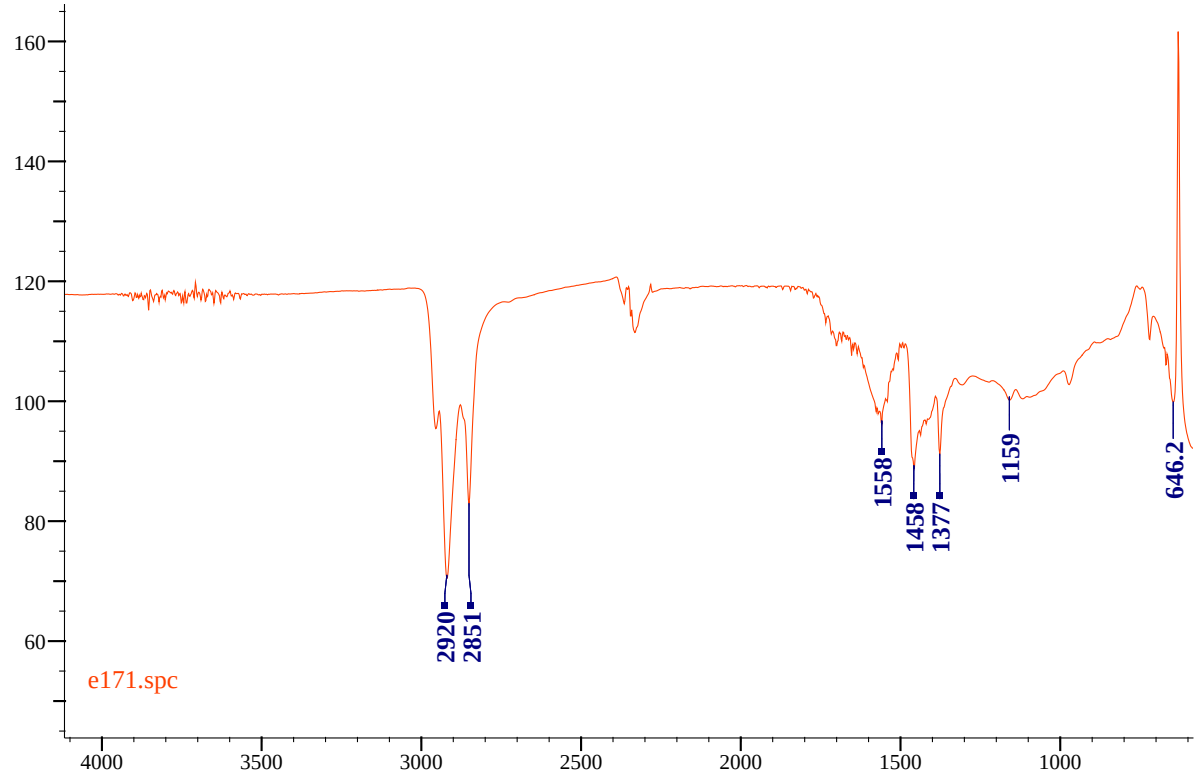

Prec: $Mn_2(CO)_{10}$ Surf: OlAm + Stac

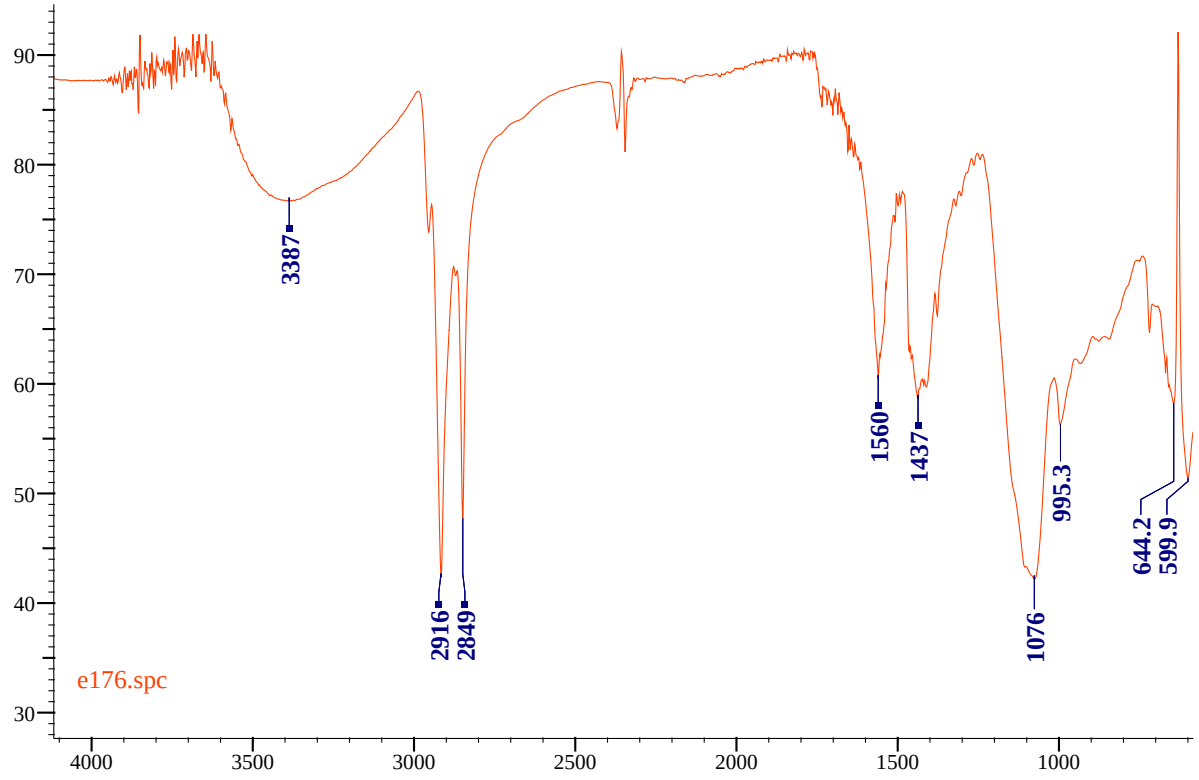

References

1. Yang, X. *et al.* Polymorphism and formation mechanism of nanobipods in manganese sulfide nanocrystals induced by temperature or pressure. *J. Phys. Chem. C* **116,** 3292–3297 (2012).

2. R I Hinesy, N L Allany, G. S. B. and W. C. M. An ab initio Hartree – Fock study of the magnetic states of the polymorphs of MnS. *J. Phys. Condens. Matter* **9,** 7105–7118 (1997).

3. Jun, Y., Jung, Y. & Cheon, J. Architectural control of magnetic semiconductor nanocrystals. *J. Am. Chem. Soc.* **124,** 615–619 (2002).

4. Papp, G. *History of minerals, rocks and fossil resins discovered in the Carpathian region, Hungarian Natural History Museum Budapest*. (2004).

5. Eriksson, L. & Mariusz, P. Mn1-xFexS, x= 0.05, an example of an anti-wurtzite structure. *Acta Crystallogr. Sect. E* **E57,** 92–93 (2001).

6. Ma, L. Y. *et al.* NiO-thickness dependent magnetic anisotropies in Fe / NiO / Au (001) and Fe / NiO / MgO (001) systems. *J. Magn. Magn. Mater. Mater.* **324,** 528–533 (2012).

7. Corliss, L., Elliott, N. & Hastings, J. Magnetic Structures of the Polymorphic Forms of Manganous Sulfide. *Phys. Rev.* **104,** (1956).

8. STEVENS, B. A. Danielian. A. K. W. H. Exchange Interactions in the Polymorphic Forms of MnS. *proc. phys. soc* 124–128 (1961).

9. Viswanath, R.; Naik, H. S. B.; Kumar, G. S. Y.; Kumar, P. N. P.; Harish, K. N.; Prabhakara, M. C. Luminescence properties of blue-red emitting multilayer coated single structure ZnS/MnS/ZnS nanocomposites. *Spectrochim. Acta, Part A* **125,** 222–227 (2014).

10. Zhang, X. V, Martin, S. T., Friend, C. M., Schoonen, M. A. A. & Holland, H. D. Mineral-Assisted Pathways in Prebiotic Synthesis : Photoelectrochemical Reduction of Carbon (+ IV) by Manganese Sulfide. *J. Am. Chem. Soc.* 12503–12507 (2004).

11. Beltran-Huarac, J.; Resto, O.; Carpena-Nunez, J.; Jadwisienczak, W. M.; Fonseca, L. F.; Weiner, B. R.; Morell, G. Crystal gamma-MnS Nanowires Conformally Coated with Carbon. *ACS Appl. Mater. Interfaces* **6,** 1180–1186 (2014).

12. Tang, Y., Chen, T. & Yu, S. Morphology controlled synthesis of monodispersed manganese sulfide nanocrystals and their primary application in supercapacitors with high performances. *Chem. Commun.* **51,** 9018–9021 (2015).

13. Ge, J. P.; Li, Y. D. Controllable CVD route to CoS and MnS single-crystal nanowires. *Chem. Commun.* 2498–2499 (2003).

14. Ge, J. P.; Wang, J.; Zhang, H. X.; Li, Y. D. A General Atmospheric Pressure Chemical Vapor Deposition Synthesis and Crystallographic Study of Transition-Metal Sulfide One-Dimensional Nanostructures. *Chem. Eur. J.* **10,** 3525–3530 (2004).

15. Kim, D. S.; Lee, J. Y.; Na, C. W.; Yoon, S. W.; Kim, S. Y.; Park, J.; Jo, Y.; Jung, M. H. Synthesis and Photoluminescence of Cd-doped α-MnS Nanowires. *J. Phys. Chem. B* **110,** 18262–18266 (2006).

16. An, C. *et al.* Hydrothermal preparation of α-MnS nanorods from elements. *J. Cryst. Growth* **252,** 575–580 (2003).

17. Gui, Y., Qian, L. & Qian, X. Hydrothermal synthesis of uniform rock salt (α-) MnS transformation from wurtzite (γ-) MnS. *Mater. Chem. Phys.* **125,** 698–703 (2011).

18. Mu, J. *et al.* Phase and shape controlling of MnS nanocrystals in the solvothermal process. *J. Nanoparticle Res.* **10,** 197–201 (2008).

19. Moloto, N., Moloto, M. J., Kalenga, M., Govindraju, S. & Airo, M. Synthesis and characterization of MnS and MnSe nanoparticles: Morphology, optical and magnetic properties. *Opt. Mater. (Amst).* **36,** 31–35 (2013).

20. Puglisi, A. *et al.* Monodisperse Octahedral alpha -MnS and MnO Nanoparticles by the Decomposition of Manganese Oleate in the Presence of Sulfur. *Chem. Mater.* 2804–2813 (2010).

21. Tian, Q. *et al.* Large-scaled star-shaped a -MnS nanocrystals with novel magnetic properties. *ChemComm* 8100–8102 (2011).

22. Yang, X. *et al.* Size-controlled synthesis of bifunctional magnetic and ultraviolet optical rock-salt mns nanocube superlattices. *Langmuir* **28,** 17811–17816 (2012).

23. Peng, L., Shen, S., Zhang, Y., Xu, H. & Wang, Q. Journal of Colloid and Interface Science Controllable synthesis of MnS nanocrystals from a single-source precursor. *J. Colloid Interface Sci.* **377,** 13–17 (2012).

24. Kan, S. H.; Felner, I. . B. Synthesis, Characterization and Magnetic Properties of a-MnS Nanocrystal. *U. Isr. J. Chem.* **41,** 55–61 (2001).

25. Pradhan, N.; Katz, B.; Efrima, S. Synthesis of High-Quality Metal Sulfide Nanoparticles from Alkyl Xanthate Single Precursors in Alkylamine Solvents. *J. Phys. Chem. B* **107,** 13843–13854 (2003).

26. Tian, L.; Yep, L. Y.; Ong, T. T.; Yi, J.; Ding, J.; Vittal, J. Synthesis of NiS and MnS Nanocrystals from the Molecular Precursors (TMEDA)M(SC{O}C6H5)(2) (M = Ni, Mn). *J. Cryst. Growth Des.* **9,** 352–357 (2009).

27. Wang, D. S.; Zheng, W.; Hao, C. H.; Peng, Q.; Li, Y. D. A Synthetic Method for Transition-Metal Chalcogenide Nanocrystals. *Chem. Eur. J.* **15,** 1870–1875 (2009).

28. Joo, J. *et al.* Generalized and facile synthesis of semiconducting metal sulfide nanocrystals. *J. Am. Chem. Soc.* **125,** 11100–5 (2003).

29. Zhang, H., Hyun, B. R., Wise, F. W. & Robinson, R. D. A generic method for rational scalable synthesis of monodisperse metal sulfide nanocrystals. *Nano Lett.* **12,** 5856–5860 (2012).

30. Choi, S. H.; An, K.; Kim, E. G.; Yu, J. H.; Kim, J. H.; Hyeon, T. Simple and Generalized Synthesis of Semiconducting Metal Sulfide Nanocrystals. *Adv. Funct. Mater.* **19,** 1645–1649 (2009).

31. Shannon, B. Y. R. D. *et al.* Revised Effective Ionic Radii and Systematic Studies of Interatomie Distances in Halides and Chaleogenides. *Acta Cryst A* **A32,** 751–767 (1976).

32. Hÿtch, M. J.; Snoeck, E.; Kilaas, R. Quantitative measurement of displacement and strain Þelds from HREM micrographs. *Ultramicroscopy* **74,** 131–146 (1998).

33. Mayr, H.; Ofial, A. R. Do general nucleophilicity scales exist? *J. Phys. Org. Chem.* **21,** 584–595 (2008).

34. Mondini, S.; Cenedese, S.; Marinoni, G.; Molteni, G.; Santo, N.; Bianchi, C. L.; Ponti, A. One-step synthesis and functionalization of hydroxyl-decorated magnetite nanoparticles. *J. Colloid Interface Sci.* **322,** 173–179 (2008).

35. Maryudi. Synthesis and characterization of manganese carboxylates. *J. Appl. Sci.* **9,** 3156–3160 (2009).

36. Pan, D.; Senpan, A.; Caruthers, S. D.; Williams, T. A.; Scott, M. J.; Gaffney, P. J.; Wickline, S. A.; Lanza, G. M. Sensitive and efficient detection of thrombus with fibrin-specific manganese nanocolloids. *Chem. Commun.* 3234–3236 (2009).

37. Laurence, C.; Gal, J.-F. *Lewis Basicity and Affinity Scales: Data and Measurement; John Wiley & Sons*. (2010).

38. Mourdikoudis, S. & Liz-marza, L. M. Oleylamine in Nanoparticle Synthesis. *chem mater* **25,** 1465–1476 (2013).

39. Baran, J.; Marchewka, M. K.; Ratajczak, H.; Borovikov, A. Y.; Byckov, V. N.; Naumovets, A. G.; Podzelinsky, A. V.; Puchkovskaya, G. A.; Styopkin, V. I. Investigation of stearic acid and manganese stearate films obtained by Langmuir-Blodgett and vacuum deposition methods. *Thin Solid Films* **254,** 229–239 (1995).

40. Hironaka , S.; Y. Yahagi, Y.; Sakurai, T. Effect of adsorption of some surfactant on antiwear properties. *A S L E Trans.* **21,** 231–235 (1978).

41. Klokkenburg, M., Hilhorst, J. & Erne, B. H. Surface analysis of magnetite nanoparticles in cyclohexane solutions of oleic acid and oleylamine. *vib. spectrosc* **43,** 243–248 (2007).

42. Dluhy, R. A.; Cornell, D. G. In situ measurement of the infrared spectra of insoluble monolayers at the air-water interface. *J. Phys. Chem.* **89,** 3195–3197 (1985).

43. Hyeon, T.; Lee, S. S.; Park, J.; Chung, Y.; Na, H. B. Synthesis of Highly Crystalline and Monodisperse Maghemite Nanocrystallites without a Size-Selection Process. *J. Am. Chem. Soc.* **123,** 12798–12801 (2001).

8. MnO@FeOx Core-Shell Nanoparticles

8.1. Introduction

In the field of nanoscience and nanotechnology there is a current effort to develop novel multifunctional materials that are able to simultaneously perform different functions.[1] In this contest, it is important to study the chemical and physical properties of multifunctional homogeneous NPs but it is even more important to design and implement new hybrid multicomponent NPs, which are very attractive since they combine the properties of each component thus enabling unprecedented applications.[2] In particular, magnetic core-shell NPs could be applied in many fields: magnetic recording media (enhanced blocking temperature), hard magnets (increased energy products), electromagnetic interference shielding (superior microwave absorption), magnetoresistive devices (enhanced magnetoresistance after field cooling), magnetocaloric materials, magnetic resonance amplifiers, catalysis, biomedical applications[3] (hyperthermia, magnetic resonance imaging, protein separation, specific cell targeting, and drug delivery[1] or sensing applications.[2]

Coupling different materials can be very useful to, e. g., combine optically active materials (such as gold, silver) or semiconductor material.[1] In particular, interface coupling between magnetically ordered materials is a very promising tool to control and tune the magnetic properties. In 1956 Meiklejohn and Bean, studying Co@CoO NPs, discovered that, after field cooling below the CoO Néel temperature (T_N), the hysteresis loop was shifted to the negative field direction. Such effect, called exchange bias (EB), arises from the exchange coupling between a ferromagnetic (FM) material (large exchange integral, low anisotropy) and an antiferromagnetic (AFM) material (small exchange integral, high anisotropy). It was later proposed that exchange coupling could be used to beat the superparamagnetic limit[4] in core-shell NPs comprising a ferro- or ferri-magnetic shell and an AFM core (or viceversa).[5] As anticipated, the FM/AFM coupling induces the shift of the hysteresis loop known as exchange-bias. At the interface, the moments of the FM material are exchange-coupled with the moments of the AFM material (below T_N). The antiferromagnetic spins are characterized by a very high anisotropy and remain fixed in space even when a moderately high magnetic field is applied in the opposite direction.

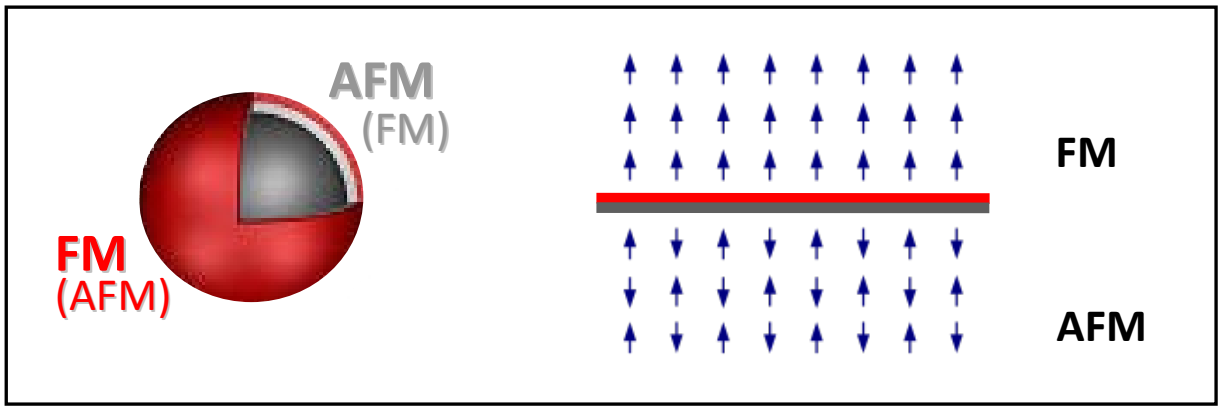

Figure 1: scheme of a generic core-shell structure and representation of a possible spin configuration at the interface between the two exchange-coupled materials featuring the exchange-bias effect.

Thus, during an hysteresis loop, under the action of a magnetic field opposed to the cooling field, the effective anisotropy of the FM component is increased at the interface and the FM spins have to overcome a higher energy barrier to reverse their orientation. Conversely, returning the FM magnetization along the preferred orientation (along the cooling field) is easier and requires a less positive applied field.

The increase in coercivity of the magnetization curve is also attributed to the AFM/FM coupling and probably originates from uncompensated interfacial spins in the antiferromagnetic part. Generally, most of the magnetization is due to the FM (or FiM) component and the role of the AFM constituent is to keep the moment fixed in space.[6] In this way, NPs with blocked magnetization at room temperature can be obtained.[5] The exchange coupling can be a key tool to obtain NP with the desired magnetic properties, useful for biomedical and technological applications. In fact, the magnetic properties of transition metal oxide NPs are highly dependent on their size, oxidation state, crystal structure,[7] shape, surface-volume ratio, composition, and interfacial characteristics.[5] In particular, size is a major factor affecting magnetic moment and magnetocrystalline anisotropy energy, the latter being a critical quantity to be optimized to obtain nanomaterials with magnetic stability at room temperature.[5] Moreover, the recent progress in wet chemistry NP synthesis allows one to fine control the structural parameters of core-shell systems, which are critical to obtain the desired exchange coupling.[2]

To prepare core-shell NPs with appealing magnetic properties (e. g, large interfacial exchange coupling and RT magnetic stability), it is required to couple an antiferromagnetic

material with a ferro- or ferri- magnetic one. In principle, it is immaterial whether the core is AFM and the shell FM or viceversa in order to observe exchange bias.

As to the antiferromagnetic material we used as a core, manganese monoxide (MnO) is a well-known material. As other binary oxides, (such as FeO, NiO and CoO), bulk MnO exhibits antiferromagnetic behaviour below 116 K, but a FM-like component is observed at the nanoscale level. This is due to the uncompensated spins on the NPs surface which carry a measurable net magnetic moment. As is well known, the relative contribution of this FM-like component of AFM NPs grows when the particle size is reduced (because surface/volume ratio increases with decreasing particle size).[1] On the other hand, for the ferro-/ferri-magnetic material is preferable to choose a material which exhibits high magneto-crystalline anisotropy, high saturation magnetization, as well as high maximum energy product.[1] By combining materials with the previously described characteristics, it is possible to obtaine core-shell NPs which show increased exchange bias, magnetic coercivity, and blocking temperature.[1] Some example of AFM/F(i)M (or viceversa) core-shell NPs are: $MnO@Fe_2O_3$, $Fe_3O_4@MnO$, $CoO@ Fe_2O_3$, $CoFe_2O_4/MnO$ and $MnO@Mn_3O_4$.

The final step of our work is the development of an effective protocol for the coating of anisotropic MnO NPs with a shell of iron oxide of adequate quality (thickness, compactness) for the build up of a strong exchange coupling between the AFM core and FM shell leading to increased magnetic stability. The main challenge in the synthesis of core-shell NPs starting from a pre-formed NP core is to find the conditions under which the shell precursor efficiently coats the core without nucleating homogeneous NPs.

To begin with, we first set at developing a coating protocol using spherical MnO cores. When the formation of iron oxide coating on such NPs will be well controlled, we will refine the synthetic protocol for core-shell NPs using anisotropic MnO NPs as substrate in order to achieve our final goal of synthesizing anisotropic AFM/FM NPs with increased magnetic stability thanks to the synergic effect of shape anisotropy and exchange coupling.

8.2. Results and discussion

Several examples of core-shell *metal*/metal oxide solvothermal synthesis were reported in the last years, nevertheless the synthesis of *metal oxide*/metal oxide core-shell structures remains a major challenge. Indeed, a significantly lower number of articles were published on this oxide/oxide coupling and, in particular, reports on MnO/FeOx (FeOx = $Fe_{3-x}O_{4-x}$, $0 \leq x \leq 1$) core-shell NPs are very rare. Growing a metal oxide shell on a preformed different metal oxide core presents two main critical points:

1. achieve a significant deposition of the shell material on the preformed nuclei (in particular, a continuous shell is better than a discontinuous shell layer comprising more or less isolated, small crystallites)
2. avoid an independent nucleation of the second material (independent means that the second material homogeneously nucleates in the solvent and not on the first material surface)

The reaction conditions need to be optimized in order to satisfy both requirements simultaneously. Thus, the synthesis of core-shell MnO/FeOx NPs with the desired structure, size, and magnetic properties is a very difficult challenge.

One of the most influent factor in this type of synthesis is the iron precursor (and, accordingly, the iron oxidation state). Two type of precursors were compared during our work: iron pentacarbonyl (Fe(0)) and iron acetylacetonate (Fe(III)).

Working at an appropriate temperature is important to avoid the dissolution of the MnO seeds which may occur at high temperature. Furthermore, high temperature could also promote independent nucleation of FeOx NPs, so a low temperature is preferable. However, also the heterogeneous growth has an energy barrier activation, thus we have to find the optimal temperature (and other conditions) to achieve heterogeneous but not homogenous nucleation and growth. It is important to find the optimal energy level, because the heterogeneous growth requires an energetic level higher than the heterogeneous nucleation but both these energetic barrier still remain under the energy level required for the homogeneous nucleation that could be avoid.[8 9 10]

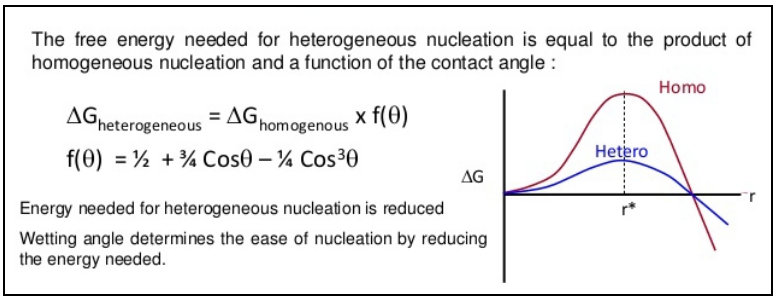

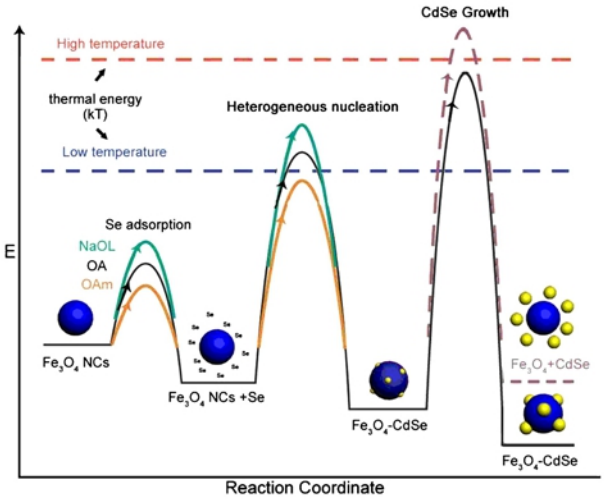

Figure 2: Schematic illustration of the different energy barriers required for the nucleation and growth step. In this case, the energy levels for a Fe_3O_4/CdSe structure are reported. Image from ref. 10

Moreover, it is expected that, to avoid an independent iron oxide nucleation, it is better to continuously add the iron precursor with a controlled rate instead of performing a one-shot injection. One-shot injection easily generates high supersaturation conditions that induce homogeneous iron oxide NPs formation. The use of a syringe pump helps to avoid homogeneous nucleation but at the same time lengthens the reaction time and could again lead to an erosion of the MnO seeds.

Finally, the concentration of oleic acid and oleylamine have to be optimized. An appropriate surfactant : iron precursor molar ratio promotes the correct rate of iron-oleate/iron-oleyalmine complex formation and decomposition for the heterogeneous growth, but a surfactant excess could promote the formation of iron oxide independent NPs and/or induce a modification/dissolution of the MnO seeds. Temperature control is important to preserve the MnO seeds size and shape. Some previous tests demonstrated that washed and isolated MnO NPs, at least, could be heated at 300°C for 1 hour and remain unchanged.

8.2.1. Measurement of shell thickness

Before describing the synthetic results, we briefly outline how the FeOx shell thickness was measured. A more detailed description may be found below. We used different methods in order to achieve a reliable thickness value: conventional TEM, ESI, and EDX. Measuring very thin shell thickness can be difficult due to poor statistics, background noise and sample inhomogeneity. Comparison between different techniques guarantees a greater accuracy of the shell thickness data. In this way we could ascertain that

- the most accurate measure of the shell thickness is obtained from ESI images;
- EDX thickness serves to support ESI data provided that poor statistics is taken into account;
- CTEM thickness is flawed by the core size variation that is often larger than the shell thickness.

8.2.2. Iron pentacarbonyl as precursor

A first series of reactions was planned starting from a procedure[11] where iron pentacarbonyl was used to cover/decorate titanium oxide nanorods. The reaction procedure was modified and many parameters changed. In particular, the key varied parameters were: the molar ratio between surfactants and MnO nuclei, the amount of iron precursor, the method to inject iron pentacarbonyl (low temperature one-shot or with high temperature continuous injection with controlled rate by syringe pump), the growth temperature and time.

All experimental details are reported in the table below. [table *1*]

Reactions	MnO seeds	$Fe(CO)_5$: MnO	Injections	Temp. (°C)	Time (min)	Outcomes
E85	E55	5:1	one pot	280	60	No changes
E92	E87	4:1	one pot	240	60	FeOx NPs nucleation + MnO seeds unchanged
E94	E87	10:1	one pot	200	60	FeOx NPs nucleation + MnO NPs with a small amount of iron
E97	E87	4:1	one pot	200	60	FeOx NPs nucleation + MnO seeds unchanged
E100	E86	2:1	one pot	180	60	**NO** FeOx NPs nucleation + MnO NPs with a small amount of iron
E103	E86	4:1	one pot	180	60	FeOx NPs nucleation (very large NPs)
E110	E102	3:1	one pot	170	60	FeOx NPs nucleation + MnO NPs with a small amount of iron
E115	E102	3:1	one pot	150	60	FeOx NPs nucleation + MnO NPs with a small amount of iron
E116	E102	4:1	one pot	150	60	FeOx NPs nucleation + MnO NPs with a small amount of iron

E127	E117	4:1	0.1 mL/min syringe pump	150	60	FeOx NPs nucleation + MnO NPs with a small amount of iron
E130	E117	4:1	2a1 one pot + 2a1 0.1 mL/min syringe pump	150	60	FeOx NPs nucleation + MnO NPs with a small amount of iron
E133	E117	4:1	0.02 mL/min syringe pump	150	40 after inject.	FeOx NPs nucleation + MnO NPs with a small amount of iron
E143	E117	4:1	0.02 mL/min syringe pump	125	40 after inject.	**NO** FeOx NPs nucleation + MnO NPs with a small amount of iron
E144	E139	4:1	0.02 mL/min syringe pump	150	40 after inject.	**NO** FeOx NPs nucleation + MnO NPs with a small amount of iron
E150	E139	8:1	0.02 mL/min syringe pump	150	40 after inject.	**NO** FeOx NPs nucleation + MnO NPs with a small amount of iron
E159	E139	8:1	0.02 mL/min syringe pump	180	40 after inject.	FeOx NPs nucleation + MnO NPs with a small amount of iron
E163	E139	24:1	0.02 mL/min syringe pump	150	40 after inject.	**NO** FeOx NPs nucleation + MnO NPs with a small amount of iron
E164	E160	24:1	0.02 mL/min syringe pump	150	5h after inject.	FeOx NPs nucleation + MnO seeds erosion
E168	E160	24:1	0.02 mL/min syringe pump	150	5h after inject.	FeOx NPs nucleation
E169	E160	8:1	0.02 mL/min syringe pump	150	5h after inject.	FeOx NPs nucleation

Table 1: experimental details and results of the reactions prepared using iron pentacarbonyl as iron precursor and 1-octadecene as solvent.

In the reaction series using iron pentacarbonyl as iron precursor, the best outcome were core-shell NPs free from homogeneously nucleated iron oxide NPs and having MnO cores with unchanged size but with a low iron content (probably the shell thickness is less than about 1 nm as in analytical ESI and EDX mapping the signal from iron was very weak). The main point is that it was not even clear whether iron oxide was present on the MnO surface or it had somehow diffused into the MnO core. Due to the low iron content, no iron-related crystal structure could be identified by electron diffraction and HRTEM. Actually, it was not even possible to discern whether iron was present as a metal or oxide.

To increase the shell thickness, we tested a series of reactions with progressively increasing iron precursor concentration. A reaction series where the amount of iron was increased was carried out. Even when the iron precursor concentration was so high that the formation of homogeneous iron oxide NPs occurred, no increase in the iron oxide shell thickness was obtained. The use of a precursor comprising iron(0) did not give encouraging results. Using iron pentacarbonyl as a precursor did not seem promising for the synthesis of MnO@FeOx core-shell NPs with a significant shell thickness.

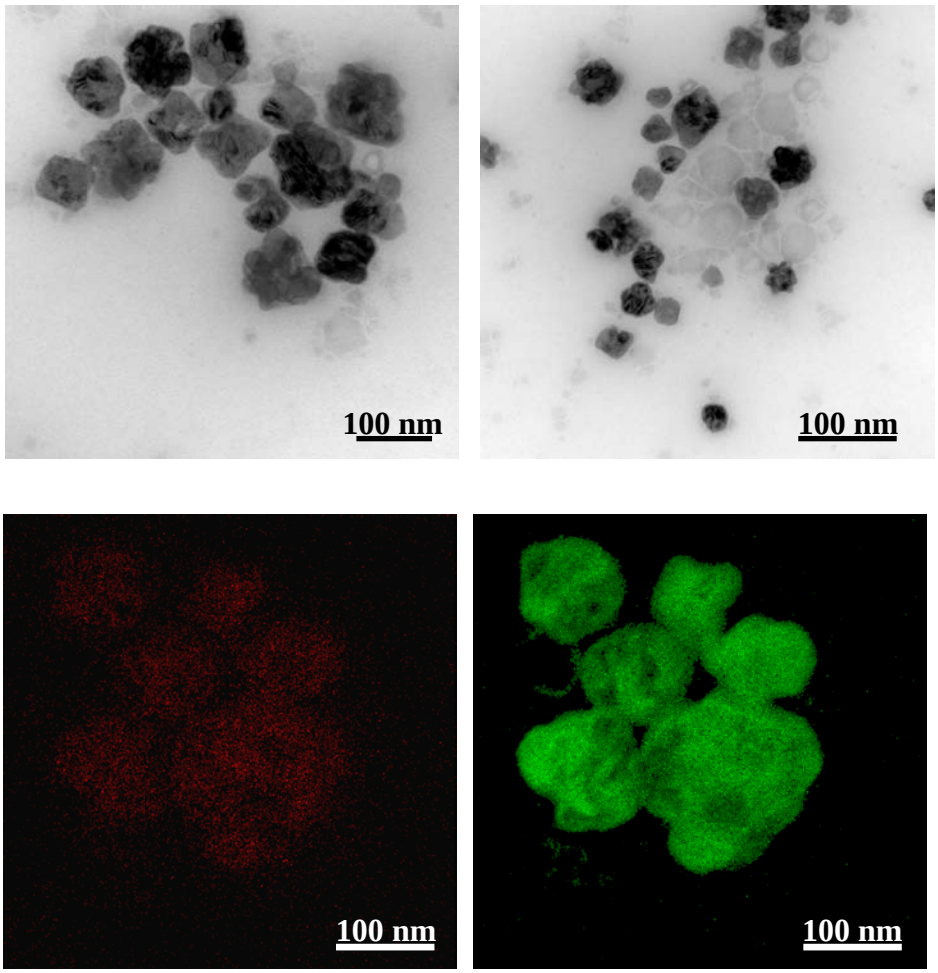

Figure 3 : conventional TEM images and energy filtered TEM images of a MnO@FeOx sample prepared by solvothermal method starting from iron pentacarbonyl as precursor. Iron signal is red and manganese signal is green.

8.2.3. Iron(III) acetylacetonate as precursor

The disappointing results obtained with $Fe(CO)_5$ prompted us to reconsider the solvothermal method. We decided to start from a different procedure published by Nogués and his collaborators in 2013[3] and planned a new series of reaction using iron(III) acetylacetonate as a precursor and dibenzyl ether (instead of 1-octadecene) as a solvent. The use of a (slightly) polar solvent is thought to favour the formation of a continuous shell while non-polar solvents are thought to promote NP decoration and heterodimer formation[12].

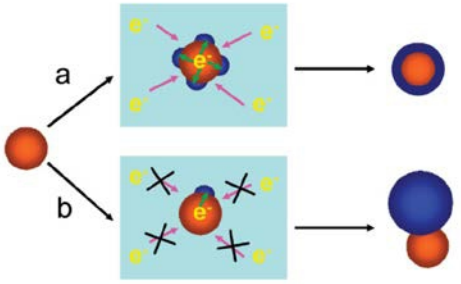

Figure 4: Scheme of the solvent influence on the deposition of the second material: a) heterogeneous growth of a solid shell; b)growth of a decorated or heterodimeric structure. Image from ref. 12

Another important difference from the previous series of solvothermal reactions is the use of an high concentration of MnO seeds. In the $Fe(CO)_5$ series, we generally used [MnO] = 0,01 M (0,1 mmol of MnO in 10 mL of 1-octadecene), whereas in this reaction procedure we generally used [MnO] = 0.10 M (about 0,57 mmol of MnO in 5,5 mL of dibenzyl ether). The high MnO nuclei concentration increases the total surface area available for reaction and favours the shell nucleation and growth.

The reaction is of the heat-up type. The composition of the reaction mixture is MnO : OlAc : OlAm : HDD : $Fe(acac)_3$ = 2 : 1 : 1 : 1.25 : 0.375 (molar ratio). All reagents were added to the solvent right from the start before heating and then the solution was kept at 250 °C for 20 min as described in the experimental section [paragraph 8.4.1]. Many repetitions and tests of this procedure were made.

Reaction	Iron Conc.	Solvent	FeOx NPs	Shell thickness (nm)	
				ESI	EDX
E200	1x	benzyl ether	NO iron oxide NPs		
E202A	1x	benzyl ether	NO iron oxide NPs	**0.45**	2.4
E203A	1x	benzyl ether	Average d = 5.6 nm	**1.90**	1.2
E210A	1x	benzyl ether	NO iron oxide NPs	**1.25**	1.8
E215A	1x	benzyl ether	NO iron oxide NPs	**1.25**	
E216A	1x	benzyl ether	NO iron oxide NPs	**2.05**	
E228A	1x	benzyl ether	NO iron oxide NPs	**0.50**	0.7
E229	2x	benzyl ether	Average d = 4.4 nm		
E230	4x	benzyl ether	NO iron oxide NPs (separation)	**2.35**	2.3
E231	8x	benzyl ether	Average d = 9.2 nm		
E232	4x	benzyl ether	rare iron oxide NPs (separation)		
E233	1x	diphenyl ether	NO iron oxide NPs	**0.65**	3
E234	1x	octyl ether	NO iron oxide NPs	**0.20**	1.5

Table 2: Summary of replications and variations on the heat-up 20-min procedure. The main variations are the iron concentration and the solvent type. The iron concentration affects the occurrence of homogeneous FeOx nucleation while the solvent affects the FeOx heterogeneous deposition and shell formation. The indication 1x means that in the reaction the iron acetylacetonate : manganese oxide molar ratio is equal to 0,36.

MnO seeds	C-TEM diameter (nm)	MnO@Fe2O3 core-shell
E198	20.6	E200,E202A
E30b	24.8	E203A
E209	28.8	E210A
E214	35.7	E215A,E216A,E217A
E226	21	E228A,E229,E230,E231,232,233,E234

Table 3: for every reaction has been reported the original MnO seed size

Figure 5: Morphological TEM images of the core-shell nanoparticles and energy filtered TEM (ESI) images of the samples described in the previous table 2.

Synthesis: iron concentration = 1x and solvent: benzyl ether

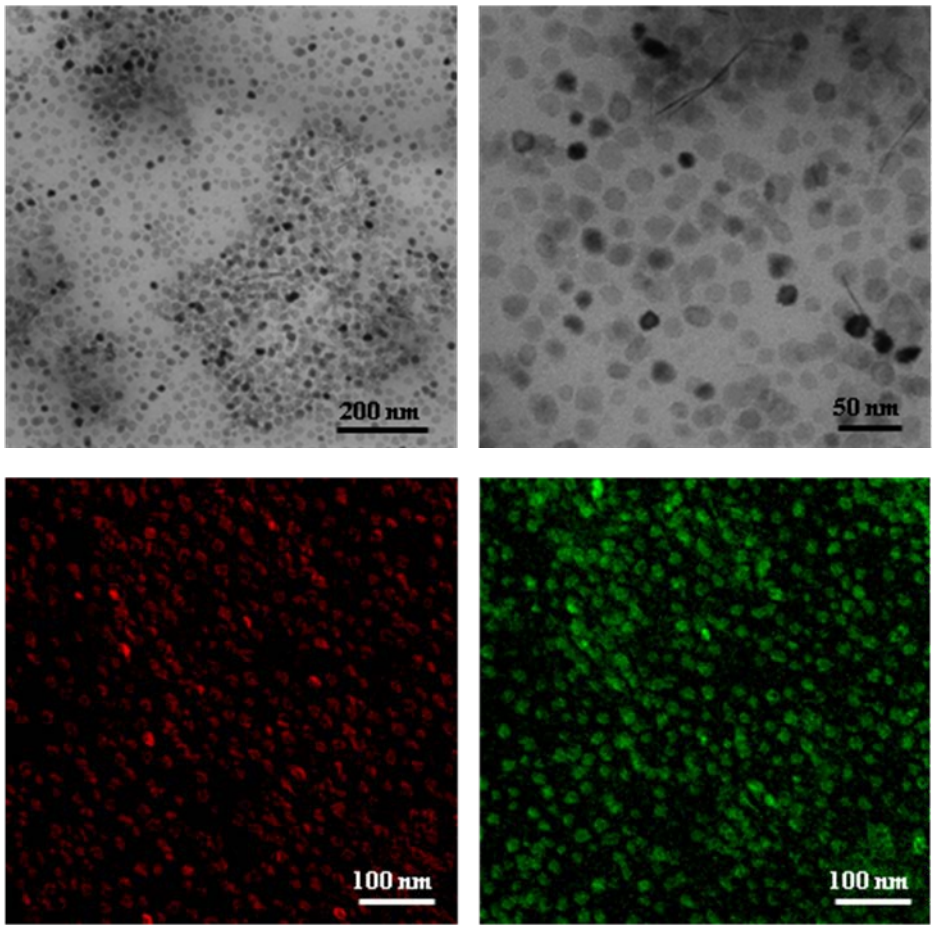

Synthesis: iron concentration = 1x and solvent: benzyl ether

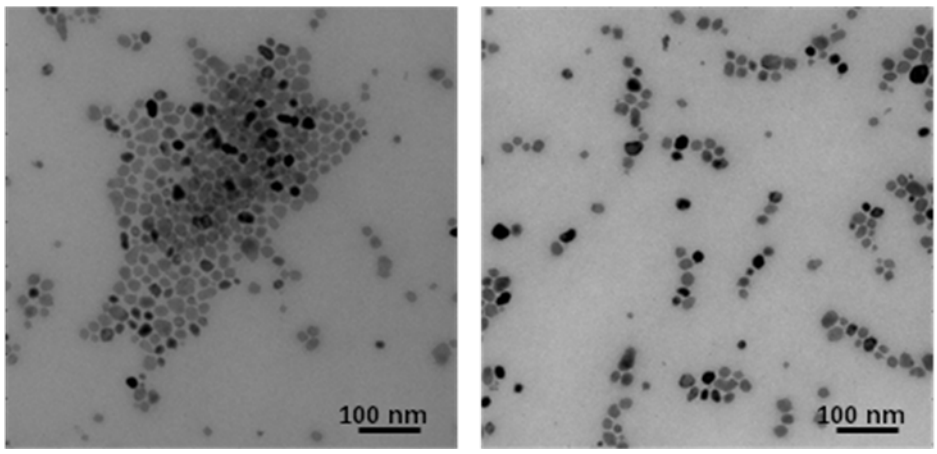

Synthesis: iron concentration = 2x and solvent: benzyl ether

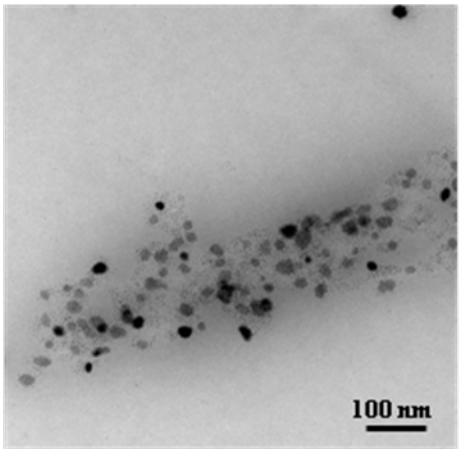

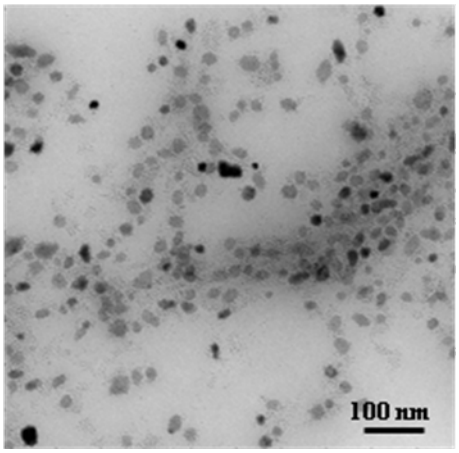

Synthesis: iron concentration = 4x and solvent: benzyl ether

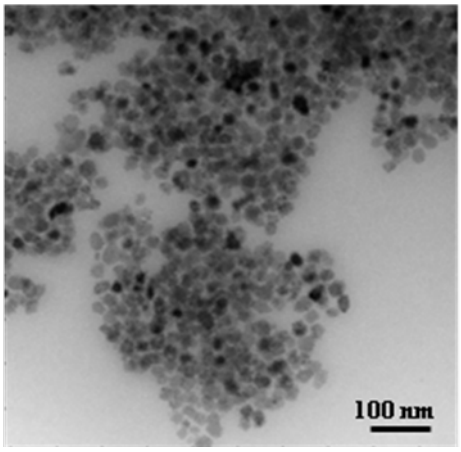

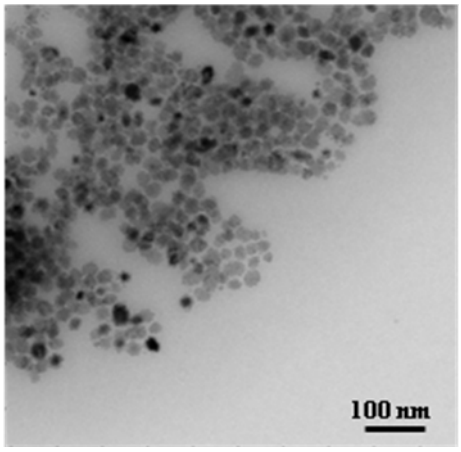

Synthesis: iron concentration = 8x and solvent: benzyl ether

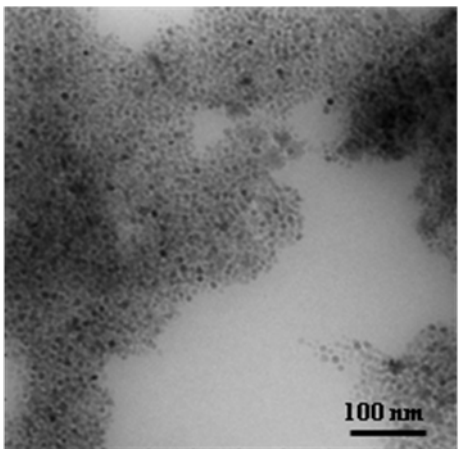

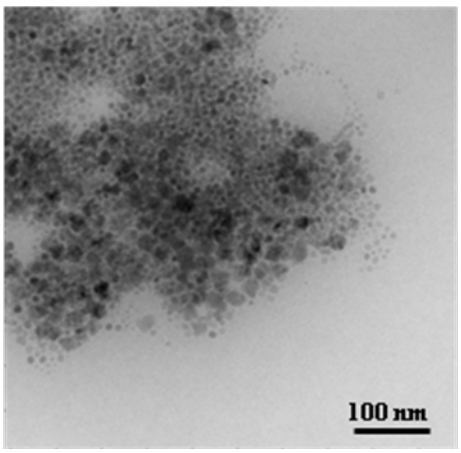

Synthesis: iron concentration = 4x and solvent: benzyl ether

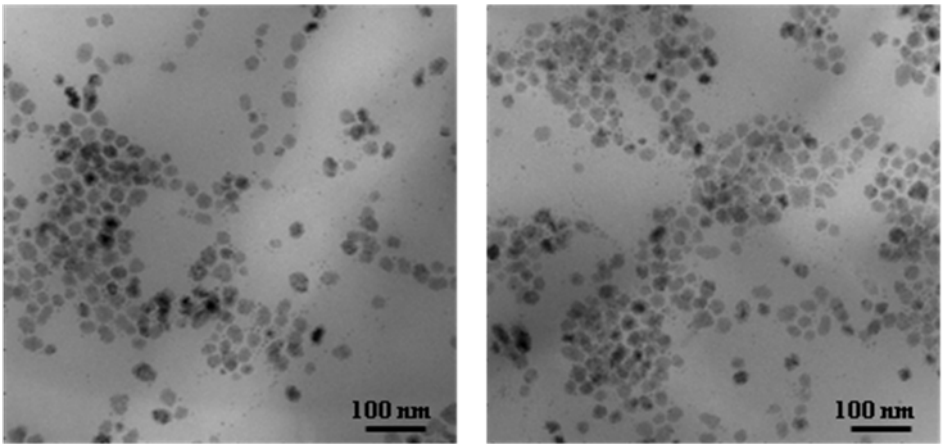

Synthesis: iron concentration = 1x and solvent: diphenyl ether

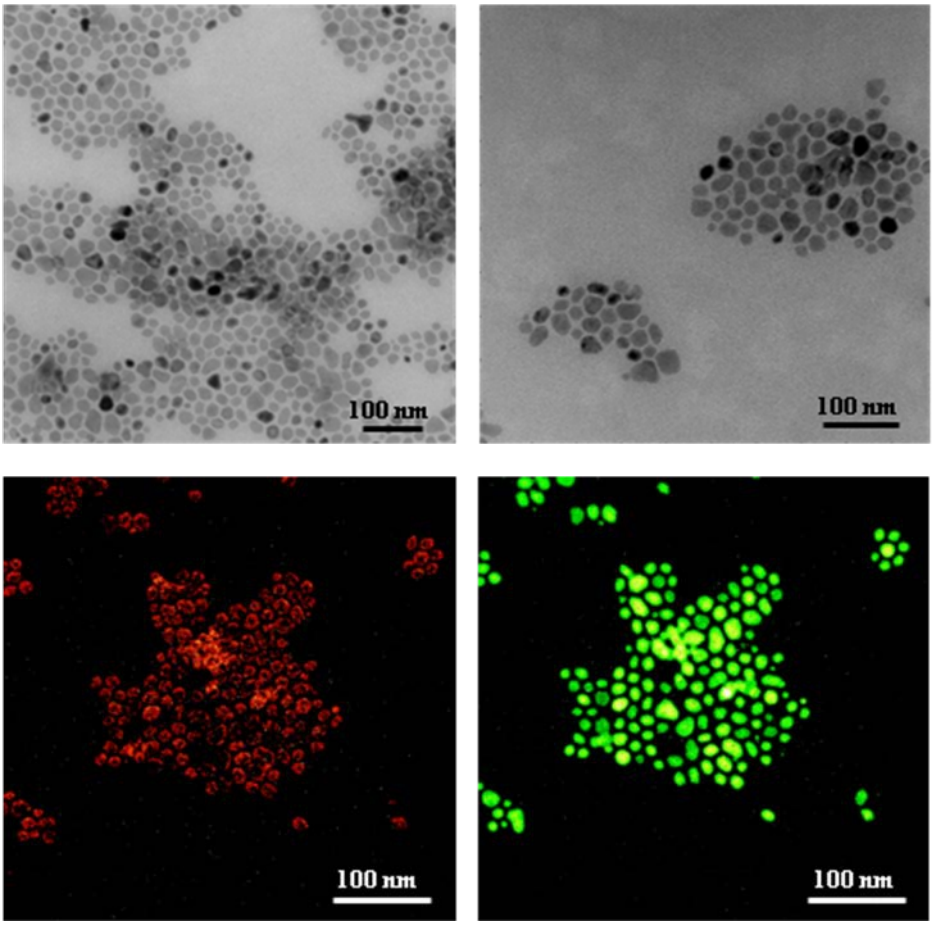

Synthesis: iron concentration = 1x and solvent: octyl ether

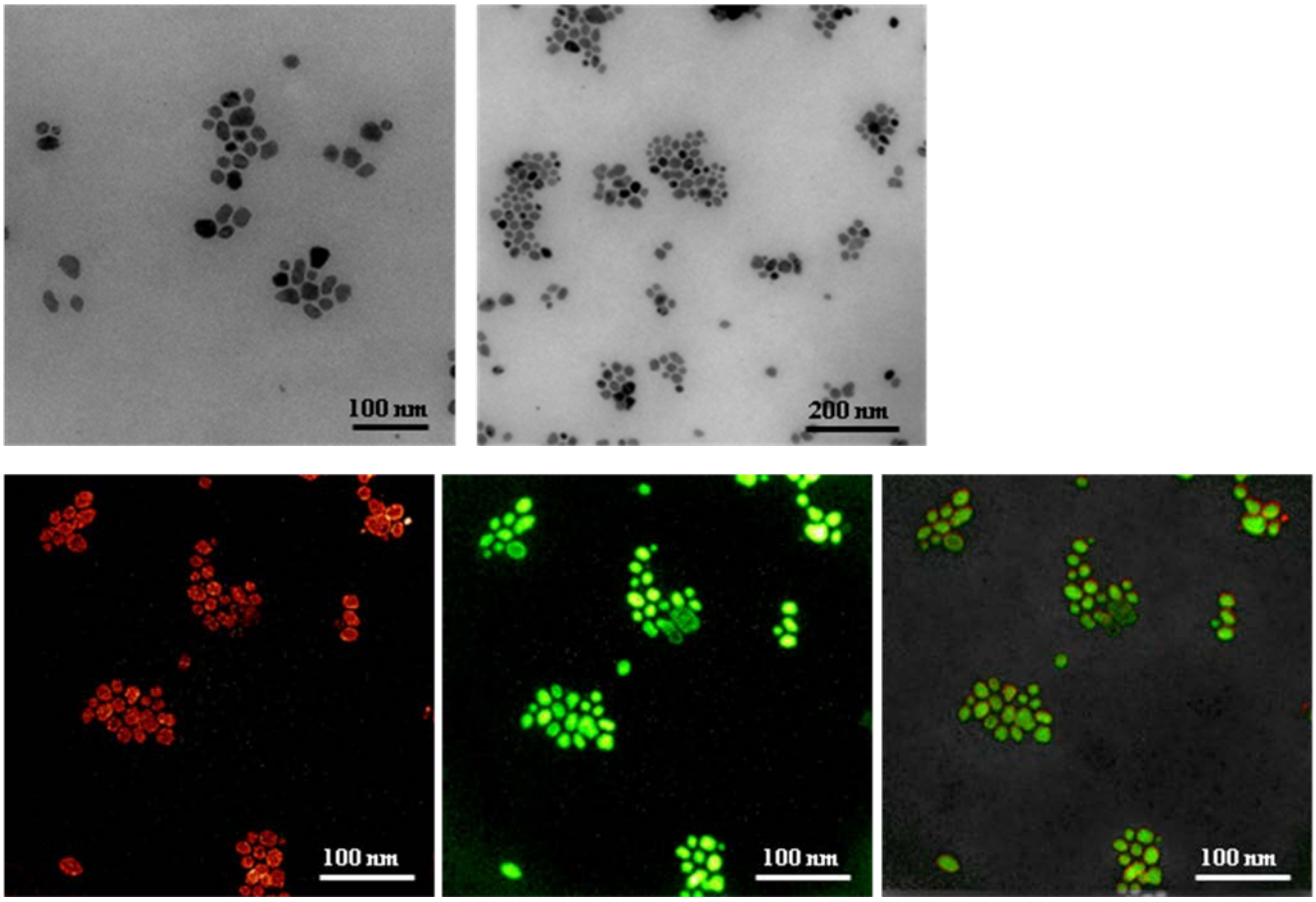

In most reaction products there is no independent iron oxide nucleation and the MnO seed display a good resistance at high temperature when a low concentration of surfactant is used.

By this method we obtained FeOx shell of thickness ranging from 0.5 and 2 nm. This large variability is not due to irreproducibility of the synthetic procedure but to the use of MnO seeds with different size. The total MnO surface area present in the reaction affects the thickness of the FeOx shell. Nanoparticles with 30 nm diameter have smaller surface area per unit mass than 25 and 20 nm diameter NPs. The samples with the thickest shell were prepared starting from MnO seeds with diameter about 35 – 30 nm whereas the other samples, prepared from MnO seeds with a diameter about 25-20 nm, displayed thinner shells. The shell thickness is approximately linearly related to the area of the total available MnO surface. Since in each reaction the same Mn:Fe ratio was used, we can conclude that for Mn seeds of diameter in the 20 – 35 nm range, the kinetics of FeOx heterogeneous nucleation and growth shell does not depend on the seed size and the shell thickness is limited by the amount of iron precursor.

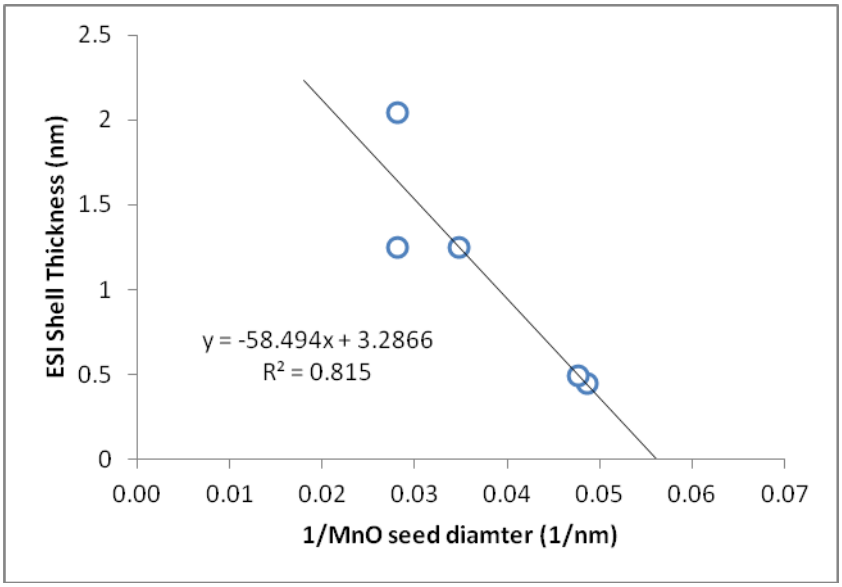

Figure 6: the graph shows the proportional trend between the total surface area of MnO seeds and the thickness of the iron oxide shell observed in one-step reactions.

By this procedure, we obtained samples with a FeOx shell 0.5 – 2 nm thick. Such values are still too low for our goal of magnetic stabilization but it was demonstrated that this reproducible synthesis is a good starting point to achieve our purpose. Thus, to increase the FeOx shell thickness, we first simply increased the concentration of the iron precursor.

Unfortunately, when the iron precursor concentration is increased, an independent iron oxide nucleation occurs. In particular, the iron oxide NPs in the 2x reaction have approximately 5 nm diameter while those in the 8x reaction have approximately 9 nm diameter. Surprisingly, in the case of the 4x reaction, no or rare FeOx NPs are present in the final hexane dispersion because a 10 min centrifugation at 10000 rpm allowed to separate the iron oxide NPs by collecting a black supernatant where the NPs are stably dispersed even during centrifugation. These globally unsatisfying results prompted us to change over to varying another reaction element: the solvent. Diphenyl ether and dioctyl ether were used instead of dibenzyl ether but they brought no advantage. Despite the absence of iron oxide homogeneous nucleation, no significant improvement (diphenyl ether) or even a decrease (octyl ether) in the shell growth was observed.

Since the results of the standard heat-up one-step reaction are however promising and not having found a simple modification to increase the shell thickness, we decided to revert to a multi-step reaction procedure starting from the MnO/FeOx core-shell NPs obtained by the

above procedure and where each step is similar to the heat-up one-step reaction. Three different approaches were tested:

a) the core-shell NPs were isolated (washing/centrifugation) between growth steps;

b) the core-shell NPs were not isolated but the reaction mixture was cooled, added with fresh iron oxide precursor, and then heated again between growth steps;

c) the core-shell NPs were not isolated and the temperature kept constant between growth steps.

Reaction	**Total no. of steps**	**Method**	**FeOx nucleation**	**shell thickness (nm)**	
				ESI	EDX
E202	2	a)	Absent	**2.50**	
E203	2	b)	Present, <d> = 7.5 nm	**1.65**	
E212	5	b)	Present, <d> = 7.8 nm		3.1
E210	2	c)	Absent	**2.95**	2.3

Table 4: Comparison of the different procedures to achieve a thicker shell. The number of steps is the total number of times that the reaction was aged for 20 minutes at high temperature.

Figure 7: Morphological TEM images of the core-shell nanoparticles and selected energy filtered TEM (ESI) images of the samples described in the previous table 4

Synthesis: washed and isolated NPs , after first step

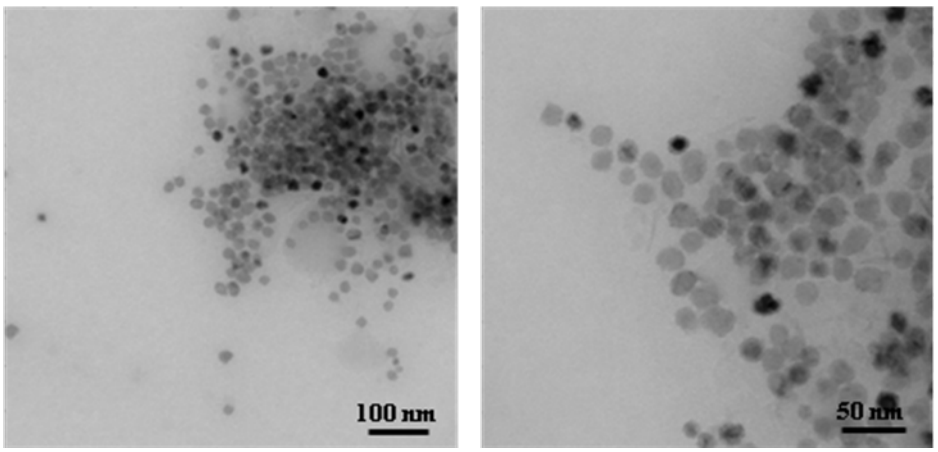

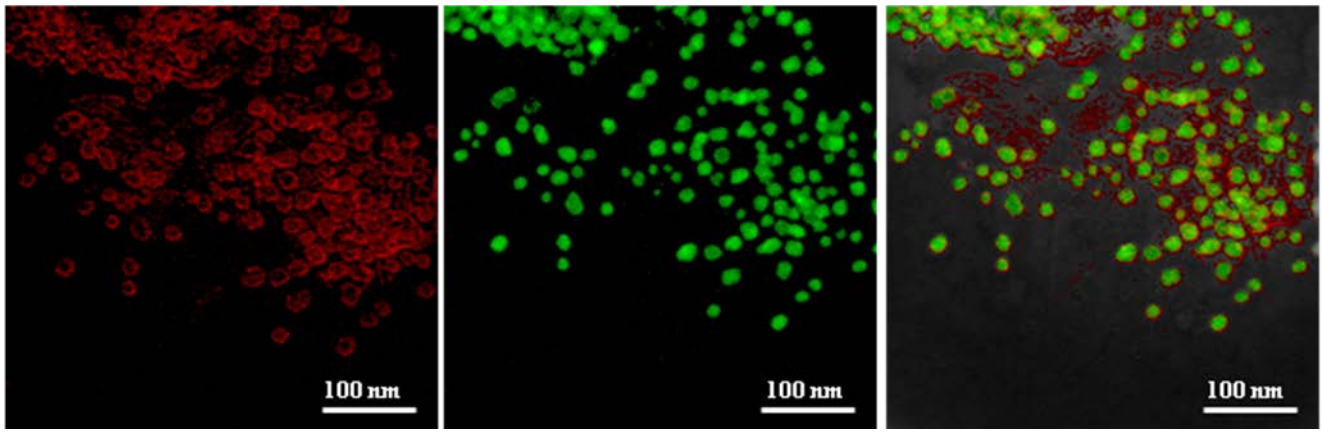

Synthesis: washed and isolated NPs , after second step

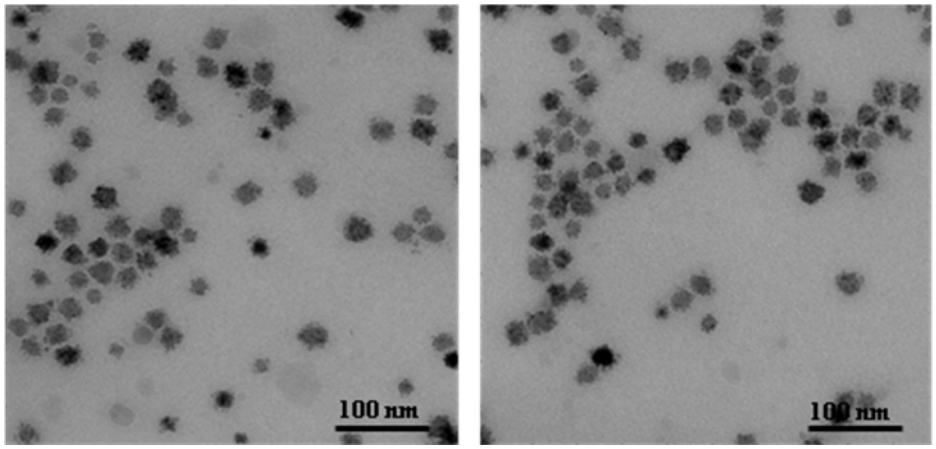

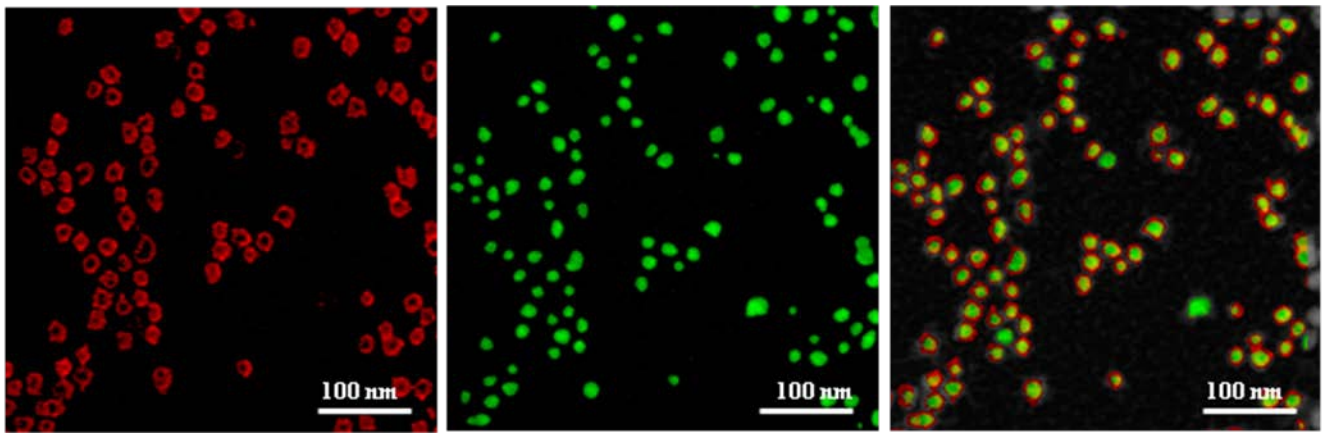

Synthesis: cooled not isolated NPs , after first step

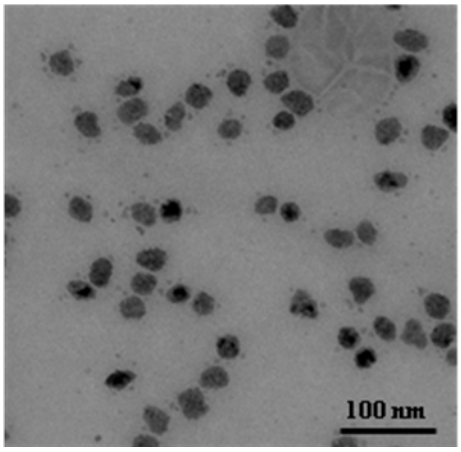

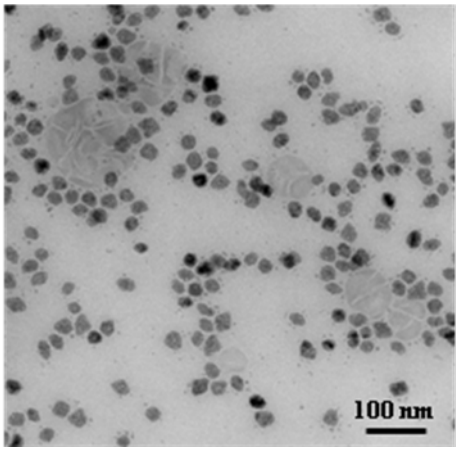

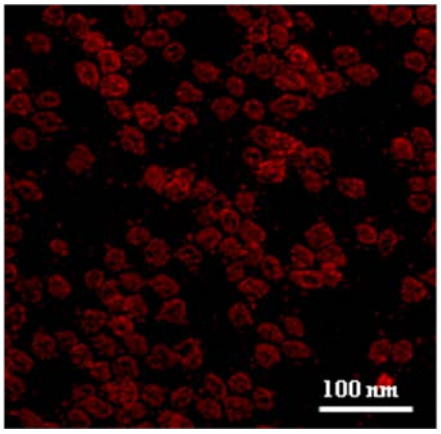

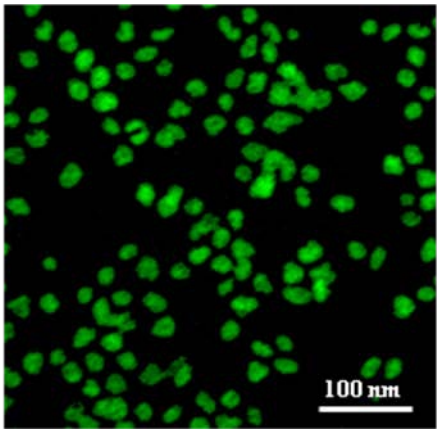

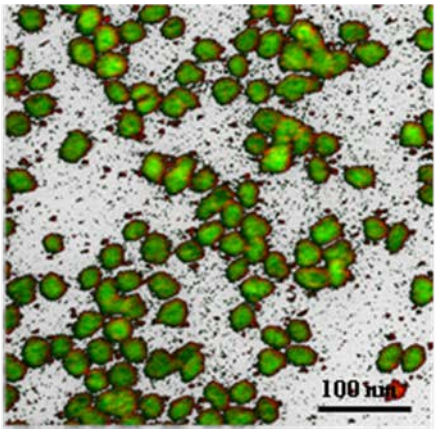

Synthesis: cooled not isolated NPs, after second step

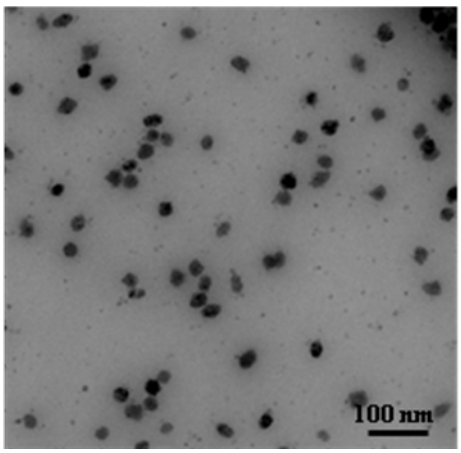

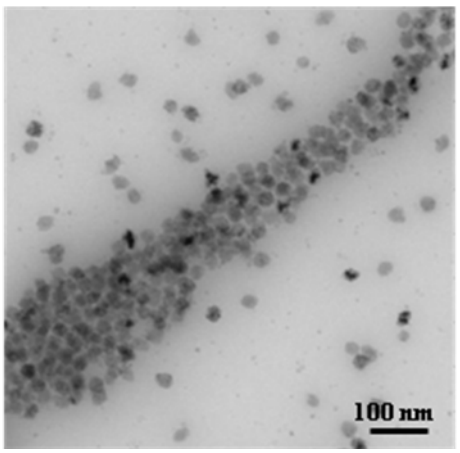

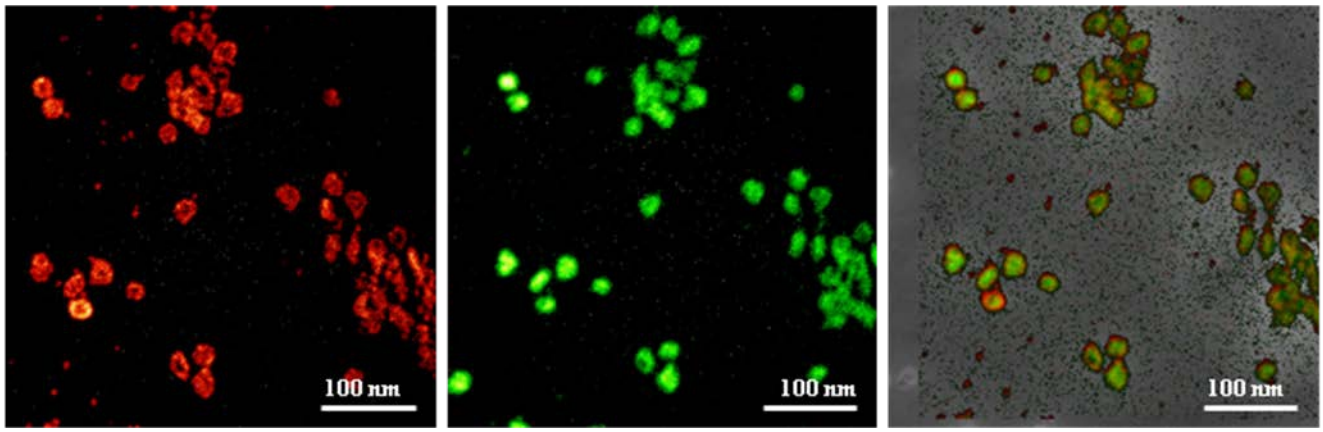

Synthesis: cooled not isolated NPs, after third step

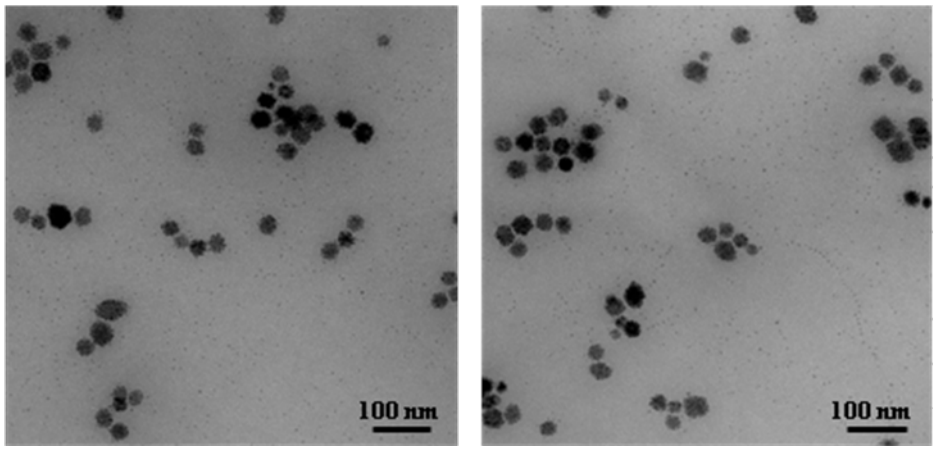

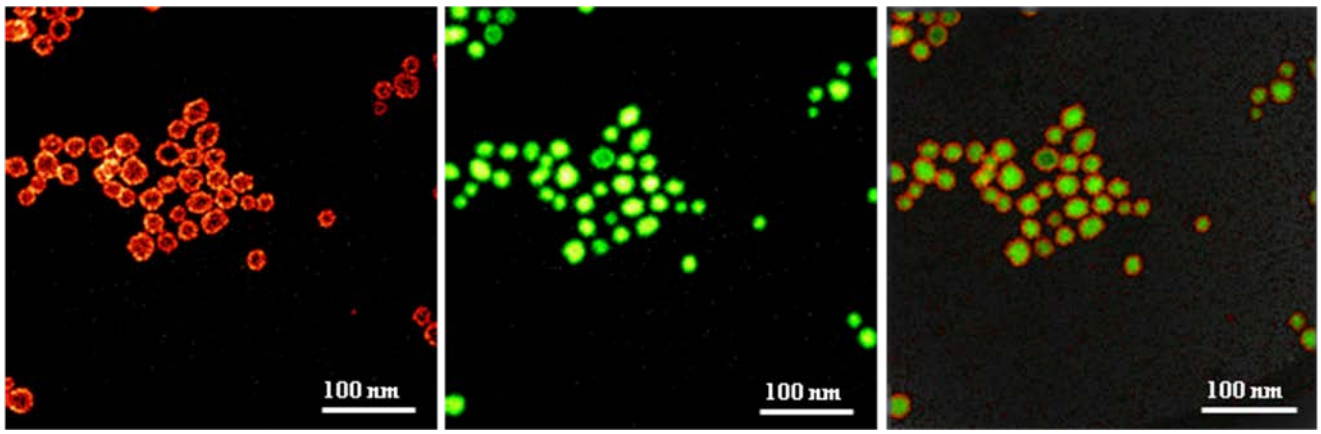

Synthesis: cooled not isolated NPs, after fifth step

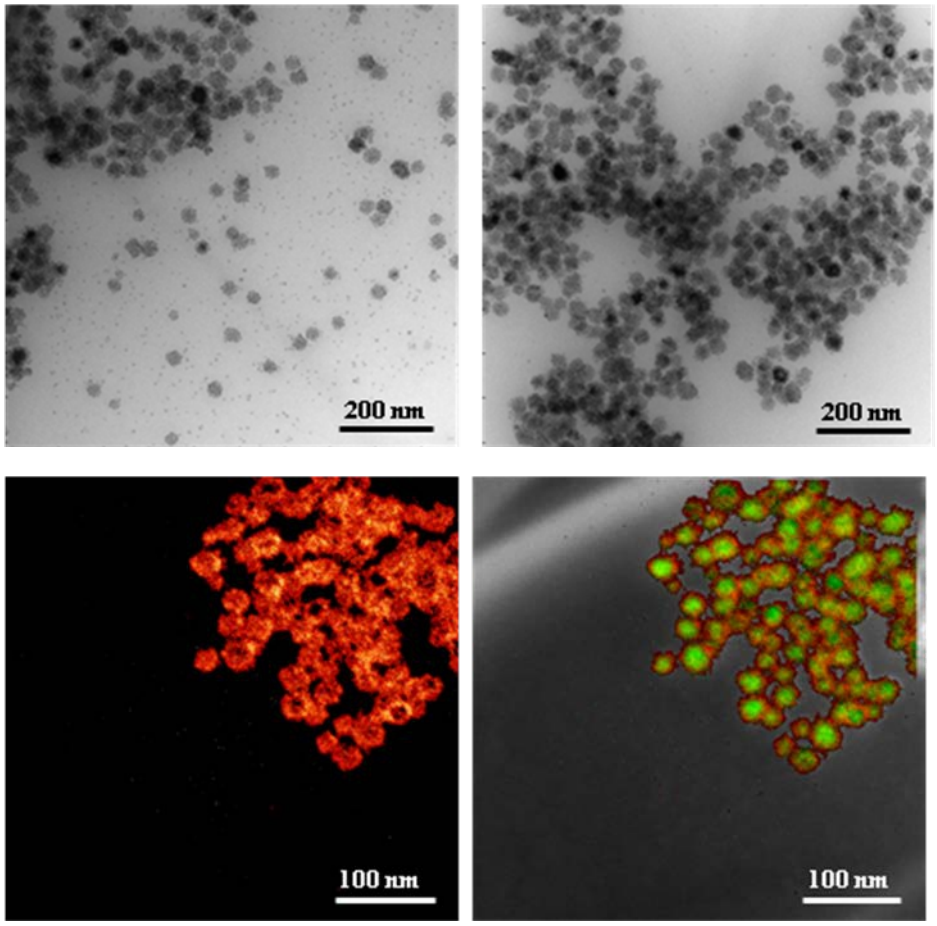

Synthesis: not isolated, constant temperature NPs, after first step

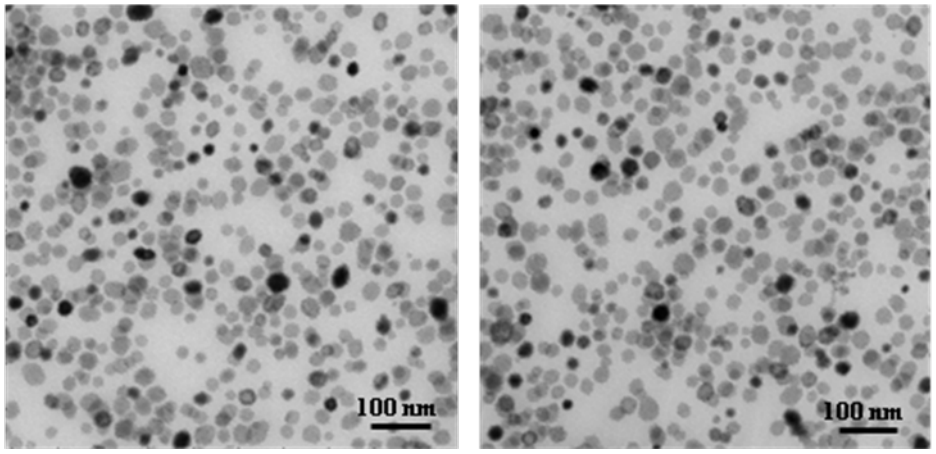

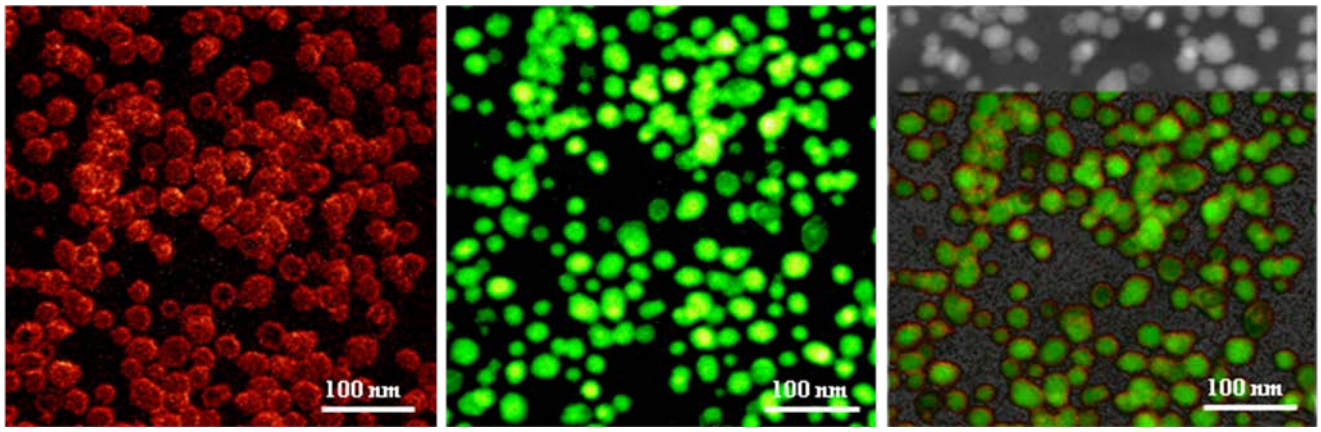

Synthesis not isolated, constant temperature NPs, after second step

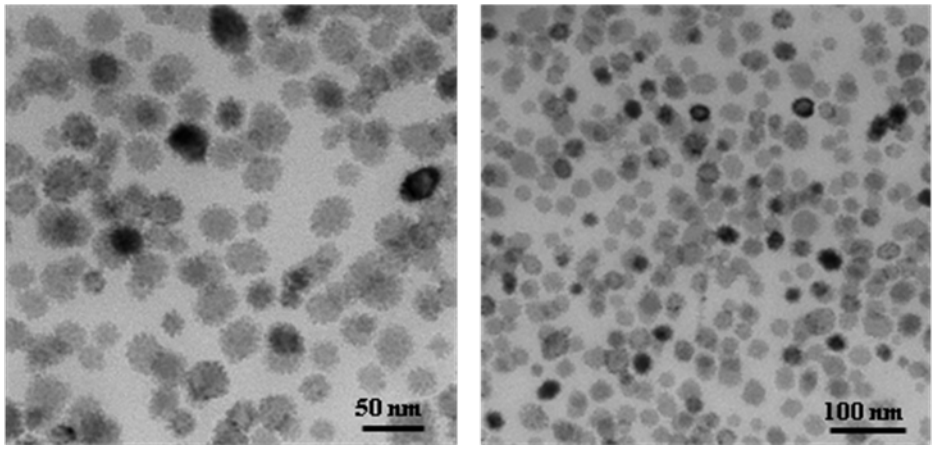

In the long multi-step reactions, surfactants were added to the reaction using either the reaction solvent dibenzyl ether (so that the final volume and reagent concentration change at every step) or using a low-boiling solvent, which should evaporate at 250 °C, so that the final volume and reagent concentration were unchanged. Hexane, toluene and chloroform were tested as solvent using for the injections. The solubility of iron(III) acetylacetonate is low in hexane, so an unfeasibly large amount of solvent is required to completely dissolve the precursor before injection. Chloroform was a better solvent for dissolving the metal precursor and surfactants but it was able to heavily erode and dissolve the MnO nuclei [figure *8*]. Thus, toluene turned out to be a good choice due to its capability of dissolve all the reagents and to preserve the MnO seeds.

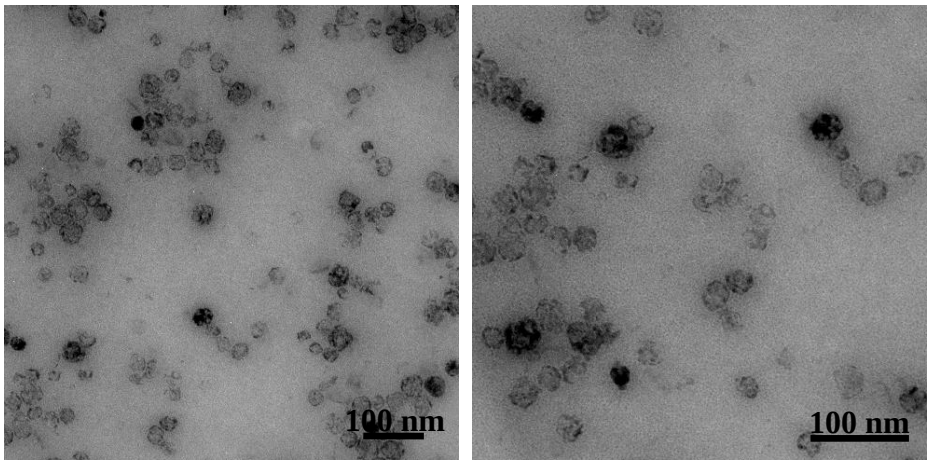

Figure 8: MnO seeds after the two-step reaction with iron precursor injection in chloroform

In the “a” case, involving core-shell NP isolation, a substantial growth of the FeOx shell thickness is observed. However, the isolation procedure inevitably leads to a loss of core-shell NPs changing the molar ratio conditions in the subsequent steps. Consequently, in a procedure involving several steps there is a considerable loss of NPs and a very poor final reaction yield. Furthermore, the isolation procedure at each step significantly adds to the experimental effort. This experiment was necessary to understand if a second growth on the initial shell deposition was feasible. However, the not negligible NP loss, low yield, and large experimental effort, led us to design another procedure.

In the second procedure “b”, the iron precursor addition was carried out at low temperature in order to reproduce reaction conditions similar to those of the one-step reaction. The “b” case showed no second growth of the thickness shell (similar to the previous “a” case) and this procedure also promoted the independent nucleation of homogeneous iron oxide NPs as shown by the presence of FeOx NPs with diameter ≈ 7 nm after the second reaction step. Hence, this procedure does not satisfy to requirement 2 and is not an improvement compared to the “a” case. Despite these shortcomings, the “b” procedure was also tested in 5-step procedure to explore the shell growth at longer times. At the end of the reaction, the shell thickness is very similar to the shell thickness after 2 steps and the thickness improvement is not very interesting compared to the initial one-step reaction. Therefore, another synthetic strategy is needed.

In the “c” case, the addition of iron precursor is carried out at the growth temperature (250 °C). No iron oxide nucleation was observed in the initial steps and a good shell growth was achieved. In this new series of long-times experiments, the first reaction example lasted 2 hours and 40 minutes with 7 iron precursor injections (each injection contained as much iron

precursor as in the initial reaction mixture) spaced by 20 minutes. The reaction was monitored at different times. The sampling after 20 minutes reproduced the previous results from the heat-up one-step synthesis. After 2 hours, the shell had considerably grown but FeOx NP nucleation occurred (FeOx NPs size was *ca*. 10 nm). At the end of the reaction, a FeOx shell approximately 6.5 nm thick was observed. Curiously, the shell appears to comprise a number of small FeOx spheres (ca. 8.5 nm diameter) linked to each other rather than a compact shell layer.

In order to obtain a compact shell, it was thought that injecting the surfactant mixture along with the iron precursor at every injection (using always the initial amounts for every reagent) could be useful as some previous works reported the importance of the surfactants, in particular 1,2-hexadecanediol, to obtain a compact shell layer.[13] In this case, the reaction was heated for 4 hours and sampled at 20 min, 2 hours and 4 hours. The 20 min sample is very similar to the outcome of the heat-up one-step reaction. After 2 and 4 hours the shell thickness is similar to the 2 hours and 2:40 h samples of the previous reaction. The surfactant has beneficial effect on the layer structure that appeared more compact though some small spherical NPs were still present in the shell layer. Unfortunately, the high amount of surfactants also helped the homogeneous iron oxide nucleation that showed up as ≈ 11 nm NPs after 2 h and ≈ 17 nm NPs at the end of the reaction.

Thus, to regain to absence of FeOx independent nucleation (requirement 2), we decided to decrease the amount of injected iron precursor and surfactants to 1/3 of the previous amount in every injection. The reaction lasted 4 hours. At the end of the reaction, the core-shell NPs presented a non-compact shell about 4 nm thick and a significant number of homogeneous FeOx NPs of approximately ≈ 9 nm diameter was observed. The reduced availability of reagents decreased the size of the homogeneous iron oxide NPs but did not avoid their formation; the shell thickness was lower compared to the previous long-time reaction.

Reaction	**No. of injections**	**Injection solvent**	**No. of sampling**	**Sampled volume**	**Injected materials**
E215	7	0.4 mL dibenzyl	8	0.2 mL	$Fe(acac)_3$
E216	11	0.6 mL dibenzil + 0.3 toluene	6	0.5 mL	$Fe(acac)_3$ + surfactants as starting
E217	11	0.6 mL dibenzil + 0.3 toluene	3	0.2 mL	1/3 of $Fe(acac)_3$ + 1/3 surfactants as starting

Reaction	Time	FeOx nucleation	shell thickness (nm)	
			ESI	EDX
E215A	20min	Absent	**1.25**	
E215F	2h	Present, <d> = 10.2 nm	**2.95**	
E215H	2h 40min	Very minor		
E216A	20min	Absent	**2.05**	
E216D	2h	Present, <d> = 11.4 nm	**3.80**	6.1
E216F	4h	Present, <d> = 16.9 nm	**6.25**	7.6
E217C	4h	Present, <d> = 9.2 nm		

Table 5: above, experimental detail of reactions involving a large number of consecutive steps at high temperature. Every 20 minutes iron precursor was injected, in some cases together with surfactants. To check the reaction progress, the reaction mixture was sampled at various times. Below, iron oxide nucleation and shell thickness data.

Figure 9: Morphological TEM images of the core-shell nanoparticles and energy filtered TEM (ESI) images of the samples described in the previous table 5

Synthesis: adding $Fe(acac)_3$ (time = 20 min)

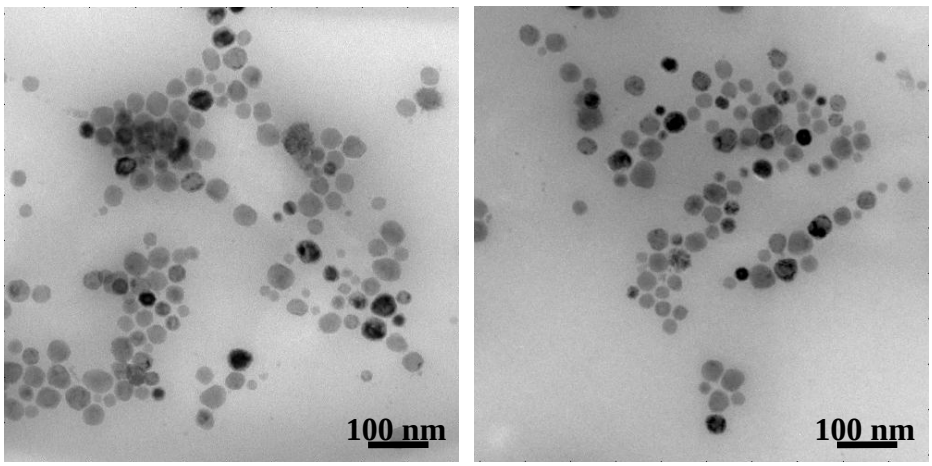

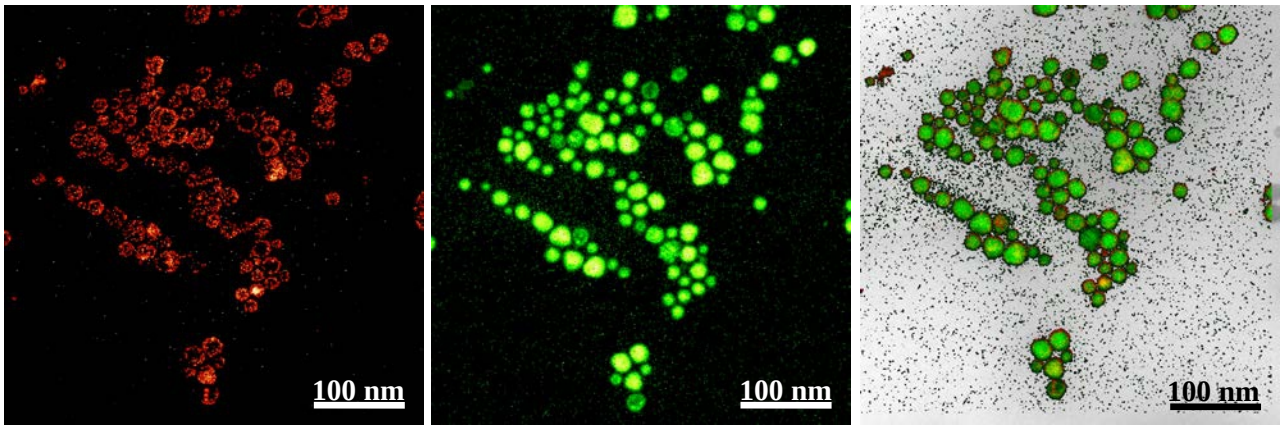

Synthesis: adding $Fe(acac)_3$ (time = 2h)

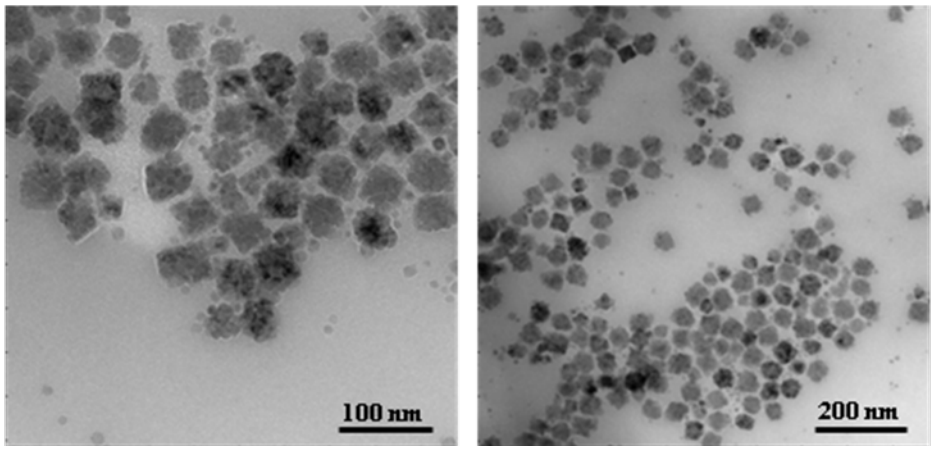

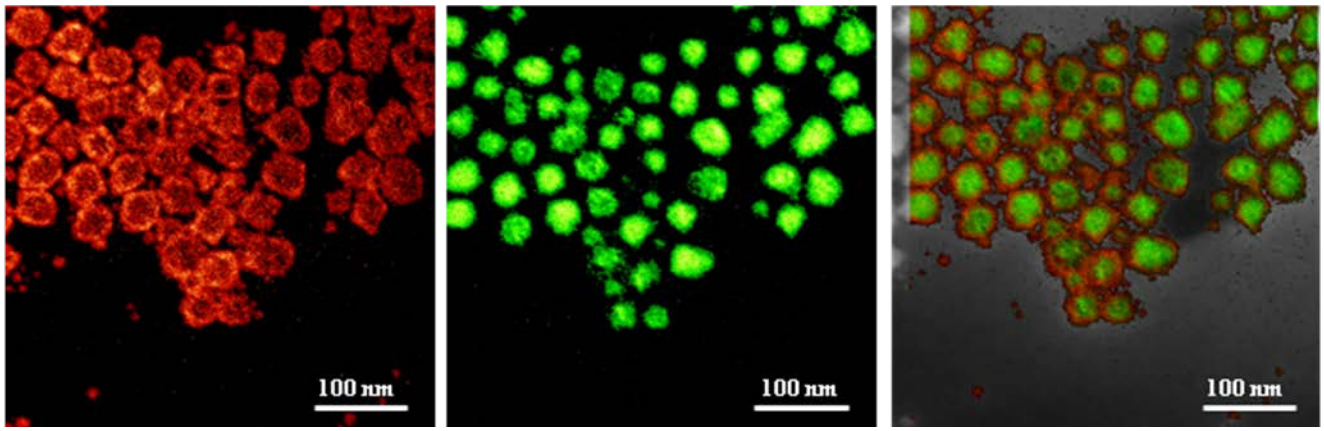

Synthesis: adding $Fe(acac)_3$ (time = 2h and 40 min)

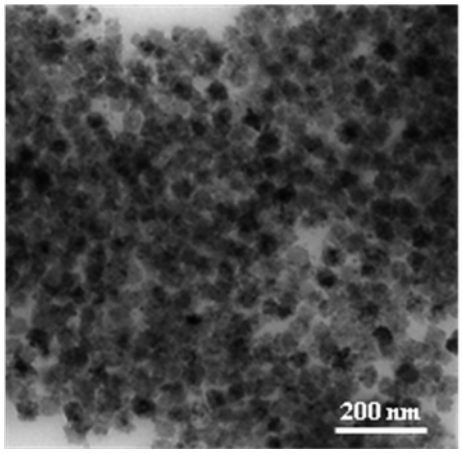

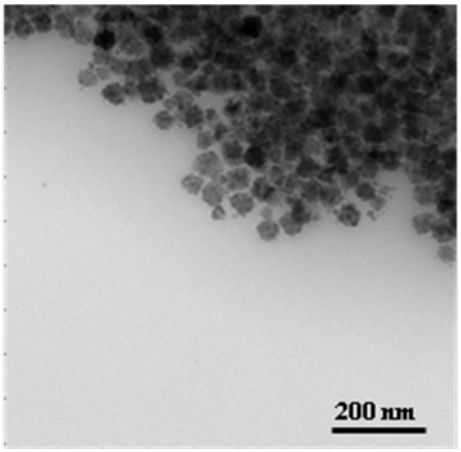

Synthesis: adding $Fe(acac)_3$ and surfactant as starting (time = 20 min)

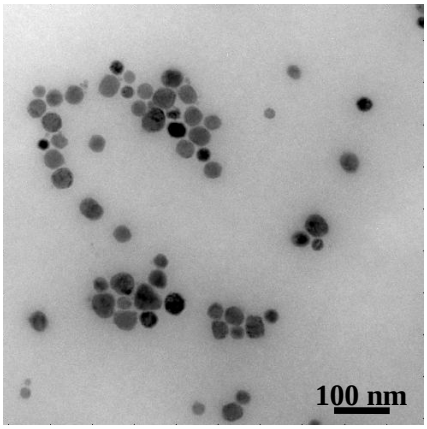

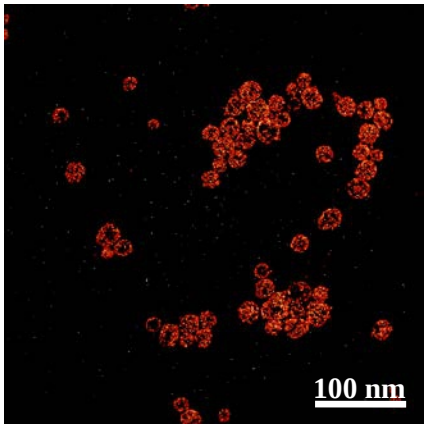

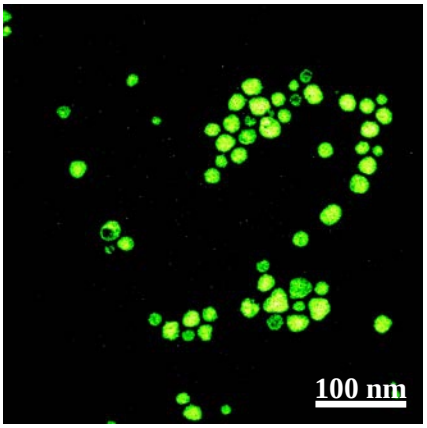

Synthesis: adding $Fe(acac)_3$ and surfactant as starting (time = 2h)

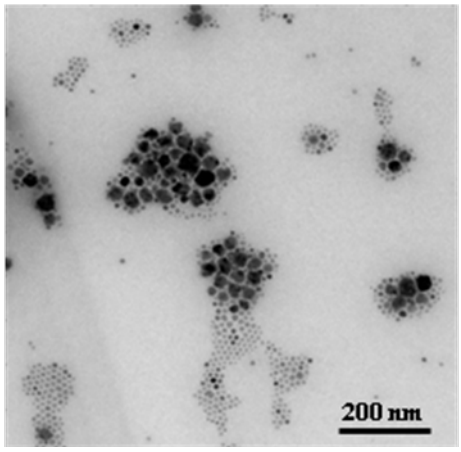

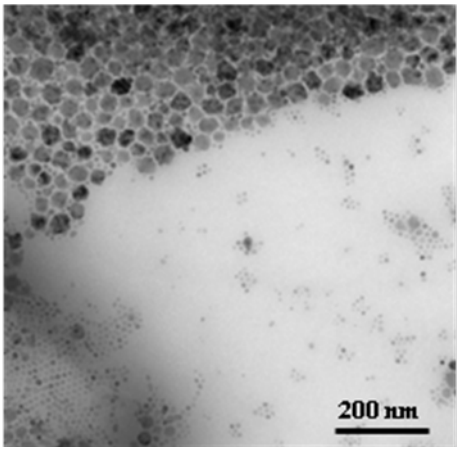

Synthesis: adding $Fe(acac)_3$ and surfactant as starting (time = 4h)

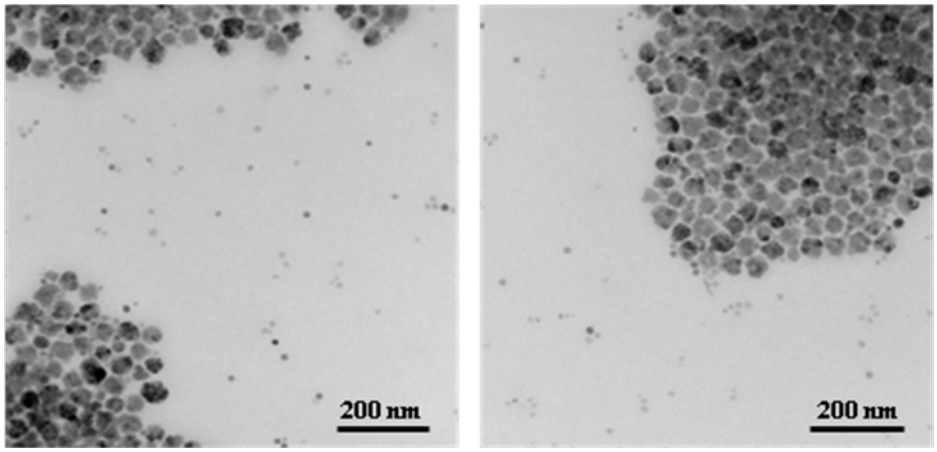

Synthesis: adding 1/3 $Fe(acac)_3$ and 1/3 surfactant as starting (time = 4h)

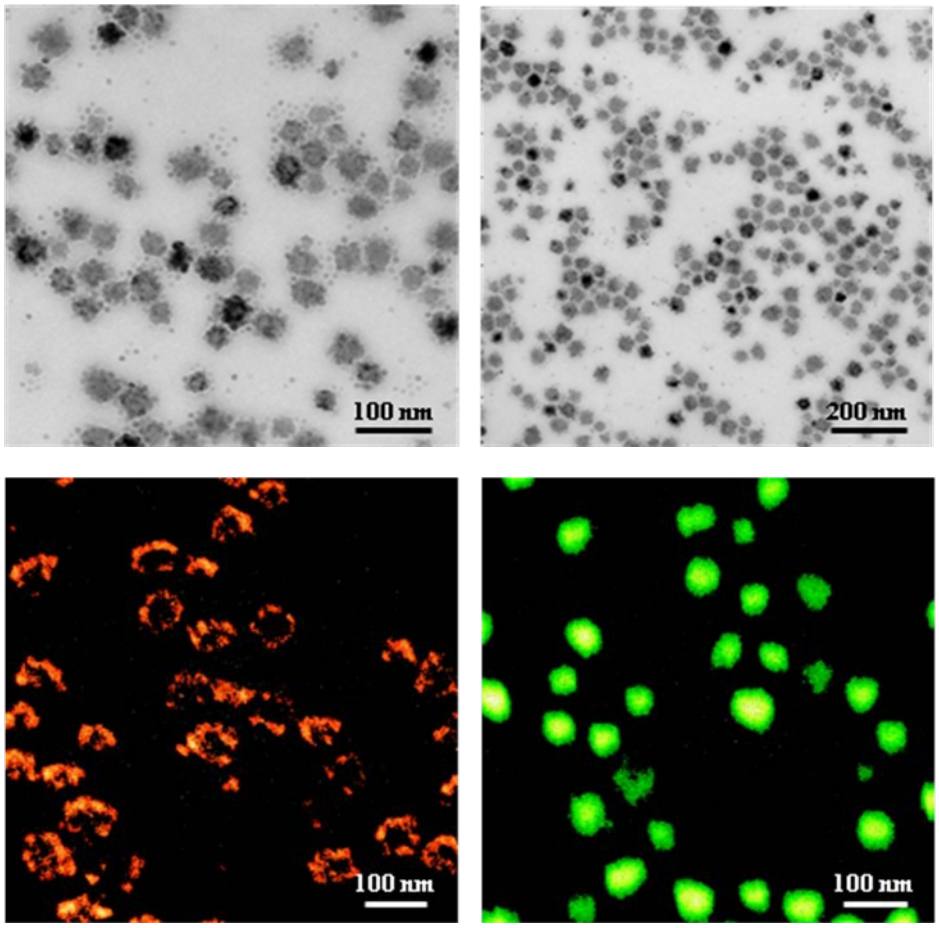

In order to keep the iron concentration in the reaction mixture lower than the critical supersaturation (where homogeneous nucleation occurs) even just after the injection, we

replaced the discrete injection method with a slow constant-flow injection by syringe pump. Syringe pump experiments unexpectedly showed a considerable formation of homogeneous iron oxide NPs. Hence this strategy was not considered promising.

In summary, we found a good method to build a 0.5 – 2 nm thick FeOx shell on MnO seeds, which satisfies both synthetic requirements. The iron amount introduced at the beginning of the reaction, form a FeOx shell on the MnO cores which preserves them and limits the erosion during the reaction. Unfortunately, from the magnetic standpoint, such shell is too thin as 2 nm FeOx nanocrystals are superparamagnetic even at very low temperature and very difficult to stabilize. We therefore searched for a good method to increase the shell thickness but could not as yet find one satisfying both synthetic requirements of thick shell and absence of FeOx homogeneous NPs.

In this synthesis, the main challenges remain: to avoid the homogeneous iron oxide nucleation and to obtain compact shells promoting a coalescence between the small iron oxide spherical patches on the MnO seed surface. It is possible that nucleation is helped by keeping high temperature for long time, whereas, some papers[10] suggest to heat core-shell NPs at high temperature for hours to promote coalescence of the small iron oxide spheres and obtain a solid shell. Another work reported a possible role of the hexadecanediol[14] in the coalescence process to form a solid FeOx shell. These procedures are clearly critic in our case in order to avoid new nucleation and degradation of the MnO seeds. The shell thickness and coalescence still are critical points in this work because a thick and compact shell is a basic requirement to achieve an effective exchange coupling at the FM-AFM interface and an improved magnetization stability.

8.2.4. Measurement of shell thickness: details

The FeOx shell thickness was measured by different methods in order to achieve a reliable thickness value. Measuring very thin shell thickness can be difficult due to poor statistics, background noise and sample inhomogeneity. Comparison between different techniques guarantees a greater accuracy of the shell thickness data. In our study we measured the shell thickness by means of three electron transmission microscopy techniques:

a) Conventional TEM morphological images allow us to measure the initial diameter of MnO seeds d_{seed} and the core-shell NP total diameter d_{cs}. Half of the difference between these two

diameters corresponds to the shell thickness $t_{CTEM} = (d_{seed} - d_{cs})/2$, provided that the size of the MnO seeds is retained by the MnO cores throughout the reaction. Unfortunately, this was not the case since the MnO cores are smaller than the MnO seeds and, sometimes, $t_{CTEM} < 0$! Thus, t_{CTEM} provides at most a lower bound to the true thickness t.

b) Energy filtered TEM images (ESI) allow us to measure the diameter of the MnO core $d_{core,ESI}$ and the inner and outer diameters of the FeOx shell (the inner diameter often is not well defined). The half of the difference between the outer FeOx diameter $d_{outer,ESI}$ and the MnO core diameter corresponds to the ESI shell thickness $t_{ESI} = (d_{outer,ESI} - d_{core,ESI})/2$.

c) Energy dispersive x-ray (EDX) line-scans allow us to measure the MnO core diameter $d_{core,EDX}$, and the inner and outer diameters of the FeOx shell, as previous seen for the ESI technique. In this case however, it is only possible to analyze a few NPs because measurement is very slow. The statistical set is thus much smaller than for the ESI case. Half of the difference between the FeOx outer diameter and the MnO diameter corresponds to the EDX shell thickness $t_{EDX} = (d_{outer,\ EDX} - d_{core,\ EDX})/2$.

Therefore, the most statistically accurate measure of the shell thickness is obtained from ESI images; EDX thickness serves to support ESI data provided that poor statistics is taken into account; CTEM thickness is flawed by the core size variation that is often larger than the shell thickness.

The diameter of the homogeneous iron oxide NPs diameters were obtained only by conventional TEM.

Reaction	**Reaction time**	**Final shell thickness (nm)**			**Size FeOx NPs**
		C-TEM	ESI	EDX	
E200	20 min	-1.05			No
E202A	20 min	-0.35	0.45	2.4	No
E202B	20 + 20 min	1.6	2.5		No
E203A	20 min	0.95	1.9	1.2	5.6
E203B	20 + 20 min	1.35	1.65		7.5
E210A	20 min	-0.65	1.25	1.8	No
E210B	40 min	-0.05	2.95	2.3	No

E212C	20+20+20 min	1.4		3.1	5.2
E212E	20+20+20+20+20 min	3.65		3.1	7.8
E215A	20 min	-1.15	1.25		No
E215F	120 min	4.4	2.95		10.2
E215H	160 min	6.5			rare
E216A	20 min	0.3	2.05		No
E216D	120 min	-1.35	3.8	6.1	11.4
E216F	240 min	3.6	6.25	7.6	16.9
E217C	240 min	3.95			9.2
E228A	20 min	0.3	0.5		No
E229	20 min	0.05			4.4
E230	20 min	1.7	2.35	2.3	No (separation)
E231	20 min	1.5			9.2
E232	20 min	2.25			rare (separation)
E233	20 min	-0.35	0.65	3	No
E234	20 min	1	0.2	1.5	No

Table 6: Comparison of shell thickness of core-shell nanoparticles measured by different techniques in order to assess the data accuracy.

Reaction	**linescan**		**analyzer**		**Theoretically % from ESI shell thickness**	
	Mn%	**Fe%**	**Mn%**	**Fe%**	**Mn%**	**Fe%**
E202A	86	14			90	10
	83	17				
E202B	49	51	52	48	56	44
E203A	82	18			70	30
E210A	85	15			80	20
	83.5	16.5				
	77.5	22.5				
E210B	67.5	31.5	70	30	58	42
E212C	79.5	20.5	62.5	37.5		
E212E	57	43	49.5	50.5		
	62	38				

E216D	51	49			44	56
E216F	30	70			42	58
E230	70	30			57	43
	68	32				
E233	81	19	79	21	85	15
	77.5	22.5				
E234			82	18		

Table 7: atomic percentage of iron and manganese present in the samples. Data are calculated from EDX analysis and compared to the theoretical percentage calculated from ESI MnO seed and shell thickness measures.

MnO seeds	**C-TEM diameter (nm)**	**MnO@Fe2O3 core-shell**
E198	20.6	E200,E202
E30b	24.8	E203
E209	28.8	E210,E212
E214	35.7	E215,E216,E217
E226	21	E228,E229,E230,E231,232,233,E234

Table 8: here are reported the MnO starting cores samples with the corresponding core-shell samples prepared.

In the previous table [table *6*] some conventional TEM shell thickness are negative because the average diameter of the core-shell structure is lower than the starting MnO seed diameter. This behaviour could be ascribed to the effect of the oleic acid that at high temperature could be able to produce a minor dissolution of the MnO surface. In some reactions the shell growth is not enough to compensate the MnO seed reduction thus the NP shrinks despite an initial thin shell formation.

8.2.5. Hydrothermal method[15]

Due to the difficulties met in solvothermal reactions, we also tried to grow a FeOx shell on MnO seeds in aqueous solvent. This method is complex due to the requirement of a ligand exchange in order to stabilize the NPs in an aqueous environment replacing the original oleate coating. Some experiments were performed to prepare either MnO/FeOx and FeOx/MnO structures. Reactions were respectively set starting from MnO seeds and $Fe(NO_3)_3*9H_2O$ as iron precursor and $Fe_3O_4/\gamma\text{-}Fe_2O_3$ seeds and $Mn(NO_3)_2*4H_2O$ as manganese precursor.
Generally reactions were conducted for 2 hours and heated at 100°C. We observed absence of an homogeneous nucleation of the shell material and size preservation of the seeds, probably thanks to the low growth temperature. However, the shell material deposition on the preformed core is not significant. An iron signal could be detected on MnO NPs, but it was weak that it was not possible to gather reliable information about the chemical nature (metal or oxide) and structure (amorphous or crystalline) of the deposited material.

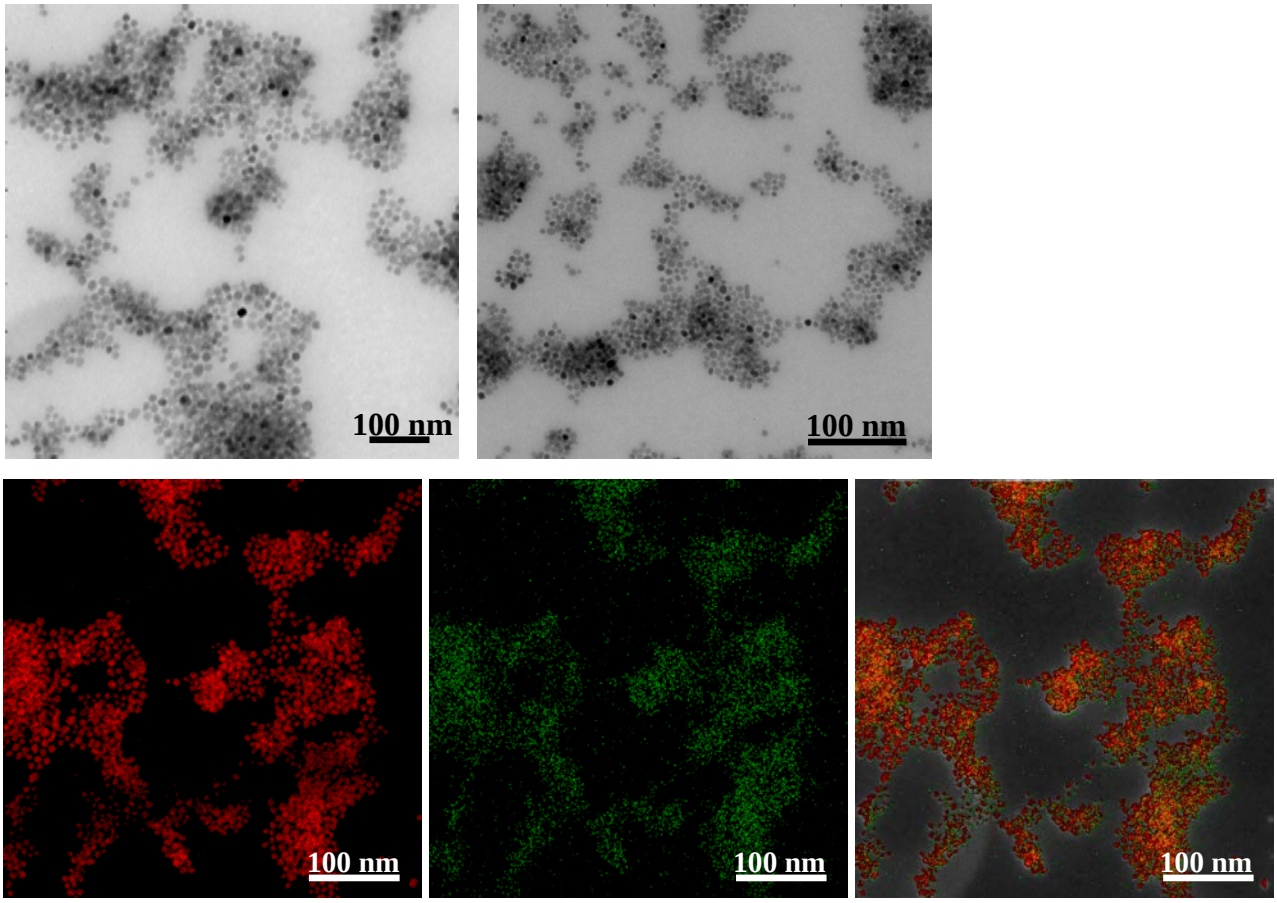

Figure 10: conventional TEM images and energy filtered TEM images of a FeOx@MnO sample prepared by hydrothermal method. Iron signal is red and manganese signal is green.

8.3. Conclusion

Briefly, we can summarize that solvothermal method is the best strategy to grow an iron oxide shell on MnO preformed seeds to prepare MnO@FeOx core-shell structures for exchange coupling. At the beginning a reproducible heat-up one-step reaction procedure was optimize in order to obtain a discrete iron oxide shell deposition (ca. 1-2 nm) without iron oxide homogeneous independent nucleation. Then we investigated different procedure to build a multi-step procedure which allows to improve the shell thickness with high yield and absence of iron oxide homogeneous NPs. The strategy with no NPs isolation and constant temperature seems to be the most promising. Long-time multi-step reaction (maximum 12 steps and 4 hours reaction) were performed testing different amount of iron oxide and surfactants for injections. By now, the best results gave iron oxide shell thickness approximately of 6.5 nm. Shells appear not smooth surface but made by little iron oxide linked spheres. Unfortunately, as expected, long-time reactions show iron oxide independent nucleation. The future purpose is to avoid the iron oxide homogenous nucleation and obtain most solid shells to guarantee a good interface quality between the FeOx and the MnO to accordingly improve the exchange coupling.

A detail procedure with a comparison between data from different TEM analysis such as, conventional TEM, energy filtered (ESI) and energy dispersive x-ray (EDX) analysis, was finely developed to achieve a reliable value thickness of the iron oxide shell grown on the MnO seeds surface.

8.4. Experimental section

8.4.1. Synthesis of MnO@FeOx core-shell nanoparticles by solvothermal method[3]

Materials

Pre-synthesized MnO nanoparticles, oleic acid (reagent grade, 90%), oleylamine (technical grade 70%), 1,2-hexadecanediol (98%), iron (III) acetylacetonate (99%) and dibenzyl ether (purum $\geq$ 99%) were purchased from Sigma-Aldrich. All chemicals were used as received without further purification.

Procedure

In a three-necked flask, the pre-synthesized MnO nanoparticles (25 mg, 0.28 mmol), was dissolved in 4 mL of dibenzyl ether and oleic acid (0.20 mmol, 70 μL), oleylamine (0.21 mmol, 70 μL), 1,2-hexadecanediol (0.25 mmol, 57 mg), and iron (III) acetylacetonate (0.075 mmol, 27 mg) were added to the solution. The solution was heated to 120 °C (heating rate 10 °C/min) under vacuum and magnetic stirring. After 30 minutes, the reaction mixture was heated to 250 °C under nitrogen and aged for 20 min. Then the solution mixture was cooled to room temperature. The NPs were precipitated by adding the reaction crude with a large excess of acetone and then collected by centrifugation (6000 rpm, 10 min). Nanoparticles were washed with acetone and collected by centrifugation (five times). The precipitate was finally dispersed in hexane (5-10 mL) by sonication (ultrasonic bath, 30 min, RT). The obtained NPs dispersions are stable for several months.

Different molar ratio between surfactant and MnO NPs have been tested. Moreover other iron precursor (such as iron pentacarbonyl) has been tried. One-pot or syringe pump (controlled rate) addition were used as strategy to add the iron precursor at high temperature.

Sintesi	Starting NPs	Starting reagents molar ratio					Type of reaction	Plateau time 250°C	Number iron injection	Volume single iron injection	Number sample	Volume sample
		MnO	OlAc	OlAm	Esdiol	$Fe(acac)_3$						
E200	*E198*	2	1.26	1.21	1.25	0.46	one step	20 min	-	-	-	-
E202	*E198*	2	1.26	1.21	1.27	0.49	one step (x2) **washing**	20 min	1	-	1	0.2 mL
E203	*E30B*	2	1.29	1.23	1.40	0.51	one step (x2) **cooling**	20 min	1	2.5 mL hexane	1	0.2 mL
E207	*E199*	2	1.31	1.26	1.32	0.45	one step	20 min	-	-	-	-
E210	*E209*	2	1.38	1.33	1.32	0.45	one step (x2) at 250°C	40 min	1	0.2 mL dibenzilether	1	0.2 mL
E212	*E209*	2	1.38	1.33	1.30	0.46	one step (x5) **cooling**	20 min	4	1 mL hexane (x2) + 0.2 mL dibenzilether (x2)	4	0.2 mL
E215	*E214*	2	1.06	1.02	1.03	0.36	one step (x8) at 250°C	2 h 40 min	7	0.4 mL dibenzilether	7	0.2 mL
E216	*E214*	2	1.12	1.07	1.01	0.37	one step (x12) at 250°C	4 h	11	0.6 mL dibenzilether + 0.3 toluene	5	0.5 mL
E217	*E214*	2	1.12	1.07	1.01	0.36	one step (x12) at 250°C	4 h	11	0.6 mL dibenzilether + 0.3 toluene	2	0.2 mL
E218	*E214*	2	1.12	1.07	1.00	0.37	one step (x12) at 250°C	4 h	11	0.6 mL dibenzilether	0	-
E219	*E214*	2	1.12	1.07	1.02	0.36	one step (x12) at 250°C	4 h	11	0.6 mL dibenzilether	0	-
E221	*E214*	2	1.12	1.07	0.99	0.35	one step	4 h	continuous flow	5.6 mL dibenzilether	1	0.1 mL
E223	*E214*	2	0.00	0.00	0.00	0.00	one step	44 min	continuous flow	0.8 mL chloroform	0	-
E228	*E226*	2	1.12	1.07	1.03	0.36	one step	2 h	5	0.1 mL toluene	1	0.1 mL
E229	*E226*	2	1.12	1.07	0.97	0.71	one step	20 min	-	-	-	-
E230	*E226*	2	1.12	1.07	1.01	1.44	one step	20 min	-	-	-	-
E231	*E226*	2	1.12	1.07	0.97	2.78	one step	20 min	-	-	-	-
E232	*E226*	2	1.12	1.07	1.00	1.37	one step	20 min	-	-	-	-
E233	*E226*	2	1.12	1.07	1.01	0.35	one step	20 min	-	-	-	-
E234	*E226*	2	1.12	1.07	1.01	0.34	one step	20 min	-	-	-	-

8.4.2. Synthesis of MnO@ FeOx core-shell nanoparticles by solvothermal method[11]

Materials

Pre-synthesized MnO nanoparticles, oleic acid (reagent grade, 90%), oleylamine (technical grade 70%), 1,2-hexadecanediol (98%), iron(0) pentacarbonyl (99.99%) and octadecene (purum $\geq$ 95.0%) were purchased from Sigma-Aldrich. All chemicals were used as received without further purification.

Procedure

In a three-necked flask, the pre-synthesized MnO nanoparticles (7.1 mg, 0.1 mmol), was dissolved in 10 mL of octadecene and oleic acid (0.15 mmol, 47 μL), oleylamine (0.075 mmol, 25 μL), 1,2-hexadecanediol (0.125 mmol, 32.3 mg), and iron(0) pentacarbonyl (from 0.2 to 2.4 mmol) were added by syringe pump (with different speeds) to the solution. The solution was heated to 120 °C (heating rate 10 °C/min) under vacuum and magnetic stirring. After 30 minutes, the reaction mixture was heated to 150 °C under nitrogen and aged for 40 or 60 min. Then the solution mixture was cooled to room temperature. The NPs were precipitated by adding the reaction crude with a large excess of acetone and then collected by centrifugation (6000 rpm, 10 min). Nanoparticles were washed with acetone and collected by centrifugation (five times). The precipitate was finally dispersed in hexane (5-10 mL) by sonication (ultrasonic bath, 30 min, RT). The obtained NPs dispersions are stable for several months.

Different molar ratio between surfactant and MnO NPs with very high presence of oleic acid and oleylamine have been tested.

Sintesi	Starting NPs	Reagents molar ratio					injection	Temp. 1 (°C)	Time 1 (min)	Temp. 2 (°C)	Time 2 (min)
		MnO	OlAc	OlAm	Esdiol	$Fe(CO)_{10}$					
E85	*E55*	0.1	0.12	0.052	0.092 (dodecantiolo)	0.5	one pot	120	30	280	60
E92	*E87*	0.03	0.047	0.031	0.037	0.148	one pot	120	30	240	60
E94	*E87*	0.03	0.047	0.031	0.045	0.296	one pot	120	30	200	60
E97	*E87*	0.03	0.047	0.031	0.040	0.296	one pot	120	30	200	60
E100	*E86*	0.12	0.24	0.091	0.151	0.223	one pot	120	30	180	60
E103	*E86*	0.1	0.158	0.076	0.125	0.446	one pot	120	30	180	20 + 60
E110	*E102*	0.1	0.158	0.076	0.125	0.30	one pot	120	30	170	20 + 60
E115	*E102*	0.1	0.158	0.076	0.127	0.30	one pot	120	30	150	60
E116	*E102*	0.1	0.158	0.076	0.128	0.44	one pot	120	30	150	60
E127	*E117*	0.1	0.158	0.076	0.127	0.37	0.1 mL/min	120	30	150	60
E130	*E117*	0.1	0.158	0.076	0.125	0.223	one pot + 0.1 mL/min	120	30	150	60
E133	*E117*	0.1	0.158	0.076	0.127	0.37	0.02 mL/min	120	30	150	40 after inject
E143	*E117*	0.1	0.158	0.076	0.123	0.37	0.02 mL/min	105	30	125	40 after inject
E144	*E139*	0.1	0.411	1.22	0.130	0.37	0.02 mL/min	120	30	150	40 after inject.
E150	*E139*	0.1	0.411	1.22	0.125	0.74	0.02 mL/min	120	30	150	40 after inject.
E159	*E139*	0.1	0.411	1.22	0.125	0.74	0.02 mL/min	120	30	180	40 after inject.
E163	*E139*	0.1	0.411	1.22	0.125	2.23	0.02 mL/min	120	30	150	40 after inject.
E164	*E160*	0.1	0.411	1.22	0.125	2.23	0.02 mL/min	120	30	150	5h after inject.
E168	*E160*	0.1	0	1.68	0.130	2.37	0.02 mL/min	120	30	150	5h after inject.
E169	*E160*	0.1	0.411	1.22	0.127	0.74	0.02 mL/min	120	30	150	5h after inject.

8.4.3. Synthesis of MnO@FeOx core-shell nanoparticles by hydrothermal method[15]

Materials

Pre-synthesized Fe_2O_3 nanoparticles coated by zwitterionic dopamine sulfonate, manganese (II) nitrate tetrahydrate (reagent grade ≥ 97 %), deionized water.

Procedure

In a three-necked flask a clear solution with manganese (II) nitrate tetrahydrate (1.2 g, 4.8 mmol), and pre-synthesized Fe_2O_3 nanoparticles coated by zwitterionic dopamine sulfonate (2 g, 0.01 mmol) in deionized water (final volume = 5 mL) was prepared and heating at 100°C for 1 hour under argon and magnetic stirring. The solution wad cooled to room temperature. Nanoparticles were precipitated by adding the reaction crude with a large excess of acetone and then collected by centrifugation at 6000 rpm for 10 minutes. The NPs were washed with acetone and collected by centrifugation (three times). The precipitate was finally redispersed in some mL of deionized water by sonication (ultrasonic bath, 30 min, RT). The obtained NPs dispersion are stable for several months.

The same procedure could be followed also starting from iron (III) nitrate nonahydrate as metal precursor to form the final oxide shell and pre-synthesized MnO NPs coated by zwitterionic dopamine sulfonate as pre-formed core for the heterostructure. MnO NPs have been synthesized as described previously in the MnO NPs solvothermal synthesis and surfactant exchange between oleic acid and ZDS polymer has been made as reported in the following page.

Synthesis	Core	mmol NPs	Volume H_2O (mL)	Salt	Mass (g)	Number addition	Temp	Time
E190	Fe2O3	0.196	5	$Mn(NO_3)_2$*$4H_2O$	1.25	one pot	100°C	1h
E191	Fe2O3	0.196	5	$Mn(NO_3)_2$*$4H_2O$	1.25	one pot	100°C	2h
E192	**MnO**	0.139	10	**Fe(NO3)3*9H2O**	4	2 (each 2g)	100°C	2h
E193	Fe2O3	0.196	5	$Mn(NO_3)_2$*$4H_2O$	1.25	5 (each 250mg)	100°C	2h

8.4.4. Surfactant exchange: from oleate to zwitterionic dopamine sulfonate (ZDS)[16]

Starting from MnO or Fe_2O_3 nanopaoarticles, it is possible to change their coating from oleate to ZDS polymer via 2-[(2-2-methoxyethoxy)ethoxy]acetic acid (MEEA) exchange. 10 mg of nanoparticles were washed three times with a larege excess of acetone and collected by centrifugation at 6000 rpm for 5 minutes. Then acetone was evaporated and nanoparticles were dispersed in methanol (1-2 mL) and the solution was added with MEAA (0.25 mL). The reaction mixture was heating at 70°C for 5 h under inert atmosphere and magnetic stirring. Afterwards, nanoparticles were washed with a mixture of acetone : hexane (4 : 1) for two times and collected by centrifugation at 6000 rpm for 10 minutes.
Nanoparticles were dispersed in a mixture of deionized water (3 mL) and DMF (6 mL) added with 50 mg of ZDS polymer. The reaction mixture was kept at 70°C for 12 h under inert atmosphere and magnetic stirring. Nanoparticles were washed with acetone for two times and collected by centrifugation at 6000 rpm for 10 minutes. Finally, the sample was dispersed in 8-10 mL of deionized water with some mg of PBS by 30 minutes in ultrasonic bath.

References

1. Schladt, T. D. *et al.* Synthesis and magnetic properties of FePt@MnO nano-heteroparticles. *Chem. Mater.* **24,** 525–535 (2012).

2. López-Ortega, a. *et al.* Strongly exchange coupled inverse ferrimagnetic soft/hard, MnxFe3−xO4/FexMn3−xO4, core/shell heterostructured nanoparticles. *Nanoscale* **4,** 5138 (2012).

3. Estrader, M. *et al.* Robust antiferromagnetic coupling in hard-soft bi-magnetic core/shell nanoparticles. *Nat. Commun.* **4,** 1–8 (2013).

4. J. Nogues, I. K. S. Exchange bias. *J. Magn. Magn. Mater.* **192,** 203–232 (1999).

5. Baaziz, W. *et al.* High Exchange Bias in Fe 3−δ O 4 @CoO Core Shell Nanoparticles Synthesized by a One-Pot Seed-Mediated Growth Method. *J. Phys. Chem. C* **117,** 11436–11443 (2013).

6. Nerio Fontaíña Troitiño, Beatriz Rivas-Murias, Benito Rodríguez-González, and V. S. Exchange Bias Effect in CoO@Fe3O4 Core−Shell Octahedron-Shaped Nanoparticles. *Chemestry Mater.* **26,** 5566–5575 (2014).

7. Ullrich, A., Hohenberger, S., Özden, A. & Horn, S. Synthesis of iron oxide/manganese oxide composite particles and their magnetic properties. *J. Nanoparticle Res.* **16,** 2580 (2014).

8. Choi, S. H. *et al.* Simple and generalized synthesis of oxide-metal heterostructured nanoparticles and their applications in multimodal biomedical probes. *J. Am. Chem. Soc.* **130,** 15573–15580 (2008).

9. Costi, R., Saunders, A. E. & Banin, U. Colloidal Hybrid Nanostructures: A New Type of Functional Materials. *Angew. Chemie Int. Ed.* **49,** 4878–4897 (2010).

10. Figuerola, A. *et al.* One-pot synthesis and characterization of size-controlled bimagnetic FePt-iron oxide heterodimer nanocrystals. *J. Am. Chem. Soc.* **130,** 1477–1487 (2008).

11. Buonsanti, R. *et al.* Architectural control of seeded-grown magnetic-semicondutor iron oxide-tiO2 nanorod heterostructures: The role of seeds in topology selection. *J. Am. Chem. Soc.* **132,** 2437–2464 (2010).

12. Zeng, H. & Sun, S. Syntheses, Properties, and Potential Applications of Multicomponent Magnetic Nanoparticles. *Adv. Funct. Mater.* **18,** 391–400 (2008).

13. Moya, C., Morales, M. D. P., Batlle, X. & Labarta, A. Tuning the magnetic properties of Co-ferrite nanoparticles through the 1,2-hexadecanediol concentration in the reaction mixture. *Phys. Chem. Chem. Phys.* **17,** 13143–13149 (2015).

14. Moya, C., Morales, M. D. P., Batlle, X. & Labarta, A. Tuning the magnetic properties of Co-ferrite nanoparticles through the 1,2-hexadecanediol concentration in the reaction mixture. *Phys. Chem. Chem. Phys.* **17,** 13143–13149 (2015).

15. Gomes, J. D. A. *et al.* Synthesis of Core - Shell Ferrite Nanoparticles for Ferrofluids : Chemical and Magnetic Analysis. 6220–6227 (2008).

16. Wei, H. *et al.* Supporting Information Compact Zwitterion-Coated Iron Oxide Nanoparticles for Biological Applications. *Nano Lett.* **12,** 1–11 (2012).

9. Ni@NiO Core-Shell Nanoparticles

9a. Comparison between oxidation method[1]

9a.1. Introduction

In order to find a strategy to increase the magnetic stability, ferromagnetic and antiferromagnetic materials were matched to develop an exchange-bias effect for biomedical[2] or magnetic recording[3] applications. In collaboration with the group of Prof. S. D'Addato (CNR-NANO, Modena and Dipartimento FIM, Università di Modena e Reggio Emilia) a magnetic study of Ni@NiO core-shell nanoparticles was carried out. Magnetic measurements were recorded in our laboratory by a Quantum Design MPMS XL-5 SQUID magnetometer. Ni@NiO core-shell NPs were synthesized by the group in Modena using a gas aggregation source. Several similar Ni metal NPs samples were oxidized using different procedures in order to create a metal oxide shell. Then, the magnetic properties have been measured and compared. Five of sample types were prepared by subjecting similar Ni NPs to different treatments as follows[4]

A) 6 nm Ni NPs with native oxide due to exposure to the air for 24 h;

B) 9 nm Ni NPs with native oxide due to exposure to to the oxygen in the NPs source;

C) 6 nm Ni NPs deposited in presence of dioxygen in the deposition chamber ($p_{O2}= 10^{-6}$ mbar);

D) 6 nm Ni NPs annealed at 250°C in air for 30 min;

E) Tri-layer NiO (1 nm)/ Ni (6 nm)/ NiO (3.5 nm) sequentially deposited.

The field cooled (FC) and zero-field cooled (ZFC) curves were recorded in the 5–300 K range with H_{cool} = 100 Oe and H_{meas} = 100 Oe. Magnetization isotherms were recorded between +2000 Oe and −2000 Oe at 5 K after field cooling (H_{cool} = +2000 Oe). The data were corrected for support diamagnetism then scaled to the nominal deposited nickel mass.

9a.2. Results and Discussion

	Sample				
	A	B	C	D	E
T_{max} (K) [a]	140	220	65	220	200
M_{2000} (emu/g) [b]	35.6	15.6	21.7	35.0	18.1
M_{rem} (emu/g) [b,c]	5.6	6.9	5.7	6.3	3.8
M_{rem}/M_{2000}	16%	45%	26%	34%	39%
H_c (kOe)	0.19	0.34	0.12	0.31	0.40
H_{cr} (kOe)	0.41	0.49	0.45	0.81	0.70
H_{bias} (kOe)	0.002	0.011	0.023	0.16	0.30

[a] Temperature where M_{ZFC} reaches its maximum value. The estimated uncertainty is ±10 K.

[b] Magnetization is reported as magnetic moment / nominal mass of deposited nickel.

[c] The remanence value has been corrected for the shift of the $M(H)$ loop due to exchange bias.

Table 1: Magnetic parameters of the Ni@NiO core-shell NPs

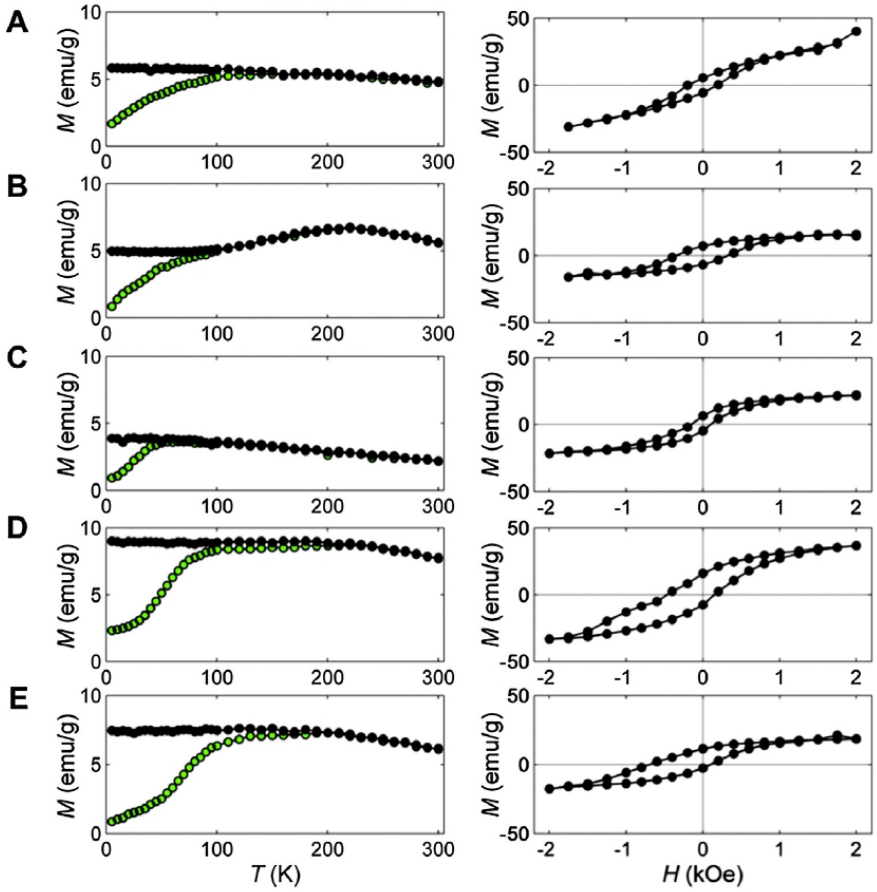

Figure 1: Left: FC (black circles, H_{cool} = 100 Oe) and ZFC (green circles) magnetization curves. Right: FC (H_{cool} = 2000 Oe) magnetization isotherms at 5 K.

Our samples contain NPs with diameters smaller than the critical diameter for single-domain state and coherent magnetization rotation (48 and 50 nm, respectively).[5] Thus, they are single-domain NPs where magnetization inversion occurs by coherent rotation. The zero-field cooled (ZFC) and field cooled (FC) magnetization curves $M(T)$ are displayed in Figure *1* and the temperature T_{max} corresponding to maximum M_{ZFC} are reported in Table *1*. T_{max} can be considered as an approximation to the blocking temperature T_B , which is the temperature boundary between the blocked state at low temperature and the reversible regime dominated by superparamagnetism at high temperature. T_{max} is an average blocking temperature for the NPs set and also takes into account the interparticle interactions. All samples have a reversible region down to T_{max} where the ZFC and FC curves are linear, as previously observed,[4] This

feature was attributed to coupling between NPs.[6] In the blocked regime ($T < T_{max}$), samples A and C show a decrease of M_{ZFC} an increase of M_{FC}. Samples D and E have a constant M_{FC} while M_{ZFC} shows a complex behavior. Sample B has constant M_{FC} the irreversible region and peak shape in the 100–300 K range. These curves can be understood as follows. Samples A and C–E display the blocking of the (interacting) NP from the SPM regime into a blocked state where the magnetic moments are randomly oriented. In samples D and E, blocking sets in at higher temperature, supporting the presence of stronger Ni/NiO interaction. Sample B shows sign of spin-glass-like state[7] because of the magnetic dipole-dipole interactions that in this case are stronger due to the larger nanoparticle density.

On inspection of the magnetization isotherm measured at 5 K, it is clear that all samples show an open hysteresis loop that closes at $H = \pm 2000$ Oe. However, samples A, C and D are not magnetically saturated at 2000 Oe.[8] The loop of sample A is a partially blocked single-domain NPs hysteresis,[9] while the loop of sample D has a "wasp-waisted" shape which is typical of samples containing NPs with largely different coercivity.[10] Furthermore, D and E samples have an asymmetric isotherm with a larger distance between the ascendant and the descendent branches at the negative-field side. The ratio between remanence magnetization and magnetization at 2000 Oe is always lower than the expected values. This means that a certain fraction of the NPs is in the superparamagnetic regime at 5 K, in agreement with the measured size distribution.

The shape of the hysteresis loops and the M_{rem}/M_{2000} indicates that the SPM magnetization is ordered as A > C > D > E > B. it is clear the presence of the metal oxide shell and its stabilizing effect on the NPs. Similar ordering of the coercivity H_c was observed due the presence of SPM magnetization. The remanence coercivity H_{cr} more closely describes the magnetization inversion than H_c as it is does not depend on SPM. H_{cr} ranges between 0.4 and 0.5 kOe for samples A, B and C, and is approximately twice as large for sample D and tri-layer sample E (see Table *1*). H_c and H_{cr} values show that the NiO shell raises the barrier to

magnetization inversion. The magnetization isotherms have very different EB shifts, numerically represented by the bias field H_{bias} (figure *1*). H_{bias} is zero for sample A and it is very small for samples B and C (a few % of H_{cr}). Annealed sample D displays a large bias field (20%of H_{cr}). H_{bias} of the tri-layer sample E is very large, reaching 43% of H_{cr}. The large bias field of D and E, in connection with the data above described, is proof of the presence of a strong EB interaction across the NiO/Ni interface.

9a.3. Conclusion

The dependence of the magnetic properties of core-shell NPs synthesized by different oxidation methods was investigated. The samples were oxidized by different protocols, as reported above. Magnetic measurements showed that exchange bias is negligible for samples A, B and C because NiO did not a form complete shell, with only few oxide islands on the metal Ni surface, despite they had a good quality interface.[11] Sample D (annealed at 250°C) had a thick NiO coating and displayed a significant exchange bias. At last, sample E (tri-layer NiO/Ni/NiO) showed the largest exchange bias effect thanks to the high quality at the interface between Ni/NiO.[8] This strong exchange bias and the possibility to easily modify and control the tri-layer structure, prompted us to further investigate this heterostructure in order to explore the possibility of increasing their magnetic stability.

9b. Comparison between antiferromagnetic shell thickness[12]

9b.1. Introduction

The above described results show that trilayer samples can display large exchange bias and are then a promising system for high-temparature magnetic stability due to the high quality of the interface between the ferro- and antiferro-magnetic components. An additional advantage of trilayer samples is the possibility to accurately change both the core size and the shell thickness (independent of each other). In a new series of experiments, seven different trilayers samples were prepared by (i) preparing a 1 nm thick layer of NiO on a silicon substrate; (ii) evaporating Ni from a thermal evaporator under Ar atmosphere (in three interconnected vacuum chambers)[4 13 14] thus depositing ≅12 nm ferromagnetic Ni cores on the NiO bottom layer; (iii) coating the Ni cores with a shell of antiferromagnetic NiO with different thickness:

g) 6.5 nm NiO third layer; TriL 6.5

f) 3 nm NiO third layer; TriL 3

e) 2 nm NiO third layer; TriL 2

d) 1 nm NiO third layer; TriL 1

c) 0.67 nm NiO third layer; TriL 0.67

b) 0.33 nm NiO third layer; TriL 0.33

a) No NiO third layer. TriL 0

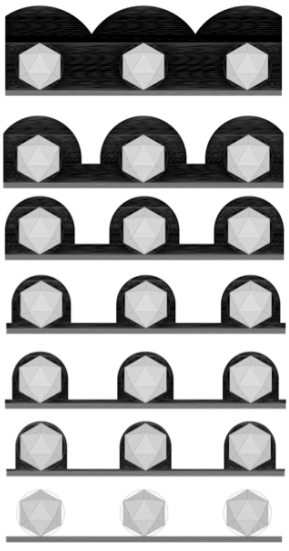

Magnetization measurements were carried out by a Quantum Design MPMS XL-5 SQUID magnetometer. Field Cooled (FC) and Zero-Field Cooled (ZFC) thermal magnetization curves were recorded in the 5 – 300 K range with cooling field Hcool = 100 Oe and measuring field

Hmeas = 100 Oe. Magnetization isotherms were recorded between +2000 Oe and –2000 Oe at 5 K after field cooling (Hcool = +2000 Oe). The data were corrected for support diamagnetism[15] and, in the case of magnetization isotherms, scaled to the nominal deposited nickel mass.

9b.2. Results and Discussion

To properly discuss the magnetic properties, it is important to note that the nominal thickness $t3_{,NiO}$ of the top NiO layer can be very different from the true thickness t_s. Extensive SEM and (S)TEM investigation by the Modena group lead to the following results:

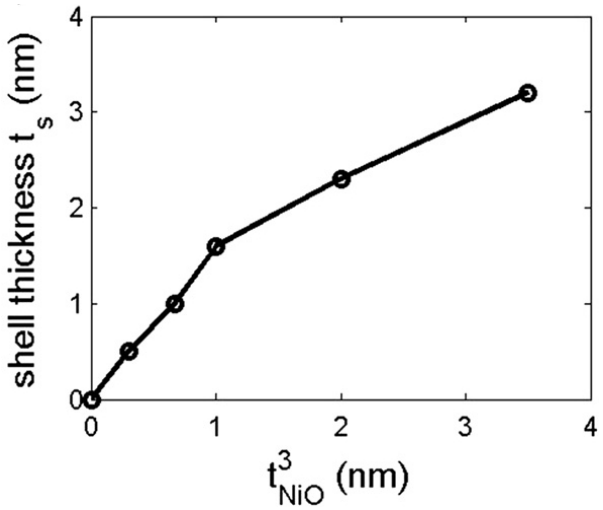

Figure 2: Plot of the true (estimated) shell thickness t_s vs.the nominal thickness $t_{3,NiO}$ of the third (top) NiO layer.

Sample	TriL 0	TriL 0.33	TriL 0.67	TriL 1	TriL 2	TriL 3.5	Tril 6.5
M_s (emu/g) [a]	13.4	12.9	17.6	21.6	31.5	16.1	14.9
M_{sr} (emu/g) [a]	5.4	6.9	9.9	8.4	16.2	7.1	6.2
M_{sr} / M_s	0.40	0.56	0.56	0.39	0.51	0.44	0.42
H_{bias} (kOe)	0.022	0.045	0.043	0.062	0.25	0.31	0.57
H_{bias} / H_c	0.13	0.19	0.17	0.27	0.56	0.75	1.03
H_c (kOe)	0.17	0.23	0.25	0.23	0.44	0.42	0.55
H_{cr} (kOe)	0.27	0.32	0.32	0.37	0.58	0.70	0.89
H_{cr} / H_c	1.6	1.4	1.3	1.7	1.3	1.7	1.6
H_{cr}(+–) (kOe)	0.27	0.36	0.37	0.43	0.82	1.03	1.41
H_{cr}(–+) (kOe)	0.27	0.29	0.26	0.31	0.35	0.37	0.46

[a] Magnetization was scaled with respect to the nominal mass of deposited nickel.

Table 2: Magnetic parameters of trilayer Ni@NiO core-shell NPs extracted from magnetization isotherms at T = 5 K.

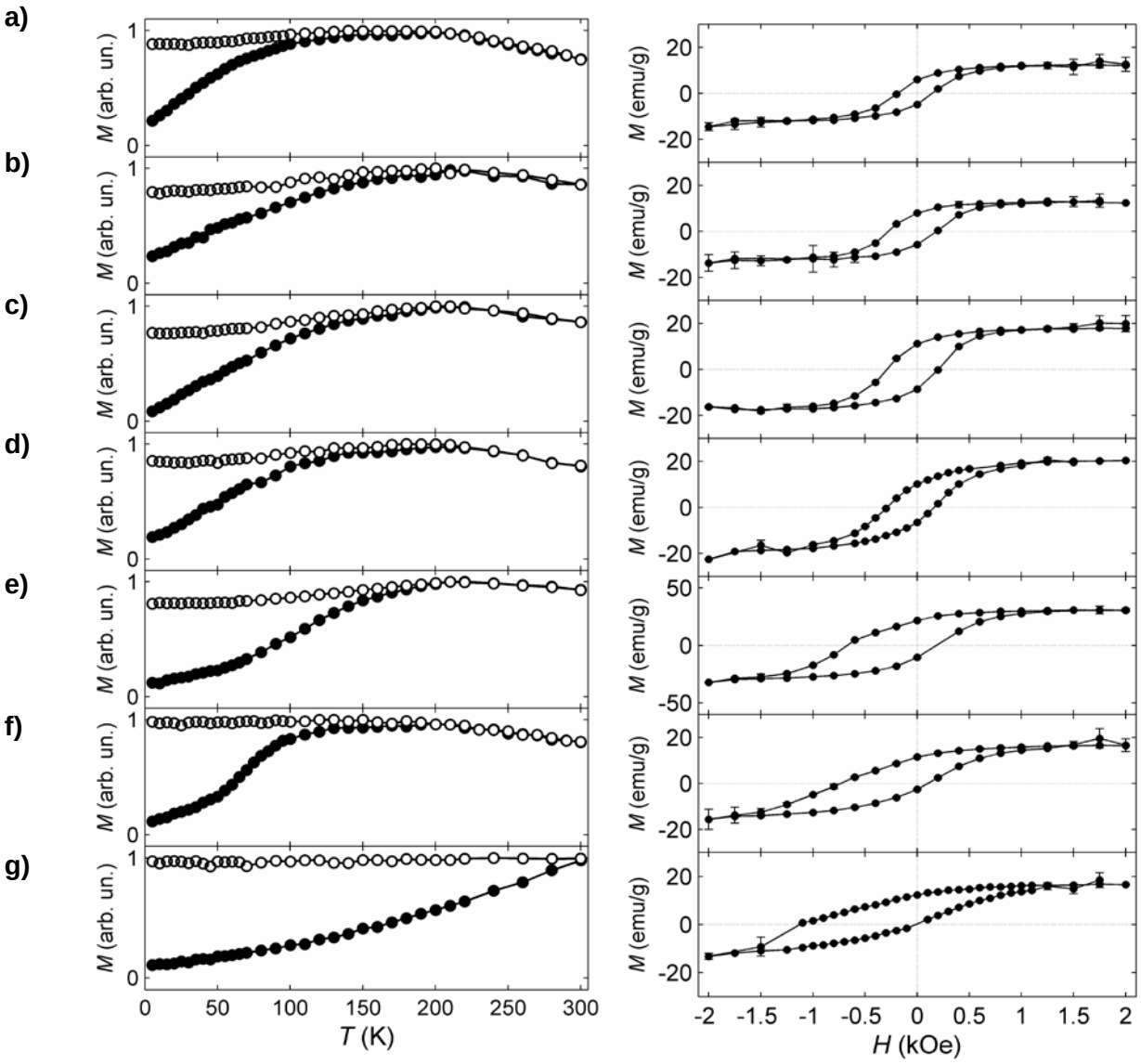

Figure 3: FC (hollow circles) and ZFC (solid circles) thermal magnetization curves (left) and FC magnetization isotherms (right, H_{cool} = +2000 Oe, T = 5 K) of Ni@NiO core-shell NPs. Magnetization M has been corrected for the support diamagnetic contribution and, in the case of magnetization isotherms, scaled to the nominal deposited nickel mass. a) TriL 0; b) TriL 0.3; c) TriL 0.67; d) TriL 1; e) TriL 2; f) TriL 3.5; g) TriL 6.5.

Before discussing the magnetic data, it is important to recall that an ideal Ni NP with diameter d < 50 nm is a single domain NP and coherent rotation is required to induce a

magnetization reversal. The superparamagnetic (SPM) blocking diameter of an ideal Ni NPs is ≅ 34 nm at room temperature and ≅ 9 nm at 5 K. A population of ideal Ni NPs (similar to those used in this work) with diameter around 12 nm would have a mean blocking temperature $<T_B>$ = 15 K and standard deviation σ_{T_B} = 4 K. Therefore, NPs in such population would be well into the SPM regime at room temperature and almost completely blocked at 5 K.

The ZFC and FC curves have a similar behavior for samples from "a" to "e" and a very different shape for sample "g"; sample "f" is intermediate in behavior. The zero-field-cooled (M_{ZFC}) and field-cooled (M_{FC}) magnetizations diverges at low temperature because of the alignment induced in the sample by the applied field on cooling; such difference decreases with the temperature increase because the thermal energy allows the magnetic moments to pass over the energy barrier caused by the magnetic anisotropy. When this difference vanishes, the magnetization has entered the superparamagnetic reversible regime. In the tri-layer samples, reversibility sets in at temperature T_{max} where M_{ZFC} is maximum. This temperature is a common estimate of the blocking temperature T_B. Samples from "a" to "f" have T_{max} = 200-220 K, much higher than the blocking temperature expected for Ni NPs of equal size. At high temperature (reversible regime) the M_{ZFC} and M_{FC} curves are linear as previously observed for interacting superparamagnetic NPs.[4] Another common estimate of the blocking temperature is the $T_{1/2}$ temperature, where M_{ZFC} reaches half of its maximum value. $T_{1/2}$ is approximately constant value for samples from "a" to "f", just like T_B. For samples "a" to "e" a decrease of M_{FC} at low temperature is also observed. This is a signal of the formation of a collective spin-glass-like state due to the random interaction between the NPs.[7 16] Sample "g" has a completely different behavior. It does not reach reversibility even at 300 K and has high T_{max} > 300 K and $T_{1/2}$ ≅ 190 K, meaning that its magnetic anisotropy barrier is much larger than other samples' barrier. M_{FC} is constant throughout the whole temperature range for "g" and below 150 K for "f", showing that samples "f" and "g" do not undergo transition to a

spin-glass-like state. Samples from “a” to “f” have T_{max} (about 200 K) much higher than the blocking temperature of equally-sized ideal NPs [T_B = (15 ± 4) K].[7]

Exchange bias not seems to be the cause of the high blocking temperature as judged from magnetic data. It is more likely that the presence of magnetostatic interactions between the NPs, suggested by the estimate of NP density on the substrate and the linearity of the reversible portion of the $M_{(Z)FC}$, is responsible for the high T_B of these samples. Sample “g” manifests a larger T_{max} despite having similar Ni core size and density and, accordingly to this, having average magnetostatic interactions similar to those of the others samples. A similar T_{max} increase has been previously observed for Co@CoO NPs in Al_2O_3 matrix.[17] This phenomenon was attributed to the local recovery of antiferromagnetic properties and to the interfacial coupling between two or more core-shell structures which are in contact. A similar situation could be present in the “g” sample, maybe reinforced by the large NiO thickness coating the Ni NPs. The strong coupling between Ni and NiO interface leads to an enhanced magnetic anisotropy, a blocking temperature higher than the room temperature and reduced magnetostatic inter-nanoparticle interaction in agreement with the absence of spin-glass-like state.

We now switch to analyzing the magnetization isotherms, measured at 5 K after field cooling (Hcool = +2 kOe). It is easy to see that all samples have an open hysteresis loop and are magnetically saturated before the field reaches ±2 kOe, as expected for blocked NPs. The remanence/saturation M_{sr}/M_s ratio demonstrates that TriL NPs display uniaxial anisotropy due to surface effects. Moreover, the M_{sr}/M_s ratio corroborates the idea that the Ni@NiO NPs are blocked at low temperature as previous suggested by the shape of the magnetization isotherm. It is important to notice that samples “a” to “f” show major loops where magnetic saturation is achieved at both loop extremes and no vertical shift is present.[18] On the other hand, the loop of sample “g” is an exception with a slight vertical shift. Accordingly, its coercive and exchange-bias field values will be slightly less accurate.

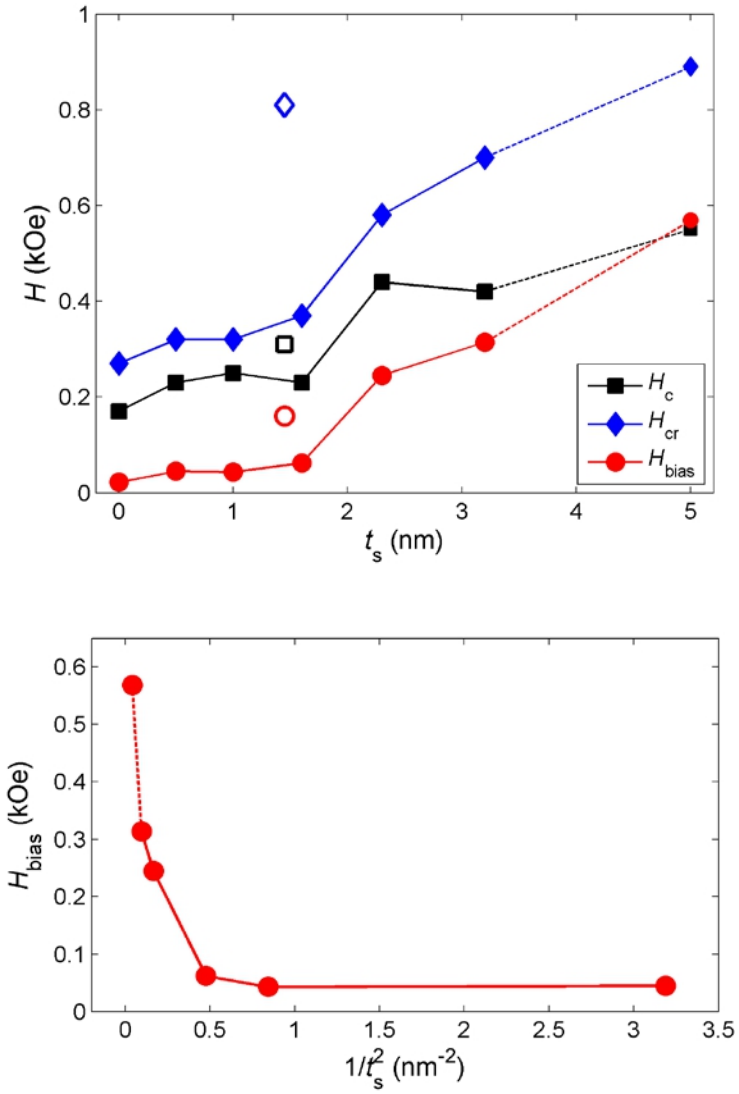

Figure 4: Dependence of the magnetic parameters of Ni@NiO core-shell NPs on the estimated NiO shell thickness t_s. The shell thickness of TriL 6.5 was extrapolated as denoted by the dashed lines. The shell thickness of the Ann sample was estimated from STEM images. (Top) Thickness dependence of coercivity H_c (black squares), remanence coercivity H_{cr} (blue diamonds), and bias field H_{bias} (red circles). TriL samples: solid markers; Ann sample: hollow markers. (Bottom) Dependence of H_{bias} of TriL samples on $1/t_s^2$.

A change in the isotherm loop shape is reflected also in a variation of the coercivity and exchange-bias fields. It is interesting to observe a plot where these fields are related to the shell thickness [figure *4*]. Coercivity field tends to increase with the shell thickness but the

variation is irregular and not easily explicable, whereas the exchange-bias field grows monotonically with increasing t_s. In detail, sample "a" has a very small but not negligible exchange-bias field due to the presence of the first NiO layer and also the presence of a possible oxidative process that occurs when a sample is exposed to the air.[19] H_{bias} is slightly larger for samples "b" and "c" where the NiO shell is not complete on the Ni metal surface. From sample "d" on, H_{bias} increases according with the shell thickness and it does not saturate for the largest top layer thickness we studied. For samples "d" to "g", the increase is steep because the NiO shell is complete around the Ni core, in particular in the "g" sample the NiO forms a discontinuous film which embeds the Ni cores.

In exchange-coupled magnetic structures, the exchange-bias effect is closely linked to the thickness of the antiferromagnetic layer because the anisotropy energy is proportional to the layer thickness *t*. Other important magnetic parameters such as the antiferromagnetic anisotropy constant *K*, the Neél temperature T_N and the antiferromagnetic blocking temperature $T_{B,AFM}$ depend strongly on the antiferromagnetic layer thickness.[6] Lastly, the good quality of the interface between ferro- and antiferro- magnetic materials and their coupling are the crucial point that needs a fine control in order to achieve an effective core-shell structure with a detectable exchange-bias effect. It is noticed that T_N of NiO is close to room temperature for $t_s \approx 1$ nm and $T_{B,AFM}$ of NiO is often a few tens of K below the T_N.[20] Thus, the NiO anisotropy energy E_{an} and the NiO anisotropy constant *K* likely are the parameters involved to explain how the shell thickness affects the EB. The Meiklejohn-Bean approach is based in the assumption that the anisotropy energy E_{an} is linearly dependent on the shell thickness and ignores the thickness influence on other magnetic parameters.[21] Within this model, H_{bias} is null when t_s is below a critical value $t_{s,crit}$ and H_{bias} is proportional to t_s^{-2} for $t_s > t_{s,crit}$, setting for an asymptotic value $H_{bias}(t_s \rightarrow \infty)$ for very large t_s. As shown, in Figure *444*, our data are far from the linear dependence predicted by the Meiklejohn-Bean model. It

is conceivable that trilayer samples differ from each other in some magnetic parameters (in addition to the E_{an}) which are essential for the exchange-bias effect.[22] It is possible that the main contribution to the variation of H_{bias} could be ascribed to the enhancement of the NiO anisotropy constant K when the shell thickness increases. It has been recently shown[22] that the uniaxial anisotropy in a Fe/NiO bilayer is small for $t_s < 1.5$ nm, increases up to $H_K = 150$ Oe when $t_s = 5.5$ nm, and is then essentially constant. This is very similar to the behavior of H_{bias} in TriL samples. Thus, we therefore propose that the main contribution to H_{bias} in our TriL core–shell NPs can be attributed to the increase of the NiO anisotropy constant K as t_s increases.

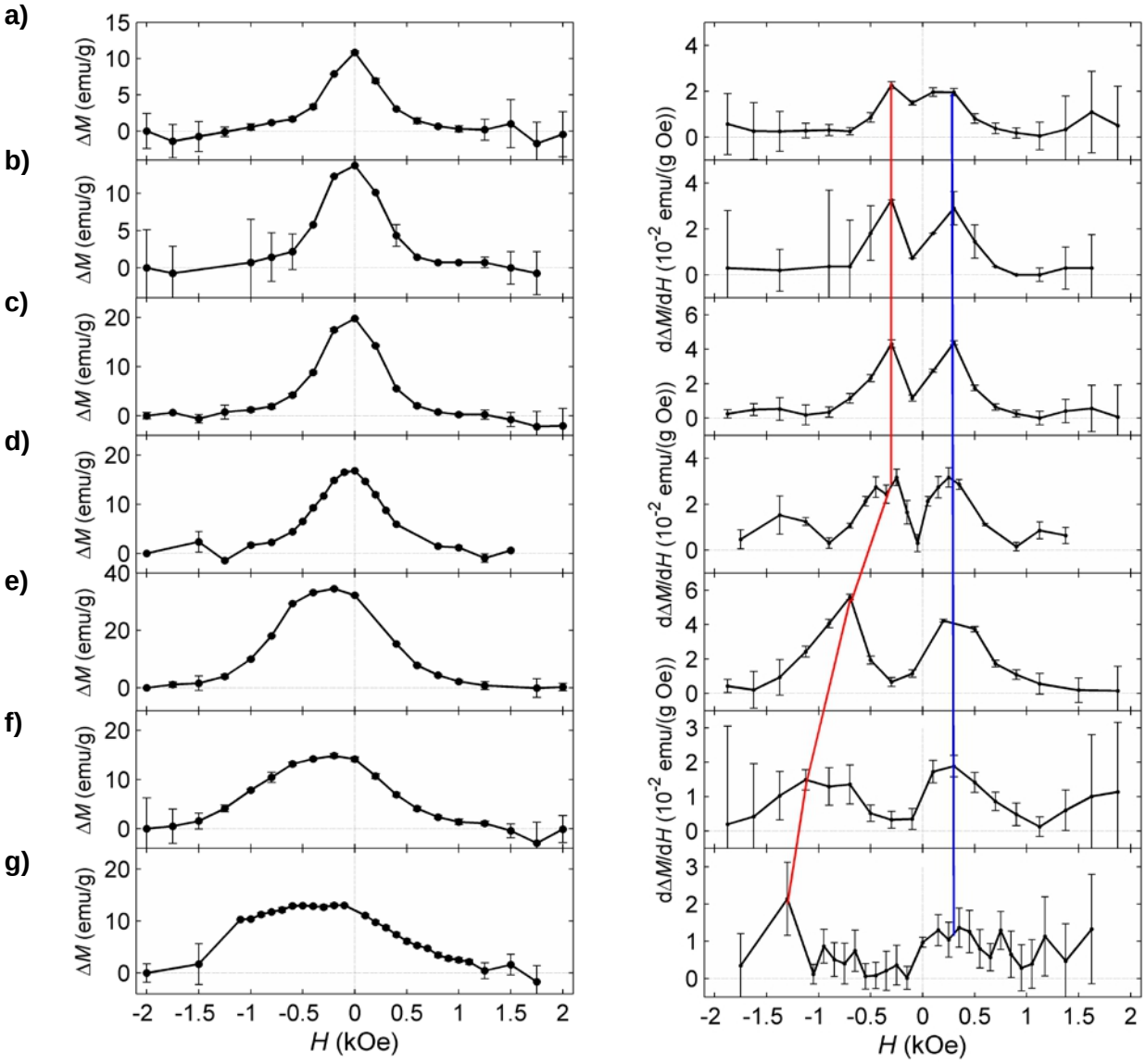

Figure 5: Remanence coercivity of the FC magnetization isotherms of Ni@NiO core-shell NPs calculated by the ΔM method. Left: cumulative remanence coercivity spectrum ΔM; right: remanence coercivity spectrum |dΔM/dH|. Both coercivity spectra have higher uncertainty than M(H) isotherms in Fig. 9 due to error propagation in algebraic manipulation. The red line puts in evidence the shift of the maxima of |dΔM/dH| for the (+M, –M) reversal; the blue line is for the (–M, +M) reversal. a) TriL 0; b) TriL 0.3; c) TriL 0.67; d) TriL 1; e) TriL 2; f) TriL 3.5; g) TriL 6.5.

To deeply understand the trilayer magnetic behavior, another quantity could be considered: the remanence coercivity $H_{cr.}$ This parameter is the field needed to achieve a vanishing remanence and summarizes irreversible magnetization reversal better than H_c. Generally, H_{cr} increases with the increase of NiO shell thickness similarly to $H_{bias.}$ The slope change in the H_{cr} *vs.* t_s plot [Figure *4*] is again due to the formation of complete NiO shells on the Ni cores. This similar trends of both H_{bias} and H_{cr} is evidence that both these phenomena are generated by the exchange coupling at the Ni/NiO interface. The remanence coercivity of ideal Ni NPs (with uniaxial anisotropy) is about 1.048 $|K_{Ni}|/M_s \cong 0.32$ kOe.[9] [23] This value is very similar to the H_{cr} of "a" and "b" samples where the NiO has a very small effect on the Ni core coercivity. On the other hand in "e", "f" and "g" samples, high values of H_{cr} are evidence of higher barriers to magnetization reversal. The H_{cr} / H_c ratio ranges from 1.3 to 1.7 as expected for single-domain NPs which reverse their magnetization by coherent rotation.[15]

The magnetic parameters H_{bias}, H_c, and H_{cr} are used to summarize in few numbers the complex magnetic behavior of a nanoparticle population. Further information can be gathered by considering the micro-coercivity, that is, the barrier to magnetization reversal of individual NPs. The magnetization difference ΔM, (used above to calculate H_{cr}), is an approximation to the cumulative distribution of micro-coercivity.[24] ΔM is best understood by separately looking at the left ($H < 0$) and right ($H > 0$) semi-plots. [figure *5*] The left semi-plots show the (cumulative) distribution of the micro-coercivity for the $+M$ to $-M$ reversal where the magnetic moments are removed from the preferred orientation to the opposite direction, while the right semi-plots refer to the $-M$ to $+M$ reversal, where the Ni core magnetic moments return to the preferred orientation. The left semi-plot dramatically changes shape when the NiO shell thickness increases. It broadens, shifts toward more negative fields, and becomes flat in the (–1, 0) kOe range.

To the right of Figure [figure *5*], the (differential) distribution of micro-coercivity is approximated by $|d\Delta M/dH|$. The most probable micro-coercivity corresponds to the maximum

in these curves. Considering the $-M$ to $+M$ reversal (left semi-plot), the maximum is shifted by about 1 kOe from sample “a” to “g” upon NiO shell thickness increasing. In particular, it is more or less constant at –0.4 kOe for “a” and “b” sample, while progressively shifts to more negative values for “e”, “f” and “g” samples (–0.7, –1.1, and –1.3 kOe, respectively).

For small $t_{s,}$ the coercivity distribution is shifted and broadened but for “f” and “g” samples, where NiO shell is thickest, a probability decrease of finding the individual NP coercivity in the range (–1, 0) kOe occurs and the micro-coercivity distribution for the $+M$ to $-M$ reversal peaks are at –1.3 kOe. In the right semi-plot, the micro-coercivity distribution is much less affected by the NiO shell thickness. The NiO shell thickness is not able to affect the most remanence probable coercivity (+0.3 kOe) depicted by the blue dashed line [figure *5*] and there is an increase in $H_{cr}(-+)$ from 0.26 to 0.46 kOe related to a shape change in the right semi-plot with an enhanced probability for coercive fields in the (+0.5, +1) kOe.

9b.3. Conclusions

Ni@NiO core-shell NPs with equal core size and different shell thickness, prepared as trilayer NiO/Ni/NiO structures, have been investigated to understand the relationships between morphology and magnetic properties.

Samples with thin NiO top layer displayed a small EB field, but H_{bias} steeply grows from t_s = 1.6 on and, for the thickest shell, H_{bias} = 0.57 kOe, a value slightly larger than the corresponding coercivity. This behavior is related to the different morphology of the NiO external layer. For thin layers, NiO islands form and enlarge on the Ni cores, and a complete shell is achieved only at t_s = 1.6 nm. In the sample with the thickest NiO shell, a discontinuous NiO matrix (that embedding the Ni cores) was formed. The generalized Meiklejohn-Bean model could not explain the thickness-dependence of H_{bias} showed by these samples and a thickness dependence of the NiO anisotropy constant must be taken into account. Trilayer samples have lower H_{bias} than the annealed sample (with a similar shell thickness) due to the quality of the interface and the different mutual arrangement of the Ni and NiO crystal lattice. However, the main advantage of the trilayer NPs compared to the annealed NPs is that we are able to grow NiO with different shell thickness on a fixed Ni core size by an accurately controlled method. In this way, it was possible to separately investigate the contributions to the exchange bias arising from the thickness and interface quality. Furthermore, it was possible to prepare magnetic NPs with enhanced magnetic stability which demonstrates that the regulation of a “bulk” parameter (such as the antiferromagnetic anisotropy) could tune the exchange bias. These results are a first step towards the synthesis of magnetic NPs with tunable magnetic properties.

References

1. Addato, S. D. *et al.* Controlled growth of Ni / NiO core – shell nanoparticles : Structure , morphology and tuning of magnetic properties. *j Appl. Surf. Sci.* **306,** 2–6 (2014).

2. R. Hao, R. Xing, Z. Xu, Y. Hou, S. Gao, S. H. S. Synthesis, Functionalization and Biomedical Applications of Multifunctional Magnetic Nanoparticles. *Adv. Mat.* **22,** 2729 (2010).

3. J. Nogues, J. Sort, V. Langlais, V. Skumryev, S. Suri˜naz, J.S. Mu˜noz, M. D. B. Surface phase separation in nanosized charge-ordered manganites. *Phys. Rep.* **422,** 65 (2005).

4. S. D'Addato, L. Gragnaniello, S. Valeri, A. Rota, A. di Bona, F. Spizzo, T. P. & Schifano, S. F. Morphology and Magnetic properties of size-selected Ni nanoparticle films. *J. Appl. Phys.* **107,** 104318 (2010).

5. Coey, J. M. D. *Magnetism and Magnetic Materials, Cambridge University Press, Cambridge*. (2010).

6. C. Binns, M.J. Maher, Q.A. Pankhurst, D. Kechrakos, K. N. T. Magnetic behavior of nanostructured films assembled from preformed Fe clusters embedded in Ag. *Phys. Rev. B* **66,** 184413 (2002).

7. . S. Bedanta, W. K. Supermagnetism. *J. Phys. D Appl. Phys.* **42,** 013001 (2009).

8. A.C. Johnston-Peck, J. Wang, J. B. T. Synthesis and structural and magnetic characterization of Ni(core)/NiO(shell) nanoparticles. *ACS Nano* **3,** 1077–1084 (2009).

9. L. Tauxe, T.A.T. Mullender, T. P. Potbellies, wasp-waists, and superparamagnetism in magnetic hysteresis. *J. Geophys. Res. Solid Earth* **101,** 571–583 (1996).

10. Verosub, A. P. R. C. L. wasp-waisted hysteresis loop:mineral magnetic characteristics and discrimination of component in in mixed magnetic system. *J. Geophys. Res. Solid Earth* **100,** 17909–17924 (1995).

11. S. D'Addato, V. Grillo, S. Altieri, S. Frabboni, S. V. Assembly and structure of Ni/NiO core-shell nanoparticles. *Appl. Surf. Sci.* **260,** 13 (2012).

12. Maria Chiara Spadaro, Sergio D'Addato, Paola Luches, Sergio Valeri, Vincenzo Grillo, Enzo Rotunno, Manuel A Roldan, Stephen J Pennycook, Anna Maria Ferretti, E. C. and A. P. Tunability of exchange bias in Ni@NiO core-shell nanoparticles obtained by sequential layer deposition. *Nanotechnology* **26,** (2015).

13. Valeri, D. S. . G. V. . A. S. . F. S. . R. F. . Assembly and Fine Analysis of Ni/MgO Core/Shell Nanoparticles. *J. Phys. Chem. C* **155,** 14044 (2011).

14. S., D. S. . G. V. . A. S. ;Tond. R. ;Valer. S. ;Frabbon. Structure and stability of nickel/nickel oxide core–shell nanoparticles. *J. Phys. Condens. Matter* **23,** 175003 (2011).

15. Schlager, H. G.; v. Löhneysen, H. . Susceptibility of local magnetic moments in phosphorus-doped silicon near the metal-insulator transition. *Eur. Lett.* **40,** 661 (1997).

16. Del Bianco, L.; Hernando, A.; Fiorani, D. *Surface Effects in Magnetic Nanoparticles-Springer, New York, USA.* (2005).

17. Nogués, J.; Skumryiev, V.; Sort, J.; Stoyanov, S.; Givord, D. Shell-Driven Magnetic Stability in Core-Shell Nanoparticles. *Phys. Rev. Lett.* **97,** 157203 (2006).

18. Geshev, J. Comment on: 'Exchange bias and vertical shift in CoFe2O4 nanoparticles'. *J. Magn. Magn. Mater.* **320,** 600–602 (2008).

19. Frabboni, D. S. . G. V. . A. S. . T. R. . V. S. . Structure and stability of nickel/nickel oxide core-shell nanoparticles. *J. Phys. Condens. Matter* **23,** 175003 (2011).

20. J. Nogues, I. K. S. Exchange bias. *J. Magn. Magn. Mater.* **192,** 203–232 (1999).

21. Ch. Binek, A. Hochstrat, W. K. Exchange Bias in a generalized Meiklejohn-Bean approach. *J. Magn. Magn. Mater.* **234,** 353 (2001).

22. L.Y. Ma, G. Chen, J. Li, J. Zhu, Z.Q. Qiu, Y. Z. W. NiO-thickness dependent magnetic anisotropies in Fe/NiO/Au(001) and Fe/NiO/MgO(001) systems. *J. Magn. Magn. Mater.* **324,** 528–533 (2012).

23. Cullity, B. D.;Graham, C. *Introduction to Magnetic Materials, 2nd ed, IEEE Press-Wiley, USA.* (2009).

24. Jackson, M.; Worm, H. U.; Banerjee, S. K. *Phys. Earth Planet. Inter.* (1990).

Acknowledgements

Vorrei ringraziare innanzitutto il Dott. Ponti per avermi dato la possibilità di lavorare a questo progetto di dottorato ed il Dott. Martinazzo per la sua disponibilità come tutor.

Inoltre ringrazio anche tutti coloro che sono stati coinvolti maggiormente in questo lavoro ed hanno contribuito all'ottenimento dei risultati riportati in questa tesi come la Dott.ssa Anna Ferretti (per le analisi TEM), il gruppo del Prof. D'Addato (per lo studio delle nanoparticelle di Ni@NiO sviluppato in collaborazione) ed il gruppo di elettrochimica dell'Università degli Studi di Milano (Dott. Minguzzi, Dott. Lugaresi e Dott. Visibile) che hanno iniziato ad interessarsi e si stanno tuttora occupando della caratterizzazione elettrochimica delle nanoparticelle di MnO.

Non posso certo dimenticarmi di ringraziare per tutto il supporto, la pazienza ed il tempo trascorso insieme il mitico lab fantolico di questi anni: Sara, Cristina, Alessandro, Marcello, Primiano, Marta e Sandro. Senza di voi, fantoli non sarebbe la stessa (anche se prima di conoscervi io ero una persona elegante!).

Grazie di tutto.